Magnetic Properties of Rare Earth Zirconate Pyrochlores

vorgelegt von
Master of Physics
Jianhui Xu
aus Hebei, China

von der Fakultät II - Mathematik und Naturwissenschaften
der Technischen Universität Berlin
zur Erlangung des akademischen Grades
Doktor der Naturwissensschaften
Dr. rer. nat.

g e n e h m i g t e D i s s e r t a t i o n

Promotionsausschuss:
Vorsitzender: Prof. Dr. Wolf-Christian Müller
Gutachterin: Prof. Dr. Bella Lake
Gutachter: Prof. Dr. Andrew Boothroyd
Gutachter: Prof. Dr. Steve T. Bramwell

Tag der wissenschaftlichen Aussprache: 04.10.2017

Berlin 2017

Acknowledgements

This thesis cannot be accomplished without the help from many people. I would like to thank them in the following lines. First of all, I would like to thank my supervisor Prof. Bella Lake for providing me the precious opportunity to perform my doctoral study. Her passion for science and critical thinking have been always encouraging me to move forward and will be valuable for my scientific career. I would like to thank Konrad Siemensmeyer for sharing his experience in experimental physics, data analysis and his help on my life in Germany. I would like to thank Nazmul Islam for teaching me how to prepare samples and for growing the single crystals for me without which I could not start my study. I would like to thank Dr. Vivek Anand for showing me how to work with PPMS and for sharing his research experiences. I would like thank Sokolowski André for the help on the some measurements. I would also thank the other colleagues in the group for your accompanying, Ralf, Anup, Diana, Christian, Shravani, Ekaterina, Alexandros. Life with you is full of fun.

I benefit a lot from many people outside the group and many of them I have not meet. Most of the experiments were done with the help from the instrument scientists and I would like to thank all of you, M. Frontzek, D. L. Abernathy, N. Casati, G. Ehlers, Y. Su, E. Feng, C. Ritter, Jens-Uwe Hoffmann, Manfred Reehuis, C. Baines, H. Luetkens, H. Walker and D. Adroja. I am indebted to the theoreticians Yi-Ping Huang, Michael Hermele and Owen Benton. The discussions with you upgrade greatly my understanding in physics. In this thesis several softwares have been used which greatly speed up the progress of the my study. I would like to thank all the authors of the softewares. First, thank Konrad again for sharing his Mathematica code for crystal field analysis where I started my experience of physical simulation. Second, thank Prof. Dr. Andrew Boothroyd for sharing SPECTRE and his patient enlightening discussions. Third, thank Sándor Tóth for developing the open source SpinW based on which I have done a lot of calculations and learnt lots of practical knowledge on the theoretical calculation. Finally, I would like to thank Joseph Paddison for his Reverse Monte Carlo code, Andrew Steele for his dipolar field calculation software, Shang Gao for showing me ALPS and Erxi Feng for showing me PyPlot.

I also want thank all the colleagues working in the same field. Although at some point we crash with each other, I really learn a lot of from your works and you make me keep improving myself and always trying to do a better job.

Finally, thank you Ying for all the love and care!

Abstract

This thesis is about the experimental investigation of three magnetic pyrochlore compounds $Nd_2Zr_2O_7$, $Sm_2Zr_2O_7$ and $Gd_2Zr_2O_7$. Powder and single crystal samples are synthesized and synchrotron X-ray diffraction and neutron diffraction indicate that the former two compounds crystallize in the well-ordered pyrochlore phase while $Gd_2Zr_2O_7$ has some Gd/Zr antisite defects. All three compounds show anomalies at 0.4, 0.5 and 0.7 K in the bulk property measurements, respectively, but only $Nd_2Zr_2O_7$ is found to develop a long-range magnetic order in its ground state. The crystal field splitting schemes of Nd^{3+} and Sm^{3+} ions are determined with inelastic neutron scattering which shows that the crystal field ground states of the two ions in pyrochlores are well-isolated dipolar-otcupolar doublets with Ising anisotropy, which is confirmed by the analyses of the susceptibility and specific heat data. The neutron diffraction reveals "all-in/all-out" magnetic order in $Nd_2Zr_2O_7$ and liquid-like spin correlations in the Heisenberg antiferromagnet $Gd_2Zr_2O_7$. The absence of long-range order in $Gd_2Zr_2O_7$ is related to the antisite defects and the neutron diffraction pattern is analysed by the reverse Monte Carlo method, which reveals dipolar spin correlations and the local Palmer-Chalker type spin configuration on the tetrahedron. Muon spin relaxation spectra (above 20 mK) of $Nd_2Zr_2O_7$ indicates persistent spin dynamics in the ordered state and anomalously slow paramagnetic spin dynamics. The muon spin relaxation spectra of $Gd_2Zr_2O_7$ (above 1.5 K) and $Sm_2Zr_2O_7$ (above 20 mK) indicate the strong dynamical nature of the system.

The single crystal inelastic neutron scattering of $Nd_2Zr_2O_7$ reveals spin wave excitations in the ordered state and the spectra are fitted using linear spin wave theory allowing the spin Hamiltonian to be extracted. The spin Hamiltonian provides an explanation for the pinch point pattern observed in the polarized neutron scattering data as well as the scattering sheets perpendicular to the crystallographic (110) direction shown in the unpolarized neutron scattering experiment with field along the (1-10) direction. The Hamiltonian also explains the field-induced spin-flip transition and the hysteresis in the ordered state in the AC susceptibility measurements with DC fields along the [111] direction. According to the spinon calculation and the inelastic neutron scattering data above the ordering temperature, $Nd_2Zr_2O_7$ shows some features expected for the quantum spin ice state.

Zusammenfassung

Diese Dissertation behandelt experimentelle Untersuchungen an drei magnetischen Pyrochloren, $Nd_2Zr_2O_7$, $Sm_2Zr_2O_7$ and $Gd_2Zr_2O_7$. Es wurden einkristalline und pulverförmige Proben hergestellt wobei die zwei erstgenannten Substanzen in der Pyrochlor Struktur kristallisieren, während $Gd_2Zr_2O_7$ einige Platzwechsel-Defekte von Gd/Zr aufweist. Alle Verbindungen zeigen in den makroskopischen Eigenschaften Anomalien jeweils bei 0.4, 0.5 und 0.7K, allerdings zeigt nur $Nd_2Zr_2O_7$ langreichweitige Ordnung. Die Termaufspaltung der Nd^{3+} und Sm^{3+} Ionen im Kristallfeld wird aus Messungen mit inelastischer Neutronenstreuung bestimmt. Der Kristallfeld Grundzustand dieser Ionen im Pyrochlor-Gitter besteht aus Dipol-Oktupol Dubletts mit Ising Anisotropie, die gut von anderen Zuständen getrennt sind. Dies wird bestätigt durch eine Analyse der Suszeptibilität und der spezifischen Wärme. Neutronenstreuung zeigt magnetische Ordnung vom Typ "all in/all out" in $Nd_2Zr_2O_7$ sowie Korrelationen wie in einer Spinflüssigkeit bei $Gd_2Zr_2O_7$. Das Fehlen von langreichweitiger Ordnung in $Gd_2Zr_2O_7$ hängt zusammen mit Platzwechsel-Defekten. Die Diffraktionsdaten aus der Neutronenstreuung werden mit der "reverse Monte Carlo" Methode analysiert, dies ergibt dipolare Spin Korrelationen und eine lokale Anordnung der Spins vom Typ Palmer-Chalker auf den Tetraedern. Die Spektren der Myon-Spin Resonanz (oberhalb von 20 mK) zeigen fortbestehende Spin-Dynamik im geordneten Zustand sowie ungewöhnlich langsame Dynamik im paramagnetischen Bereich. Die Myon Spektroskopie von $Gd_2Zr_2O_7$ (oberhalb 1.5 K) und $Sm_2Zr_2O_7$ (oberhalb 20 mK) zeigt das stark dynamische Verhalten der Systeme.

Die inelastische Neutronenstreuung an Einkristallen von $Nd_2Zr_2O_7$ zeigt im geordneten Zustand Spinwellen. Der magnetische Hamiltonian wird aus einer Anpassung der Spektren mit linearer Spinwellen-Theorie bestimmt. Der Hamiltonian erklärt die Muster von Einschnürungen die mit polarisierter Neutronenstreuung beobachtet werden sowie die 2D Flächen in der Streuung senkrecht zur (110) Richtung mit unpolarisierter Neutronenstreuung und Feld entlang der (1-10) Richtung. Weiter kann damit der feldinduzierte Spin-Flop Übergang und die Hysterese der AC Suszeptibilität im geordneten Zustand in (1-10) verstanden werden. Aus Spinon Rechnungen und den inelastischen Neutronendaten an $Nd_2Zr_2O_7$ oberhalb der Ordnungstemperatur folgen einige Eigenschaften, die für einen Quanten-Spin Eis Zustand erwartet werden.

Contents

1 Introduction to the thesis

The topic of the thesis is the experimental study of three new pyrochlore compounds with light rare earth elements $Nd_2Zr_2O_7$, $Sm_2Zr_2O_7$ and $Gd_2Zr_2O_7$. $Nd_2Zr_2O_7$ and $Sm_2Zr_2O_7$ are Ising anisotropic according to the crystal field theory and the less-localized $4f$ electrons could enhance the transverse coupling between the spins which are necessary for the quantum spin ice phase. $Gd_2Zr_2O_7$ is a Heisenberg pyrochlore antiferromagnet with nearly zero orbital moment and is a candidate for the classical spin liquid. The experimental techniques used include macroscopic measurements, X-ray and neutron diffraction and single crystal neutron scattering.

The thesis is organised as follows. The first two following chapters present the theoretical background and the principles of the experimental techniques involved in the thesis. Chapter 2 provides a short introduction on the related theory with emphasis on the topics relating to the three compounds. It begins with the single-ion magnetism and then introduces the interactions between the magnetic ions in solids and the conventional magnetic order and spinwave excitation. Finally, the concept of geometrical frustration and the spin ice physics in pyrochlores are introduced which are closely related to this thesis. Chapter 3 presents the principles of the experimental techniques of bulk property measurements, neutron scattering and muon spin relaxation. The main experimental method used is neutron scattering which is a valuable tool for the investigation of the static and dynamic properties of condensed matters.

There are six chapters providing the details of the studies on the three compounds with various experimental and theoretical methods. Chapter 4 presents synthesis and basic properties of the three compounds (powder and single crystal) including crystal structure, DC and AC susceptibility, magnetisation and specific heat. Chapters 5-7 present the main results of $Nd_2Zr_2O_7$. In chapter 5, the crystal field state and magnetic order are determined with inelastic neutron scattering and neutron diffraction experiments on the powder sample. In chapter 6, the single crystal inelastic neutron scatter data are presented and the observed magnetic excitations are analysed using linear spinwave theory where the exchange constants are extracted. The same chapter also presents the data and analyses of the single crystal polarized neutron scattering, unpolarized neutron

scattering with fields and AC susceptibility in DC fields. In chapter 7, the spin dynamics of $Nd_2Zr_2O_7$ is investigated using muon spin relaxation where persistent spin dynamics are found in the ordered state. Chapter 8 presents the study on the short-range spin correlations and spin dynamics of the Heisenberg antiferromagnet $Gd_2Zr_2O_7$ using neutron powder diffraction (above 60 mK) and muon spin relaxation (above 1.55 K). Reverse Monte Carlo refinement reveals dipolar spin correlations and Palmer-Chalker type local spin configuration on a tetrahedra. Chapter 9 presents the crystal field and spin dynamics studies on $Sm_2Zr_2O_7$ with powder inelastic neutron scattering and muon spin relaxation (above 20 mK) which shows that the crystal field ground state of Sm^{3+} is dipolar-octupolar Kramers doublet and there is a dynamical ground state in $Sm_2Zr_2O_7$. Finally the main results of all the studies of the three compounds are summarised in Chapter 10 and suggestions are given for the future research.

2 Magnetism in rare earth pyrochlores

2.1 Single ion magnetism

2.1.1 Free ion

Magnetism is generally related to the atoms or ions with unfilled electron shells where the unpaired electrons could show spin and orbital magnetic moments, such as the $3d$ transition metal elements and the $4f$ rare earth elements. The Hamiltonian for the electrons in the unfilled shells is

$$\mathcal{H} = \sum_i [\frac{p_i^2}{2m} + V(\boldsymbol{r}_i)] + \sum_{i<j} \frac{q^2}{r_{ij}} + \sum_i \xi(r)(\boldsymbol{l}_i \cdot \boldsymbol{s}_i). \tag{2.1}$$

On the right side, the first term is the summation of the single electron Hamiltonians for the electrons in the unfilled shells ("i" indicates the i^{th} electron) where $V(\boldsymbol{r}_i)$ is the electric potential due to the nucleus and the electrons in the inner closed shells. The second term is the Coulomb interaction between the electrons in the unfilled shells and the last term is the spin-orbital coupling interaction. The single electron Hamiltonian is mostly treated with the central field approximation and thus the orbital angular momentum l_i is a good quantum number. Due to the electron-electron Coulomb interaction and the Pauli exclusion principle, the orbital angular momenta of the electrons are coupled forming the total orbital angular momentum, $\boldsymbol{L} = \sum_i \boldsymbol{l}_i$, and the spin angular momenta form the total spin angular momentum, $\boldsymbol{S} = \sum_i \boldsymbol{s}_i$. The spin-orbital interaction couples the total orbital angular momentum with the total spin angular momentum, $\boldsymbol{J} = \boldsymbol{L} + \boldsymbol{S}$ (or $\boldsymbol{L} - \boldsymbol{S}$). The total angular momentum $\boldsymbol{J}$ takes the values $|L+S|$, $|L+S-1|$, ..., $|L-S|$ and each $\boldsymbol{J}$ corresponds to a manifold state of $2J+1$ degeneracy, $m_J = J, J-1, ..., -J$. Such a coupling scheme is called *Russell-Saunders* or *LS-coupling scheme* which applies to the lighter atoms where spin-orbital coupling is small compared with the Coulomb interaction between the electrons [1, 2]. The magnetic moment of these states can be calculated by

$$\boldsymbol{\mu} = -g_J \mu_{\text{B}} \boldsymbol{J}, \tag{2.2}$$

where g_J is the Landé g-factor,

$$g_J = \frac{3}{2} + \frac{S(S+1) - L(L+1)}{2J(J+1)}. \tag{2.3}$$

The ground state among these states is given by Hund's rules [3]. For example, the ground states of the ions studied in this thesis are: $^4I_{9/2}$ for Nd^{3+}, $^6H_{5/2}$ for Sm^{3+} and $^8S_{7/2}$ for Gd^{3+} (the $^{2S+1}L_J$ notation is used with S, P, D, F, G, H, I ..., corresponding $L = 0, 1, 2, 3, 4, 5$ ..., respectively) and the corresponding ion magnetic moments are 3.27, 0.71 and 7.0 μ_B.

Regarding the heavier atoms or ions, the spin-orbit interaction becomes stronger than the electrostatic repulsion interactions. The *j-j coupling scheme* should be adopted where the couplings of the spin and orbital angular momenta of individual electrons are first considered, $\boldsymbol{j_i} = \boldsymbol{l_i} + \boldsymbol{s_i}$, and then the coupling between $\boldsymbol{j}_i$s is considered. For rare earth ions, the Coulomb electrostatic interactions and spin-orbit interactions have the same order of magnitude. Therefore, another coupling scheme, *intermediate coupling scheme*, should be used which can be developed from the LS-coupling scheme [1, 2]. The intermediate-coupling wave function is formed by a linear combination of LS-coupling states of the same J with the Hund's-rules ground state as the dominating term.

In a magnetic field $\boldsymbol{H}$, the degeneracy of a J manifold is lifted by the Zeeman interaction,

$$\mathcal{H}_{\text{Zeeman}} = -g_J \mu_B \boldsymbol{H} \cdot \boldsymbol{J}. \tag{2.4}$$

In general, the splitting due to spin-orbit coupling is much larger than the Zeeman splitting, the magnetization of an ion can be calculated based on the thermal population of the Zeeman levels of the ground state J multiplet,

$$m_z = g_J J \mu_B B_J(x), \tag{2.5}$$

where the field direction is taken as the z axis, $x = g_J \mu_B m_J H / k_B T$ (k_B is the Boltzmann constant) and $B_J(x)$ is the Brillouin function [3].

If the Zeeman splitting is much smaller than the thermal energy $k_B T$, Eq. 2.5 can be expanded for $x \to 0$ and the leading term yields the Curie formula,

$$m_z = \frac{g_J^2 J(J+1) \mu_B^2 H}{3 k_B T}. \tag{2.6}$$

And the susceptibility is

$$\chi = \frac{\mathrm{d}m_z}{\mathrm{d}H} = \frac{g_J^2 J(J+1)\mu_\mathrm{B}^2}{3k_\mathrm{B}T} = \frac{\mu_\mathrm{eff}^2}{3k_\mathrm{B}T}. \tag{2.7}$$

where $\mu_\mathrm{eff} = g_J\sqrt{J(J+J)}\mu_\mathrm{B}$ is the effective magnetic moment. The effective moment in μ_B can be obtained from the susceptibility in emu/mol using [3]

$$\mu_\mathrm{eff} = 2.827\sqrt{\chi T}, \tag{2.8}$$

which is useful for tracking the evolution of the single ion moment with temperature.

2.1.2 Ion in crystals

The magnetic ion in a crystal is generally coordinated by oppositely charged (mostly negatively charged) ions which create a crystal electric field (CEF) of a lower symmetry than the symmetry of the free ion. The $2J+1$ degeneracy of a J multiplet is lifted by the crystal field due to the different orbital shapes of the different m_J states. The CEF potential can be calculated with the point charge approximation (ignoring the shapes and the overlaps of the electron clouds of the surrounding ions) [4],

$$\mathcal{H}_\mathrm{CEF} = \sum_i q_i V_i^\mathrm{CEF} = \sum_i \sum_j \frac{q_i q_j}{|(\boldsymbol{R}_j - \boldsymbol{r_i})|}, \tag{2.9}$$

where q_i and r_i is the charge and position of the i^th electron in the unfilled shells and q_j is the charge of the j^th neighboring ion at site $\boldsymbol{R}_j$. It is more convenient to express the CEF potential as the addition of the spherical harmonics functions or the related tensor operators so that the $\mathcal{H}_\mathrm{CEF}$ matrix elements of the magnetic electron wave functions can be easily calculated, that is [1, 2],

$$V_\mathrm{CEF} = \sum_{k,q} B_q^k C_q^k, \tag{2.10}$$

where B_q^k is the crystal field parameter and C_q^k is the tensor operator defined based on the spherical harmonics [1, 2],

$$C_q^k = (\frac{4\pi}{2k+1})^{1/2} Y_{kq}, \tag{2.11}$$

The crystal field interactions can be treated as the perturbation of the free ion Hamiltonian, which make corrections to the free ion eigenstates. The $\mathcal{H}_\mathrm{CEF}$ is diagonalized

together with the free ion Hamiltonian (also expressed in terms of tensor operators and parameterized according to the experiments) in the Hilbert space formed by the free ion states [1, 2]. Finally, the crystal field Hamiltonian is solved by calculating the reduced matrix elements which can be done according to some quantum mechanics formulas. In addition, a simpler way to solve the CEF Hamiltonian is with Stevens operator equivalents where $\mathcal{H}_{\mathrm{CEF}}$ is presented by the LS-coupling ground state multiplet with the mixing between the J multiplets ignored [1, 2]. In general, this method applies to the heavy rare earth elements for which the J-mixing effect is small due to the large energy gaps between ground state multiplet and the excited multiplets.
The site symmetry of the magnetic ion determines the set of the non-vanishing crystal field operators because the crystal field Hamiltonian must be invariant under the symmetry operations. Take a rare-earth ion in the pyrochlore as an example. The local symmetry is D_{3d} which allows six non-vanishing terms in the crystal field Hamiltonian (the z axis is chosen along the local cubic $\langle 111 \rangle$ direction of pyrochlore) [5],

$$\mathcal{H}_{\mathrm{CEF}} = B_0^2 C_0^2 + B_0^4 C_0^4 + B_3^4 (C_{-3}^4 - C_3^4) + B_0^6 C_0^6 + B_3^6 (C_{-3}^6 - C_3^6) + B_6^6 (C_{-6}^6 + C_6^6) \quad (2.12)$$

The symmetry analysis can also give indications for the CEF splitting scheme and degeneracy. The point group of the site symmetry can be presented in the single-ion manifold state. This representation is reducible and each irreducible representation corresponds to an energy level with the degeneracy being the dimension of the representation. The degenerate CEF states have the symmetry of the irreducible representation. According to Kramers theorem, time-reversal symmetry leads to degeneracy of the crystal field states: when J is a half integer, the crystal field states are a series of Kramers doublets like $|\pm m_J\rangle$; when J is a integer they split into a singlet $|0\rangle$ and a series of doublets. The rare earth ions in the pyrochlore compounds studied in this thesis are all Kramers ions. After obtaining the CEF energy levels and wave functions, the CEF moment, susceptibility, magnetization and specific heat can be calculated. The CEF wave functions are of the form of $\sum_i c_i |J, L, S, m_J\rangle_i$ where c_i are the normalized coefficients and the magnetic moment of a crystal field state is $m = \sum_i c_i^2 (g_J m_J)_i \, \mu_{\mathrm{B}}$. The temperature dependence

of the susceptibility due to the CEF effect is [6]

$$\chi_{\mathrm{CEF}} = \frac{\mu_{\mathrm{B}}^2}{Z}\Big[\frac{1}{k_{\mathrm{B}}T}\sum_i |\langle\phi_i|(\boldsymbol{L}_z + g_0\boldsymbol{S}_z)|\phi_i\rangle|^2 \exp(-\frac{E_i}{k_{\mathrm{B}}T}) + \sum_{i,j} 2\frac{|\langle\phi_j|(\boldsymbol{L}_z + g_0\boldsymbol{S}_z)|\phi_i\rangle|^2}{E_j - E_i}\exp(-\frac{E_i}{k_{\mathrm{B}}T})\Big] \quad (2.13)$$

with

$$Z = \sum_i n_i \exp(-\frac{E_i}{k_{\mathrm{B}}T}) \quad (2.14)$$

where the z axis is along the field direction, g_0 is the gyromagnetic factor of electron spin and E_i, ϕ_i, and n_i are the energy, wave function and degeneracy of the CEF level, respectively. The second term in Eq. 2.13 is the Van Vleck paramagnetic susceptibility which is temperature independent for a large CEF splitting. The magnetization in a small magnetic field can be calculated in a similar way. But for a large field with the Zeeman splitting comparable with the crystal field splitting, the Zeeman term should be included in the CEF Hamiltonian during the diagonalization.

When the temperature is very low compared with the first CEF excitation energy, the low-temperature magnetism is determined by the CEF ground state which is often a doublet of two-fold degeneracy. In this case, the pseudospin-1/2 model is adopted to describe the system at low temperature with a $\boldsymbol{g}$ tensor defined by $\boldsymbol{m} = \boldsymbol{g}\cdot\boldsymbol{\sigma}$ ($\mu_{\mathrm{B}}/\,\mathrm{ion}$) where $\boldsymbol{m}$ is the magnetic moment and $\boldsymbol{\sigma}$ is the pseudospin operator [7]. The $\boldsymbol{g}$ tensor is generally anisotropic due to the low symmetry of the CEF state. For example, the CEF ground state of the Yb^{3+} ion in $Yb_2Ti_2O_7$ is a well-isolated Kramers doublet and the $\boldsymbol{g}$ tensor has the planar anisotropy with $g_{xx}(\mathrm{or}\, g_{yy})/g_{zz} = 2.4$ [8]. The $\boldsymbol{g}$ tensor has Ising anisotropy (only g_{zz} nonzero) for Pr^{3+}, Nd^{3+}, Sm^{3+}, Dy^{3+} and Ho^{3+} in the pyrochlores. In this case the field dependence of the powder-averaged magnetization in the paramagnetic state can be calculated by [9]

$$\langle M\rangle = \frac{(k_BT)^2}{g_{zz}\mu_B\sigma H^2}\int_0^{g_{zz}\mu_{\mathrm{B}}\sigma H/k_{\mathrm{B}}T} x\tanh(x)\,dx, \quad (2.15)$$

where $\sigma = 1/2$ and H is the field. The derivation is given in Appendix A.

The crystal field splitting also contributes to the temperature dependence of the specific heat and the CEF specific heat (per mole magnetic ions) can be calculated by [10]

$$C_{\mathrm{CEF}} = 2N_A\frac{\mathrm{d}\,[Z^{-1}\sum_i n_iE_i\exp(-\frac{E_i}{k_BT})]}{\mathrm{d}\,T} \quad (2.16)$$

where Z is the partition function given by Eq. 2.14 and N_A is Avogadro constant.
In the case of transition metal ions, the orbital moment can be quenched by the crystal field. This is because the partially filled d shell is the outermost shell in contrast to the f shell which is partially shielded by outer electrons. However, a small orbital moment can be induced by the spin-orbital coupling though it is much weaker than the crystal field and a similar theory can be applied.

2.2 Magnetic interactions

2.2.1 Exchange interactions

The *direct exchange interaction* occurs when there is an orbital overlap between two atoms or ions and the Coulomb repulsion between the nearby electrons and the Pauli exclusion principle result in spin correlations of the electrons. Since electrons are fermions, the wave function must be antisymmetric which means that either the spatial part of the wave function is antisymmetric and the spin part is symmetric or vice versa. The energy difference between the two states depends on the exchange integral, which means that different spin orientations have different energies. Therefore, a spin Hamiltonian can be defined

$$\mathcal{H} = J_{12}\boldsymbol{S}_1 \cdot \boldsymbol{S}_2, \tag{2.17}$$

which is the famous Heisenberg model (J_{12} is the exchange constant).
In insulators (e.g. the $3d$ transition metal oxides), the magnetic electrons are localized and far away from each other. In this case, there is little direct orbital overlap between the magnetic ions and thus the direct exchange interaction is weak. However, the wave functions of the magnetic ions and the neighboring anions are hybridized and as a result, anion bridged *superexchange interaction* can exist. A set of semi-empirical rules for $3d$ transition element oxides were developed by Goodenough and Kanamori [11, 12] which shows that the sign and strength of the superexchange interaction depends on the specific geometry of the orbitals and exchange path.
The exchange interactions introduced above are generally isotropic with the exchange constant being a scalar. An *anisotropic exchange interaction* can be induced by single ion anisotropy (or spin orbital coupling) and the specific exchange path in which case the exchange interaction is described by a vector or a tensor. With an anisotropic interaction, the alignments of the spins along specific directions are favored. One example is the antisymmetric superexchange interaction or the so-called Dzyaloshinsky-Moriya (DM) interaction which occurs when the magnetic ions is not in a centre of inversion symmetry

and it can be written as [13, 14],

$$\mathcal{H}_{\mathrm{DM}} = \boldsymbol{D} \cdot (\boldsymbol{S}_1 \times \boldsymbol{S}_2), \tag{2.18}$$

where $\boldsymbol{D}$ is a vector perpendicular to the plane spanned by the two magnetic ions and the intermediate ion responsible for the superexchange interaction. The DM interaction tends to align the two spins perpendicularly.

2.2.2 Multipole interactions

The simplest multipole interaction is the classical dipole-dipole interaction,

$$\mathcal{H}_{\text{dipole-dipole}} = \frac{\mu_0}{4\pi r^3}[\boldsymbol{\mu}_1 \cdot \boldsymbol{\mu}_2 - 3(\boldsymbol{\mu}_1 \cdot \hat{\boldsymbol{r}})(\boldsymbol{\mu}_2 \cdot \hat{\boldsymbol{r}})], \tag{2.19}$$

where $\boldsymbol{\mu}_i$ is the magnetic moment and $\boldsymbol{r}$ is the displacement between the two moments. This interaction is anisotropic and falls off with r^{-3}. The dipolar interaction is present in all magnetic materials but it is normally very weak compared to the exchange interaction and only becomes significant at low temperature for large moments.
Many rare earth ions have a large J and the multipole expansion contains higher rank multipoles. For example, multipolar moments exists up to rank 15 for the Dy^{3+} with $J = 15/2$ in $Dy_2Ti_2O_7$ [15, 16]. Within the LS-coupling scheme, the multipole operators can be expressed as homogeneous polynomials of J_x, J_y and J_z [15]. Therefore, the multipole interactions between rare-earth ions are possible which includes several sources of interactions: electro- and magnetostatic interactions, superexchange, direct exchange, lattice-mediated exchange, etc [15]. The interactions between the multipolar moments are imposed by symmetry [15, 17] and in general, the multipoles at different sites transforming similarly are coupled with each other. For example, the wave functions of the CEF ground states of $Nd_2Zr_2O_7$ are composed of $|\pm 9/2\rangle$ and $|\pm 3/2\rangle$ which have non-vanishing magnetic octupole moment, $\langle \pm | i(J_+^3 - J_-^3) | \mp \rangle \neq 0$ ($|\pm\rangle$ is the CEF doublet). When transformed into the pseudospin-1/2 model at low temperature, the σ^y component corresponds to the octupolar moment (in the local coordinate system defined in Appendix B) and the terms $\sigma_i^y \sigma_j^y$ appears in the spin Hamiltonian.

2.2.3 Mean field theory and Curie-Weiss law

In mean field theory, the interactions of a spin with its neighboring spins are approximated by a mean field of the neighboring interactions (Weiss' molecular field) which is

(for the i^{th} spin) [3],

$$\boldsymbol{H}_i = \boldsymbol{H}_{\text{ext}} + \sum_j J_{ij} \cdot \boldsymbol{S}_j, \tag{2.20}$$

where $\boldsymbol{H}_{\text{ext}}$ is the external field and the summation is over the exchange fields from the interactions with the neighboring spins. By replacing $\boldsymbol{H}$ in Eq. 2.5 with the equation above, the paramagnetic susceptibility of a magnet with interacting spins is given by

$$\chi = \frac{g_J^2 \mu_{\text{B}}^2 J(J+1)}{3k_{\text{B}}(T - \theta_{\text{p}})}, \tag{2.21}$$

which is the Curie-Weiss law. The Curie-Weiss temperature θ_{p} is

$$\theta_{\text{p}} = \frac{J(J+1)}{3k_{\text{B}}} \sum_j J_{ij}. \tag{2.22}$$

2.3 Magnetic order and collective excitation

2.3.1 Long range magnetic order and its determination

When a magnet is cooled down, the atomic magnetic moments order in certain ways due to the coupling between them and their anisotropy. Many different types of magnetic orders have been observed, such as ferromagnetic, antiferromagnetic, ferrimagnetic, sine helical orders, etc [3]. Based on the spin Hamiltonian, magnetic order can be obtained conveniently by defining a wavevector-dependent exchange Hamiltonian because of the periodicity of the crystal structure. If there is only one magnetic atom in the unit cell with Heisenberg exchange between the neighboring atoms, we can write [18]

$$\mathcal{H} = \sum_{\boldsymbol{k}} J_{\boldsymbol{k}} \boldsymbol{S}_{\boldsymbol{k}} \cdot \boldsymbol{S}_{-\boldsymbol{k}}, \tag{2.23}$$

where

$$\begin{aligned} J_{\boldsymbol{k}} &= N^{-1} \sum_{i,j} J_{ij} \exp[-\mathrm{i}\boldsymbol{k} \cdot (\boldsymbol{r}_i - \boldsymbol{r}_j)], \\ \boldsymbol{S}_{\boldsymbol{k}} &= N^{-1/2} \sum_i \boldsymbol{S}_i \exp(-\mathrm{i}\boldsymbol{k} \cdot \boldsymbol{r}_i), \end{aligned} \tag{2.24}$$

which is the Fourier transformation of the real-space exchange Hamiltonian. The minimum of $\mathcal{H}$ or $J_{\boldsymbol{k}}$ yields the magnetic order which occurs at certain wavevector $\boldsymbol{k}$. The wavevector gives the periodicity of the magnetic structure. For a general $\boldsymbol{k}$, a helical order is stabilized and for $\boldsymbol{k} = 0$, it is the ferromagnetic order. For the case with multiple

magnetic ions in the unit cell, it can be considered similarly but the magnetic structure is complicated.

Due to the symmetry of the crystal structure, the magnetic Hamiltonian also has a certain symmetry. As a result, the magnetic structure should minimize the magnetic energy while preserving the related symmetries. In one description, a magnetic structure can be defined with a magnetic unit cell. The magnetic unit cell contains the positions, magnitudes and orientations of the moments. The symmetry operations developed to describe the crystal symmetry are not sufficient to describe the magnetic symmetry because the magnetic moment is an axial vector (a current loop). The time-reversal operator is added in the magnetic space group in order to reverse the magnetic moment which is the main difference from the crystal space group. Thus the magnetic space group (Shubnikov groups) was developed which consist of 1651 groups. According to Landau's theory for the second-order transition, the magnetic structure only has the symmetry of one irreducible representations.

The other way to describe a magnetic structure is based on the nuclear unit cell in terms of basis vectors and propagation vectors [19, 20]:

$$\boldsymbol{m}_i(\boldsymbol{l}) = \sum_{\boldsymbol{k}_\mathrm{m}} \phi_i^{\boldsymbol{k}_\mathrm{m}} \exp(-2\pi \mathrm{i} \boldsymbol{k}_\mathrm{m} \cdot \boldsymbol{l}), \tag{2.25}$$

where $\boldsymbol{m}_i(\boldsymbol{l})$ is the magnetic moment of the i^{th} atom or ion in the crystal unit cell with the lattice translation vector $\boldsymbol{l}$ and $\phi_{\mathrm{i}}^{\boldsymbol{k}_\mathrm{m}}$ is the basis vectors (projections of the magnetic moment along the crystallographic axes) corresponding to wave vector $\boldsymbol{k}_\mathrm{m}$ in the first Brillouin zone of the crystal structure. The magnetic structure may involve multiple propagation vectors which can be commersurate and incommersurate with respect to the crystal lattice periodicity. The magnetic satellite peaks in neutron diffraction can be simply related to the propagation vectors involved [19, 20].

Neutron diffraction is commonly used to determine the magnetic structure. The propagation vector $\boldsymbol{k}_\mathrm{m}$ can be found directly in the neutron diffraction pattern and representation analysis of the group theory classifies the possible magnetic structures which provides clues for the final determination of the magnetic structure by Rietveld refinement. For the representation analysis, the little group $G_{\boldsymbol{k}_\mathrm{m}}$ of the propagation vector is first found which contains the crystal symmetry operations that leave $\boldsymbol{k}_\mathrm{m}$ invariant. The symmetry operation has two effects on a magnetic moment: permuting the symmetry equivalent magnetic atoms and reorienting the magnetic moments. Therefore the little group can be presented in the permutation representation Γ_{perm} and the axial vector representation Γ_{axial}. Because the atom positions and the moment orientations are not coupled, the

direct product of the presentations yields the magnetic representation Γ_{mag}:

$$\Gamma_{\mathrm{mag}} = \Gamma_{\mathrm{perm}} \times \Gamma_{\mathrm{axial}}. \tag{2.26}$$

The magnetic representation can be reduced to the direct summation of the irreducible representations of the little group $G_{\boldsymbol{k}_{\mathrm{m}}}$:

$$\Gamma_{\mathrm{mag}} = \sum_{\nu} n_{\nu} \Gamma_{\nu}^{d}, \tag{2.27}$$

where Γ_{ν}^{d} is an irreducible representation of d dimensions which appears n_{ν} times. The basis vectors of the irreducible representations can be calculated using the projection operator formula which is a standard method in group theory. All the combinations of the basis vectors which belong to the same irreducible representation are the possible magnetic structures.
In Chapter 5 The representation analysis is performed on $Nd_2Zr_2O_7$ using the program BasIreps available in the FullProf Suite [21].

2.3.2 Spin wave excitations

At finite temperatures, the ordered system has probabilities to be in excited states. The simplest excited state is created by flipping one spin. However, because the spins are correlated, this state appears as a collective excited state where the flipped spin is at every lattice point with certain probabilities. This is a simple picture of spin wave excitations which exist commonly in magnetically ordered systems and can be described as flipped spins propagating through the lattice in a wave-like manner (Fig. 2.1). Linear spin wave theory is introduced in many magnetism books, i.e. in Ref. [3], and in Chapter 6 of this thesis it is used for analysing the inelastic neutron scattering data of $Nd_2Zr_2O_7$ using the Matlab package SpinW [22].

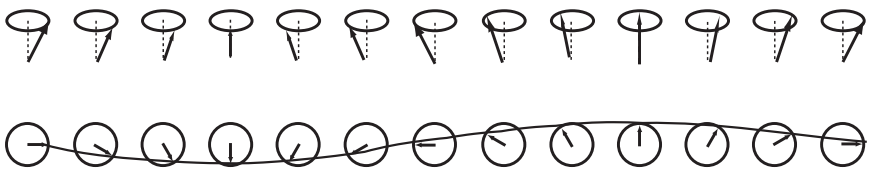

Figure 2.1: Illustration of spin wave on a line of spins viewed in perspective (upper panel) and from above (lower panel). Taken from Ref. [3].

2.4 Geometrical frustration

In the sections above, the magnetic interactions and the resulting magnetic orders were introduced. However, not all the systems with spin interactions achieve a long range order as the ground state. Magnetic frustration can suppress the tendency to order (i.e. reducing the ordering temperature and/or ordered moment) or even lead to a disordered ground state. Frustration in magnetism is generated by the competition of different interactions and/or by the special lattice geometry. The conflicting interactions make the system fail to find a spin configuration that fully satisfies all the bonds between every pair of spins. For example, consider a chain of spins where the nearest-neighbor (nn) interaction J_1 is ferromagnetic while the next-nearest-neighbor (nnn) interaction J_2 is antiferromagnetic [Fig. 2.3(a)]. As long as $J_1 \gg J_2$, the ground state is ferromagnetic: every nn bond is satisfied although the nnn ones are not. When J_2 exceeds a critical value, the ferromagnetic ground state is no longer valid and neither the nn nor the nnn bonds can be fully satisfied. One example of geometrical frustration is the triangular lattice with antiferromagnetic interactions between the spins. When two of the spins on a triangle are antiparallel, the bond connecting them is fully satisfied but there is no choice for the third spin to have an orientation antiparallel to the other two spins at the same time. Then the third spin is "frustrated". Finally, all the spins lie in a plane pointing 120° from each other and none of the three bonds are fully satisfied as shown in Fig. 2.2. Fig. 2.3 shows some more lattices with geometrical frustration.

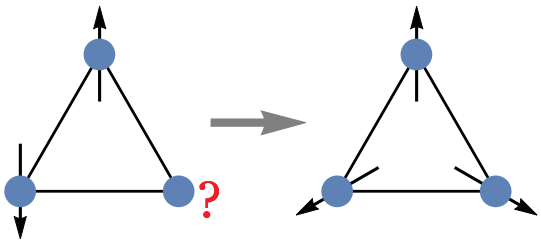

Figure 2.2: Frustration in the triangle-lattice antiferromagnet.

Frustration gives rise to macroscopic degeneracy of the lowest energy levels, encouraging alternative ground states to long-range magnetic order such as gapped or gapless spin liquids, spin nematics etc. These states often exhibit exotic phenomena, such as residual entropy and algebraic correlations [23]. Therefore, frustrated magnetism provides excellent opportunities for discovering new states and new properties of matter which has become a very active field of research. To date, there have been a lot of inter-

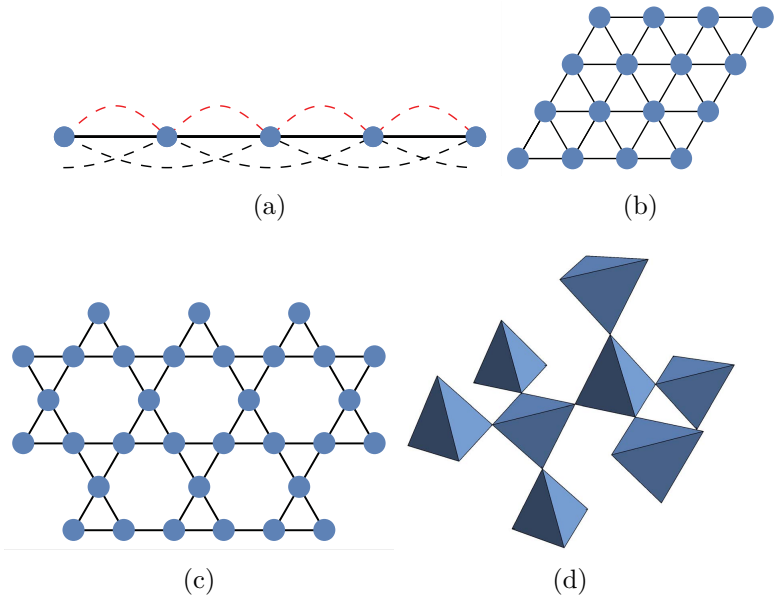

Figure 2.3: Frustrated magnetism. (a) One dimensional chain with nearest-neighbor ferromagnetic interaction and next-nearest-neighbor antiferromagnetic interaction. (b) Triangle lattice (networks of edge-sharing triangles). (c) Kagomé lattice (networks of corner-sharing triangles) (c) Pyrochlore lattice (networks of corner-sharing tetrahedra).

esting experimental and theoretical results on frustrated magnetism (see, for example, Refs. [23, 24]). In this thesis, several magnetic pyrochlore oxides which contain magnetic networks of frustrated corner-sharing tetrahedra are studied.

2.5 Magnetic pyrochlore oxides

Over the past two decades, many interesting and exotic magnetic and thermodynamic phenomena have been found in the rare earth pyrochlore oxides $R_2B_2O_7$ (R is a trivalent rare earth ion and B is a tetravalent transition metal ion) [25–28]. For example, $Dy_2Ti_2O_7$ and $Ho_2Ti_2O_7$ have the spin ice ground state and their excitations are monopole-like [29–32], $Tb_2Ti_2O_7$ has a spin-liquid ground state [25] and $Er_2Ti_2O_7$ develops an antiferromagnetic order through the order-by-disorder mechanism [25, 33]. Among these states, the spin ice phase is probably the most striking which exhibits an apparent violation of the third law of thermodynamics owing to geometrical frustration. In this section, the general physics of the rare earth pyrochlore are given with emphasis

on the spin ice physics which is related to the main study of this thesis.

2.5.1 Crystal structure

The general formula $A_2B_2O_7$ represents a large family of oxides isostructural to the mineral pyrochlore (NaCa)(NbTa)O_6F/(OH) which consists of a wide variety of chemical substitution on the A, B and O sites provided the ionic radius and charge neutrality criteria are satisfied [34]. The valences of A and B ions can be (+3, +4) or (+5, +2) according to the known pyrochlore compounds [25, 34] and the possible elements for the (+3, +4) pyrochlores are shown in Fig. 2.4. The pyrochlore compounds here are the ones containing trivalent rare earth ions, that is $R_2B_2O_7$ with R being a rare earth ion and B being either a transition metal or a p-block metal ion such as Ti, Zr, Hf, Sn, Ge, Pb, Pt (see references, for example, [25, 27, 28, 35]).

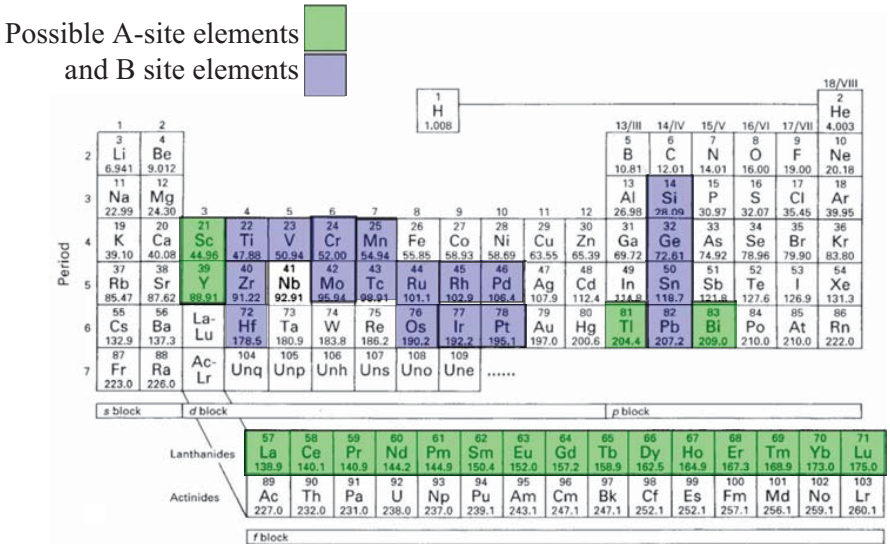

Figure 2.4: Elements known to form the $A_2^{3+}B_2^{4+}O_7$ pyrochlore oxides. Taken from Ref. [25].

The $R_2B_2O_7$ pyrochlores crystallize in the space group $Fd\bar{3}m$ (No. 227). The three elements occupy four symmetrically equivalent sites: R at 16d site, B at 16c site and O at 48f and 8b sites. Because the oxygen ion occupies two different types of sites, the formula can be written as $R_2B_2O_6O'$ ("O" is the oxygen at the 48f site and "O′" is at the 8b site). Both the sublattices formed by the R and B ions are networks of corner-sharing tetrahedra which are called pyrochlore lattice.

The pyrochlore structure can be viewed as an ordered defected fluorite CaF_2 structure

(space group $Fm\bar{3}m$) [34]. In fluorite, the Ca cations form a cubic close packed lattice and the fluorine anions fill all the tetragonal interstices. In the pyrochlore structure, there are two types of R-B ordered close packed layers stacked alternating along the [111] direction: one with the Kagomé lattice formed by R ions with B ions located at the hexagon centres, and the other one with the reversed R/B occupation. The O^{2-} anions sit in the tetrahedral interstices formed by the R_4 ($8b$ site) and the R_2B_2 ($48f$ site), leaving the B_4 tetrahedral interstices ($8a$ site) unoccupied. Due to the different sizes of the R and B cations, the position of the O($48f$) is not the centre of the R_2B_2 tetrahedron and a coordination parameter describes this situation. In the diffraction pattern, the pyrochlore superlattice peaks will show at such as [111], [311], [331] and [511] and so on due to the lowering of the crystal symmetry.

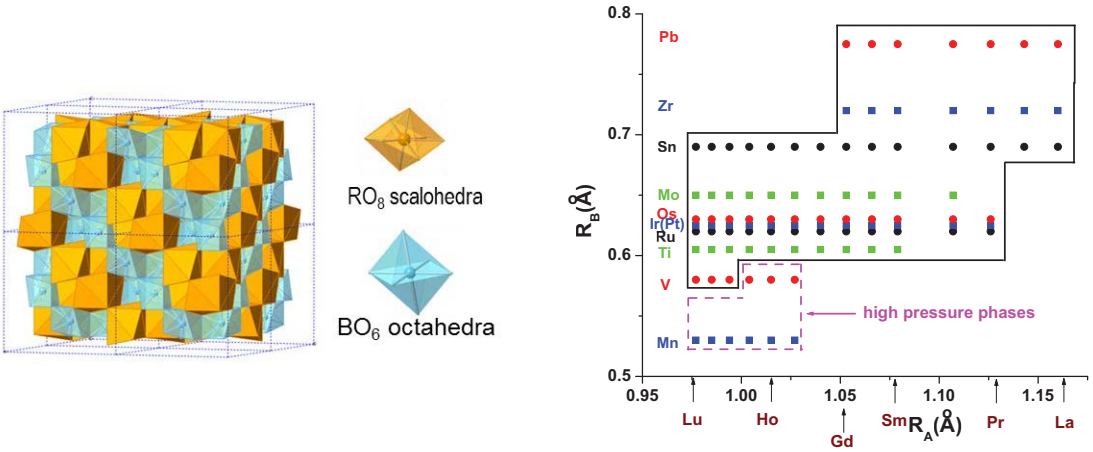

Figure 2.5: (left) Pyrochlore structure and (right) structural stability map for $A_2B_2O_7$ ($\sim R_2B_2O_7$) materials. Taken from Ref. [25].

The R/B ordering is generally governed by the ratio of the ionic radii of the trivalent and tetravalent cations r_R/r_B. At ambient pressure, a stable ordered pyrochlore phase is found for $1.36 < r_R/r_B < 1.71$ [25]. Figure 2.5 shows the structure-stability map for $R_2B_2O_7$. The pyrochlore compounds transform to the high-entropy fluorite phase at high temperatures and the transition temperature decreases with the decrease of the r_R/r_B ratio [36, 37].

2.5.2 Spin Hamiltonian

The ground states of the rare earth pyrochlores generally depend on three competing interactions: exchange interaction, dipolar (and/or multipolar) interaction and crystal

electric field (CEF) interaction [25]. Among these interactions, the CEF interactions is usually the strongest and dominates much of the underlying physics because of the strong anisotropic electric field created by the surrounding oxygen anions (Fig. 2.6) and the strong spin-orbital coupling of the rare earth ions. In $R_2B_2O_6O'$, the R ion is coordinated by six O ions and two O′ ions as shown in Fig. 2.6. The six O ions form a puckered six-membered ring and the O′-R-O′ (along the local [111] direction) forms a stick perpendicular to the average plane of the six-membered ring. The R-O′ bond distance is much shorter than that of the R-O bond (typically 2.2 Å vs 2.4 Å). Thus the crystal field has axial anisotropy and the Hamiltonian is given by Eq. 2.12 in the coordinate system with the z axis along the three-fold axis. Accordingly, the $R_2B_2O_7$ compounds display strongly anisotropic magnetic behavior, e.g. local $\langle 111 \rangle$ Ising anisotropy in $Dy_2Ti_2O_7$ and XY anisotropy (local $\langle 111 \rangle$ easy plane) in $Er_2Ti_2O_7$ [25]. In most cases, the crystal field ground state is a well-isolated doublet and a pseudospin-1/2 with a specific g factor or tensor can be defined to model the low-temperature behaviors of the system. The CEF ground state doublet can have multipolar moments (ordering parameters) which can be related to the components of the pseudospin [17, 38].

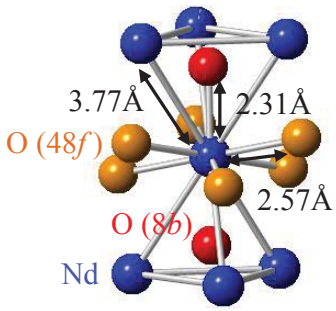

Figure 2.6: Local environment of the rare earth ion in pyrochlore (here $Nd_2Zr_2O_7$ is taken as a example).

The nearest-neighbor exchange interaction in pyrochlores is generally the oxygen-mediated superexchange interaction (including the multipolar interactions) [38] which is anisotropic due to the anisotropy of the CEF ground state. The non-vanishing terms in the exchange interaction can be determined by symmetry analysis. Considering the effective pseudospin-1/2 description of the Kramers doublet, the exchange Hamiltonian is [8, 39]

$$\mathcal{H} = \sum_{\langle ij \rangle} \Big\{ J_{zz}\sigma_i^z\sigma_j^z - J_{\pm}(\sigma_i^+\sigma_j^- + \sigma_i^-\sigma_j^+) + J_{\pm\pm}\left[\gamma_{ij}\sigma_i^+\sigma_j^+ + \gamma_{ij}^*\sigma_i^-\sigma_j^-\right] + J_{z\pm}\left[\sigma_i^z(\zeta_{ij}\sigma_j^+ + \zeta_{ij}^*\sigma_j^-) + i \leftrightarrow j\right] \Big\}, \quad (2.28)$$

where σ_i^α are the α component of the i^{th} pseudospin $\boldsymbol{\sigma}_i$ in the local coordinate frames and

$$\begin{aligned}\sigma_i^+ &= 1/2\sigma_i^x + \mathrm{i}/2\sigma_i^y,\\ \sigma_i^- &= 1/2\sigma_i^x - \mathrm{i}/2\sigma_i^y.\end{aligned} \tag{2.29}$$

The local frames take the symmetry axes of the crystal field with the local [111] axes being the z axes (see Appendix B). ζ and γ specifies the phase factors for the six bonds on a tetrahedron because of the different orientations of the six bonds. Different contributions to the spin interaction can be identified as [40]

- $J_{zz} \rightarrow$ "Ising" with respect to the local bond
- $\{J_\pm, J_{\pm\pm}\} \rightarrow$ "XY" with respect to the local bond
- $J_{z\pm} \rightarrow$ Dzyaloshinskii-Moriya with respect to the local bond

The pseudospin and the exchange interaction can also be defined in the global crystal coordinate system after doing the corresponding geometric transformations (see Appendix B).
The bond-dependent phase factors vanish (equal to one) for the Kramers doublet whose CEF wavefunctions are composed of $|\pm 15/2\rangle, |\pm 9/2\rangle$ and $|\pm 3/2\rangle$ terms because the two states of the doublet do not mix under the C_3 rotation [17]. This type of doublet is called dipolar-octupolar doublet with the σ_x and σ_z components of the related pseudospin corresponding to magnetic dipoles and the σ_y component corresponding to a component of magnetic octupolar tensor. It has been proposed that Nd^{3+} and Dy^{3+} have this type of CEF ground state in pyrochlores [17]. In addition, the spin Hamiltonian for the non-Kramers doublet is similar to Eq. 2.28 but the $J_{z\pm}$ bilinear coupling terms are prohibited because of the non-Kramers nature of the moment: σ_z changes sign under the time-reversal operation corresponding to a magnetic dipole, while σ_x and σ_y do not change corresponding to electric quadrupole moments.
The magnetic dipole-dipole interaction can be strong owing to the large moment of the rare earth ions which is given by

$$\mathcal{H}_{\text{dip}} = \frac{\mu_0\mu_{\text{B}}^2}{4\pi r_{ij}^3}\sum_{i<j}(\boldsymbol{g}_i\cdot\boldsymbol{\sigma}_i)\cdot(\boldsymbol{g}_j\cdot\boldsymbol{\sigma}_j) + 3[(\boldsymbol{g}_i\cdot\boldsymbol{\sigma}_i)\cdot\hat{\boldsymbol{r}}_{ij}][(\boldsymbol{g}_j\cdot\boldsymbol{\sigma}_j)\cdot\hat{\boldsymbol{r}}_{ij}], \tag{2.30}$$

where $\boldsymbol{g}_i$ is the g tensor and $\boldsymbol{r}_{ij} = \boldsymbol{r}_i - \boldsymbol{r}_j$ is the displacement between the magnetic ions. The nearest-neighbor dipolar interaction can be translated into the $\{J_{zz}^{\text{dip}}, J_\pm^{\text{dip}}, J_{\pm\pm}^{\text{dip}}, J_{z\pm}^{\text{dip}}\}$

notation [41],

$$\begin{pmatrix} J_{zz}^{\mathrm{dip}} \\ J_{\pm}^{\mathrm{dip}} \\ J_{\pm\pm}^{\mathrm{dip}} \\ J_{z\pm}^{\mathrm{dip}} \end{pmatrix} = \frac{\mu_0 \mu_{\mathrm{B}}^2}{12\pi r_{\mathrm{nn}}^3} \begin{pmatrix} 20 g_{zz}^2 \\ -g_{xy}^2 \\ 7 g_{xy}^2 \\ -2\sqrt{2} g_{xy} g_{zz} \end{pmatrix}, \tag{2.31}$$

where r_{nn} is the nearest-neighbor distance. For the Ising spins with only g_{zz} nonzero, the nearest-neighbor dipolar interaction only contributes to the Ising term of the spin Hamiltonian, which is the case for $Dy_2Ti_2O_7$ and $Ho_2Ti_2O_7$.

The terms in the spin Hamiltonian can be estimated by a microscopic calculation of the electron hopping between the orbitals of the rare earth and oxygen ions [16, 38, 42, 43]. Because the calculation is rather complex and contains many approximations, the estimated exchange interaction is not accurate. In practice, the spin Hamiltonian is determined experimentally, e.g. fitting the spinwave dispersions. The setting up of the Hamiltonian for the spin wave calculation for $Nd_2Zr_2O_7$ in this thesis is given in Appendix B.

2.5.3 Classical spin ice

In 1930s, specific-heat experiments by William Giauque *et al.* indicated that hexagonal water ice has non-zero entropy at very low temperatures which violates the third law of thermodynamics [44, 45]. In 1935, Linus Pauling showed that a finite entropy $R\ln(3/2)/\mathrm{mol}$ is possible in water ice at zero temperature due to the proton configuration disorder [46]. As shown in Fig. 2.7, in water ice the oxygen ions form a diamond lattice and each oxygen ion is coordinated by four hydrogen ions sitting in the O-O bonds forming a tetrahedron. Because the O-O bond length is more than two times of the length of the covalent O-H bond (2.76 Å vs 2×0.97 Å), the hydrogen ions form a "2-near-2-far" configuration around an oxygen ion. There are six equivalent local configurations which lead to macroscopic number degeneracy of the proton order in water ice structure. Similarly, Ising spins on the verticies of the corner-sharing tetrahedra can have the local "2-in-2-out" (2I2O) configuration for each tetrahedron, which forms spin ice in analogy to the water ice (Fig. 2.7). The classical spin ice phase was discovered in $Ho_2Ti_2O_7$ and $Dy_2Ti_2O_7$ in 1990s and recently in $CdEr_2Se_4$ [29, 47, 48]. Neutron diffraction and muon spin relaxation indicate that $Ho_2Ti_2O_7$ does not order at temperatures down to $T = 0.05\,\mathrm{K}$ although the Curie-Weiss temperature is 1.9 K (indicating ferromagnetic spin interactions) [29, 49] and an ice-like state induced by the geometrical frustration was proposed. The origin of the spin ice state is that the local [111] Ising

anisotropy forces the spins to point either into or out of the tetrahedron and the effective ferromagnetic interaction between the spins induces the 2I2O spin configuration on each tetrahedron. While every tetrahedron has the 2I2O order at lowest temperatures, there is no long-range magnetic order in the conventional sense of a repeating magnetic unit cell or ordering $\boldsymbol{k}$ vector because of the many possible ways in which the 2I2O state can pattern the pyrochlore lattice. Instead the spin ice ground state possesses topological order.

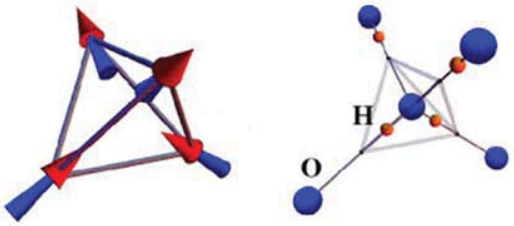

Figure 2.7: Spin ice and water ice: the "2-in-2-out" spin orientation configuration on a tetrahedron in spin ice (left) and the "2-near-2-far" (from the oxygen ion) proton position configuration in water ice (right). There are six equivalent ice configurations for a tetrahedron, which causes the macroscopic number of degeneracy of the ground state. Taken from Ref. [50].

The ice rule constraint can be expressed as a zero-divergence condition on a notional magnetic field and thus spin ice is a realization of classical magnetostatics with the local violation of the ice rule corresponding to magnetic charge (magnetic monopole) as shown in Fig. 2.8. The violation of the ice rule is created in pairs by flipping a spin forming "3-in-1-out" (3I1O) and "1-in-3-out" (1I3O) spin configurations on the neighboring tetrahedra (Fig. 2.8). The 3I1O and 1I3O spin configurations can move to other tetrahedra by flipping spins on neighboring 2I2O tetrahedra successively without further energy cost. Therefore, the excitation is fractionalized and becomes two magnetic-monopole-like particles interacting with dipolar interaction. The spin correlation in spin ice has the dipolar form in real space yielding the "pinch point" singularities in reciprocal space (Fig. 2.9) with the line width being an indicator of the monopole density or the ice-rule correlation length [32, 51].
The classical spin ice phase in $Ho_2Ti_2O_7$ and $Dy_2Ti_2O_7$ is described by the *dipolar spin-ice model* which only considers the Ising exchange interaction and the long-range dipolar interaction due to the strong Ising anisotropy and the large magnetic moments of the

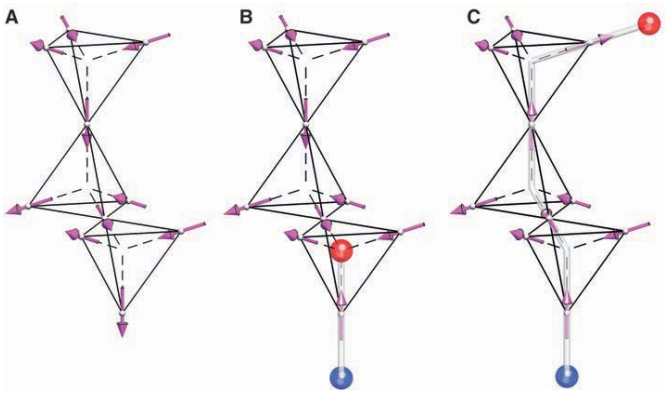

Figure 2.8: Monopole-like excitations in spin ice. (a) Spin ice consist of "2-in-2-out" spin configurations on the tetrahedra. (b) Creation of a pair of oppositely-charged monopoles ("3-in-1-out" and "1-in-3-out" spin configurations) on the neighboring tetrahedra by flipping a spin. (c) Free monopoles caused by the fractionation of the excitation. Taken from Ref. [32].

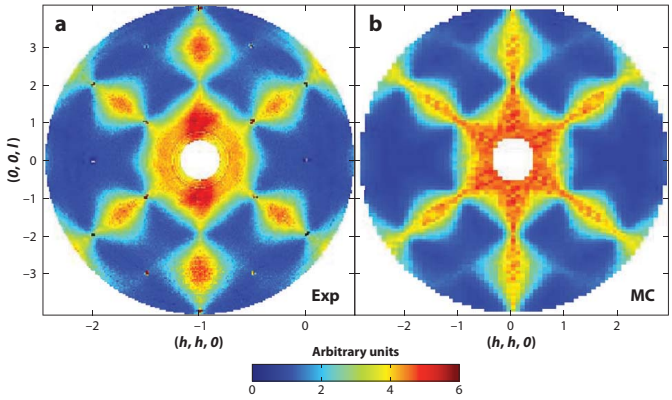

Figure 2.9: (a) Pinch point pattern in the (HHL) reciprocal plane in the elastic neutron scattering experiment of single crystal $Ho_2Ti_2O_7$. (b) Monte Carlo simulation with the nearest-neighbor spin ice model. Taken from Ref. [32, 51].

Ho^{3+} and Dy^{3+} ions, that is [16, 25]

$$\mathcal{H}_{\text{dsi}} = -J_{zz}\sum_{\langle ij\rangle}\sigma_i^z\sigma_j^z + D\sum_{i<j}\sigma_i^z\sigma_j^z(\frac{r_{\text{nn}}}{r_{ij}})^3[\hat{\boldsymbol{z}}_i\cdot\hat{\boldsymbol{z}}_j - 3(\hat{\boldsymbol{z}}_i\cdot\hat{\boldsymbol{r}}_{ij})(\hat{\boldsymbol{z}}_j\cdot\hat{\boldsymbol{r}}_{ij})], \tag{2.32}$$

where r_{nn} is the nearest-neighbor distance, $\boldsymbol{r}_{ij} = \boldsymbol{r}_i - \boldsymbol{r}_j$ is the displacement vector between two sites and $\hat{\boldsymbol{z}}_i$ is the quantization axis along the local [111] axis at site $\boldsymbol{r}_i$. The first term on the right side is the nearest-neighbor Ising exchange interaction. The second

term is the long-range dipole interaction with $D = \mu_0 \mu^2 \mu_B^2/(4\pi r_{nn}^3)$ (μ is the magnetic moment of the magnetic ion). It has been shown that the high-rank multipolar interactions could induce quantum effect but the scale of the quantum effects in $Ho_2Ti_2O_7$ and $Dy_2Ti_2O_7$ are well below experimentally relevant temperatures [16]. Therefore, the calculations based on the dipolar spin ice model show a very good agreement with the experiment [24].

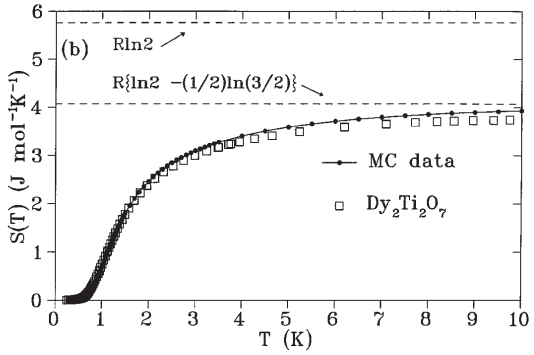

Figure 2.10: Results of the Monte Carlo simulations based on the nearest-neighbor spin ice model for $Dy_2Ti_2O_7$. Taken from Ref. [52].

Truncation of the long-range dipolar interaction at the nearest neighbor yields the *nearest-neighbor spin ice model* [24, 25]

$$\mathcal{H}_{\text{nnsi}} = J_{\text{eff}} \sum_{\langle ij \rangle} \sigma_i^z \sigma_j^z, \tag{2.33}$$

where $J_{\text{eff}} = -J_{\text{nn}} + D_{\text{nn}}$ ($J_{\text{nn}} = J_{zz}$) with $D_{\text{nn}} \equiv 5D/3$ since $\hat{\boldsymbol{z}}_i \cdot \hat{\boldsymbol{z}}_j = -1/3$ and $(\hat{\boldsymbol{z}}_i \cdot \hat{\boldsymbol{r}}_{ij})(\hat{\boldsymbol{z}}_j \cdot \hat{\boldsymbol{r}}_{ij}) = -2/3$ (the local z axes are not collinear). This model also gives a good explanation to the experiment as shown in Fig. 2.9 and Fig. 2.10.
The phase diagram based on Monte Carlo simulations of the dipolar spin ice model is shown in Fig. 2.11 [25, 52, 53] which contains the classic spin ice phase, the ordered spin ice phase and the antiferromagnetic (AFM) ordered phase. The calculation reveals that when the ferromagnetic (FM) dipolar interaction dominates over the AFM exchange interaction, the spin ice state is stabilized and otherwise the "all-in/all-out" (AIAO) antiferromagnetic order is stabilized where the spins alternate between pointing all into and all out of successive tetrahedra. The long-range-ordered ice-rule state is predicted below the spin ice state but not observed in experiments.

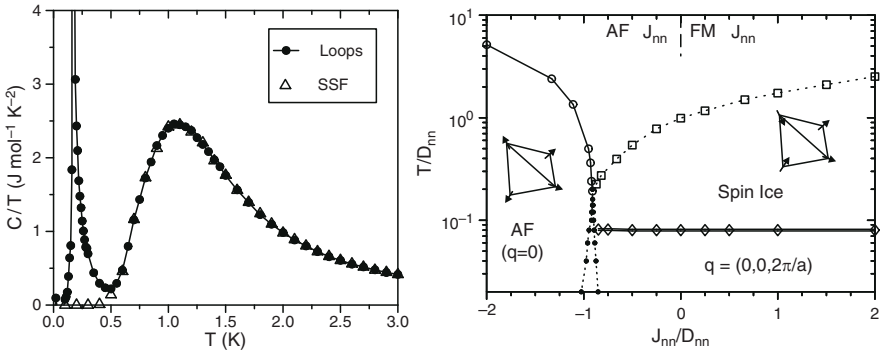

Figure 2.11: Results of the loop Monte Carlo simulations based on the dipolar spin ice model. Left: magnetic specific heat calculated with $J_{\rm nn} = -1.24\,{\rm K}$ and $D_{\rm nn} = 2.35\,{\rm K}$ interactions of $Dy_2Ti_2O_7$. The open triangles show the data obained based on the single-spin-flip (SSF) Metropolis algorithm. Right: phase diagram of the dipolar spin ice model according to the loop Monte Carlo simulation. Taken from Ref. [24].

2.5.4 Quantum spin ice

The classical spin ice state is static with the ice configurations isolated and the monopole excitations interact through a magnetostatic field. With introducing the quantum-mechanical tunnelling between different ice configurations (Fig. 2.12), the classical spin ice is converted to a quantum spin ice (QSI) (or a quantum spin liquid) that realizes a fully dynamical, lattice analogue of quantum electromagnetism [54–56]. The divergence free condition allows a gauge field $\boldsymbol{A}$ to be defined by $\nabla \times \boldsymbol{A} = \boldsymbol{B}$ where $\boldsymbol{B}$ is the local magnetization of the system. Fluctuations of $\boldsymbol{A}$ can be induced by the tunnelling between ice configurations which result in an electric field $\boldsymbol{E} = \frac{\partial \boldsymbol{A}}{\partial t}$. Therefore, quantum spin ice supports several types of excitations as shown in Fig. 2.12 [54–56]. At high energies, on the scale of the Ising interaction, there are gapped magnetic monopole or spinon excitations resulted from single spin flips which break the ice rule. The excitations are coherent and interact with the emergent magnetic and electric fields. At medium energies there are vison excitations. Resonances of spin ice configurations induce electric flux loops and flipping a spin not only generates magnetic monopoles but also breaks these electric loops. Visons appear at the ends of the broken electric string. At low energies, the photon excitation exists which is a linearly dispersing transverse excitation of the gauge field $\boldsymbol{A}$.

Quantum effect (or dynamics) can be induced by the transverse couplings, such as $J_{\pm\pm}$ and $J_{\pm}$ in the Ising pyrochlore [54–56]. For example, the low energy Hamiltonian with

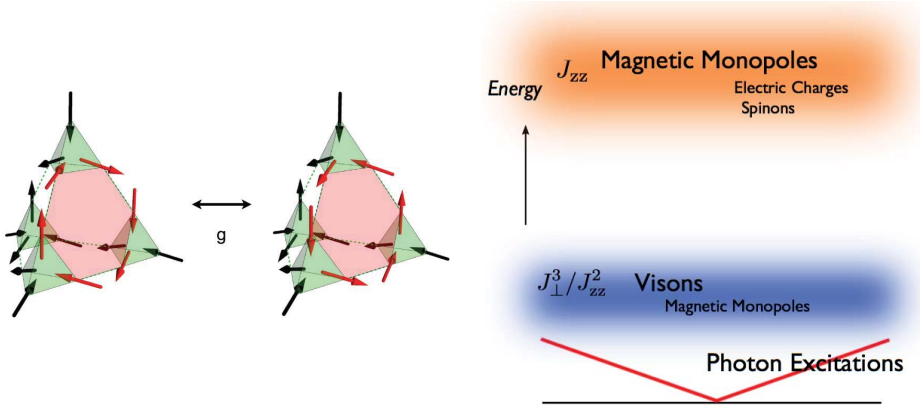

Figure 2.12: Left: illustration of the simplest tunneling process between different spin-ice configurations based on the closed hexagonal spin loops where "g" is the transition matrix element. Taken from Ref. [56]. Right: schematic of the excitations in quantum spin ice. Taken from Ref. [55].

$J_\pm$ that preserves the ice rule is the ring exchange interaction that lives on the hexagonal loops which corresponds to the simplest tunnelling process between two ice configurations [reversal of the spins forming a closed loop on a hexagonal plaquette (Fig. 2.12)] [54]

$$\mathcal{H}_{ring} \sim \frac{J_\pm^3}{J_{zz}^2} \sum_{h\in\{\text{hex}\}} \sigma_{h,1}^+ \sigma_{h,2}^- \sigma_{h,3}^+ \sigma_{h,4}^- \sigma_{h,5}^+ \sigma_{h,6}^- + \text{h.c.}, \tag{2.34}$$

where the summation is taken over all the hexagonal plaquettes.
The anisotropic spin Hamiltonian (Eq. 2.28) has been analysed by gauge mean field theory and the phase diagrams for the pyrochlores with Kramers and non-Kramers ions are obtained (Fig. 2.13) [57, 58]. It is found that besides the conventional Higgs AFM and FM phases for large J_{zz} and $J_\pm$, the exchange Hamiltonian for the Kramers ion allows two exotic phases: a $U(1)$ spin liquid (quantum spin ice) and a Coulombic ferromagnet [57]. The Coulombic ferromagnet is a polarized version of the $U(1)$ spin liquid with non-zero magnetization which hosts spinon instead of magnon excitations and the gapless photon mode. The phase diagram in the non-Kramers case (without the J_{xz} term in the Hamiltonian) contains the quantum spin ice phase and two ordered phases [an antiferroquadrupolar order and a non-coplanar ferroquadrupolar order (the $\sigma^{x,y}$ components of the pseudospin corresponds to quadrupole moments)] [58]. Recently, Huang *et al.* proposed that the crystal field ground state doublets of the Nd^{3+} and Dy^{3+} ions in pyrochlores are dipolar-octupolar doublets and the Hamiltonian takes the

form of the XYZ model [17]. The phase diagram of the dipolar-octupolar Hamiltonian calculated in Ref. [17] contains two types of quantum spin ice phases (a dipolar and an octupolar) as well as two corresponding ordered phases (Fig. 2.14).

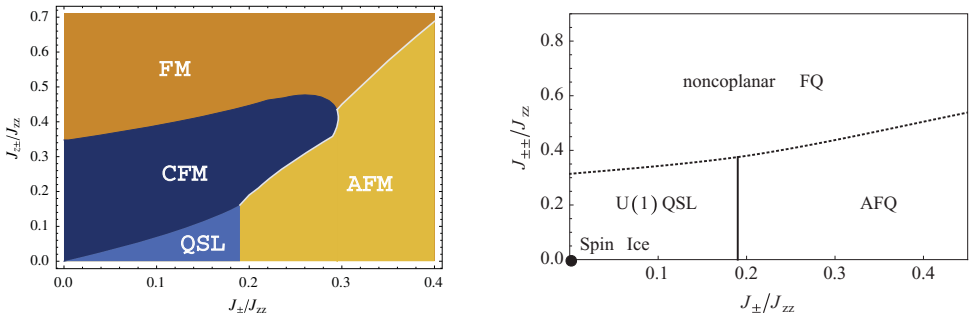

Figure 2.13: Phase diagrams of the anisotropic exchange Hamiltonian for pyrochlores with Kramers (left) and non-Kramers (right) ions. Taken from Refs. [57, 58].

As for the experimental signatures of quantum spin ice, the pinch points in the static structure factor characteristic for classical spin ice fades away owing to the spin fluctuations in time and space [56, 59]. Two-particle continuum should appear in the inelastic neutron scattering because two spinons can be excited by one neutron [8, 57]. The linearly-dispersing photon can also be detected directly by inelastic neutron scattering with a scattering intensity that increases with energy. In addition, the photon excitations contribute to the low-temperature specific heat by $\mathcal{B}T^3$ with $\mathcal{B} = \frac{\pi^2}{120} N_{\mathrm{A}} \frac{k_{\mathrm{B}}^4 a_{\mathrm{lattice}}^3}{\hbar^3 v_{\mathrm{photon}}^3}$ (a_{lattice} is the lattice parameter and v_{photon} is the velocity of the excitation) [57].
The pyrochlores with heavy rare earth elements are well studied and classical spin ice behaviour is found in $R_2B_2O_7$ (R = Ho, Dy and B = Ti, Ge, Sn) which has large Ising anisotropic moments resulting in a dominant Ising interaction between the spins [25, 27, 29, 31, 32, 47, 60]. Exceptions are $Tb_2Ti_2O_7$ and $Yb_2Ti_2O_7$. $Tb_2Ti_2O_7$ is the first material proposed to be a candidate of quantum spin ice [61]. The non-Kramers Tb^{3+} ion is Ising anisotropic in $Tb_2Ti_2O_7$ (the first CEF excited state is at 18 K above) and the Curie-Weiss temperature of $Tb_2Ti_2O_7$ is ~ -10 K [62, 63]. Most of the experiments give no evidence for long range order at temperatures well below the Curie-Weiss temperature and neutron scattering indicates that both spin-ice correlations and transverse fluctuations exist in $Tb_2Ti_2O_7$ [64–66]. Several models have been proposed to explain the observations but the true ground state of $Tb_2Ti_2O_7$ is still not clear [61, 67–69]. It is believed that crystal field ground state doublet splitting, low-energy crystal field excitation and magneto-elastic coupling may be at play [61, 67–69]. $Yb_2Ti_2O_7$ shows a specific heat bump at about 2 K followed by a sharp peak at ~ 0.214 K indicating an or-

dering transition [70]. Muon spin relaxation and neutron powder diffraction did not find long-range order at first but quite recently splayed ferromagnetic order has been found by neutron diffraction [71–77]. The spin Hamiltonian was determined by fitting the spin waves observed in high-field inelastic neutron scattering which indicates that $Yb_2Ti_2O_7$ may have a quantum spin ice ground state in low magnetic fields [8]. It was also found that $Yb_2Ti_2O_7$ should be viewed as a XY system ($g_\perp > g_\parallel$) but J_{zz} is the largest interaction in the anisotropic exchange Hamiltonian. The dominant Ising exchange together with significant transverse terms makes it possible to show the quantum spin ice state in $Yb_2Ti_2O_7$. However, according to the recent results in Refs. [78, 79], $Yb_2Ti_2O_7$ could lie near the phase boundary between the FM and AMF phases rather than proximate to the quantum spin ice phase and the multiphase competition may be responsible for the quantum fluctuations observed in $Yb_2Ti_2O_7$.

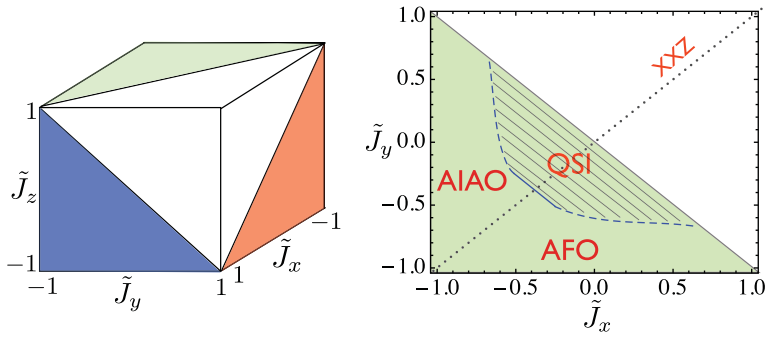

Figure 2.14: (left) Unit cube in the ($\tilde{J}^{xx}$, $\tilde{J}^{yy}$, $\tilde{J}^{zz}$) parameter space of the XYZ model and (right) phase diagram of the model on the $\tilde{J}_{zz} = 1$ surface of the cube calculated based on the gauge mean field theory where the quantum spin ice (QSI) and "all-in/all-out" (AIAO) and antiferro-octupolar (AFO) orders are found. Taken from Ref. [17].

It was pointed out in Ref. [55] that there are generally three criteria for the search of a quantum spin ice in pyrochlores: Ising anisotropic crystal field ground state, large first CEF excitation energy and small dipolar magnetic moment. The Ising anisotropic crystal field ground state is expected to induce a dominant J^{zz} Ising term in the spin Hamiltonian, which ensures the ice rule. A small moment reduces the long range dipolar interaction so that its main contribution to the Ising interaction is reduced. The Ising anisotropic pyrochlores with light rare earth ions are promising quantum spin ice candidates because the light rare earth elements have smaller moments and their less localized electrons (compared with the heavy rare earth elements) can enhance the transverse terms. It has been reported that $Pr_2B_2O_7$ (B =Sn, Zr, Hf) and $Ce_2Sn_2O_7$ have the

desirable crystal field ground state and show spin-ice features in their bulk properties (e.g. susceptibility and specific heat) and significant inelastic signals in powder inelastic neutron scattering data [80–83]. The single crystal neutron scattering of $Pr_2Zr_2O_7$ shows spin-ice-like spin correlations with broad pinch point pattern at energy transfer 0.25 meV suggesting that there are fluctuations breaking the ice rule [82]. However, the crystal field ground state doublet of the non-Kramers Pr^{3+} is not protected by the time reversal symmetry and structural distortion and spin-lattice coupling could break the CEF ground state degeneracy which could strongly modify the ground state. Interestingly, the structural disorder may introduce a random disordered transverse coupling which can be a route to a quantum spin ice [84]. An antiferromagnetic quadrupole liquid state is also proposed as the ground state of $Pr_2Zr_2O_7$ [85]. The pyrochlores with the Nd^{3+} and Sm^{3+} ion are also promising candidates for quantum spin ice. Both Nd^{3+} and Sm^{3+} are Kramers ions with small magnetic moment (3.27 and 0.71 μ_B for free ion). The Nd^{3+} ion in pyrochlore has been predicted to have an Ising anisotropic dipolar-octupolar doublet as the crystal field ground state and the dipolar-octupolar spin Hamiltonian supports two distinct quantum spin ice phases [17]. The exploration of $Nd_2Zr_2O_7$ forms the main topic of this thesis.

2.5.5 Classical spin liquid: Heisenberg pyrochlore antiferromagnet

The pyrochlore antiferromagnet with nearest-neighbor antiferromagnetic Heisenberg exchange interactions is predicted to show the classical spin liquid state or a disordered state with fluctuations at zero temperature which possesses a macroscopic number of degenerate spin configurations [51, 86, 87]. These ground states obey a local constraint – each tetrahedron has vanishing total spin – which dictates the novel dipolar form for the spin correlations in real space and pinch points in reciprocal space (Fig. 2.15) [51, 88, 89]. Neutron diffuse scattering indicates that $(YSc)Mn_2$ and $CsNiCrF_6$ have the classical spin liquid state [90, 91]. The degeneracy can be lifted by weak perturbations such as single-ion anisotropy, dipole-dipole interaction and further-neighbor exchange interactions [92–94] and the system is forced to adopt a particular ground state configuration. For example, by including the dipolar interaction, Palmer and Chalker showed that quartic terms in the free energy lift the infinite degeneracy and stabilize a four-sublattice state with the ordering vector $\boldsymbol{k} = (0, 0, 0)$ (the PC phase) [92].
An isotropic Heisenberg interaction between the spins can be realised when the orbital momentum vanishes. This could happen either to the $3d$ transition metal ions whose spin-orbital coupling interactions are normally much weaker than the crystal field interactions leading to "orbital moment quenching" or to the rare earth ions with total

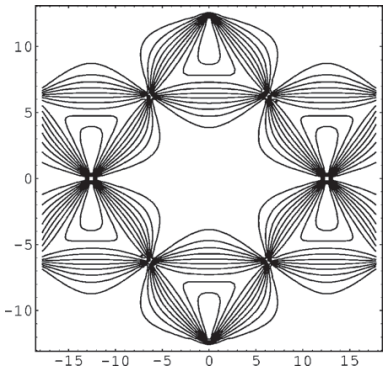

Figure 2.15: Structure factor of the Heisenberg pyrochlore antiferromagnet in the [HHL] plane (the vertical axis of the plot is [HH0] and the horizontal one is [00L]). Taken from Ref. [89].

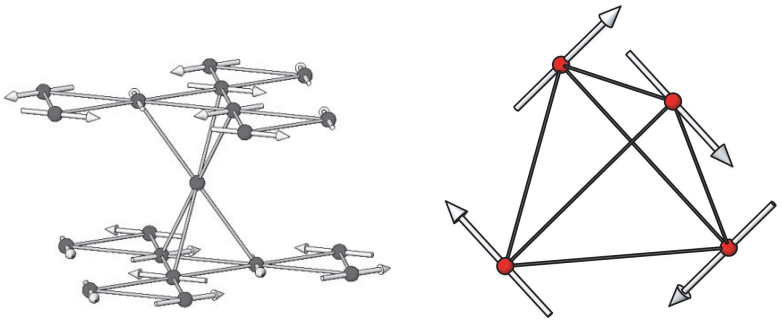

Figure 2.16: One-k order (left) and Palmer-Chalker state (right) observed in $Gd_2Ti_2O_7$ and $Gd_2Sn_2O_7$, respectively. Taken from Refs. [93, 95].

orbital momentum $\boldsymbol{L} = 0$. According to Hund's rules, the Gd^{3+} ion has the ${}^8S_{7/2}$ ground state with no orbital momentum and the $Gd_2B_2O_7$ are generally treated as spin-7/2 Heisenberg systems. Macroscopic measurements show that $Gd_2Ti_2O_7$, $Gd_2Sn_2O_7$ and $Gd_2Pt_2O_7$ order magnetically and neutron powder diffraction experiments reveal different magnetic structures for the former two compounds [25, 35, 93, 95]. $Gd_2Ti_2O_7$ has a magnetic structure of $\boldsymbol{k} = (1/2, 1/2, 1/2)$ with coplanar spin order on the Kagomé plane and disorder on the interstitial triangle lattice (Fig. 2.16) [95]. The neutron diffuse scattering shows that it is possibly a 4-k structure [96] but new evidence points to a single k ordering [97]. A recent theoretical calculation shows that the anisotropic exchange interaction can cause partial order and thermal fluctuations are responsible for the selection of the single-k or multi-k structure [98]. $Gd_2Sn_2O_7$ adopts the Palmer-Chalker phase (Fig. 2.16) due to a specific type of third-neighbour superexchange interaction

[93]. Fig. 2.17 shows the phase diagram for the Heisenberg pyrochlore antiferromagnet with further-neighbor exchange interactions and long range dipolar interactions. The different weightings of the weak perturbations to the Hamiltonian are responsible for the different ground state states of the two compounds [93]. The long range dipolar interaction not only leads to the transition to the Palmer-Chalker phase but also gapped magnon excitations [94]. As has been confirmed by the specific heat and inelastic neutron scattering data [99, 100].

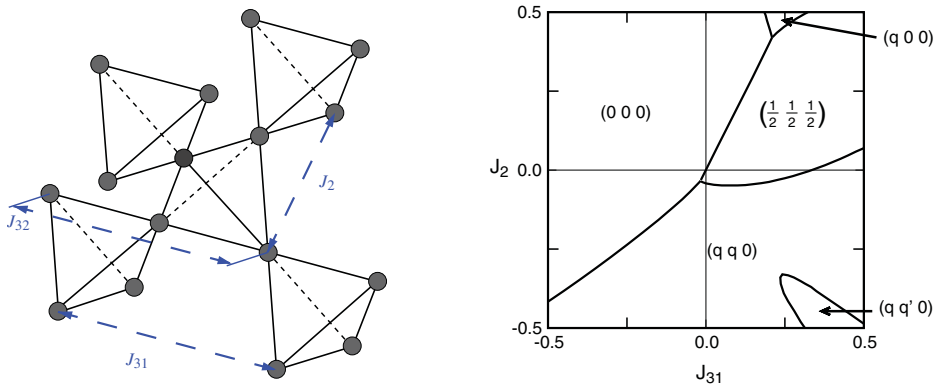

Figure 2.17: Phase diagram for Heisenberg pyrochlore antiferromagnet with further-neighbor exchange interactions and long-range dipolar interactions. Taken from Ref. [93].

However, the Gd^{3+} ion may not be ideally isotropic in the pyrochlore because a crystal field splitting of the ${}^8S_{7/2}$ manifold can occur as a result of the strong spin-orbit coupling which breaks the simple LS-coupling scheme and leads to the admixture of the $L \neq 0$ states into the ground state. Recent electron spin resonance experiments provided evidence for the single-ion anisotropy of Gd^{3+} with a strength comparable with the strength of the nearest-neighbor exchange interaction for both Ti and Sn compounds [101–103]. $Gd_2Zr_2O_7$ is explored in this thesis in Chapter 8.

3 Experimental techniques

3.1 Introduction

This chapter provides the principles of the experimental techniques used in this thesis for studying the structure and magnetic properties of the pyrochlores $R_2Zr_2O_7$ (R = Nd, Sm, Gd).

Both polycrystalline and single-crystalline samples were synthesized in the Chemical lab and Crystal lab in Helmholtz-Zentrum Berlin (HZB), Germany. The primary structure characterization was done by using lab-based powder X-ray diffraction (XRD) on the Bruker-D8 diffractometer in the XLab at HZB. Synchrotron X-ray diffraction experiments were further performed for the powder samples for a more precise analysis on the MS-Beamline [104] at the Paul Scherrer Institute (PSI), Switzerland. The structure parameters were determined with the Rietveld refinement of the XRD pattern using the softwares FullProf suite [21] and Topas Academic v3 (Bruker). The orientation of the single crystals was checked with the Laue diffractometer in the XLab, HZB.

Bulk properties of both powder and single crystal samples, including DC susceptibility, AC susceptibility, magnetization and specific heat, were measured using Physical Properties Measurement System (PPMS, Quantum Design) and Magnetic Properties Measurement System (MPMS-SQUID-VSM, Quantum Design) at the MagLab, HZB. The low-temperature (below 2 K) specific heat of the crystals $Nd_2Zr_2O_7$, $Sm_2Zr_2O_7$ and $Gd_2Zr_2O_7$ in magnetic fields along the [111] crystallographic direction were conducted in the group of Prof. Dr. P. Gegenwart in Augsburg University, Germany and the low-temperature AC susceptibility along the [111] direction of the crystal $Nd_2Zr_2O_7$ was measured by the group of Dr. T. Herrmannsdörfer at Hochfeld-Magnetlabor Dresden (HZDR), Germany. The low-temperature AC susceptibility of the single crystal $Gd_2Zr_2O_7$ and the powder $^{160}Gd_2Zr_2O_7$ was measured by André Sokolowski (Dipl.-Phys.) at HZB. These measurements provide the basic information of the magnetism and are important for planning neutron scattering experiments.

Powder neutron diffraction was performed on $Nd_2Zr_2O_7$ and $^{160}Gd_2Zr_2O_7$ [prepared with the low-neutron-absorbing isotope $^{160}Gd_2O_3$ from Oak Ridge National Lab (ORNL),

USA] for the determination of the possible magnetic long-range order using the DMC diffractometer at PSI and the D20 diffractometer at Institut Laue-Langevin (ILL) in France. High resolution neutron diffraction experiment was performed on $^{160}Gd_2Zr_2O_7$ on the D2B diffractometer at room temperature to study the structural defects.
Time-of-flight inelastic neutron scattering was conducted on powder $Nd_2Zr_2O_7$ and $^{154}Sm_2Zr_2O_7$ (prepared with low-neutron-absorbing isotope $^{154}Sm_2O_3$) for the determination of the crystal field state using the ARCS spectrometer [105] at the Spallation Neutron Source (SNS) at ORNL and the Merlin spectrometer in ISIS, UK. The non-magnetic $La_2Zr_2O_7$ powder sample was also prepared and measured as a background reference.
Polarized neutron diffuse scattering was performed on the single crystal $Nd_2Zr_2O_7$ using the DNS spectrometer at FRM2 in Munich, Germany, to investigate the short-range spin correlations. Unpolarized neutron diffuse scattering with applied field along the [110] and [111] directions was performed using the E2 diffractometer at HZB, to study the field effect on the system.
Time-of-flight inelastic cold neutron scattering experiment was performed on the single crystal $Nd_2Zr_2O_7$ using the CNCS spectrometer at SNS to study the magnetic excitations.
Muon spin relaxation was used to study the spin dynamics of the three compounds. The longitudinal positive muon spin relaxation experiments were performed on the powder $Nd_2Zr_2O_7$ and $Sm_2Zr_2O_7$ on the spectrometers LTF (20 mK-4.2 K) and GPS (1.5-300 K) at PSI. For $Gd_2Zr_2O_7$, only the spectra at temperatures between 1.5 K and 50 K were recorded on the GPS instrument.

3.2 Sample synthesis and physical property measurement

3.2.1 Preparation of powder and single crystal samples

All the powder samples were synthesized through the conventional solid state reaction method. The commercial pure R_2O_3 (R is the rare earth element) and ZrO_2 were used as the raw materials. A mortar and pestle was used for grinding and homogenizing of the reactants. Alumina crucibles and electric furnaces (20-1550 °C) were used for heating the samples in ambient atmosphere. A mechanical compressor was used for pelletizing the powder. The synthesis details for each sample are given in Chapter 4.
The single crystals were grown using a four mirror high-temperature optical floating zone furnace by Dr. A. T. M. N. Islam at the Crystal Lab, HZB. This instrument contains four tungsten halide lamps whose optical radiation is focused by four ellipsoidal mirrors

on two solid rods to be melted. The melting zone is held between the two rods by its own surface tension. During the crystal growth, the two rods are shifted continuously with melting a new zone and solidifying the former one.

3.2.2 Lab X-ray and synchrotron X-ray powder diffraction

X-rays are electromagnetic waves with a wavelength typically on the order of 1 Å, much shorter than the visible light. Because the wavelength of X-ray is of the same order of magnitude of the crystal lattice parameter, X-rays can be diffracted by crystals. Up to date, X-ray diffraction (XRD) has been widely used for crystal structure studies. X-rays can be scattered by electrons of an atom through electronic interactions: the varying electric field of X-ray accelerates and decelerates the electrons, which radiate X-rays of the same frequency. The addition of the scattered X-rays from all the electrons of an atom yields the atom scattering factor. Due to the spacial spread of the electron cloud of an atom, the scattering intensity decreases with increasing the module of the scattering vector $\boldsymbol{Q} = \boldsymbol{k}_\mathrm{f} - \boldsymbol{k}_\mathrm{i}$ ($\boldsymbol{k}_\mathrm{i}$ and $\boldsymbol{k}_\mathrm{f}$ are the initial and final wave vectors of the X-rays) and this relation is referred as atom scattering form factor $f(Q)$.
A crystal is a three-dimensional periodic arrangement of atoms or ions and the X-rays scattered by a crystal have maximum and minimum intensities due to the coherent effect of the scattered X-rays from different atoms. The scattering maxima happen at certain scattering angle which is given by Bragg's law (Fig. 3.1). According to Bragg's law, the crystal lattice can be viewed as a stacking of groups of parallel planes and the diffraction can be described as reflections by different groups of the parallel planes. The scattering maximum occurs if the incident angle θ and the distance d between the neighboring planes satisfy

$$n\,\lambda = 2\,d\,\sin\theta\,(n = 1, 2, 3...), \tag{3.1}$$

where λ is the X-ray wavelength and n is the order of the diffraction. Another way to put Bragg's law is that the diffraction maxima happen when the scattering vector $\boldsymbol{Q}$ is equal to a reciprocal vector of the crystal. For the non-Bravais lattice, the unit cell contains not only one atom but multiple atoms of the same kind or different kinds and a structure factor can be defined serving as the scattering unit of the lattice which is given by

$$F(\boldsymbol{Q}) = \sum_i f_i(Q)\exp(\mathrm{i}\boldsymbol{r}_i \cdot \boldsymbol{Q}), \tag{3.2}$$

where $f_i(Q)$ is the atom scattering factor of the i^{th} atom at $\boldsymbol{r}_i$ in the unit cell.
There are two types of X-ray sources: sealed hot-cathode tube and synchrotron radiation.

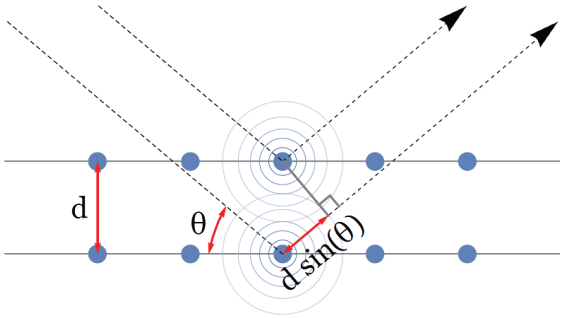

Figure 3.1: Bragg diffraction. X-rays of identical wavelength and phase approach a crystalline solid and then are scattered off by the atoms. The lower beam travels an extra distance of $2d \sin\theta$ and constructive interference occurs when this distance is equal to an integer multiple of the X-ray wavelength.

The first one is widely used on the lab-based X-ray diffractometer which generates X-rays by striking a metal target (e.g. copper) with accelerated electrons (energy 20-50 keV). Both continuous-wavelength X-rays and characteristic radiation is generated depending on the acceleration voltage. The characteristic radiation originates from the electron ejection and refilling of a inner orbital of the atoms in the target and contains X-rays of several discrete, narrow wavelength bands which are used for the normal X-ray diffraction. The continuous-wavelength X-rays are emitted during the braking of the accelerated electrons in the target and is used on the single crystal Laue diffractometer (see Sec. 3.2.3). For the synchrotron radiation, electrons are first accelerated in a booster synchrotron which increases the energy of electrons to $\sim$ 500 MeV and then are guided to go through magnetic fields created by bending magnets during which X-rays are emitted. Synchrotron X-rays have several advantages over the former one, such as high monochromaticity, low beam divergence, high brightness and high polarisation, which makes them suitable for precise analysis.

3.2.3 X-ray Laue diffraction

X-ray Laue diffraction was used for aligning the crystals and for this purpose only the diffraction angles were analysed. A monochromatic beam illuminating a crystal can be diffracted only by certain crystal plane families which form the Bragg angle θ with the incident beam (satisfying Bragg's law). The use of a white beam allows simultaneous observation of a large number of reflections. It is convenient to think in reciprocal space using Ewald's construction as shown in Fig. 3.2 [106]. Since diffraction is elastic scattering, the modules of the initial and final wave vectors are the same, which means

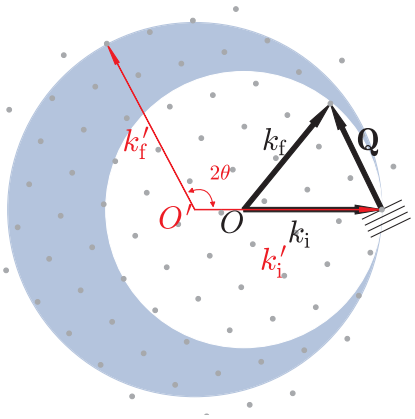

Figure 3.2: Ewald's construction showing the polychromatic X-ray Laue diffraction of a single crystal. Gray points show the reciprocal lattice. Arrows show the incident ($\boldsymbol{k}_i$), final ($\boldsymbol{k}_f$) wave vectors and the scattering vector ($\boldsymbol{Q}$). Two Ewald's spheres correspond to the minimum and maximum X-ray wavelength and the shaded area is the reciprocal space measured. The parallel lines show a group of crystal planes.

that if putting the origins of the two vectors at the same point, the ending points of the two vectors are on the same spherical surface (Ewald's sphere) whose centre is the origin point of the two vectors and radius is the module. According to Bragg's law, the difference between the wave vectors of the incident beam and the diffracted beam is the reciprocal vector corresponding to the reflection planes. Therefore, by choosing the centre of Ewald's sphere to make the incident wave vector terminate at a point in the reciprocal space, all the reciprocal points on the Ewald's sphere are the possible reflections. Different Bragg peaks can be accessed by rotating the crystal (the reciprocal lattice is attached to the crystal lattice). For a polychromatic beam, reflections relating to multiple Ewald's spheres can be measured simultaneously which corresponds to the reciprocal points within the volume between the Ewald's spheres defined by the maximum and minimum wavelengths.

The Laue diffractometer used here has a continuous-wavelength X-ray source (1-1.5 Å, molybdenum target, 20 KV). Back scattering geometry is used and the diffraction pattern is measured by a plate coated with X-ray fluorescence material. The pattern is digitized by a scanner and indexed using the software OrientExpress [107].

3.2.4 Susceptibility, magnetization and specific heat

Macroscopic measurements, such as DC susceptibility, AC susceptibility, magnetization and specific heat, were conducted on the Physical Properties Measurement System (PPMS) and Magnetic Properties Measurement System (MPMS). The measurements below 2 K were performed by the collaborators using home-made setups with similar principles as the commercial instruments.

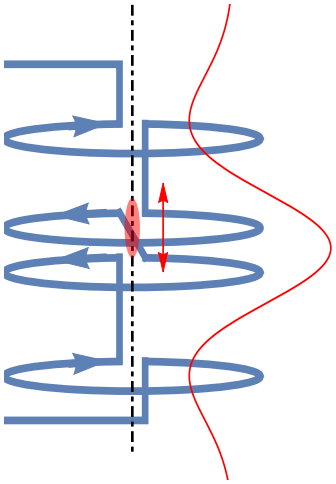

Figure 3.3: Pick-up coil for the magnetometer. The sample (assumed to be a dipole) moving vertically in the coil in a vertical magnetic field leads to the change of the flux (red curve).

The DC susceptibility and magnetization is measured by the flux method. As shown in Fig. 3.3, the sample is put at the centre of a compensated pick-up coil which contains oppositely wounded coils so that the fluxes in the coils add. A uniform magnetic field is applied to magnetize the sample. By moving the sample along the axis of the coil, the flux through the coil changes because the non-uniform field generated by the magnetised sample. During this process, an electric field is induced in the coil from which the magnetization of the sample can be extracted with assuming that the sample is a ideal magnetic dipole. The vibrating sample magnetometer (VSM) on the MPMS adopts this method and during the measurement, the sample is vibrated and the induced electric voltage is measured with a lock-in amplifier. A higher sensitive way to measure the flux change through the pick-up coil is with a superconducting quantum interference device (SQUID) which contains Josephson junctions. A circuit couples the flux into the SQUID and the change of the flux causes voltage oscillations for every one flux quantum $\Phi_0 = h/2e = 2.07 \times 10^{-15}\mathrm{Tm}^2$.

AC susceptibility is the susceptibility of the sample in an alternating field which measures the additional time-dependent properties of the magnetization (i.e. the magnetic dynamics) which is not given in the DC measurement. In the measurement, the sample is put inside a similar compensated pick-up coil and magnetised in an AC field generated by a outer coil. Because the sample magnetization changes over time due to the AC field, an inductive current can be induced in the pick-up coil without moving the sample (no current is generated by the space-uniform AC field because of the compensation). There are two quantities to measure: the amplitude of the susceptibility χ_{AC} and the phase difference ϕ between the time-dependent magnetization and the driving AC field due to the finite responding time of sample. The data is commonly presented in terms of the real part χ' and the imaginary part χ'' of χ_{AC},

$$\begin{aligned} \chi' &= \chi_{\mathrm{AC}} \cos(\phi), \\ \chi'' &= \chi_{\mathrm{AC}} \sin(\phi). \end{aligned} \tag{3.3}$$

At low frequencies, the magnetization could follow the driving AC field leading to $\phi \to 0$ and χ' is approximately the DC susceptibility. At high frequencies, the magnetization may lag behind the drive field and a non-zero χ'' appears indicating the relaxation of the magnetization.

Specific heat provides information on the phase transition and energy spectrum of the investigated system. The entropy can be extracted which tells the number of degrees of freedom and the ground state degeneracy in the system. For example, the specific heat of the spin ice material reveals that there is no long range order in the system and the entropy at low temperature is far from zero which violates the third law of thermodynamics indicating a macroscopic number of degeneracy in the ground state. The isobaric specific heat is usually measured with the adiabatic relaxation method. The sample is glued to a platform with heaters and thermometers and the measurement is conduced in high vacuum in the following steps. First, the heater is switched on to heat up the sample and after a short time, the heater is switched off. Second, record the temperature of the sample as function of time. Third, calculate the specific heat of the sample at this temperature based on the relaxation time and the known thermal link to the heat bath.

3.3 Neutron scattering

Neutron scattering is the main technique used in this thesis for studying the crystal structure, magnetic structure and magnetic excitations. The principles of different neutron

scattering techniques are outlined in this section (see Ref. [108] for more details).

3.3.1 Basic theory of neutron scattering

Thermal neutrons have a de Broglie wavelength of the order of interatomic distances in liquids and solids which can be used for diffraction to study the structure of condensed matter. The energy of thermal neutrons is similar to many excitations in condensed matter and the inelastic scattering provides information on the excited states. The neutron is uncharged but has a magnetic moment and thus it interacts with magnetic unpaired electrons, which could yield information on the magnetic properties of the materials.

Neutron scattering experiments are generally performed on two large scale facilities: reactor and spallation neutron sources. The reactor produces neutrons through nuclear fission in the chain reaction:

$$^{235}\mathrm{U} + {}^{1}\mathrm{n} \rightarrow {}^{92}\mathrm{Kr} + {}^{141}\mathrm{Ba} + 3\ {}^{1}\mathrm{n}\ .$$

The neutrons produced have a spectrum of energy or wavelength following the Maxwell-Baltzmann distribution which can be controlled by varying the modulator temperature. Some neutron scattering experiments in the thesis are carried out with the reactor neutron sources at BER2 (Berlin), FRM2 (Munich) and ILL (Grenoble). For a spallation source, first protons are accelerated in a synchrotron and then they collide with a heavy metal target (e.g. W, Ta and Hg) and excite the nuclei. When the excited nuclei decays, neutrons are emitted. The experiments performed with the spallation source are at SNS in the US and ISIS in UK.

In a scattering experiment, a beam of neutron is incident on a scattering system (solid, liquid or gas) and the number of neutrons scattered in a given direction is counted as a function of energy. The scattering intensity can be quantified by the partial differential cross section which is defined by [108],

$$\frac{\mathrm{d}^2\sigma}{\mathrm{d}\Omega \mathrm{d}E'} = \begin{array}{l}(\textit{number of neutrons scattered per second into} \\ \textit{a small solid angle } \mathrm{d}\Omega \textit{ in the direction at } \theta,\ \phi \\ \textit{with final energy between } E' \textit{ and } E' + \mathrm{d}E')/\Phi\, \mathrm{d}\Omega\, \mathrm{d}E',\end{array} \tag{3.4}$$

where θ and ϕ defines the direction of the scattering and Φ is the flux of the incident neutrons.

In a scattering process, the incident neutron is scattered by the system owning to the

interaction potential $\mathcal{V}$ and the partial differential cross section can be calculated by

$$\frac{\mathrm{d}^2\sigma}{\mathrm{d}\Omega dE'} = \frac{k'}{k}(\frac{m}{2\pi\hbar^2})^2 \sum_{\lambda_i,s_i} p_{\lambda_i} p_{s_i} \sum_{\lambda_f,s_f} |\langle k_f s_f \lambda_f|\mathcal{V}|k_i s_i \lambda_i\rangle|^2 \delta(E_{\lambda_i} - E_{\lambda_f} + E_i - E_f), \quad (3.5)$$

where k_i and k_f are the initial and final neutron wave vectors and E_i and E_f are the corresponding neutron energies. The two summations are over the initial and final neutron spin states s_i and s_f and the initial and final system states λ_i and λ_f. p_{λ_i} and p_{s_i} are the statistical weight factor for the system at the λ_i state and for a neutron in the spin state s_i. E_{λ_i} and E_{λ_f} are the initial and final system energies. The interaction potential $\mathcal{V}$ can be nuclear or magnetic. The scattering process follows the laws of momentum conservation and energy conservation

$$\begin{aligned} \boldsymbol{Q} &= \boldsymbol{k}_f - \boldsymbol{k}_i, \\ \hbar\omega &= E_i - E_f, \end{aligned} \quad (3.6)$$

where $\hbar\boldsymbol{Q}$ is the momentum transfer from neutrons to the sample and $\hbar\omega$ is the energy transfer corresponding to the energy change of the sample $E_{\lambda_f} - E_{\lambda_i}$.

3.3.2 Nuclear scattering

The explicit form the partial differential cross section is obtained by inserting the specific function of the interaction potential in Eq. 3.5. In the nuclear scattering, the potential can be described by the Fermi pseudo potential,

$$\mathcal{V}_l(\boldsymbol{r}) = \frac{2\pi\hbar^2}{m} b_l \delta(\boldsymbol{r} - \boldsymbol{R}_l), \quad (3.7)$$

where b_l is the scattering amplitude of the l^{th} nuclei at position $\boldsymbol{R}_l$. The scattering amplitude is determined by experiments and it is different for different nuclei and also depends on the relative orientation of the spins of the neutron and the nucleus. The three dimensional δ function is used here because the nuclear force is short ranged (shorter that the neutron wavelength) and thus the nuclear scattering is spherically symmetric. This point is different from the X-ray scattering of a atom where the X-rays are scattered by the electrons within a volume resulting in the Q dependence of the scattering intensity. With this potential, the partial differential cross section can be written as

$$\frac{\mathrm{d}^2\sigma}{\mathrm{d}\Omega\mathrm{d}E'} = \frac{\mathrm{d}^2\sigma_{\mathrm{coh}}}{\mathrm{d}\Omega\mathrm{d}E'} + \frac{\mathrm{d}^2\sigma_{\mathrm{inc}}}{\mathrm{d}\Omega\mathrm{d}E'}. \quad (3.8)$$

The two terms on the right side are the coherent and incoherent scattering,

$$\begin{aligned}\frac{\mathrm{d}^2\sigma_{\mathrm{coh}}}{\mathrm{d}\Omega\mathrm{d}E'} &= \frac{\sigma_{\mathrm{coh}}}{4\pi}\frac{k'}{k}\frac{1}{2\pi\hbar}\sum_{l,l'}\int_{-\infty}^{\infty}\langle\exp[-i\boldsymbol{Q}\cdot\boldsymbol{R}_{l'}(0)]\exp[i\boldsymbol{Q}\cdot\boldsymbol{R}_l(t)]\rangle\times\exp(-i\omega t)\mathrm{d}t,\\ \frac{\mathrm{d}^2\sigma_{\mathrm{inc}}}{\mathrm{d}\Omega\mathrm{d}E'} &= \frac{\sigma_{\mathrm{inc}}}{4\pi}\frac{k'}{k}\frac{1}{2\pi\hbar}\sum_{l}\int_{-\infty}^{\infty}\langle\exp[-i\boldsymbol{Q}\cdot\boldsymbol{R}_{l}(0)]\exp[i\boldsymbol{Q}\cdot\boldsymbol{R}_l(t)]\rangle\times\exp(-i\omega t)\mathrm{d}t.\end{aligned} \tag{3.9}$$

where

$$\begin{aligned}\sigma_{\mathrm{coh}} &= 4\pi(\bar{b})^2,\\ \sigma_{\mathrm{inc}} &= 4\pi[\bar{b^2}-(\bar{b})^2],\end{aligned} \tag{3.10}$$

The bars in equation Eq. 3.10 indicate the average over all nuclei in the sample. The coherent scattering depends on the position correlation of the same nucleus at different times and the correlation between the positions of different nuclei at different times. The latter contribution produces the well-known Bragg (elastic) scattering ($t\rightarrow\infty$) of the crystal lattice and the inelastic scattering of the cooperative excitations of the lattice. The incoherent part depends on the correlation of the same nucleus at different times which cannot yield interference effect and thus leads to an isotropic background scattering.

The equations above are valid for a crystal containing only one type of element. If the sample contains several elements, the summation is over all the nuclei of different types. For example, the elastic scattering cross section of a crystallized compound is given by

$$\frac{\mathrm{d}\sigma_{\mathrm{coh}}}{\mathrm{d}\Omega} = \frac{N(2\pi)^3}{V_0}\sum_{\boldsymbol{\tau}}|F_{\mathrm{N}}(\boldsymbol{Q})|^2\delta(\boldsymbol{Q}-\boldsymbol{\tau})\delta(\hbar\omega) \tag{3.11}$$

where N is the number of unit cells in the volume V_0 contributing to the scattering, $\boldsymbol{\tau}$ is reciprocal vector and $F_{\mathrm{N}}(\boldsymbol{Q})$ is the unit cell structure factor which is the coherent addition of the scattering from all the nuclei in the unit cell,

$$F_{\mathrm{N}}(\boldsymbol{Q}) = \sum_d \bar{b}_d\exp(i\boldsymbol{Q}\cdot\boldsymbol{R}_d)\exp[-W_d(\boldsymbol{Q},T)] \tag{3.12}$$

where $\exp[-W_d(\boldsymbol{Q},T)]$ is the Debye-Waller factor taking account of the attenuation of the scattering due to the thermal vibrations of the nuclei at temperature T.

3.3.3 Magnetic scattering

Nuclear scattering yields information on the position correlation of the nuclei in materials. Similarly, magnetic scattering measures the correlations of the magnitudes and orientations of the magnetic moments in the sample. Magnetic scattering arises from the dipole-dipole interaction between the magnetic moments of neutron and spin or/and orbital magnetic moment of the unpaired electron. The interaction potential can be written as

$$\begin{aligned} \mathcal{V}_m &= -\boldsymbol{\mu}_\mathrm{n} \cdot \boldsymbol{B} \\ &= -\frac{\mu_0}{4\pi}\gamma\mu_\mathrm{N} 2\mu_\mathrm{B}\boldsymbol{\sigma} \cdot [\nabla \times (\frac{\boldsymbol{s}\times\boldsymbol{R}}{R^2}) + \frac{1}{h}\frac{\boldsymbol{p}\times\boldsymbol{R}}{R^2}] \end{aligned} \tag{3.13}$$

where $\boldsymbol{B}$ is the magnetic filed in the materials, γ is the gyromagnetic ratio of neutron, μ_N is the nuclear magneton, $\boldsymbol{\sigma}$ is the Pauli spin operator for the neutron and $\boldsymbol{s}$ and $\boldsymbol{p}$ are the spin and orbital momentum operators of the magnetic electron. It is convenient to write this in the form of a Fourier transformation which is

$$\begin{aligned} \mathcal{V}_m(\boldsymbol{Q}) &= r_0\boldsymbol{\sigma} \cdot \boldsymbol{M}_\perp(\boldsymbol{Q}) \\ \text{with } \boldsymbol{M}_\perp(\boldsymbol{Q}) &= \hat{\boldsymbol{Q}} \times (-\frac{1}{2\mu_\mathrm{B}}\boldsymbol{M}(\boldsymbol{Q}) \times \hat{\boldsymbol{Q}}) \end{aligned} \tag{3.14}$$

where r_0 is the classical electron radius, $\boldsymbol{M}(\boldsymbol{Q})$ is the Fourier transformation of the magnetic field in the sample and $\hat{\boldsymbol{Q}}$ is the unit vector of the scattering vector $\boldsymbol{Q}$. The magnetic neutron scattering with the scattering vector $\boldsymbol{Q}$ measures the Fourier component of magnetic field in the sample that is perpendicular to $\boldsymbol{Q}$. With this interaction potential, the magnetic scattering cross section for a Bravais crystal is

$$\frac{\mathrm{d}^2\sigma}{\mathrm{d}\Omega dE'} = \frac{(\gamma r_0)^2}{2\pi\hbar}\frac{k'}{k}N[\frac{1}{2}gf(\boldsymbol{Q})]^2 \exp[-W(\boldsymbol{Q},T)]\sum_{\alpha,\beta}(\delta_{\alpha\beta} - \hat{Q}_\alpha\hat{Q}_\beta)S^{\alpha\beta}(\boldsymbol{Q},\omega) \tag{3.15}$$

where N is the number of the magnetic ions, g is the Landé g-factor, $f(\boldsymbol{Q})$ is the magnetic form factor and $S^{\alpha\beta}(\boldsymbol{Q},\omega)$ is the dynamical correlation function. The term $(\delta_{\alpha\beta} - \hat{Q}_\alpha\hat{Q}_\beta)$ ensures that only spin components perpendicular to the scattering vector $\boldsymbol{Q}$ contribute to the cross section. Eq. (3.15) is valid either for spin-only ions or for ions to which the dipole approximation applies.

The magnetic form factor is different for different magnetic ions depending on the spacial distribution and orbital motion of the magnetic electron. For an ion with only spin moment,

$$f(\boldsymbol{Q}) = \int s(\boldsymbol{r})\mathrm{e}^{i\boldsymbol{Q}\cdot\boldsymbol{r}}\mathrm{d}\boldsymbol{r} \tag{3.16}$$

where $s(\boldsymbol{r})$ is the spin density at the position $\boldsymbol{r}$. Different from the isotropic nuclear scattering, the magnetic scattering cross section decreases with increasing Q. The magnetic form factor of an ion with orbital moment is more complicated and they are normally treated within the dipolar approximation when Q^{-1} is large compared with the mean radius of the orbital of the unpaired electrons,

$$\frac{1}{2}gf(\boldsymbol{Q}) = \frac{1}{2}g_{\mathrm{S}}\tilde{F}_0 + \frac{1}{2}g_{\mathrm{L}}(\tilde{F}_0 + \tilde{F}_2) \tag{3.17}$$

where

$$\begin{aligned} g_{\mathrm{S}} &= 1 + \frac{S(S+1) - L(L+1)}{J(J+1)}, \\ g_{\mathrm{L}} &= \frac{1}{2} + \frac{L(L+1) - S(S+1)}{2J(J+1)}, \\ \tilde{F}_n &= 4\pi \int_0^\infty j_n(Qr)s(r)r^2 \mathrm{d}r. \end{aligned} \tag{3.18}$$

The function $j_n(Qr)$ is the spherical Bessel function of order n and $s(r)$ is the normalised density of the unpaired electrons. The form factors are parameterized with the parameters tabulated [109]. Fig. 3.4 shows the form factors for the ions Nd^{3+}, Sm^{3+} and Gd^{3+}.

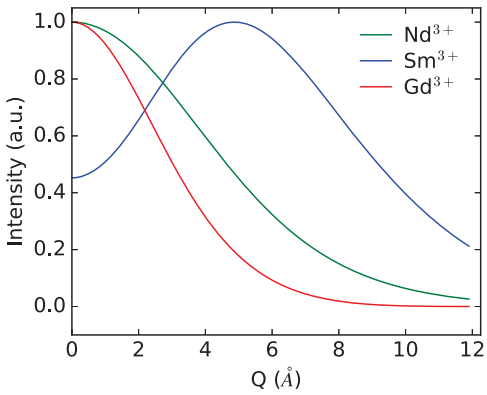

Figure 3.4: Form factors for the rare earth ions Nd^{3+}, Sm^{3+} and Gd^{3+}.

The dynamical correlation function is

$$S^{\alpha\beta}(\boldsymbol{Q},\omega) = \sum_l \exp(i\boldsymbol{Q}\cdot\boldsymbol{l}) \int_{-\infty}^{\infty} \langle s_0^\alpha(0) s_l^\beta(t)\rangle \exp(-i\omega t)\mathrm{d}t \tag{3.19}$$

where $s_l^\beta(t)$ is the β component of the spin of atom l at time t. The dynamical correlation function is the Fourier transformation of the space and time correlations of the magnetic

moment in the system. For the elastic scattering, $\langle s_0^\alpha(0) s_l^\beta(t)\rangle$ is independent of time and becomes $\langle s_0^\alpha\rangle\langle s_l^\beta\rangle$. Integrating with respect to t for Eq. 3.15 gives

$$\frac{\mathrm{d}\sigma}{\mathrm{d}\Omega} = (\gamma r_0)^2 N[\frac{1}{2} g f(\boldsymbol{Q})]^2 \exp(-W(\boldsymbol{Q},T)) \sum_{\alpha,\beta}(\delta_{\alpha\beta} - \hat{Q}_\alpha \hat{Q}_\beta) \times \sum_l \exp(i\boldsymbol{Q}\cdot\boldsymbol{l})\langle s_0^\alpha\rangle\langle s_l^\beta\rangle. \quad (3.20)$$

For a crystal with long range magnetic order, the magnetic Bragg scattering is

$$\frac{\mathrm{d}\sigma}{\mathrm{d}\Omega} = (\frac{\gamma r_0}{2\mu_\mathrm{B}})^2 N \frac{(2\pi)^3}{v_0} \sum_{\boldsymbol{\tau}} \exp[-W(\boldsymbol{Q},T)]\delta(\boldsymbol{Q}-\boldsymbol{\tau})|\hat{\boldsymbol{\tau}} \times [F_\mathrm{M}(\boldsymbol{\tau}) \times \hat{\boldsymbol{\tau}}]|^2 \quad (3.21)$$

where v_0 is unit cell volume and

$$F_\mathrm{M}(\boldsymbol{\tau}) = \int_\mathrm{cell} \langle \boldsymbol{M}(\boldsymbol{r})\rangle \exp(i\boldsymbol{Q}\cdot\boldsymbol{r})\mathrm{d}\boldsymbol{r} \quad (3.22)$$

which is the magnetic structure factor.

3.3.4 Magnetic polarized neutron scattering

The operator $\boldsymbol{\sigma}\cdot\boldsymbol{M}_\perp(\boldsymbol{Q})$ in the magnetic potential given by Eq. 3.14 indicates that the spin of a neutron can be flipped after the scattering by the magnetic moment perpendicular to the neutron spin. The equations given in the sections above are for unpolarized neutron scattering which is the summation of the scattering events with neutron spins flipped and un-flipped corresponding to the summation of all the $S^{\alpha\beta}(\boldsymbol{Q},\omega)$ components. The neutron scattering with polarization analysis examines the change of the neutron spin before and after the scattering event and makes it possible to separate these different components of the dynamical correlation function. In addition, the coherent nuclear scattering is non-spin-flip.

There are two types of polarization analysis, that is, uniaxial polarization analysis and spherical polarization analysis. The first type analyses the polarization of scattered neutrons parallel and antiparallel to the initial polarization. In some cases the polarization of the scattered neutrons can be rotated by an arbitrary angle with respect to the initial polarization and a complete analysis of the polarization is needed which corresponds to the second type. In the thesis, uniaxial polarisation analysis is used which is usually adopted for measuring the dipolar correlations of spin ice materials.

As mentioned above, only the components of the moments in the scattering plane ($\boldsymbol{M} \perp \boldsymbol{Q}$) contribute to the magnetic scattering. With a polarized neutron beam, the initial

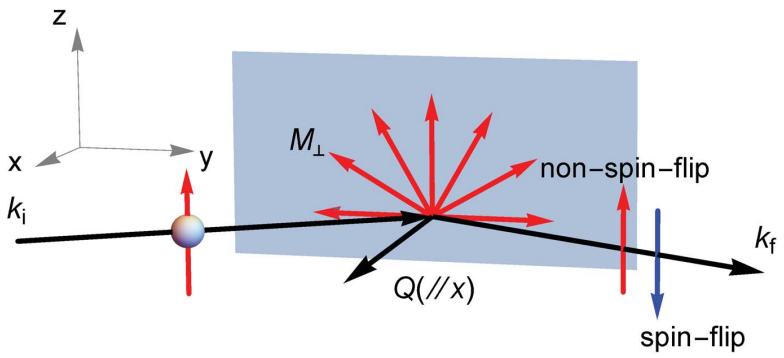

Figure 3.5: Experimental geometry of the polarized neutron scattering.

polarisation of the neutron can be flipped only by the components perpendicular to the neutron polarization. Fig. 3.5 shows the usual experiment geometry of the polarised neutron scattering. The Z axis is chosen to be vertical and along the initial neutrons polarization. In the horizontal plane, the X axis is along $\boldsymbol{Q}$ and perpendicular to it is the Y axis. With the Z polarization analysis, the spin flipping signal yields the $S^{yy}(\boldsymbol{Q},\omega)$ component of the correlation function and the non-spin-flip channel measures the $S^{zz}(\boldsymbol{Q},\omega)$ component. Spin ice materials show pinch point patterns in the spin-flip channel [32].

3.3.5 Neutron scattering instruments

Several neutron scattering instruments were used for the studies in the thesis: powder neutron diffractometers DMC (PSI), D20 and D2B (ILL); polarised neutron diffuse scattering spectrometer DNS (FRM2); diffuse scattering diffractometer E2 (HZB); time-of-flight inelastic neutron scattering spectrometer CNCS (SNS) and Merlin (ISIS). This section presents the general information of the instruments.

Powder diffractometer

Powder neutron diffraction has been widely used for studying the crystal structure and magnetic structure. According to Bragg's law, the diffraction of a crystal can be simply described as reflections by groups of parallel planes forming the Bragg angle with the incident beam. For a single crystal sample, the sample should be rotated to access certain Bragg peaks. While all the Bragg peaks within a 2θ range can be measured simultaneously with a powder sample because it contains large amount of randomly oriented small crystals which makes it possible that there are always many grains having the suitable orientations for different Bragg peaks. In a powder diffraction experiment,

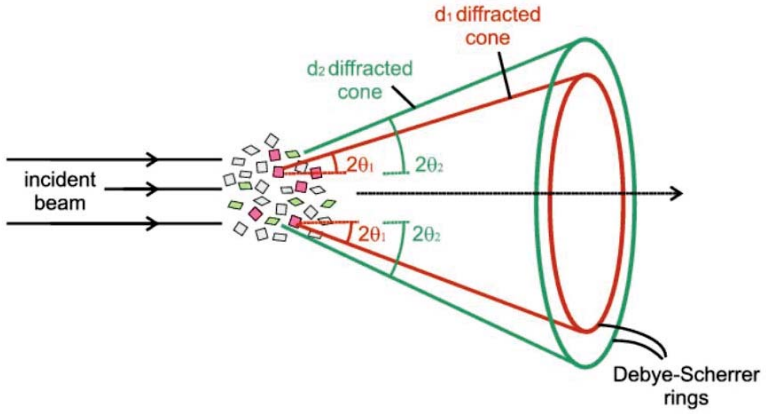

Figure 3.6: Principle of powder diffraction. Taken from Ref. [110].

each Bragg peak corresponds to a diffraction cone (apex angle $2 \times 2\theta$) (or Debye-Scherrer ring) with uniformly distributed scattering intensity if there is not a preferred orientation as shown in Fig. 3.6. Therefore many Bragg diffraction peaks could be measured at the same time with a detector array crossing the diffraction rings. However, the diffraction cones of the crystal planes with the same d spacing coincide, resulting in a loss of the information about the intensities of the individual Bragg peaks. Fig. 3.7 shows the general setup of a powder diffractometer. The diffraction pattern is normally refined with the Rietveld method which fits the data by adjusting a structure model [111].

Single crystal neutron diffuse scattering

Neutron diffuse scattering is mostly used for measuring the broad diffuse scattering of short-range correlations in contrast to neutron diffraction which measures the sharp Bragg peaks of the long-range order. Therefore, measuring a single crystal sample is preferred in order to obtain a two or three dimensional pattern rather than measuring a powder sample obtaining a spherical averaged pattern. The resolution of this type of measurement is generally lower than the diffractometer because only broad signals are to measure. A plane or a volume of the reciprocal space can be measured by rotating the single crystal and the detectors during the measurement.

Figure 3.8 shows the schematic experimental arrangement for the polarised neutron diffuse scattering. First a polarized beam is produced by the polariser (Heusler alloy monochromator, ^{3}He filter or polarizing supermirror). The polarization can be flipped by 180° by a flipper. After the scattering the polarization of the beam can be analysed by an analyser and a detector. In addition, a uniform guide field along the neutron polarisation exists on the neutron flying path for keeping the neutron polarization unchanged during

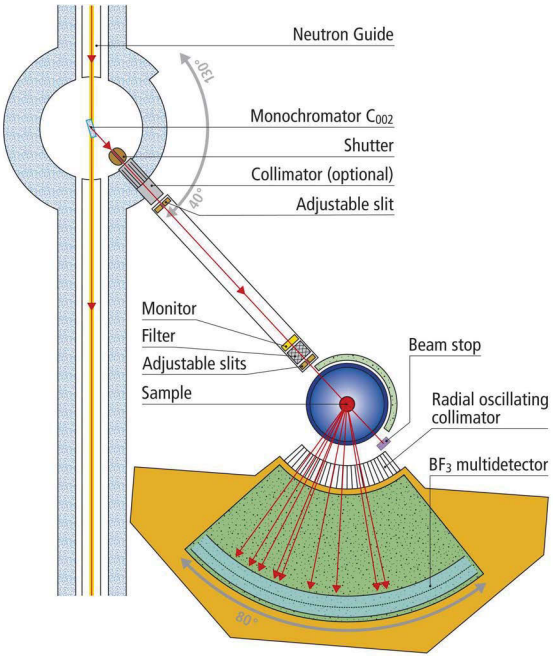

Figure 3.7: Schematic setup of the DMC diffractometer. A monochromatic beam with wavelength λ is extracted from a polychromatic beam using the graphite (002) Bragg reflection followed by the filter removing the neutrons with wavelengths λ/n (n is a integer). Then the incident beam is diffracted by the powder sample and the diffraction intensity is measured by the detector bulk covering a certain 2θ range. Taken from Ref. [112].

the flight.

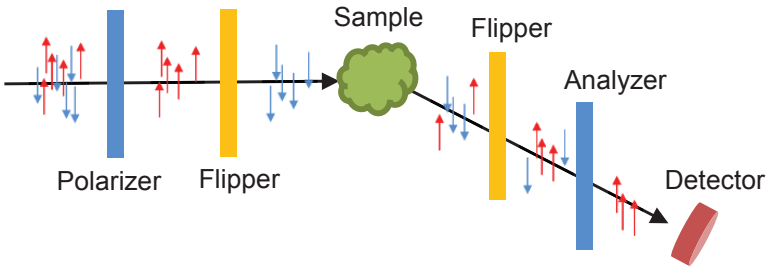

Figure 3.8: Schematic experimental arrangement for polarized neutron diffuse scattering.

Time-of-flight neutron spectrometer

In inelastic neutron scattering, the energy transfer is determined by comparing the kinetic energies of the incident and scattered neutrons. The energy of the neutron can be

determined by analysing the neutron wavelength, $E = \frac{h^2}{2m_n\lambda^2}$ where h and m_n are the Plank constant and neutron mass, respectively. For example, the Bragg scattering of a crystal of known lattice parameter is used to obtain the neutron energy on the triple-axis spectrometer. The neutron energy also can be obtained from the speed of the neutron, $E = \frac{1}{2}m_n v^2$ where v is the speed of neutron, which is realized by measuring the time for neutrons flying through a distance. The first method is generally used on the spectrometers on a continuous neutron source and the second method is mostly used for the time-of-flight (tof) spectrometer on the pulsed spallation neutron source. Fig. 3.9 shows the principles of the tof spectrometer. At t_0, a pulse of neutrons with different speeds is produced. The chopper sited at the distance L_0 ahead opens a gap at t_1 for a short time, which selects neutrons with the speed $v_1 = L_0/(t_1 - t_0)$. After travelling for another distance L_1, the neutrons with the speed v_1 come to the sample and the scattering event happens. Because of the scattering, the neutrons gain or loss energy with momenta also changed and then fly in different directions along another path L_2. Finally, the neutrons arrive at the detectors at the end of the path which are arranged to cover a certain 2θ range. The detector counts the number of neutrons with recording their arrival time t_2 and then the speed of the scattered neutron is calculated by $v_2 = \frac{L_2}{t_2-(L_0+L_1)/v_1}$. At last, the energy and momentum transfer can be obtained with using Eq. 3.6.

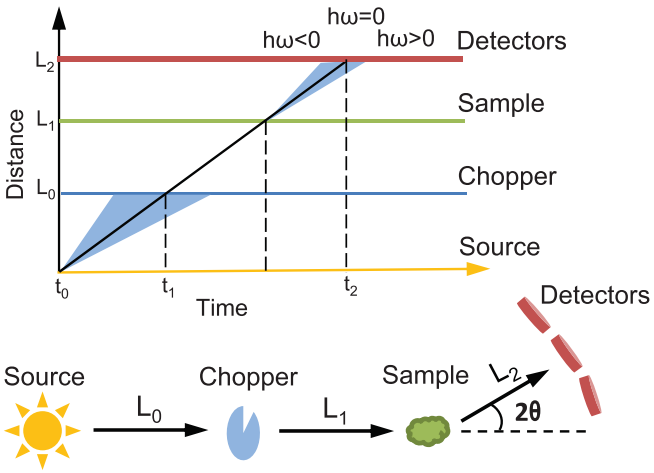

Figure 3.9: Schematic setup of the direct-geometry time-of-flight neutron inelastic scattering spectrometer.

3.4 Muon spin relaxation (μSR)

Complementary to neutron scattering which detects the collective magnetic state, Muon spin relaxation is a sensitive local probe for studying magnetic order and fluctuations. Muons can be implanted in the sample and sense the local magnetic field under which the muon spin will precess inducing oscillations of the muon polarization. The time evolution of the muon polarisation yields information on the magnitude and and direction of field at the muon stopping site and the damping of the muon polarisation gives information on the field distribution and fluctuation. This section provides the principle of the positive muon spin relaxation technique (see Ref. [113] for more details).

3.4.1 Properties of muon and the μSR technique

The muon is an elementary particle discovered in 1936 as secondary radiation from cosmic rays. It has a mass $\sim$ 200 times that of an electron. It can be positively or negatively charged (μ^+ or μ^-) so that it can interact with materials (μ^+ is generally used for μSR). Similar to electrons, the muon is spin-1/2 with a gyromagnetic ratio γ_μ =851.6 Mrad $s^{-1}T^{-1}$ which makes it possible to probe weak magnetic fields in materials.

Muon production and polarized beam: in order to produce muons, pions are first produced in the reaction of high energy protons (kinetic energy 600-800 MeV) with the protons and neutrons in the nuclei of a light element (i.e. carbon). Pions are not stable (lifetime 26 ns) and decay into muons and neutrinos. Due to the momentum conservation and the negative helicity of neutrinos, the spins of the emitted muons are antiparallel to their momentums. Therefore the propagating muon beam is fully polarized.

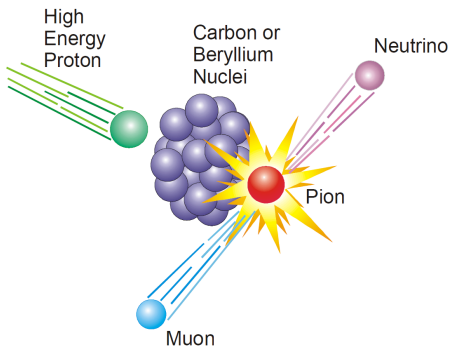

Figure 3.10: Production of the muons. Taken from Ref. [114]

Muon implantation and thermalisation in materials: when a muon enters a sample, it loses the kinetic energy quickly (less than 10^{-9} s) due to the Coulomb interaction

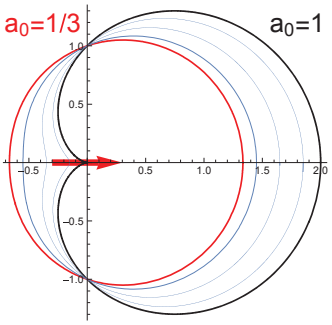

Figure 3.11: Anisotropic positron emission probability with respect to the muon spin (red arrow).

(causing inelastic scattering or forming a muonium $\mu^+ - e^-$) but the muon polarization is maintained. Then the muons localize in the interstitial crystallographic sites close to the negatively charged ions, for example, 0.9-1.1 Å away from O^{2-} forming an O-H like bond. The implantation depth depends on the energy of the muon and the density of the material and is typically 0.1-1 mm for muons with a kinetic energy 4.12 Mev.

Muon decay and its anisotropy: Muon has a lifetime of 2.2 μs and decays into a positron, a neutrino and an antineutrino. The positron will be detected during the experiment which has a kinetic energy ~ 52 MeV and interacts weakly with the sample. The positron emission probability is anisotropic with respect to the muon spin direction and the probability distribution is described by the cardioid curve (Fig. 3.11), which means that the emission probability a in the direction having a θ angle with the muon polarization is

$$a = 1 + a_0 P_0 \cos(\theta), \tag{3.23}$$

where a_0 is the asymmetry constant that depends on the energy of the emitted positron and is 1/3 when averaging on all the energies and P_0 is the initial muon polarisation. Because the positron emission is related to the muon polarization and the muon polarization can be affected by a magnetic field, the time evolution of the emission asymmetry provides information on the static and dynamical properties of the magnetic system. This is the key point of the μSR technique. Because $P_0 \cos(\theta)$ can be regarded as the projection of the polarization onto the emission direction, the asymmetry can be considered conveniently based on the vector projection.

Evolution of the muon spin: the magnetic moments of muons will do a Larmor precession under the local internal magnetic field of the sample as shown in Fig. 3.12. In analogy with nuclear magnetic resonance, the Larmor equation shows that the muon

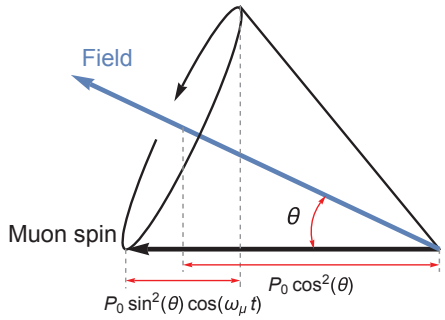

Figure 3.12: Larmor precession of the muon spin about a magnetic field and the corresponding components of the longitudinal muon polarisation function.

polarisation along the direction of the field is constant, $P_0 \cos(\theta)$ where θ is the angle between the muon polarisation $\boldsymbol{P}_0$ and the local magnetic field $\boldsymbol{B}_{\mathrm{loc}}$. The perpendicular component oscillates in the perpendicular plane and the precession frequency only depends on the magnitude of the local field, $\omega_\mu = \gamma_\mu B_{\mathrm{loc}}$ (independent on the angle θ). The amplitude of the oscillation is determined by the angle between $\boldsymbol{P}_0$ and $\boldsymbol{B}_{\mathrm{loc}}$, $P_0 \sin(\theta)$ (projection of muon polarization onto the perpendicular plane). Considering the longitudinal geometry of the spectrometer (Fig. 3.13) where two detectors are placed on the forward (f) and backward (b) directions of the muon polarisation, the detected positron signals on the two detectors are

$$\begin{aligned} N_{\mathrm{f}} &= \alpha \exp(-t/\tau_\mu) \times \{1 + a_0 P_0[\sin^2(\theta)\cos(\omega_\mu\ t) + \cos^2(\theta)]\}, \\ N_{\mathrm{b}} &= \exp(-t/\tau_\mu) \times \{1 - a_0 P_0[\sin^2(\theta)\cos(\omega_\mu\ t) + \cos^2(\theta)]\}, \end{aligned} \tag{3.24}$$

where α is the efficiency ratio of the two detectors, τ_μ is the life time of muon and $\exp(-\tau_\mu t)$ is the muon decay probability. The longitudinal muon polarisation function $P_{\mathrm{z}}(t)$ can be obtained by

$$P_{\mathrm{z}}(t) = \frac{N_{\mathrm{f}} - \alpha N_{\mathrm{b}}}{N_{\mathrm{f}} + \alpha N_{\mathrm{b}}} = a_0 P_0[\sin^2(\theta)\cos(\omega_\mu t) + \cos^2(\theta)]. \tag{3.25}$$

Figure 3.14 shows the characteristic time evolution of the signals detected by the forward and backward detectors and the extracted evolution of the muon polarisation.
During a μSR experiment, a single muon or a short pulse of muons is implanted into the sample with starting the clock and then the emitted positrons are counted by the two detectors with recording their arriving times. For a good statistics of the data, millions of events should be counted.

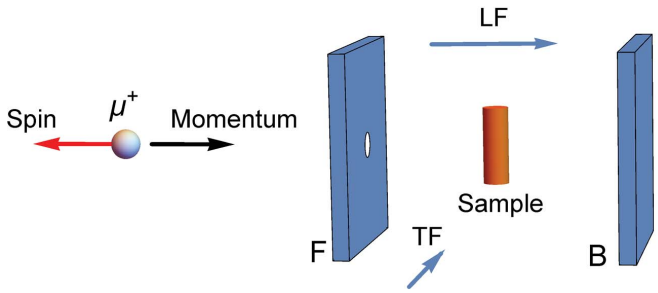

Figure 3.13: Muon spin relaxation spectrometer. Fully-polarised muons (μ^+s) are implanted in the sample, the emitted positrons are detected by the detectors at the forward (F) and backward (B) positions with respect to the muon spin direction. Longitudinal field (LF) (along muon polarisation) and transverse field (TF) (perpendicular to the muon polarisation) can be applied.

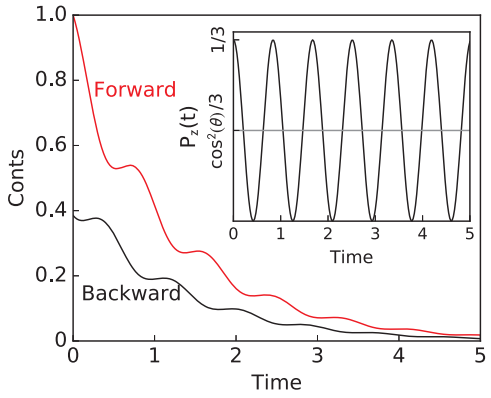

Figure 3.14: Positron counts on the forward and backward detectors and (inset) the extracted longitudinal muon polarisation function $P_z(t)$ with assuming $a_0 P_0 = 1/3$ in Eq. 3.25.

3.4.2 Muon polarisation function: field distribution and fluctuation

The field distribution approach is usually used for analysing the muon polarization relaxation spectrum which phenomenologically assumes that the ensemble of muon spins experiences a field with a certain distribution and time evolution. It provides a clear physical picture with only a few quantities which can be associated with the properties of the system under study. Below is a introduction of the characteristic muon polarization function induced by the static and dynamical fields of Gaussian-function distribution.

Static field

When the muon ensemble senses a single static field directing θ angle away from the muon

polarization as shown in Fig. 3.12, the longitudinal polarisation function (assuming the $a_0 P_0 = 1$) is

$$P_Z(t) = \sin^2(\theta)\cos(\omega_\mu t) + \cos^2(\theta), \tag{3.26}$$

indicating that the muon polarisation is oscillating at the frequency $\omega_\mu = \gamma_\mu B$ around the constant $\cos^2(\theta)$. One simple example is the case of a non-magnetic sample in a field. If muons sense several static fields in the system (e.g. in a single crystal with magnetic order with several non-equivalent muon stopping sites), the same number of oscillation frequencies can be detected and with taking account of the amplitudes of the oscillations, the percentages for the different muon stopping sites and the directions of the local fields can be obtained. Further, if the locations of the muons in the sample are known, the ordered moment can be estimated.
If the system has a single field with random orientations, for example, a magnetically ordered powder sample with only one type of muon stopping site, averaging over the signals from the randomly oriented static fields yields

$$P_Z(t) = \frac{1}{3} + \frac{2}{3}\cos(\omega_\mu t), \tag{3.27}$$

where the constant term originates from the time independent term in Eq. 3.26 and the time dependent terms is due to the oscillation. The coefficients 1/3 and 2/3 appear because on average one third of the muon spin is along the field direction and two thirds perpendicular to the field. When the field has an isotropic Gaussian-function distribution with the standard deviation Δ_G, that is,

$$\begin{aligned} D(\mathbf{B}_\mathrm{loc})\mathrm{d}^3 B_\mathrm{loc} &= (\frac{1}{\sqrt{2\pi}\Delta_\mathrm{G}})^3 \exp[-\frac{(B_\mathrm{loc}^\mathrm{X})^2}{2\Delta_\mathrm{G}^2}] \exp[-\frac{(B_\mathrm{loc}^\mathrm{Y})^2}{2\Delta_\mathrm{G}^2}] \exp[-\frac{(B_\mathrm{loc}^\mathrm{Z})^2}{2\Delta_\mathrm{G}^2}] \mathrm{d}B_\mathrm{loc}^\mathrm{X} B_\mathrm{loc}^\mathrm{Y} B_\mathrm{loc}^\mathrm{Z}, \\ &= (\frac{1}{\sqrt{2\pi}\Delta_\mathrm{G}})^3 \exp(-\frac{B_\mathrm{loc}^2}{2{\Delta_\mathrm{G}}^2}) B_\mathrm{loc}^2 \sin(\theta)\mathrm{d}\theta\mathrm{d}\varphi\mathrm{d}B_\mathrm{loc}. \end{aligned}$$

an integration should be calculated,

$$P_Z(t) = \int [\sin^2(\theta)\cos(\gamma_\mu B_\mathrm{loc} t) + \cos^2(\theta)] D(\mathbf{B}_\mathrm{loc})\mathrm{d}^3 B_\mathrm{loc}. \tag{3.28}$$

The result is the well-known Gaussian Kubo-Toyabe function,

$$P_Z(t) = \frac{1}{3} + \frac{2}{3}(1 - \gamma_\mu^2 \Delta_\mathrm{G}^2 t^2) \exp(-\frac{\gamma_\mu^2 \Delta_\mathrm{G}^2 t^2}{2}). \tag{3.29}$$

As shown in Fig. 3.15, the muon polarization function has a dip at $t_\mathrm{d} = \sqrt{3}/(\gamma_\mu \Delta_\mathrm{G})$

with $P_z = 0.03583$ and then recovers to 1/3.
There are some other different types of field distributions, such as Gaussian distribution with a longitudinal field, anisotropic Gaussian distribution and Lorentz distribution. The corresponding muon polarization function can be calculated in a similar way. These field distributions have different physical realizations. For example, the Gaussian field distribution normally appears in materials with dense magnetic ions and the Lorentz field distribution shows up in magnetic diluted materials.
Dynamical field
In practice, the muon spin always senses a field with some dynamics in materials at finite temperature. The effect of the field dynamics on the muon polarisation function is generally described by the strong collision model assuming that the local fields at muon stopping sites change suddenly at a frequency ν and no correlation exists between the fields before and after the change. The time evolution of the muon polarisation $P_Z(t)$ consists of contributions from muons whose local fields do not change within the time t, $p_z^0(t)$, from muons whose local fields undergo one change, $p_z^1(t)$, etc,

$$P_Z(t) = \sum_{n=0}^{n=\infty} p_z^n(t). \tag{3.30}$$

The first term is

$$p_z^0(t) = \exp(-\nu t) P_Z^{\text{static}}(t), \tag{3.31}$$

where $P_Z^{\text{static}}(t)$ is the polarisation function for the static field distribution, for example, the Gaussian Kubo-Toyabe function and $\exp(-\nu_c t)$ is the probability that the local field does not change within this time period. The second term is

$$\begin{aligned} p_z^1(t) &= \nu \int_0^t \exp[-\nu(t-t')] P_Z^{\text{static}}(t-t') \exp(-\nu t') P_Z^{\text{static}}(t') \mathrm{d}t' \\ &= \nu \int_0^t p_z^0(t-t') p_z^0(t') \mathrm{d}t', \end{aligned} \tag{3.32}$$

which describes the process that the muon experiences a sudden field change at t' ($0 < t' < t$). With the same method a recursion relation is obtained,

$$p_z^{l+1}(t) = \nu \int_0^t p_z^0(t-t') p_z^l(t') \mathrm{d}t', \tag{3.33}$$

Finally, $P_Z(t)$ can be evaluated numerically and for a Gaussian field distribution, the result is the dynamical Gaussian Kubo-Toyabe (dGKT) function [113, 115]. Fig. 3.15 shows the dGKT function with different fluctuation rates. For the cases with a longitudi-

nal field and other kinds of field distributions, the dynamics can be considered similarly [113].

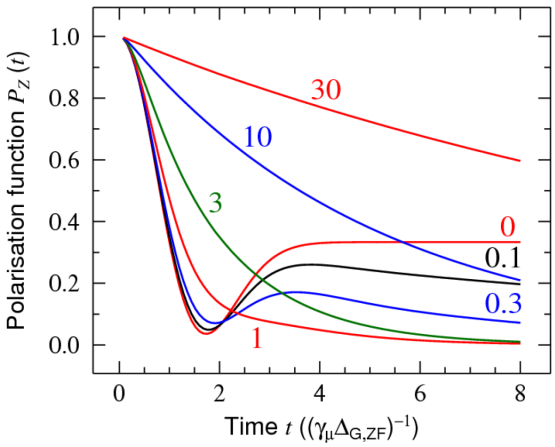

Figure 3.15: Dynamical Gassiaon Kubo-Toyabe function with different fluctuation rates νs plotted as function of $(\gamma_\mu \Delta_G)^{-1}$. The numbers near the curves are the value of $\nu/(\gamma \Delta_G)$. For $\nu/(\gamma \Delta_G) = 0$, it reduces to the Gaussian Kubo-Toyabe function (Eq. 3.29). Taken from Ref. [113].

Fast fluctuation limit (motional narrowing limit)

The exponential function $\exp(-\lambda_Z t)$ is often used for describing the μSR spectrum of a paramagnet which contains fast fluctuating spins. This function corresponds to the fast fluctuation limit ($\nu t \gg 1$ or $\nu \gg \gamma_\mu \Delta_G$) of the dynamical Gaussian Kubo-Toyabe function. At this limit, the dGKT function reduces to be an exponential function with a relaxation rate

$$\lambda_Z = \frac{2\gamma_\mu^2 \Delta_G^2}{\nu}, \tag{3.34}$$

where the relaxation rate is related simply to the parameters in the dGKT model. With a longitudinal field B_{ext}, it becomes

$$\lambda_Z = \frac{2\gamma_\mu^2 \Delta_G^2 \nu}{(\gamma_\mu B_{ext})^2 + \nu^2}, \tag{3.35}$$

which is the Redfield formula indicating that the dependence of λ_Z on the external field behaves like a Lorentz function with half width at half maximum to be ν/γ_μ. Note that the analysis is based on the assumption that the external field has no effect on the system.

The models above only applies to the systems with one relaxation process. If there is a continuous distribution of the relaxation process, the stretched exponential function is

used at the fast fluctuation limit which is

$$P_{\mathrm{Z}}(t) = \exp[(-\lambda_{\mathrm{Z}}t)^{\beta}] \ (0 < \beta < 1). \tag{3.36}$$

In addition, the static and dynamical Gaussian-broadened Gaussian Kubo-Toyabe (GbGKT) function are also commonly used as a phenomenological model describing the homogeneous disorder. In this model, instead of a Gaussian field distribution, a collection of Gaussian field distributions are included with a Gaussian-function-weighed standard deviation [113, 116]. There are two parameters describing the field distribution: the average standard deviation Δ_0 and the standard deviation of the Gaussian-function-weighted standard deviation Δ_{GbG} [116]. The ratio $R_{\mathrm{b}} = \frac{\Delta_{\mathrm{GbG}}}{\Delta_0}$ is usually used instead of Δ_{GbG}.

4 Sample synthesis and structural and magnetic characterizations

4.1 Introduction

This chapter presents the details of sample preparation and structural and magnetic characterizations of powder and single crystal samples of the pyrochlore magnets $R_2Zr_2O_7$ (R = Nd, Gd, Sm). The powder samples are prepared by the solid state reaction method and the single crystals are grown using an optic floating zone furnace. The structural characterization is based on X-ray and neutron powder diffraction which is analysed by Rietveld refinement. The magnetic characterization is based on DC and AC susceptibility, magnetization and specific heat measurements.

For most of $R_2B_2O_7$ (where R is the rare earth element) pyrochlore compounds, powder samples can be simply prepared in air by the solid state reaction method with R_2O_3 and corresponding B oxides as the raw materials. For pyrochlores containing elements which can have multiple valences (e.g. Ce, Ti), the samples should be synthesized in suitable atmospheres [83, 117]. High pressure should be applied for the preparation if the radius of the R^{3+} ion is much larger than that of the B^{4+} ions (e.g. Mn^{4+}, Ge^{4+}, Pt^{4+}) as is the case for the germanates with R = Gd – Lu [118]. The single crystals are generally synthesized using an optic floating zone furnace but for those prone to evaporate significantly at high temperatures, the flux method can be used (e.g. stannates) [119].

The possible structural defects of pyrochlores are R/B antisite mixing, R/B stuffing (not the "1-to-1" R/B mole ratio) and oxygen deficiency or oxygen stuffing (excess oxygen ions at the normally empty 8a site) [117, 120, 121]. The R/B related defects involve the phase stability of the pyrochlore. As mentioned in Chapter 2, the pyrochlore is a type of ordered defected fluorite structure with the ordering temperature decreasing with the decrease of the ion radius ratio r_R/r_B. Therefore, the R/B antisite defect can easily occur in a high-temperature-annealed sample especially if the sample has a small r_R/r_B ratio and a certain amount of R or B stuffing is tolerated with compensating oxygen

non-stoichiometry to provide the charge neutrality (for example, $(Gd_{1+x}Zr_{1-x})_2O_{7+\delta}$ with $-0.05 < x < 0.05$ is in the pyrochlore phase [120]). During the preparation, precise stoichiometry of the raw materials and annealing at low temperatures are helpful to reduce these defects. The oxygen deficiency and stuffing is normally caused by the variable valence of some elements and thus annealing in a reducing or oxidizing atmosphere is necessary. For example, the presence of Ti^{3+} or Ce^{4+} can result in oxygen deficiency or oxygen stuffing (even the pyrochlore $Ce_2^{4+}B_2^{4+}O_8$ exists [122]). Due to these possible structural defects, a sample dependence is observed and happens more frequently in single crystal samples than powders because the synthesis conditions of single crystal are more difficult to control (see references e.g. [117, 123]).

As shown in Fig. 2.5 in Chapter 2, for the zirconate series, $R_2Zr_2O_7$ with $R =$ La-Gd crystallize in the pyrochlore structure and $Gd_2Zr_2O_7$ is located at the boundary between the pyrochlore phase and the fluorite phase. The pyrochlore-fluorite transition temperature of the zirconate pyrochlores is generally higher than 2000 °C except for $Gd_2Zr_2O_7$ whose T_C is around 1600 °C [124]. A large amount of Gd/Zr antisite defects are reported in a sample annealed at 1600 °C [120]. For $Nd_2Zr_2O_7$ and $Sm_2Zr_2O_7$, the effective ionic radius of the eight-fold coordinated Nd^{3+} and Sm^{3+} and the six-fold coordinated Zr^{4+} are 1.109, 1.079 and 0.72 Å, respectively [125]. Thus the r_R/r_B ratios are 1.54 and 1.50 for the two compounds which indicates that $Nd_2Zr_2O_7$ and $Sm_2Zr_2O_7$ lie well inside the stable pyrochlore phase ($1.36 < r_R/r_B < 1.71$ as shown in Chapter 2). In addition, the trivalent Zr^{3+} ion is very rare in compounds, thus O deficiency in zirconate pyrochlores should not be present (especially after heating in air) in contrast to the titanate pyrochlores where Ti^{3+} is possible [117].

Synthesis of powder samples of the zirconate pyrochlores $R_2Zr_2O_7$ with $R =$ La-Gd was first reported by Roth in 1956 [126] and the low-temperature specific heat C_p and the susceptibility of $Nd_2Zr_2O_7$ were first measured by Blöte *et al.* in 1969 (the specific heat measurement was partly repeated by Lutique *et al.* in 2003) [70, 127]. It was found that $Nd_2Zr_2O_7$ shows a peak in the $C_p(T)$ at 0.37 K and a ferromagnetic Curie-Weiss temperature of 0.05 K. Recently, Hatnean *et al.* reported the growth of a $Nd_2Zr_2O_7$ single crystal and the susceptibility, magnetization and specific heat above 0.5 K of this sample [128]. The crystal was of good quality with the nominal stoichiometry and no measurable site disorder. The susceptibility and the magnetization indicate an effective FM interaction between the moments ($\theta_p = 0.200(8)$ K and $\mu_{eff} = 2.543(2)\,\mu_B$/Nd) and local [111] Ising anisotropy which was also confirmed by crystal field analysis of the susceptibility. More recently in a work that took place in parallel with this thesis, the low-temperature AC susceptibility and DC magnetization of that single crystal was

measured by Lhotel *et al.* which reveals a AFM transition at 285 mK (with no frequency dependence) and a field-induced metamagnetic transition [129]. In addition, neutron diffraction and inelastic scattering on a powder sample in Ref. [129] indicate an "all-in/all-out" (AIAO) antiferromagnetic order and a dipolar-octupolar CEF ground state of Nd^{3+} in $Nd_2Zr_2O_7$ (also see Chapter 5).

Several similar Nd^{3+} pyrochlores were studied previously. $Nd_2Hf_2O_7$ and $Nd_2Sn_2O_7$ were reported to show the same AIAO magnetic order below 0.55 and 0.91 K, respectively. However, $Nd_2Hf_2O_7$ has a positive Curie-Weiss temperature of 0.24(2) K ($\mu_{\text{eff}} \approx 2.45\mu_{\text{B}}$/Nd) similar to $Nd_2Zr_2O_7$ while $Nd_2Sn_2O_7$ has an negative one, $\theta_{\text{p}} = -0.32(1)$ K [$\mu_{\text{eff}} = 2.63(3)\,\mu_{\text{B}}$/Nd] [70, 130, 131]. The specific heat of Nd_2GaSbO_7 with Ga/Sb disorder also shows a sharp peak at 1.1 K indicating a similar ordering transition [70]. Additionally, $Nd_2Ir_2O_7$ and $Nd_2Mo_2O_7$ were studied focusing on the electric properties (metal-insulator transition and anomalous Hall effect) originating from the d electrons where the magnetic Ir^{4+} and Mo^{4+} dominate the underling physics [132–134]. Neutron diffraction indicated that $Nd_2Ir_2O_7$ and $Nd_2Mo_2O_7$ develop the AIAO and the 2I2O magnetic orders below 15 K and 95 K, respectively, and the inelastic neutron scattering of the crystal field excitations of $Nd_2Ir_2O_7$ also reveals the Ising-anisotropic dipolar-octupolar CEF ground state of Nd^{3+} [134–137].

The structure of $Gd_2Zr_2O_7$ has been intensively investigated for usage in the nuclear waste disposal [121], however its magnetic properties are barely studied and have only been recently investigated in Refs. [127, 138] probably due to the tendency for structural disorder. The low-temperature specific heat shows a broad peak at $\sim$ 0.7 K in Ref. [127] while a sharp peak at 0.769 K was reported in Ref. [138]. The entropy calculated is about $R\ln(8)$/mol Gd (R is the gas constant) corresponding to the full spin entropy for the ${}^8S_{7/2}$ ground state of the Gd^{3+} ion which indicates an isotropic spin (almost no CEF splitting). The exchange interaction is around -0.12 K (-0.112 K estimated from the C_{p} data and -0.122 K obtained from the susceptibility) [138]. The Curie-Weiss analysis of the susceptibility data yields $\theta_{\text{p}} = -7.7(5)$ K and $\mu_{\text{eff}} = 7.83\mu_{\text{B}}$/Gd [138]. Therefore, $Gd_2Zr_2O_7$ is a frustrated Heisenberg antiferromagnet with frustration index $\theta_{\text{p}}/T_{\text{N}} \approx 10$. Two related compounds $Gd_2Ti_2O_7$ and $Gd_2Sn_2O_7$ have been well studied. These two compounds have $\theta_{\text{p}} \sim -10$ K with the effective moment close to that of the free ion [139, 140]. $Gd_2Ti_2O_7$ shows a two-step ordering transition ($T_{\text{N1}} \sim 1$ K and $T_{\text{N2}} \sim 0.7$ K) and $Gd_2Sn_2O_7$ orders magnetically with a single transition at ~ 1 K. The specific heat measurements of $Gd_2Ti_2O_7$ with field along different crystallographic directions reveal a complicated H-T phase diagram [141, 142] and the H-T phase diagram of $Gd_2Sn_2O_7$ which was extracted from the magnetization of a polycrystalline sample

also shows several phases [143]. The phase diagram of $Gd_2Ti_2O_7$ can be simulated by including the single-ion anisotropy (the second-order axial term $\sim 0.223\,\mathrm{K}$ determined by electron spin resonance) in the nearest-neighbor Heisenberg Hamiltonian [101–103]. The specific heat and the inelastic neutron scattering of $Gd_2Sn_2O_7$ provide evidence for gapped spin wave excitations which were explained by taking the dipolar interaction into account [94, 99, 100].
The magnetic properties of $Sm_2Zr_2O_7$ have only been studied by Surjeet *et al.* [144]. The temperature dependence of the susceptibility is not Curie-Weiss-like while the Curie-Weiss analysis using a variable van Vleck term for different temperature ranges indicate $\theta_\mathrm{p} \sim -10\,\mathrm{K}$ with $\mu_\mathrm{eff} \sim 0.50\,\mu_\mathrm{B}/\mathrm{Sm}$. The specific heat exhibits an upturn below 3 K but the susceptibility at temperatures down to 0.67 K shows no sign of a transition. The magnetisations above 2 K are nearly linear with a small value $\sim 0.05\,\mu_\mathrm{B}/\mathrm{Sm}$ for a field of 5.5 T. The Raman spectra and specific heat data indicate that the first excited crystal field state is possibly at $85\,\mathrm{cm}^{-1}$ [144] and thus at very low temperatures the system can be described by the pseudospin-1/2 model. The related compound $Sm_2Ti_2O_7$ has similar properties as reported in the same paper while the θ_p is $\sim -0.26\,\mathrm{K}$ which is much lower and μ_eff is about $0.15\mu_\mathrm{B}/\mathrm{Sm}$. The susceptibility of $Sm_2Ti_2O_7$ has a clear bump at $\sim 140\,\mathrm{K}$ which is related to the CEF effect [144]. The first excited CEF level is below $87\,\mathrm{cm}^{-1}$ as suggested by the Raman spectra and specific heat data in Ref. [144]. However, the analysis of the temperature dependence of the susceptibility of $Sm_2Ti_2O_7$ indicates that the excited crystal field states of the multiplet $^6H_{5/2}$ are at 172.4 and $212.7\,\mathrm{cm}^{-1}$ [145].

4.2 Synthesis of powder and single crystal samples

Powder samples of $La_2Zr_2O_7$, $Nd_2Zr_2O_7$, $Sm_2Zr_2O_7$, $^{154}Sm_2Zr_2O_7$, $Gd_2Zr_2O_7$ and $^{160}Gd_2Zr_2O_7$, were synthesized by the conventional solid state reaction method. Commercial pure (99.999%) R_2O_3 (R is the rare earth element) and ZrO_2 were used as the raw materials. For the isotopically pure samples, $^{160}Gd_2O_3$ with purity 99.98% and $^{154}Sm_2O_3$ with purity 99.9% were used. First, the R_2O_3 and ZrO_2 were mixed with the 1 : 2 mole ratio and then ground for homogenization. The mixtures were put in alumina crucibles and heated at 1200-1550 °C in air for a few days with several intermediate grindings and pelletizing.
For the samples $La_2Zr_2O_7$, $Nd_2Zr_2O_7$ and $Sm_2Zr_2O_7$, the pyrochlore-fluorite (R/Zr order-disorder) structural transition temperatures are much higher than the synthesis temperature and high quality samples were obtained. For $Gd_2Zr_2O_7$, a significant

amount of Gd/Zr antisite mixing was reported in a sample annealed at 1600 °C [120]. Therefore, additional annealings were performed for $Gd_2Zr_2O_7$ and $^{160}Gd_2Zr_2O_7$ at 1400 and 1300 °C for nearly one month after the synthesis.

For the growth of the single crystals of $Nd_2Zr_2O_7$, $Sm_2Zr_2O_7$ and $Gd_2Zr_2O_7$, some powder was first prepared in the same way as for the polycrystalline samples but only heated at 1200 and 1400 °C for one day for homogenization. Second, the powders were filled into cylindrical balloons of 6 mm in diameter and then pressed into hard solid rods with hydrostatic pressure up to 20 kbar. The obtained rods were then heated at 1400 °C overnight for solidification and further homogenization. Finally, Dr. A. T. M. N. Islam grew single crystals from the rods using an optic floating zone furnace. The as-grown single crystals of $Nd_2Zr_2O_7$, $Sm_2Zr_2O_7$ and $Gd_2Zr_2O_7$ are cylinder-shaped ($\sim$ 4 cm long and 0.5 cm diameter). All the crystals are transparent and $Nd_2Zr_2O_7$ and $Sm_2Zr_2O_7$ have a purple and a yellow colour, respectively. The crystals have some cracks caused by the temperature gradient inside the furnace during the growth.

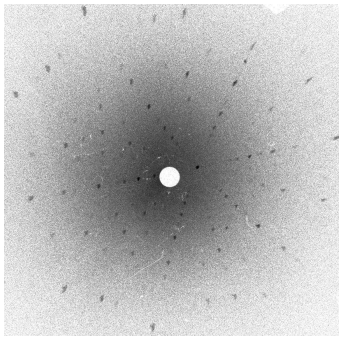

Figure 4.1: X-ray Laue diffraction pattern of $Sm_2Zr_2O_7$ single crystal with incident beam perpendicular to one facet of the crystal boule.

Initially, the structural quality of all the samples was checked using the lab-based X-ray powder diffraction (Cu Kα radiation). It was found that the as-grown $Gd_2Zr_2O_7$ single crystal is completely in the disordered fluorite phase and after annealing in succession at 1550, 1400 and 1300 °C, it shows sharp pyrochlore superlattice Bragg peaks resulting from the Gd/Zr order. Therefore all the single crystals of the three compounds were annealed after the growth. The single-crystalline quality of the crystals was checked by lab-based X-ray Laue diffraction (molybdenum, 20 kV). The Laue diffraction shows that the [111] crystallographic direction is mostly orthogonal to the facets of the single crystal boule. Fig. 4.1 shows one representative Laue diffraction pattern.

4.3 X-ray and neutron diffraction for the powder samples

4.3.1 Experimental details

Besides the room-temperature lab-based X-ray diffraction, synchrotron X-ray diffraction (X-ray energy ∼25 keV) was performed on the powder samples of $La_2Zr_2O_7$, $Nd_2Zr_2O_7$, $Gd_2Zr_2O_7$ and $Sm_2Zr_2O_7$ at several temperatures between 5 and 290 K. The samples were finely milled to avoid preferred orientation because only a small amount of powder can be used to limit absorption which can occur because the diffractometer operates in the transmission geometry. Diamond powder was added into the samples uniformly to reduce X-ray absorption by diluting the sample. Thin capillaries (0.3 mm in diameter) were used to contain the sample in order to reduce the sample diameter effect on the peak profile [146]. The capillary was continuously rotated around its axis during the measurement, which also helped to reduce the effects of preferred orientation. Standard Si and LaB_6 powders [from National Institute of Standards and Technology (NIST), US] were measured at room temperature with the same instrument settings to accurately determine the X-ray wavelength and the instrument profile parameters, respectively. In addition, a neutron diffraction experiment was conducted on ∼1.5 g $^{160}Gd_2Zr_2O_7$ powder (in a vanadium can) at room-temperature on the D2B diffractometer at the ILL with neutron wavelength 1.05 Å.

The diffraction patterns were analysed by the Rietveld refinement method and an effort was made to determine the amounts of the R/Zr antisite defect and the oxygen vacancy which have been reported to have significant effects on the underlying physics of pyrochlores [117, 123]. In the synchrotron XRD pattern, the high-intensity peaks at low angles have a round top and an extended base (Fig. 4.2) which is difficult to model using the peak profile functions available in the refinement softwares. The first feature of the peak is typical for this instrument when the X-ray energy is larger than 20 keV [146] and the second one could be an effect of the crystalline size and strain introduced during grinding. Finally, Topas (academic v3, Bruker) was used for the refinement instead of FullProf because it allows a top-hat function to be convoluted to model the peak top as suggested in Ref. [146]. The second problem was solved by including two pyrochlore phases with the same crystallographic parameters but different peak shape profiles (one phase produces high sharp peaks and the other low broad peaks as shown in Fig. 4.2). A good description of the peak shape is crucial for modelling the intensity of the Bragg peaks, which is necessary for accurately determining the structural defects.

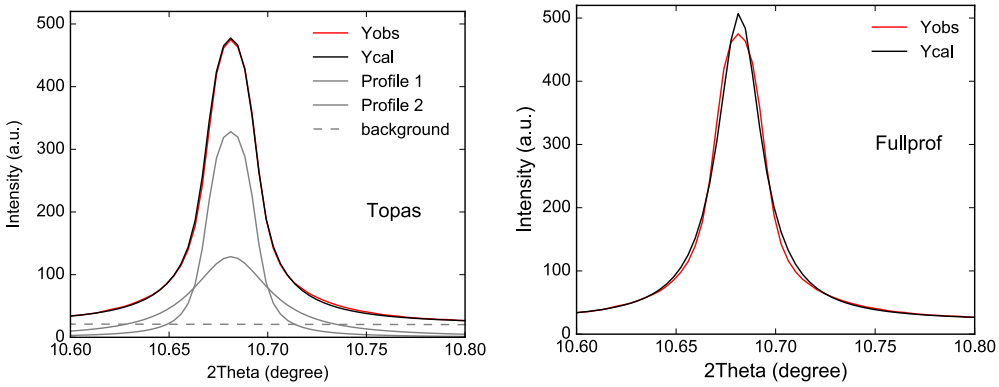

Figure 4.2: Comparison of the refinements for $Nd_2Zr_2O_7$ using (left) the user-defined peak function with two phases in Topas and (right) pseudo-Voigt function in Fullprof.

4.3.2 Rietveld refinement

Figure. 4.3 shows the synchrotron XRD patterns recorded at 5 K and the corresponding Rietveld refinements. The fitted parameters at 5 K are shown in Table 4.1. The temperature dependences of the lattice parameter and the coordination parameter x_{O1} of the 48f oxygen ion are shown in Fig. 4.4. The crystallographic parameters at room temperature are in good agreement with reported ones [127, 128, 144, 147–149] and none of the samples show a structural transition above 5 K. For the refinements of $La_2Zr_2O_7$ and $Nd_2Zr_2O_7$, varying the occupancies gives no noticeable improvement (R_{wp}: 1.94 vs 1.86 and 2.27 vs 2.18, respectively) and the antisite mixing is probably less than 0.5 %. Finally, the occupancies are fixed to be the nominal values. It was also realized that in general, varying occupancies and the overall thermal factor B_{ov} results in 2 - 5 % R stuffing and 3 - 10 % O(8b) vacancy for all the four compounds, even $La_2Zr_2O_7$. This could be a systematic error introduced by the strongly modulated background from the refrigerator. The refinement shows that $Sm_2Zr_2O_7$ potentially has a small amount of defects and $Gd_2Zr_2O_7$ has a significant number of defects ($\sim$ 20 % Gd/Zr mixing). Below are the analysis details for these two compounds.

The refinement (with varying occupancies and B_{ov}) shows that B_{ov} increases for the four compounds [0.08(1), 0.18(1), 0.66(1), 0.95(1) at 5 K from $La_2Zr_2O_7$ to $Gd_2Zr_2O_7$] and it is anomalously high for $Sm_2Zr_2O_7$ and $Gd_2Zr_2O_7$. The thermal factor of $Gd_2Zr_2O_7$ at 5 K is an order of magnitude larger than that of $La_2Zr_2O_7$ and suggests a thermal vibrational amplitude $u \sim 0.1$ Å ($B_{ov} = 8\pi^2\overline{u^2}$) which is quite high for oxides at this low temperature. This could be due to the static disorder or quenched disorder

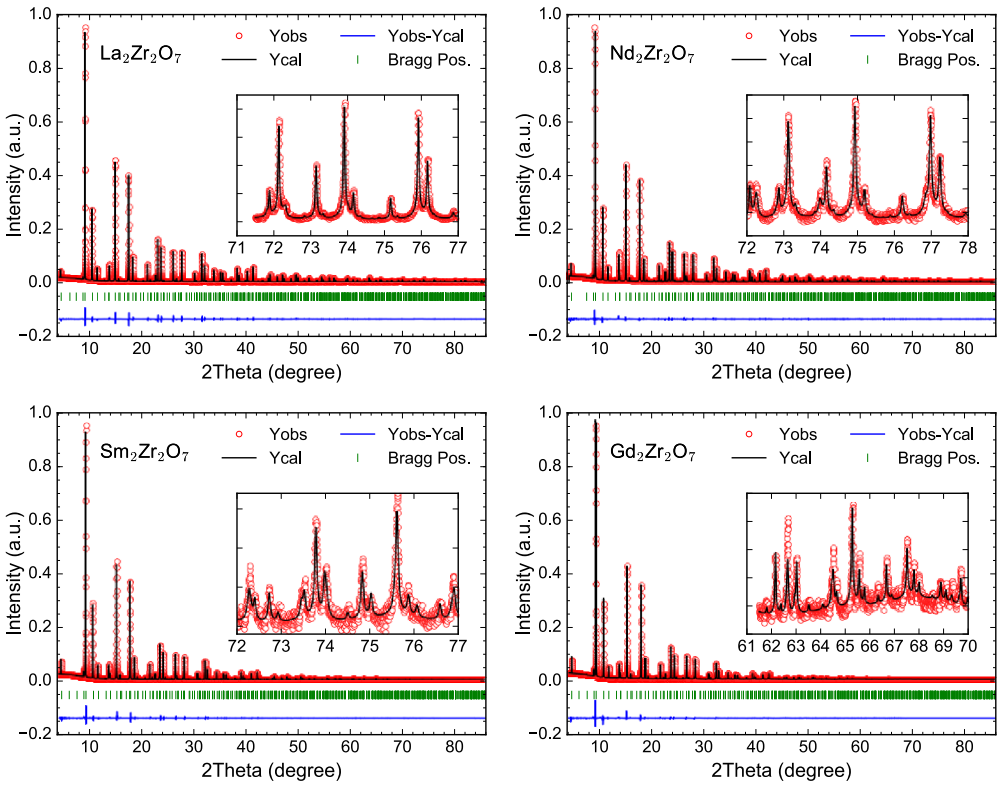

Figure 4.3: Synchrotron XRD patterns of the powder samples $La_2Zr_2O_7$, $Nd_2Zr_2O_7$, $Sm_2Zr_2O_7$ and $Gd_2Zr_2O_7$ at 5 K and the Rietveld refinements. The inset shows the refinement at high angles.

induced by structural defects. A random distribution of defects randomly introduces local distortions in the lattice which could have a similar effect as thermal vibration on the diffraction pattern. Refining the high-resolution neutron diffraction pattern of the $^{160}Gd_2Zr_2O_7$ isotope sample yields $B_{ov} \sim 1.5$ at room temperature, consistent with the synchrotron XRD result of the normal $Gd_2Zr_2O_7$ sample ($B_{ov} \sim 1.2$ for 290 K). The results here are consistent with the analysis based on the highly sensitive Zr L-edge X-ray absorption spectrum which shows that the transition from the ideal pyrochlore phase to the defect fluorite phase is not sharp for the $R_2Zr_2O_7$ series [148]. According to atomistic simulation calculations, the defect formation energy in $R_2Zr_2O_7$ decreases as the size of the R ion decreases (from $\sim$10 eV for La to $\sim$5 eV for Gd) [150], and the degree of static disorder should increase if these samples are synthesised at the same temperatures.

When the synchrotron XRD pattern of $Sm_2Zr_2O_7$ is refined with the ideal pyrochlore structure, the calculated intensity for many high-angle peaks is lower than the obser-

Table 4.1: Crystallographic parameters for the powder samples of $La_2Zr_2O_7$, $Nd_2Zr_2O_7$, $Sm_2Zr_2O_7$ and $Gd_2Zr_2O_7$ obtained from the refinements of the high-resolution synchrotron X-ray diffraction patterns at 5 K. The Wyckoff positions of R (R = La, Nd, Sm, Gd), Zr, O1 and O2 atoms in space group $Fd\bar{3}m$ are 16d (1/2,1/2,1/2), 16c (0,0,0), 48f (x_{O1},1/8,1/8) and 8b (3/8,3/8,3/8), respectively. The lattice parameter a, coordinate x_{O1}, occupancies (occ), thermal factors (B_{ov} and B_{iso}) and the refinement quality parameters are listed. This refinement was obtained using the Topas software with two phases and the results are slightly different from the results of the FullProf refinement presented in Fig. 4.4.

	$La_2Zr_2O_7$	$Nd_2Zr_2O_7$	$Sm_2Zr_2O_7$	$Gd_2Zr_2O_7$
a (Å)	10.79013(13)	10.66046(1)	10.57846(35)	10.51842(2)
x_{O1}	0.33083(8)	0.33497(10)	0.34283(13)	0.34890(26)
occ(16d)	1 La	1 Nd	1 Sm	0.98(1)Gd+0.02Zr
occ(16c)	1 Zr	1 Zr	1 Zr	0.10(1)Gd+0.90Zr
occ(8b)	1 O	1 O	1 O	1 O
occ(48f)	1 O	1 O	1 O	0.80(1)O
B_{ov}	0.08(1)	0.18(1)	-	-
B_{iso}(16c)	-	-	0.49(1)	0.72(1)
B_{iso}(16d)	-	-	0.98(1)	1.29(1)
B_{iso}(8b)	-	-	2.05(5)	2.28(10)
B_{iso}(48f)	-	-	0.54(4)	0.10(10)
R_{wp} (%)	1.94	2.27	1.95	3.20
χ^2	2.568	1.973	2.24	4.123

vation. Refining the site mixing and oxygen vacancy does not improve the refinement (R_{wp} becomes 2.29 from 2.36) and gives more than 20 % vacancy on O(8b) site which is not physically realistic. The intensity discrepancies can also not be explained by the preferred orientation effect which generally yields both stronger and weaker peaks than the data. Finally, by allowing the atoms at the different sites to have different thermal factors (B_{iso}s), the refinement becomes much better (R_{wp}: 1.95), and the individual B_{iso}s for the Sm, Zr, O(48f) and O(8b) sites are 0.49, 0.98, 2.05 and 0.54, respectively. Introducing site mixing parameters and oxygen vacancy, the refinement yields a slightly smaller R_{wp}(1.83) and shows about 5 % Sm stuffing and more than 10 % oxygen vacancy on the 8b site (the B_{iso}s do not change much). However this large percentage of defects is unlikely because the fitting is not improved (it could be a systematic error as mentioned above). Interestingly, the thermal factor of the O(48f) site is very large and can be

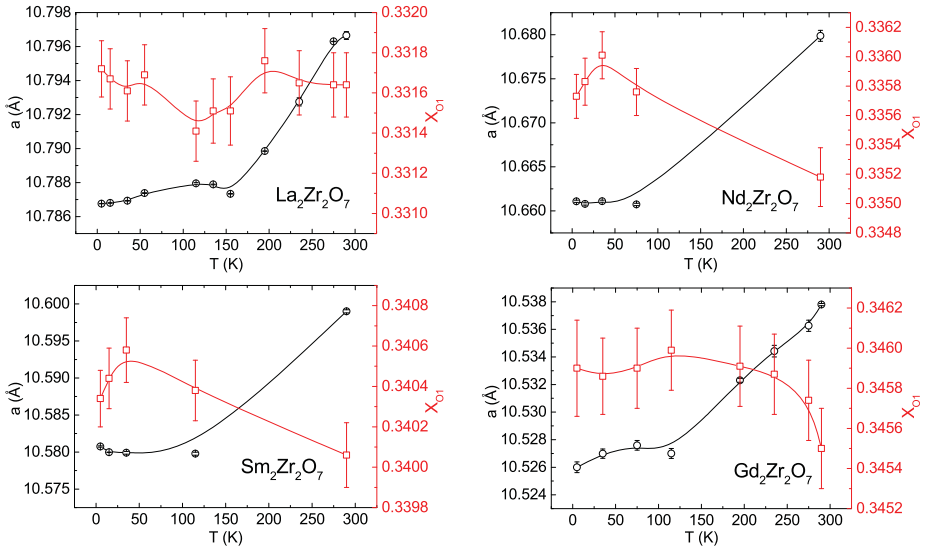

Figure 4.4: Temperature dependences of the lattice parameter and the position parameter of O($48f$) for the powder samples $La_2Zr_2O_7$, $Nd_2Zr_2O_7$, $Sm_2Zr_2O_7$ and $Gd_2Zr_2O_7$ obtained by fitting the synchrotron XRD patterns using FullProf with one phase (the refinement using Topas with two phases is very slow so that it is not used here).

associated with the static disorder. It indicates that a certain amount of site mixing happens though there is no convincing evidence found. The $48f$ oxygen is located inside the R_2Zr_2 tetrahedron but displaced away from the centre of the tetrahedron due to the different sizes of the R^{3+} and Zr^{4+} ions. Thus, its position is easily influenced by R/Zr antisite defects which change the shift direction according to the arrangement of the R/Zr atoms on the tetrahedron. Finally, the refinement of the lab-based XRD pattern of $^{154}Sm_2Zr_2O_7$ (Fig. 4.5) shows that the room-temperature lattice parameter and x_{O1} are 10.6015(7) Å and 0.33589(38), similar to those of the normal powder sample.

For the refinement of the synchrotron XRD pattern of the $Gd_2Zr_2O_7$ sample, R_{wp} is 3.58 and B_{ov} is 0.95 at 5 K if the nominal stoichiometry is assumed. When the occupancies are varied, R_{wp} becomes 3.51. Further refining the individual isotropic thermal factors, R_{wp} becomes 3.14 yielding B_{iso}s for Gd, Zr, O($48f$) and O($8b$) being 0.72(1), 1.29(1), 2.28(1) and 1.10(1) and it shows that there is around 10 % Gd^{3+} excess on the Zr^{4+} site. Similar refinement procedures were also applied to the room-temperature neutron diffraction data of the isotope $^{160}Gd_2Zr_2O_7$ sample. Refining with the ideal pyrochlore structure yields $R_{wp} = 5.21$ and $B_{ov} = 1.5(1)$ and after freeing the individual thermal factors, R_{wp} becomes 4.78 and the respective B_{iso}s for ^{160}Gd, Zr, O($48f$) and O($8b$) are 1.09,

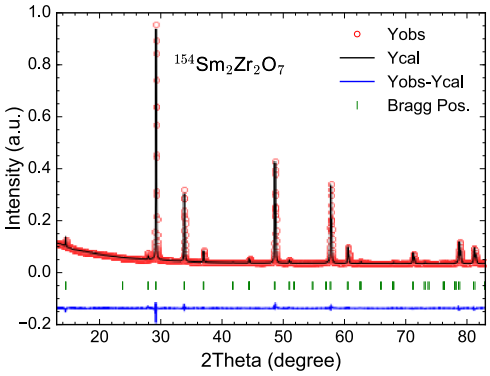

Figure 4.5: Lab-based room-temperature XRD pattern of $^{154}Sm_2Zr_2O_7$ and the refinement.

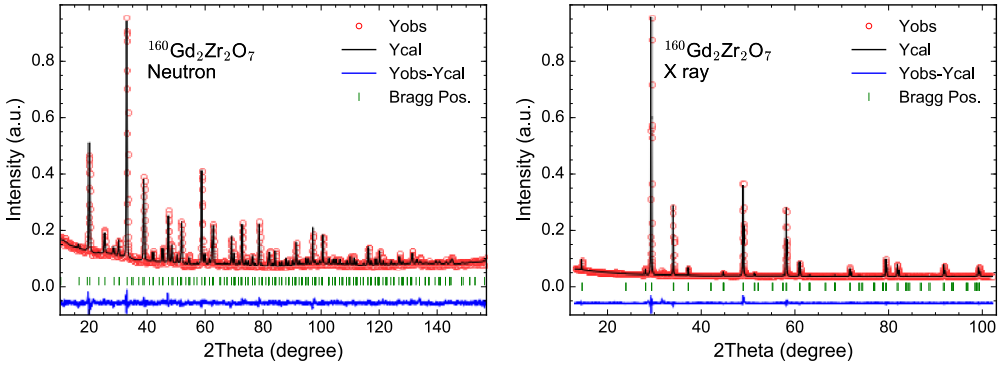

Figure 4.6: Combined Rietveld refinement of the room-temperature neutron diffraction pattern and the lab-based X-ray diffraction pattern of $^{160}Gd_2Zr_2O_7$.

1.70, 2.08 and 1.26, consistent with the synchrotron XRD analysis for the normal sample. Refining the Gd/Zr mixing with the fixed "1-to-1" ratio gives around 20% site mixing and $R_{wp} = 4.70$. Oxygen vacancy is not included for these refinements to keep the electrostatic equilibrium because the sample was prepared in air. Without the "1-to-1" site mixing constraint, R_{wp} becomes 4.54 suggesting that the sample is strongly off-stoichiometric with $\sim 40\,\%$ Zr^{4+} on the Gd^{3+} site, $\sim 19\,\%$ Gd^{3+} on the Zr^{4+} site and $3\,\%$ oxygen vacancy on the $48f$ site. The individual B_{iso}s become 1.03, 1.70, 2.06 and 1.22. However, there is no reason for the this large off-stoichiometry and the result with the "1-to-1" constraint is the most likely. The combined refinement of the lab-based XRD pattern and the neutron diffraction pattern gives the same result (see Table. 4.2 and Fig. 4.6).

Table 4.2: Refinement results for the powder sample of $^{160}Gd_2Zr_2O_7$ obtained from the combined refinement of the lab-based X-ray diffraction and neutron diffraction patterns measured at room temperature (using Fullprof). The "1-to-1" site mixing constraint is applied for the refinement and the occupancies of oxygen are not refined to keep the charge equilibrium.

a (Å)	x_{O1}	R_{wp}(%)	χ^2
10.52114(9)	0.34659(41)	2.82	5.51
B_{iso}(Gd)	B_{iso}(Zr)	B_{iso}[O(48f)]	B_{iso}[O(8b)]
1.048(50)	1.715(76)	1.800(23)	1.120(193)

About 20 % Gd/Zr antisite mixing was found.

4.4 Lab-based X-ray diffraction for the single crystal samples

Lab-based X-ray diffraction experiments were performed on crushed single crystals. The XRD patterns of the as-grown $Nd_2Zr_2O_7$ and $Sm_2Zr_2O_7$ crystals show sharp pyrochlore peaks without any impurity peaks. As mentioned above, the as-grown $Gd_2Zr_2O_7$ crystal is in the defected fluorite phase and only after annealing at 1500 °C, does it show sharp pyrochlore peaks. The refined crystallographic parameters are consistent with those of the powder samples as shown in Fig. 4.7 and Table 4.3. Similar to the powder sample, B_{ov} also increases for the Nd, Sm and Gd pyrochlore crystals and the fluorite $Gd_2Zr_2O_7$ shows the largest thermal factor which is expected because it has the highest degree of static disorder. In addition, all the samples prepared for the diffraction experiment exhibit a [111] preferred orientation probably because the [111] plane is the cleavage plane.

4.5 Bulk properties

Bulk properties of both powder and single crystal samples, including DC susceptibility, AC susceptibility, magnetization and specific heat, were measured using the PPMS and MPMS at HZB. The samples are 5 - 30 mg in weight. The single crystal samples are cuboid approximately with a dimension $2 \times 2 \times 1$ mm but for the specific heat measurement, they are 0.5 mm thick. The single crystal samples are cut perpendicular to the [1-10] direction and have the [100], [111] and [011] directions in a plane so that magnetization along the three directions can be measured with one sample. The demagnetizing

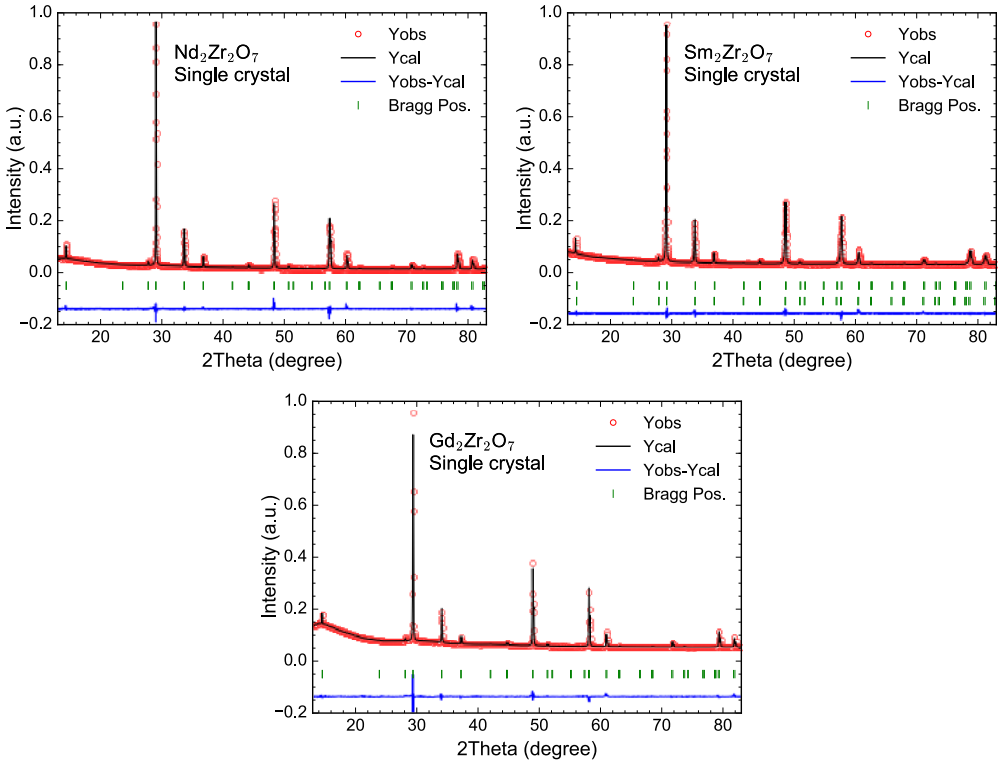

Figure 4.7: Rietveld refinement of room-temperature X-ray powder diffraction pattern of crushed single crystals. A tiny fraction (1.5 %) of the $Sm_2Zr_2O_7$ sample has a smaller lattice parameter [10.59857(21) Å vs 10.61667(34) Å] which is also fitted.

effect is estimated according to the shape of the sample by

$$H_{\text{internal}} = H_{\text{external}} - 4\pi\, N\, M,$$

where H_{internal} is the internal magnetic field of the sample, H_{external} is the applied magnetic field (they are in the unit of oersted). M is the magnetization in the unit of emu/cm^3. N is the dimensionless demagnetizing factor which is estimated according to Ref. [151] for the single crystal samples and assumed to be 1/3 for the powder samples. Low temperature (below 2 K) specific heat measurements on single crystals of $Nd_2Zr_2O_7$, $Gd_2Zr_2O_7$ and $Sm_2Zr_2O_7$ in magnetic fields along the [111] crystallographic direction were conducted by the group of Prof. Dr. P. Gegenwart in Augsburg University, Germany (the [111] direction is perpendicular to the sample plane). The low temperature AC susceptibility with field along the [111] and [100] directions for a crystalline sam-

Table 4.3: Crystallographic parameters of single crystals $Nd_2Zr_2O_7$, $Sm_2Zr_2O_7$ and $Gd_2Zr_2O_7$ obtained from the refinements of the lab-based X-ray diffraction patterns recorded at room temperature. The lattice parameter a, atomic coordinate x_{O1}, overall thermal factor B_{ov} and refinement quality parameters are shown.

	$Nd_2Zr_2O_7$	$Sm_2Zr_2O_7$	$Gd_2Zr_2O_7$	Fluorite $Gd_2Zr_2O_7$
a (Å)	10.651(1)	10.617(1)	10.531(1)	10.515(1)
x_{O1}	0.3347(1)	0.3436(1)	0.3454(12)	0.375
B_{ov}	0.53(3)	0.59(1)	0.66(7)	0.94(6)
R_{wp} (%)	4.74	3.08	2.30	5.73
R_{Bragg} (%)	4.66	4.06	5.38	8.64
χ^2	2.55	1.96	4.87	1.04

ple of $Nd_2Zr_2O_7$ were measured by the group of Dr. T. Herrmannsdörfer at Hochfeld-Magnetlabor Dresden (HZDR), Germany. The low-temperature AC susceptibility of the single crystal $Gd_2Zr_2O_7$ and the powder $^{160}Gd_2Zr_2O_7$ were measured by André Sokolowski (Dipl.-Phys.) at HZB. Because of the low sensitivity of the instrument, large samples of $Gd_2Zr_2O_7$ (above 60 mg) were used which were found to cause thermalization problems even with a waited time of ~ 10 minutes at each temperature point.

4.5.1 $Nd_2Zr_2O_7$

4.5.1.1 DC susceptibility and magnetization above 2 K

Fig. 4.8 shows the susceptibility and magnetization of powder and single crystal samples of $Nd_2Zr_2O_7$ above 2 K. The susceptibility increases smoothly with decreasing temperature without any anomaly above 2 K. There is no thermal hysteresis between the zero field cooled (ZFC) and field cooled (FC) data. The $\chi(T)$ data were fitted by the Curie-Weiss law plus the Van Vleck term $\chi(T) = \chi_0 + C/(T - \theta_p)$ for the temperature range $10\,\mathrm{K} \leq T \leq 30\,\mathrm{K}$. This temperature range was chosen to minimize the effects of the short-range magnetic correlations below 10 K revealed by the specific heat (Fig. 4.11) and the population of the crystal field excitation states at high temperatures. The fitting yields $\theta_p = 0.233(5)\,\mathrm{K}$, $\mu_{eff} = 2.55(1)\,\mu_B/\mathrm{Nd}$ and $\chi_0 = 2.82(2) \times 10^{-3}\,\mathrm{emu/mol\,Nd}$ for the powder sample [inset of Fig. 4.8(a)] and $\theta_p = 0.270(4)\,\mathrm{K}$, $\mu_{eff} = 2.47(1)\,\mu_B/\mathrm{Nd}$ and $\chi_0 = 3.5(1) \times 10^{-3}\,\mathrm{emu/mol\,Nd}$ for the single crystal sample [inset of Fig. 4.8(b)]. The fitting results of the powder and single crystal sample are consistent with each other. The

positive $\theta_{\rm p}$ indicates an effective ferromagnetic interaction between the Nd^{3+} moments which contrasts with the antiferromagnetic order inferred from neutron diffraction data (Chapter 5). This is a consequence of the dipolar-octupolar nature of the effective spin of Nd^{3+} ion in the pyrochlore compounds according to Ref. [152] (see Chapter 6). The extracted $\mu_{\rm eff} \sim 2.5\,\mu_{\rm B}$/Nd is much lower than the paramagnetic moment $3.62\,\mu_{\rm B}$/Nd for free Nd^{3+} ions ($\mu_{\rm eff} = g_J\sqrt{J(J+1)}$), revealing that the crystal field ground state is not the pure $|^4I_{9/2}, \pm 9/2\rangle$ Kramers doublet, consistent with the crystal field (CEF) analysis in Chapter 5.

Figure 4.8(c) shows the isothermal magnetization $M(H)$ curves at 2, 5, 10 and 20 K measured on the powder sample. The $M(H)$ at 2 K shows a saturation tendency with a Nd^{3+} moment of $1.27\mu_{\rm B}$ in a 5 T field which is much lower than $\mu_{\rm eff}$ extracted from the susceptibility data and the free ion saturation value of $3.27\,\mu_{\rm B}$/Nd ($M_{\rm s} = g_J J$). The strong reduction in $M_{\rm s}$ is attributed to the strong Ising anisotropy and the reduction of the Nd^{3+} single-ion moment due to the CEF effect (Chapter 5). Fig. 4.8(d) shows the $M(H)$ data for the single crystal with field along the three main cubic directions at 2 K as well as the data of the powder sample. The magnetization is also reduced and is highly anisotropic. The magnetizations with fields applied along the [100] ($M_{[100]}$) and the [110] ($M_{[110]}$) directions are the highest and the lowest, respectively, reminiscent of the spin ice materials and indicating the Ising anisotropy of the Nd^{3+} moment. For a pyrochlore with local [111] Ising anisotropy, the saturation magnetizations $M_{\rm s}$ for the three crystallographic directions [100], [110] and [111] are given by $\mu(1/\sqrt{3})$ ("2-in-2-out" spin configurations on the tetrahedra), $\mu(\sqrt{2/3}\times 2)/4$ ("1-in-1-out") and $\mu(1+1/3\times 3)/4$ ("3-in-1-out") respectively where μ is the magnetic moment of Nd^{3+} [153, 154]. As shown in Chapter 5, the moment of the CEF ground state of Nd^{3+} in $Nd_2Zr_2O_7$ is $\mu = 2.65\,\mu_{\rm B}$ and thus the saturation values for the three directions should be $M_{[100]} = 1.53\,\mu_{\rm B}$/Nd, $M_{[110]} = 1.08\,\mu_{\rm B}$/Nd and $M_{[111]} = 1.32\,\mu_{\rm B}$/Nd. The measurement shows 1.43, 1.19 and $1.38\,\mu_{\rm B}$/Nd for the three directions which is consistent with these analyses. Additionally, the weighted powder averaged M_s value can be estimated by $(6\,M_{[100]} + 12\,M_{[110]} + 8\,M_{[111]})/26 = 1.26\,\mu_{\rm B}$/Nd (the weight factors 6, 12 and 8 are the number of equivalent directions for the three directions) which is in very good agreement with the measured one $M_{\rm s} = 1.27\,\mu_{\rm B}$/Nd at 2 K in the 5 T.

In order to further investigate the Ising anisotropy and estimate the moment of Nd^{3+} at low temperatures, the powder $M(H)$ data are analysed with the effective spin-1/2 model. For an Ising anisotropic CEF ground state doublet with a large separation between the ground state and the first excited state, which is the case for the present compound (see Chapter 5), the low-temperature magnetic properties are described by an effective

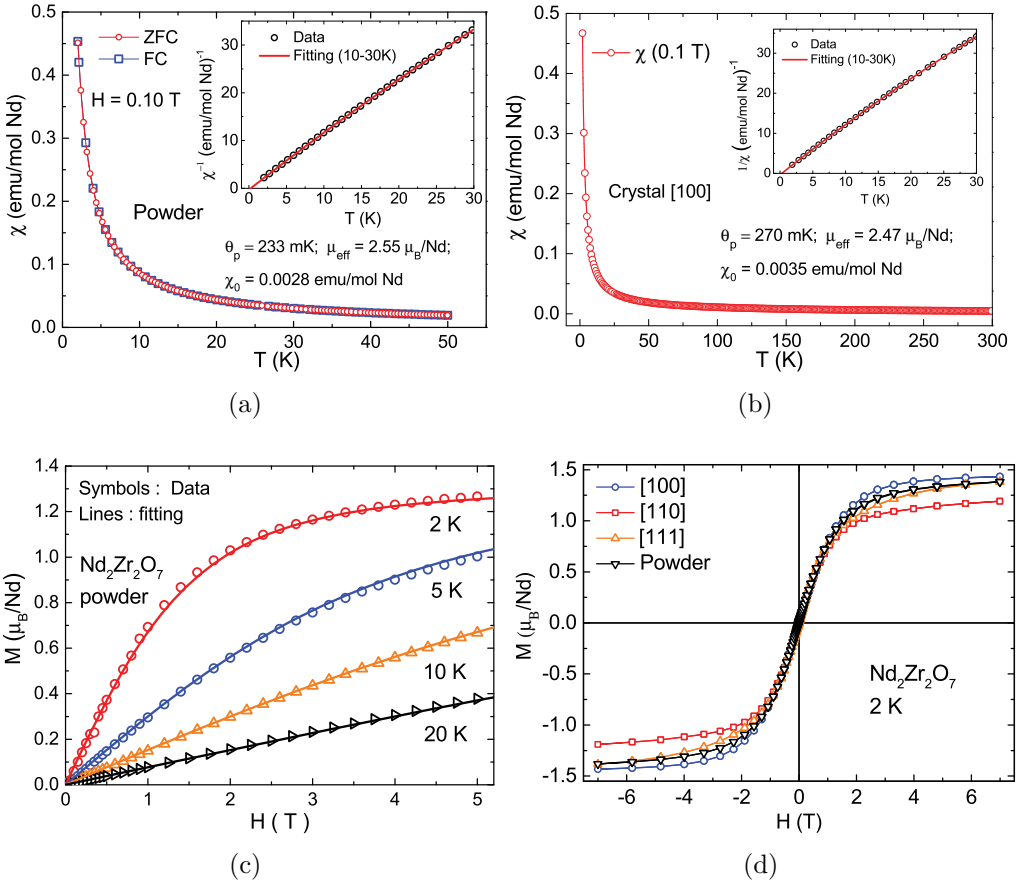

Figure 4.8: Susceptibility and magnetization of powder and single crystal $Nd_2Zr_2O_7$. (a) Zero field cooled (ZFC) and field cooling (FC) susceptibility of the powder sample and the Curie-Weiss law fitting (inset). (b) ZFC susceptibility of the single crystal with field 0.1 T applied along the [100] direction and the Curie-Weiss law fitting (inset). (c) Magnetization of the powder sample at different temperatures and the effective spin-1/2 model fitting. (d) Magnetization of the powder and single crystal samples at 2 K with fields along different directions.

Ising-anisotropic pseudospin-1/2 model and the powder-averaged magnetization in the paramagnetic state is given by Eq. 2.15. Simultaneous fitting of $M(H)$ data at 2 K, 5 K, 10 K and 20 K [Fig. 4.8(c)] yields $g_{zz} = 5.24(2)$. This g-factor is lower than the $g_{zz} = 2g_J J = 6.54$ expected for a Kramers doublet formed from the pure $m_J = \pm 9/2$ states of Nd^{3+} which again suggests mixing of the $|m_J\rangle$ states consistent with the CEF analysis in Chapter 5. The g_{zz} yields the ground state moment of $m_{\mathrm{Nd}} = g_{zz}\sigma\,\mu_{\mathrm{B}} \approx 2.62\,\mu_{\mathrm{B}}$

($\sigma = 1/2$) for $Nd_2Zr_2O_7$ which agrees with the μ_{eff} determined from the susceptibility above. The obtained g_{zz} value is comparable with that of $Nd_2Hf_2O_7$ for which the same analysis gives $g_{zz} = 5.01(3)$ [130].

4.5.1.2 AC susceptibility below 1 K

Figure 4.9 shows the temperature and DC field (along [111]) dependences of the real part of the AC susceptibility of single crystal $Nd_2Zr_2O_7$ (the AC and DC fields are parallel). The temperature dependence of χ_{AC} in zero DC field shows a peak at $T_{\text{N}} \approx 310\,\text{mK}$, indicating an AFM transition. The transition temperature is lower than that of the powder sample (400 mK) shown in the specific heat data in Ref. [127] and in the neutron diffraction data (Chapter 5). While another crystal studied in this thesis shows the same transition temperature as the powder sample in the specific heat data (Sec. 4.5.1.3) and a crystal synthesised by another group shows a transition temperature of 285 mK [129, 155]. This indicates that the sample dependence is present among $Nd_2Zr_2O_7$ single crystals as has been also observed for $Yb_2Ti_2O_7$ [123]. However the magnetic ground state of $Nd_2Zr_2O_7$ does not vary from sample to sample according to the neutron diffraction data of different samples (see Refs. [129, 155] and Chapter 5).

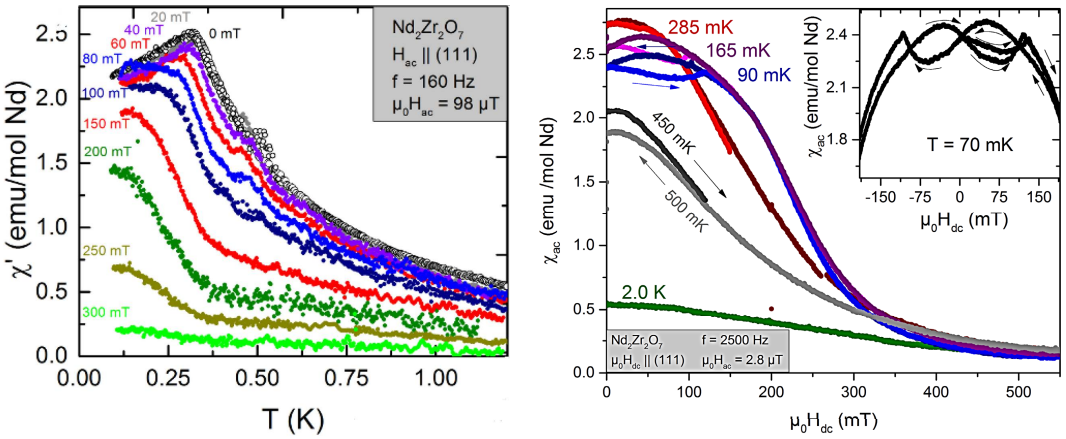

Figure 4.9: (left) Real part of the AC susceptibility of the $Nd_2Zr_2O_7$ crystal in different DC fields along the [111] direction. (right) DC field dependence of the real part of the AC susceptibility at different temperatures (the arrows show the increasing or decreasing fields). Measured by L. Opherden *et al.* at HZDR in Dresden.

Application of a DC magnetic field decreases the transition temperature (Fig. 4.9) which is consistent with the DC magnetisation data in Ref. [129] and similar to the results of

$Nd_2Hf_2O_7$ [130]. The DC field dependence of χ_{AC} at temperatures below T_N shows an anomaly indicating a metamagnetic transition with the critical field increases with decreasing temperature, in agreement with the magnetisation data in Ref. [129]. The anomaly is ascribed to a field-induced transition from the AFM state to a field polarized state. Around the transition, pronounced hysteresis is observed between increasing and decreasing fields along the [111] direction. The field-induced transition also appears for the [100] direction but with a much smaller hysteresis (Fig. 4.10). A *H*-*T* phase diagram is obtained as shown in Fig. 4.10 which is consistent with the former report [129, 156]. The field-induced transition and the hysteresis are explained qualitatively in Chapter 6 after determining the spin Hamiltonian of $Nd_2Zr_2O_7$ by fitting the spin wave spectra observed in inelastic neutron scattering experiment.

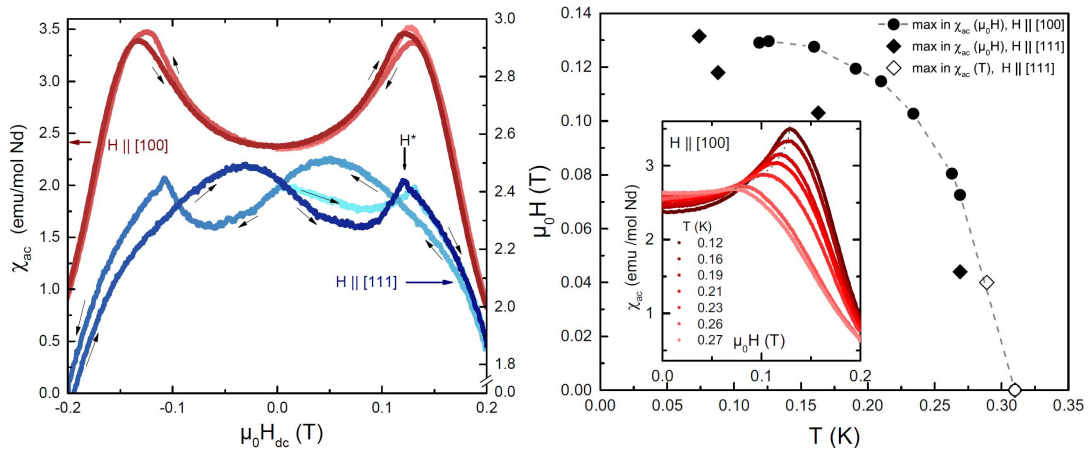

Figure 4.10: (left) DC field dependence of the real part of the AC susceptibility for the fields along the [100] and [111] directions. The arrows show the increasing or decreasing fields. (right) *H*-*T* phase diagram of $Nd_2Zr_2O_7$ extracted from the AC susceptibility and the χ_{AC} for field along the [100] direction at different temperatures (inset). Measured by L. Opherden *et al.* at HZDR in Dresden. Taken from Ref. [156].

4.5.1.3 Specific heat

The specific heat C_p data of single crystal $Nd_2Zr_2O_7$ and powder $La_2Zr_2O_7$ samples are shown in Fig. 4.11. Above 10 K, the specific heat of the two compounds are nearly the same because of their similar phonon excitations and thus the $La_2Zr_2O_7$ data can be used as a non-magnetic background [at higher temperatures they are different due to the CEF effect (see Chapter 5)]. At low temperatures, $Nd_2Zr_2O_7$ shows a λ-shape

peak at $T_N \approx 0.4\,K$ similar to the powder sample [70, 127]. The upturn below 0.1 K is caused by the nuclear hyperfine interactions whose contribution is $\sim T^{-2}$ in the high temperature region (e.g. the temperature region in this measurement, see Ref. [70] and Appendix C). The magnetic $4f$ electrons contribute to the C_p peak, which originates from the magnetic correlations and excitations.

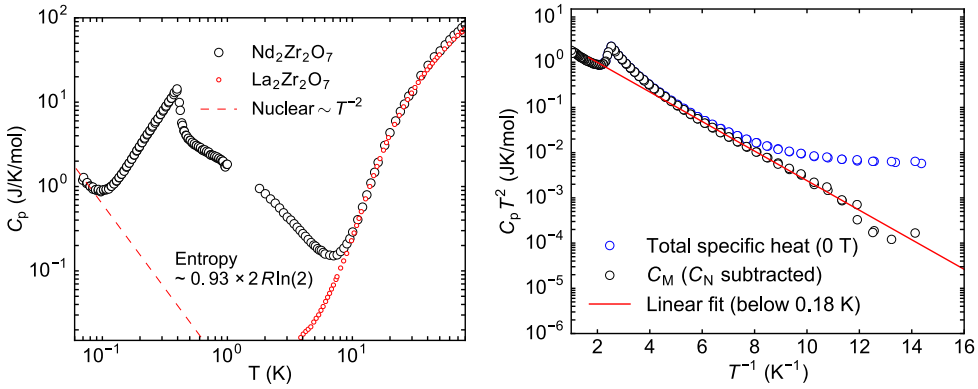

Figure 4.11: (left) Specific heat of single crystal $Nd_2Zr_2O_7$ (black circles) and powder $La_2Zr_2O_7$ (red circles) samples. The magnetic entropy is calculated based on the data below 10 K after subtracting the fitted nuclear part ($\sim AT^{-2}$) (dashed line) and the measured phonon part (the C_p of $La_2Zr_2O_7$). (right) Fit the data below 0.18 K to $AT^{-2} + BT^{-2}\exp(-\Delta/T)$ which shows the raw data (blue circles), the magnetic $4f$ electron part C_M (black circles) obtained by subtracting the fitted nuclear part C_N from the raw data and the fit (red line). Measured by Akito Sakai *et al.* in Augsburg University.

Assuming that spin wave excitations have a linear dispersion at low energy, the $C_p(T)$ should show a T^3 temperature dependence at sufficient low temperature below T_N. It was reported that the T^3 law applies to the low temperature C_p of $Nd_2Sn_2O_7$ which has the same magnetic order with $Nd_2Zr_2O_7$ (see Ref. [131] and Chapter 5). However, the inelastic neutron scattering data of $Nd_2Zr_2O_7$ clearly shows gapped magnon excitations (see Ref. [155] and Chapter 6). Therefore, the T^3 law may not be valid for this Nd pyrochlore. The phenomenological model $\sim T^{-2}\exp(-\Delta/T)$ (Δ is the magnon gap size) is normally used to describe the temperature dependence of the specific heat of gapped magnon excitations in conventional collinear antiferromagnets with single-ion anisotropy [99]. It would be a straight line in the $\log(C_pT^2)$-$1/T$ plot. The data below 0.18 K is fitted to $AT^{-2} + BT^{-2}\exp(-\Delta/T)$ (Fig. 4.11) which yields $\Delta = 0.75(3)$ K. The obtained gap is quite close to the measured one (≈ 0.07 meV $= 0.81$ K) as shown in Chapter 6.

After subtracting the phonon and nuclear contributions, the calculated magnetic entropy is $0.93\,R\ln(2)/\mathrm{mol\,Nd}$ (based on the C_p data below 10 K). The entropy released due to the phase transition is close to $R\ln(2)/\mathrm{mol\,Nd}$, indicating the establishment of long-range order in a spin-1/2 system, consistent with the neutron diffraction and crystal field analysis in Chapter 5.

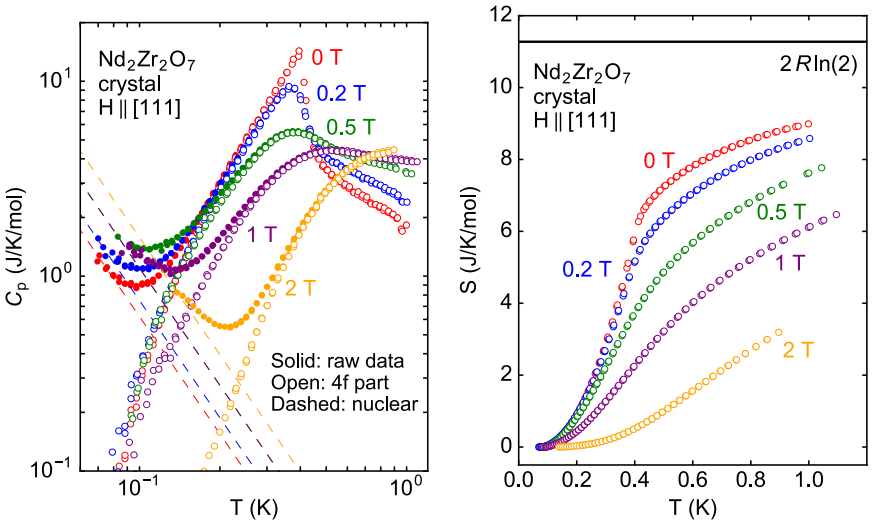

Figure 4.12: (left) Low temperature specific heat of the single crystal sample of $Nd_2Zr_2O_7$ in different fields along the [111] direction. The raw data and nuclear-part-subtracted data are shown by the solid and open circles, respectively. The nuclear contribution for subtraction (dashed line) is estimated in a similarly way with the zero field data (see Appendix C). (right) Entropy of the magnetic $4f$ electrons. The data were measured by Akito Sakai *et al.* in Augsburg University.

Figure 4.12 shows the C_p data of $Nd_2Zr_2O_7$ in magnetic fields ($0\,\mathrm{T} \leq H \leq 2\,\mathrm{T}$) along the [111] direction. The C_p peak is suppressed and finally becomes a broad peak shifting to the high temperature with increasing field. According to the H-T phase diagram (Fig. 4.10), the lowest applied field 0.2 T here completely suppresses the transition. Therefore the peak in 0.2 T may not be due to the ordering transition but due to the excitations of the field polarized state. This is in agreement with the C_p data at 0.2 T where the peak observed is no longer a sharp λ-anomaly. According to the spin wave calculations with the spin Hamiltonian determined in Chapter 6, the spin wave excitations in the field polarized state are also gapped (not shown). As a result, the C_p data in field are also fitted with $A\,T^{-2} + B\,T^{-2}\exp(-\Delta/T)$ (see Appendix C) and the entropy is calculated based on the nuclear-C_p-subtracted data as shown in Fig. 4.12.

4.5.2 $Gd_2Zr_2O_7$

Figure 4.13 shows the susceptibility and magnetization data of the powder and single crystal $Gd_2Zr_2O_7$ samples. The temperature dependence of the inverse susceptibility has good linearity and fitting to the modified Curie-Weiss law shows that $\theta_p = -6.8(1)\,K$, $\mu_{eff} = 7.84(1)\,\mu_B$ and $\chi_0 = 2.80(1) \times 10^{-4}$ emu/mol Gd, which agrees with the previously reported value ($\theta_p = -7.70\,K$, $\mu_{eff} = 7.83\,\mu_B$) [138]. The negative Curie-Weiss temperature indicates antiferromagnetic interactions between the moments. The magnetization at 2 K increases with field almost linearly below 5 T and saturates above 6 T. The saturated magnetization is $M_s \approx 6.7\,\mu_B$/Gd which is slightly lower than the theoretical value $7.0\,\mu_B$/Gd. It was reported that $Gd_2Ti_2O_7$ and $Gd_2Sn_2O_7$ also do not show the theoretical saturation value ($M_s = 6.65$ and $6.8\,\mu_B$/Gd, respectively), which was ascribed to a possible metastable unsaturated phase [143]. The $M(H)$ in low fields is much lower than the calculated one (Fig. 4.13) for the free isotropic Gd^{3+} ion as a result of the strong antiferromagnetic interactions.

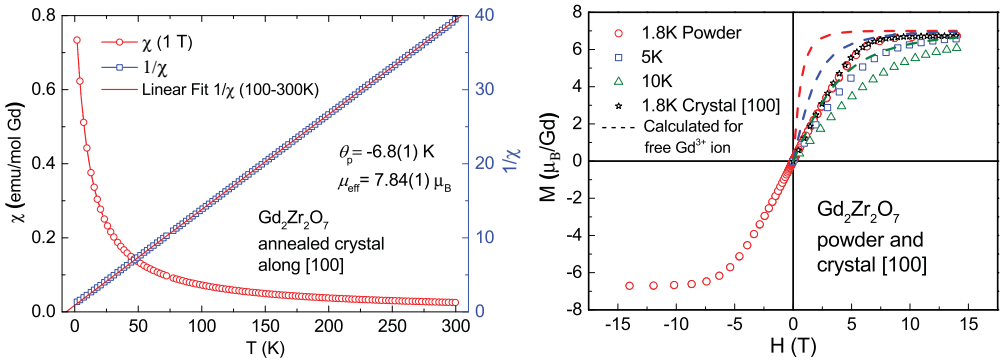

Figure 4.13: (left) Susceptibility of the annealed $Gd_2Zr_2O_7$ crystal with the field along the [100] direction. (right) Measured magnetization of powder and single crystal samples of $Gd_2Zr_2O_7$ at different temperatures (symbols) and calculated magnetization for free isotropic Gd^{3+} ion (dashed lines) at the corresponding temperatures.

The AC susceptibility χ_{AC} of the annealed single crystal measured down to 0.3 K (Fig. 4.14) shows an anomaly at ~ 0.67 K which is somewhat lower than the reported Néel temperature of 0.769 K of a powder sample where the specific heat showed a sharp peak [138]. It is remarkable that the unannealed single crystal in the fluorite phase has a similar anomaly in the susceptibility as the annealed sample but with a small frequency dependence which could be due to glassiness or caused by poor thermalization during the measurements. The isotope powder sample shows an anomaly at the temperature

with almost no frequency dependence (see Fig. 4.15). The specific heat of the annealed crystal seems to show an broad peak around 0.7 K (Fig. 4.16) in contrast to the former report for the powder sample where a sharp peak was observed [138]. Unfortunately the current measurement was confined to temperatures below 0.85 K making a detailed comparison difficult.

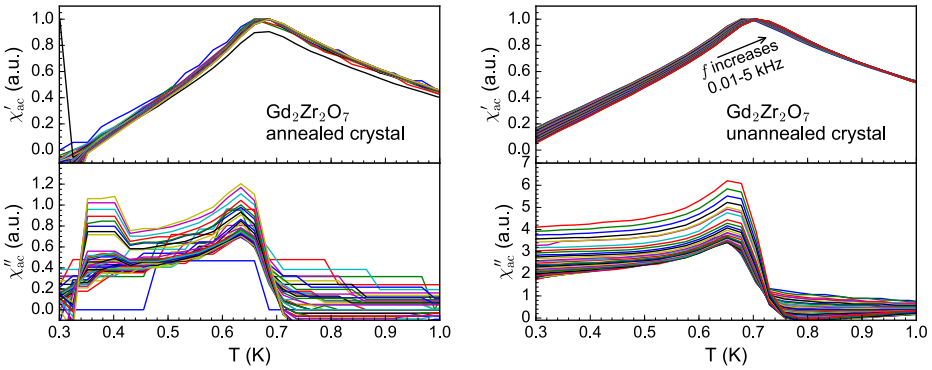

Figure 4.14: AC susceptibility of the annealed (left) and unannealed (right) $Gd_2Zr_2O_7$ single crystals. The as-grown crystal crystallizes in the fluorite phase showing no pyrochlore Bragg peaks in the XRD pattern and the annealed one shows sharp pyrochlore Bragg peaks.

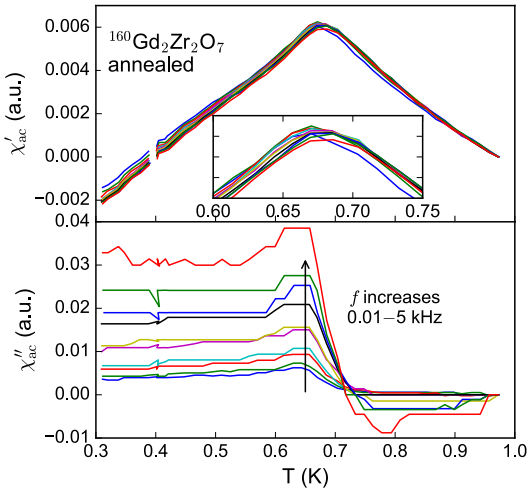

Figure 4.15: AC susceptibility of the long-time annealed $^{160}Gd_2Zr_2O_7$ powder which shows sharp pyrochlore peaks in the XRD pattern.

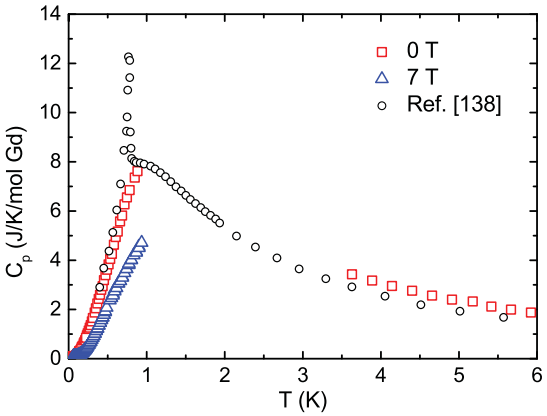

Figure 4.16: Specific heat of the short-time-annealed single crystal $Gd_2Zr_2O_7$ which only shows tiny pyrochlore peaks in the XRD pattern. The data in Ref. [138] is also shown for comparison. Measured by Akito Sakai *et al.* in Augsburg University.

4.5.3 $Sm_2Zr_2O_7$

Figure 4.17 shows the susceptibility and magnetization of the powder and single crystal $Sm_2Zr_2O_7$ samples. The susceptibility does not follow the Curie-Weiss law over any temperature range measured, which is consistent with the former report [144]. However, the Curie-Weiss fitting for a small low temperature range (1.8 - 6 K) yields $\theta_p = -1.27(3)$ K, $\mu_{eff} = 0.39(1)\mu_B$/Sm, and $\chi_0 = 0.0015(1)$ emu/mol. The temperature dependence of the effective moment calculated with Eq. 2.8 is shown in the inset. The μ_{eff} at 2 K is 0.24 μ_B/Sm which is much smaller than that of the free ion (0.84 μ_B). μ_{eff} increases with increasing temperature and becomes 1.13 μ_B at 300 K which is comparable to the effective moment of the free Sm^{3+} ion (the slightly higher value is caused by the population of the excited multiplets as shown in Chapter 9). The temperature dependence of the susceptibility can be attributed to the crystal field splitting of the $^6H_{5/2}$ manifold of Sm^{3+} and the thermal population of the low-lying crystal field excited levels (see Chapter 9). The magnetization increases almost linearly with increasing the field and is not saturated at 7 T. The magnetization of the powder sample at 2 K is fitted with the pseudospin-1/2 model assuming the Ising anisotropy (Eq. 2.15) as shown in Fig. 4.17 and the fitting indicates that the g factor is 0.64(2) (0.32(1) μ_B/Sm) which is close to the value of μ_{eff} at low temperature. The Ising anisotropy at low temperature is confirmed by the crystal field analysis in Chapter 9.

The specific heat data of the single crystal $Sm_2Zr_2O_7$ below 2 K are shown in Fig. 4.18.

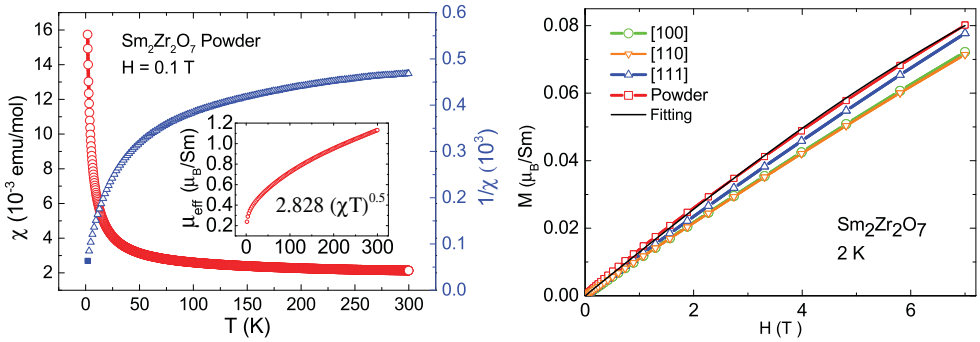

Figure 4.17: (left) Temperature dependence of the susceptibility of the powder sample of $Sm_2Zr_2O_7$. The inset shows the effective moment as a function of temperature calculated with the equation indicated. (right) Magnetization of powder and single crystal $Sm_2Zr_2O_7$. The black line is the fitting of the powder magnetization with the effective spin-1/2 model.

There is no phase transition however it exhibits a broad peak at 0.5 K which may be related to magnetic correlations. The corresponding entropy released is close to R ln(2)/mol Sm which validates the pseudospin-1/2 model at low temperature.

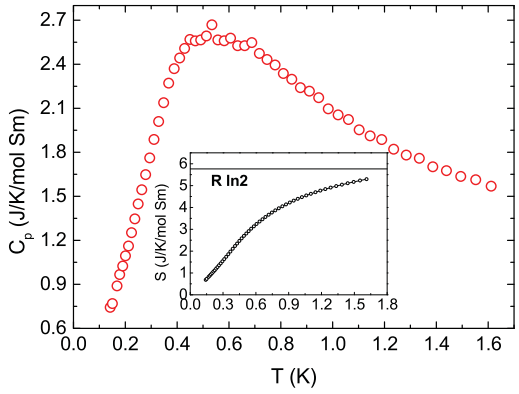

Figure 4.18: Specific heat of the $Sm_2Zr_2O_7$ single crystal below 2 K (main plot) and the corresponding entropy (inset). Because the C_p below 0.15 K is not measured and it is assumed to have a linear dependence on the temperature for estimating the entropy. Note that the temperature may be not calibrated well. Measured by Akito Sakai *et al.* in Augsburg University.

4.6 Conclusions

In this chapter, the crystal structure and macroscopic magnetic properties of $Nd_2Zr_2O_7$, $Gd_2Zr_2O_7$ and $Sm_2Zr_2O_7$ were presented. The powder diffraction shows no measurable structural defects in $Nd_2Zr_2O_7$ and $Sm_2Zr_2O_7$ and $\sim 20\,\%$ Gd/Zr site mixing in $Gd_2Zr_2O_7$. The $\chi(T)$ data of $Nd_2Zr_2O_7$ indicate $\theta_p \sim 0.25\,K$ and $\mu_{eff} \sim 2.5\,\mu_B$ /Nd, consistent with the result in Refs. [128, 129]. The $M(H)$ above 2 K for the powder sample is well-described by the paramagnetic effective spin-1/2 model with a g-factor 5.24(2) and the single crystal $M(H)$ with fields along different directions resembles those of the spin ice materials, indicating local [111] Ising anisotropy. The C_p data of the single crystal show a sharp peak at 0.4 K revealing an ordering transition, in agreement with the former result [70]. The corresponding entropy is $R\ln(2)/mol\,Nd$ which supports the pseudospin-1/2 model. The C_p at temperatures well below the ordering temperature can be fitted with $A\,T^{-2} + B\,T^{-2}\exp(-\Delta/T)$ (nuclear-hyperfine and gapped-magnon contributions), yielding a magnon gap $\sim 0.75\,K$ consistent with spin wave neutron scattering spectra in Chapter 6.

The $\chi(T)$ of $Gd_2Zr_2O_7$ follows the Curie-Weiss law for the whole temperature range 2-300 K measured and the magnetization with field along different crystallographic directions are nearly the same, suggesting a very small single-ion anisotropy. The Curie-Weiss fitting yields $\theta_p = -6.8(1)\,K$ and $\mu_{eff} = 7.84(1)\mu_B$ /Gd which is consistent with the former results for this compound and comparable with those of $Gd_2Ti_2O_7$ and $Gd_2Sn_2O_7$ [138–140]. The magnetisations below 10 K cannot be fitted with the Brillouin function with $J = 7/2$ possibly due to the strong spin interactions. The AC susceptibility shows a peak at $\sim 0.67\,K$ indicating an transition whose position has almost no frequency dependence for the annealed sample. The specific heat of the annealed single crystal sample seems to show a broad peak at $\sim 0.7\,K$ while a sharp peak was observed in Ref. [138]. Differences with the former report could be caused by the different sample qualities ($Gd_2Zr_2O_7$ tends to show the Gd/Zr antisite defect due to the low pyrochlore-fluorite transition temperature) [121, 138].

The susceptibility of $Sm_2Zr_2O_7$ does not show a Curie-Weiss behavior due to the low energy crystal field levels nevertheless the Curie-Weiss fitting for the temperature range 1.8 - 6 K indicates an effective antiferromagnetic interaction of the order of 1 K and $\mu_{eff} = 0.39(1)\mu_B$/Sm. The magnetisation above 2 K increases linearly with the field without saturation in the highest field of 7 T. Fitting with the effective spin-1/2 model yields a moment $0.32(1)\,\mu_B$/Sm. The specific heat shows a broad peak at 0.5 K indicating the establishment of short-range correlations. The entropy released up to 1.6 K is close

to $\mathrm{R}\ln(2)/\mathrm{mol\,Sm}$ revealing that the crystal field ground state is a well-isolated doublet.

5 Crystal field state and magnetic structure of $Nd_2Zr_2O_7$

5.1 Introduction

The various fascinating phenomena observed in the rare-earth pyrochlores have relations with the single-ion anisotropy. The anisotropy changes for different rare-earth species which dramatically alters the ground state of the pyrochlores. Take the titanate series as an example. The Gd^{3+} ion is isotropic and the gadolinium pyrochlore is a dipolar Heisenberg system; the Er^{3+} ion has planar anisotropy resulting in XY systems which can show the "order-by-disorder" phenomenon; Ho and Dy pyrochlores have Ising anisotropy and have the spin ice ground state [25, 29–33]. The single-ion anisotropy originates from the crystal electric field (CEF) interaction due to the surrounding anions. The degeneracy of the free ion ground state is lifted by the CEF interactions because of the breaking of the spherical symmetry, and the large variety of anisotropic CEF ground states form the playground of the low-temperature physics in the rare earth pyrochlores.

The CEF ground state also restricts the form of the exchange interaction between ions which can be analysed according to the symmetry of crystal field states. For instance, the exchange Hamiltonian for the Kramers ions has one extra term J_{xz} compared to the Hamiltonian for the non-Kramers ions due to the different transformation properties of the CEF ground state under the time reversal operation (see Chapter 2). Recently, Huang *et al.* pointed out that the CEF ground state of Nd^{3+} in pyrochlores could be a dipolar-octupolar doublet with the wave function being a linear combination of only the $|\pm 3/2\rangle$, $|\pm 9/2\rangle$ terms [17]. As a result, the x and z components of the associated pseudospin-1/2 transform under the local symmetry like magnetic dipole while the y component transforms like a component of the magnetic octupole tensor. The symmetry allowed nearest-neighbor spin Hamiltonian has the form of the XYZ model which hosts novel dipolar and octupolar quantum spin ice phases besides ordered phases [17].

The previous experimental study on the crystal field of $Nd_2Zr_2O_7$ was based on susceptibility data and the CEF parameters extracted are comparable with the parameters of

other rare earth pyrochlores which indicate local [111] Ising anisotropy consistent with the single crystal magnetization data [128]. The CEF states of the related compound $Nd_2Ir_2O_7$ were directly studied with inelastic neutron scattering using the Stevens operator equivalents [137]. These results reveal that the crystal field ground state of Nd^{3+} in pyrochlores is indeed a dipolar-octupolar Kramers doublet with Ising anisotropy. Inelastic neutron scattering data provide the most reliable measurement of the CEF excitation energies, however it is better to analyse them using tensor operator methods which take account of intermultiplet mixing rather than Stevens operators which only consider the lowest energy multiplet. This is especially important for the light rare earth elements like Nd whose J-mixing effect is normally large.

The magnetic ground state of $Nd_2Zr_2O_7$ could be an ordered state as suggested by the specific heat which shows a sharp peak at $\sim 0.4\,\mathrm{K}$ (see Chapter 4 and Ref. [70]). The susceptibility indicates effective FM interactions between the Nd^{3+} moments (inferred from the positive Curie-Weiss temperature shown in Chapter 4 and Ref. [128]). Recently it was reported that $Nd_2Hf_2O_7$ and $Nd_2Sn_2O_7$ show the "all-in/all-out" (AIAO) order below $0.55\,\mathrm{K}$ and $0.91\,\mathrm{K}$, respectively [130, 131]. Considering the similarities of these three compounds, $Nd_2Zr_2O_7$ could also have the AIAO order. Additionally, $Nd_2Ir_2O_7$ and $Nd_2Mo_2O_7$ show ordered ground states (AIAO and 2I2O, respectively) at much higher temperatures [134–136]. However, the physics of these two compounds are believed to be dominated by the d electrons of the transition metal ions and thus the order on the Nd^{3+} sublattices are strongly affected by the order of the $5d$ moments.

In this chapter, the single-ion ground state and the collective magnetic ground state of $Nd_2Zr_2O_7$ are studied by using time-of-flight inelastic neutron scattering (INS) and neutron powder diffraction. The CEF ground state is found to be a well-isolated dipolar-octupolar Kramers doublet, which confirms the theoretical prediction and former results. The long-range AIAO order is observed as the ground state of $Nd_2Zr_2O_7$ with a much reduced ordered moment. Very recently in a parallel work, Lhotel *et* al. also investigated the crystal field and magnetic order of $Nd_2Zr_2O_7$ using neutron scattering techniques and found similar results [129]. However, they only measured three CEF crystal transitions using a triple-axis spectrometer and analysed the data with the Stevens operator equivalents [129]. The data presented in this chapter shows all the crystal field transitions within the intermediate-coupling ground state which are analysed with tensor operators.

5.2 Inelastic neutron scattering: crystal field states

5.2.1 Experiment details

High energy inelastic neutron scattering for both $Nd_2Zr_2O_7$ and $La_2Zr_2O_7$ (non-magnetic reference) ($\sim$ 20 g each) are measured on the direct geometry time-of-flight spectrometer ARCS [105] at the SNS. The powder is filled in thin-walled cylindrical aluminium cans with a hollow insert giving a sample thickness $\sim$ 5 mm. The incident neutron energies E_i used are 50, 150 and 400 meV to access a large number of crystal field excitations. The energy resolution for elastic scattering is 3-5 % of E_i and gives the upper bounds of the resolution [105]. The elastic scattering peak widths are about 2, 5 and 20 meV in the data with the three incident energies. Data are collected at 5 K and 300 K to study the effect of temperature on the spectra. The data were analysed using the software SPECTRE [157] which adopts tensor operators rather than the Stevens' operator equivalents allowing the $J-$mixing effect to be included.

5.2.2 Crystal field analyses and results

Figure 5.1 shows the color contour maps of the time-of-flight INS spectra of powder $Nd_2Zr_2O_7$ with incident neutron energy $E_i = 50$, 150 and 400 meV at 5 K. These maps show the scattering cross section $S(E, Q)$ where E is the energy transfer and Q is the scattering vector. While the high intensity around $E = 0$ arises from elastic scattering, the scattering of phonons gives rise to a Q dependent intensity which increases with increasing Q. In addition to these features, it also clearly shows three strong dispersionless excitations around 23.4, 35.0 and 106.2 meV in the spectrum with $E_i = 50$ and 150 meV and two weaker ones near 240 and 310 meV (with even weaker levels in between) in the spectrum with $E_i = 400$ meV. The Q-dependent integrated intensity between 105.7 meV and 106.7 meV follows the magnetic form factor $f^2(Q)$ of Nd^{3+} [109] as shown in Fig. 5.2 and thus suggests that those excitations in the INS spectra are resulted from the scattering of single-ion CEF transitions. Further evidence that these excitations are magnetic is inferred by their absence in the spectrum of the non-magnetic isostructural compound $La_2Zr_2O_7$ (also shown in Fig. 5.1).

For the Nd^{3+} ion, the Hund's-rule ground state (GS) multiplet is $^4I_{9/2}$ and the first excited multiplet $^4I_{11/2}$ is typically 250 meV above it [2, 158]. Furthermore, in pyrochlores the CEF splitting of the GS multiplet of rare earth ions is normally $\sim$ 100 meV [5, 62, 82, 159, 160]. Therefore, the three excitations below 200 meV are assigned to transitions within the GS multiplet and the two above 200 meV to intermultiplet transitions. According to Kramers theorem, the CEF interaction should split the GS multiplet $^4I_{9/2}$

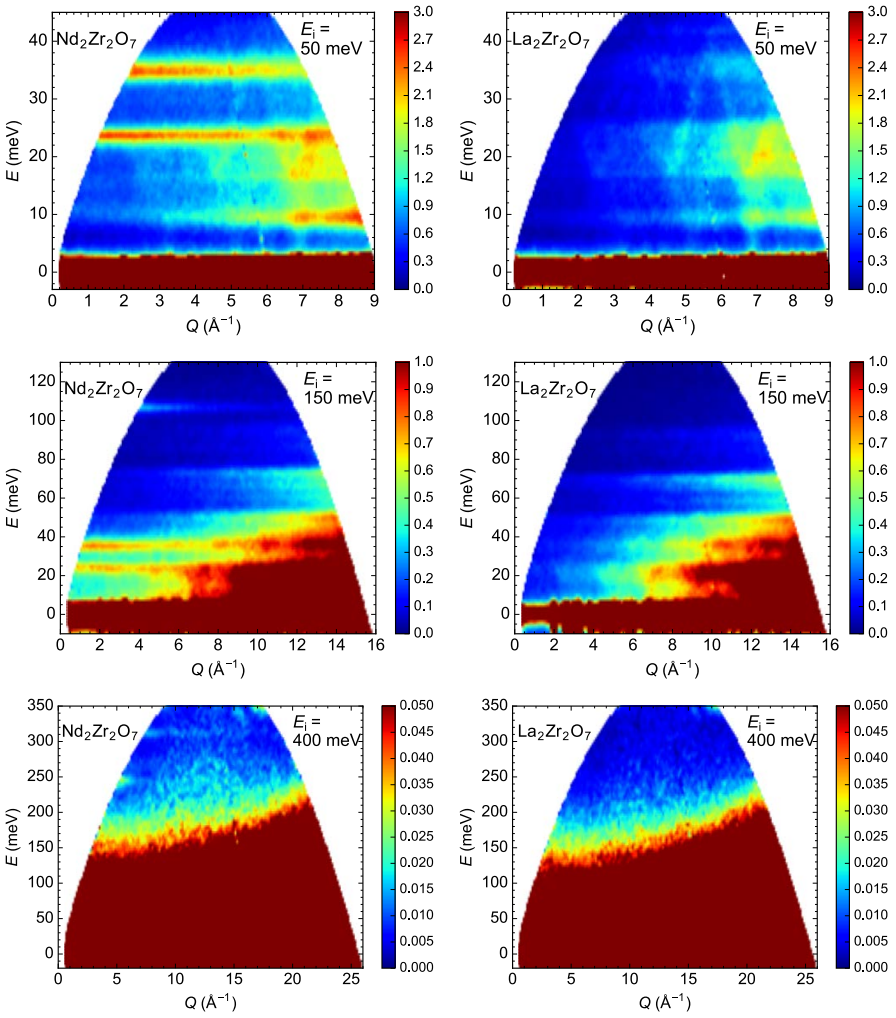

Figure 5.1: Color-coded maps of energy E vs wavevector Q of the inelastic neutron scattering intensity of $Nd_2Zr_2O_7$ (left) and $La_2Zr_2O_7$ (right) at 5 K with $E_i = 50$, 150 and 400 meV. The spectra shows the crystal field splitting of the ground state multiplet $^4I_{9/2}$ below 200 meV and the crystal field splitting of the first excited multiplet $^4I_{11/2}$ above 200 meV.

of Nd^{3+} into five doublets of $|\pm m_J\rangle$ type and thus there ought to be four excitations in the INS spectra at base temperature, corresponding to transitions from the GS doublet to the four excited doublet states. Although only three excitations within the GS multiplet at 23.4 meV, 35.0 meV and 106.2 meV are apparent, a closer inspection of the INS data (Fig. 5.3) reveals that the excitation at 35.0 meV is rather broad (compared to the instrument resolution ~ 1.5 meV) which could be due to two unresolved excitations

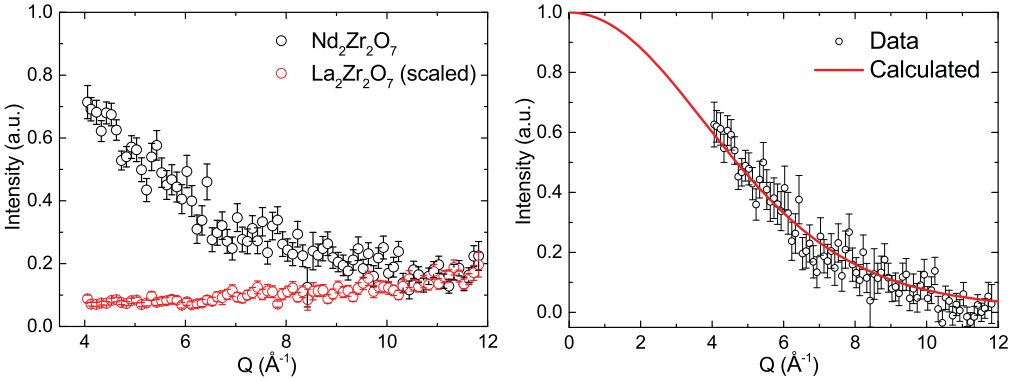

Figure 5.2: (left) Q dependence of the integrated scattering intensity of $Nd_2Zr_2O_7$ and $La_2Zr_2O_7$ over the energy region 105.7–106.7 meV at 5 K (the $La_2Zr_2O_7$ data is scaled for subtraction as a background). (right) The $La_2Zr_2O_7$-subtracted data of $Nd_2Zr_2O_7$ (open circles) and magnetic form factor $f^2(Q)$ with dipolar approximation of Nd^{3+} (solid line).

from two closely situated CEF levels (the so-called quasi-quartet). Similar unresolved excitations near 35.0 meV were observed in the INS data from a thermal neutron triple axis spectrometer in Ref. [129]. Two closely spaced CEF levels near 35.0 meV were also inferred by analysing susceptibility and heat capacity data in Ref. [128].

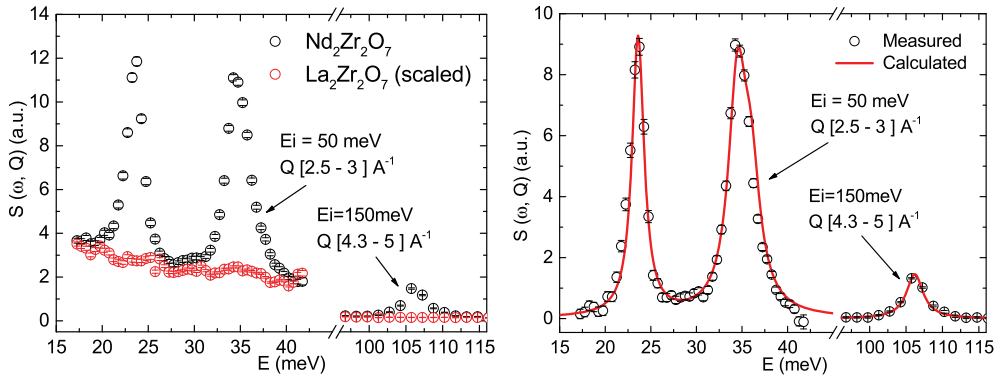

Figure 5.3: Left: comparison of the INS spectra at 5 K of $Nd_2Zr_2O_7$ and $La_2Zr_2O_7$ (the $La_2Zr_2O_7$ data is scaled by a factor for subtraction). Right: fitted inelastic neutron spectrum of the four transitions within the ground state multiplet $^4I_{9/2}$ at 5 K. The data for the three lower crystal field levels are from the dataset with incident neutron energy $E_i = 50$ meV integrated Q over the range [2.5–3] Å^{-1}. The data for the crystal field excitation at 106.2 meV are from the dataset with $E_i = 150$ meV integrated Q range [4.3–5] Å^{-1}.

For a quantitative analysis of the INS data, the crystal field model is used. In order to account for the mixing of the GS multiplet with the higher multiplets which is necessary for the situation with a large splitting of the GS multiplet (comparable with the energy separation of the first excited multiplet), tensor operators instead of Stevens' operator equivalents are used for the CEF Hamiltonian [1]. In the pyrochlore structure, the Nd^{3+} ions are subjected to a crystal electric field with D_{3d} symmetry created by the eight nearest-neighbor oxygen ions and the CEF Hamiltonian is given by Eq. 2.12. The intermediate-coupling free ion basis states are used for diagonalizing the H_{CEF}. As the CEF splitting from the ground state multiplet is within 110 meV, for simplicity the fitting includes only the 98 intermediate coupling basis states from the first 12 multiplets below 2.2 eV. Such a truncation of multiplet terms at 2.2 eV is expected to be of no consequence for the analysis as the contribution from a higher multiplet to the GS multiplet decreases rapidly as the gap between them increases ($\sim 1/\Delta$ where Δ is the energy gap) [2].

Table 5.1: Observed and calculated crystal-field transition energies (E) and integrated intensities (I) within the ground state multiplet $^4I_{9/2}$ of $N_2Zr_2O_7$ at 5 K. The I is relative with respect to the highest peak observed.

Levels	E_{obs} (meV)	E_{cal} (meV)	I_{obs}	I_{cal}
Γ_{56}^+	0	0	-	2.5
Γ_4^+	23.4(2)	23.36	0.58(5)	0.558
Γ_{56}^+	34.4(4)	34.44	⎫ 1	0.655
Γ_4^+	35.7(4)	35.81	⎭	0.345
Γ_4^+	106.2(5)	106.28	0.60(8)	0.525

Inelastic neutron scattering measures the powder averaged unpolarized neutron inelastic scattering double-differential cross section given by Eq. 3.5. For the calculation of the intensity of the transitions within the GS multiplet, the dipolar approximation is used allowing Eq. 3.5 to be rewritten as

$$\frac{d^2\sigma}{d\Omega dE'} = cf^2(Q)\frac{k'}{k}\sum_{\alpha}\sum_{\lambda\lambda'} p_\lambda \left|\langle\lambda'|J_\alpha|\lambda\rangle\right|^2 L_{\lambda\lambda'} \tag{5.1}$$

where c is a constant, $f^2(Q)$ is the magnetic form factor, k and k' are the moduli of the incident and scattered wave vectors, $|\lambda'\rangle$ and $|\lambda\rangle$ are the initial and final eigenfunctions, J_α is the x, y or z component of the total angular momentum operator, and $L_{\lambda\lambda'}$ is the Lorentzian function describing the line shape of the excitation.

The refinement of the INS spectra of the CEF transitions within the GS multiplet is performed using the program SPECTRE [157], which was recently used to analyse the

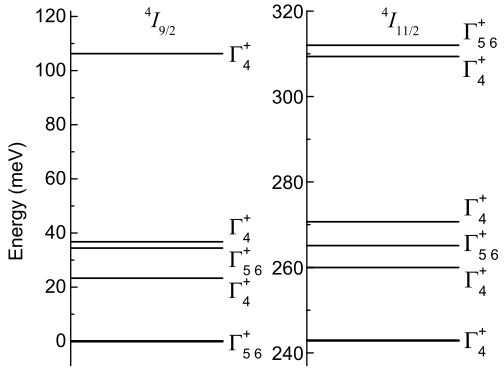

Figure 5.4: Crystal field energy schemes for (a) the ground-state multiplet $^4I_{9/2}$ and (b) the first excited multiplet $^4I_{11/2}$ corresponding to the crystal field parameters obtained from the analysis of INS data. Γ_{ab}^+ shows the irreducible representation that the corresponding CEF state transforms as [161].

INS data of the pyrochlores $Pr_2Sn_2O_7$ [159] and $Tb_2Ti_2O_7$ [62]. The energies and the integrated intensities of the levels are obtained by fitting the peaks in the spectrum with Lorentzian functions. As the two overlapping excitations near 35.0 meV are not resolved in the data, the combined intensity is used, obtained by fitting them as a single peak. On the other hand, to get their approximate positions, the peak is fitted with two Lorentz functions of same area and width. The low-Q data is used where phonon scattering is weak and the $La_2Zr_2O_7$ data is used to identify phonons and to provide the non-magnetic background that is subtracted from the data. The CEF parameters in Ref. [128] are used as the starting parameters for the least-square fitting but scaled overall to match the calculated energy levels with the measured ones. The case where the two overlapping levels are exchanged is also tested.

For the best fit, the CEF parameters are $B_0^2 = 49.2$, $B_0^4 = 408.9$, $B_3^4 = 121.6$, $B_0^6 = 148.1$, $B_3^6 = -98.0$, and $B_6^6 = 139.1$ meV yielding a standard normalized goodness-of-fit parameter $\chi^2 = 0.34$. The fitting details are shown in Table 5.1 and the fitted spectrum is shown in Fig. 5.3. As listed in Table 5.1 these CEF parameters correspond to five doublets at 0, 23.4, 34.4, 35.8 and 106.3 meV. In order to compare with other related reports, these parameters are converted into the Stevens formalism by using the relation

$$D_k^q = \theta_k \lambda_k^q B_k^q \,.$$

The θ_k are reduced matrix elements listed in Ref. [4] which for Nd^{3+} are $\theta_2 = -7/1089$, $\theta_4 = -136/467181$ and $\theta_6 = -1615/42513471$. The λ_k^q are listed in Ref. [2] which are

$\lambda_2^0 = 1/2$, $\lambda_4^0 = 1/8$, $\lambda_4^3 = \sqrt{35}/2$, $\lambda_6^0 = 1/16$, $\lambda_6^3 = \sqrt{105}/8$, and $\lambda_6^6 = \sqrt{231}/16$. After the transformation, we get $D_0^2 = -0.158$, $D_0^4 = -0.0149$, $D_3^4 = 0.105$, $D_0^6 = -0.00035$, $D_3^6 = -0.0048$, and $D_6^6 = -0.005$ meV. These CEF parameters are comparable with those obtained for $Nd_2Zr_2O_7$ from the CEF analysis of susceptibility data in Ref. [128]. However the results here differ significantly with those in Ref. [129], where only excitations below 70 meV were measured using a triple axis spectrometer and were analysed within the ground state multiplet using Stevens' operator equivalents. The analysis is also consistent with that of $Pr_2Sn_2O_7$ [159].

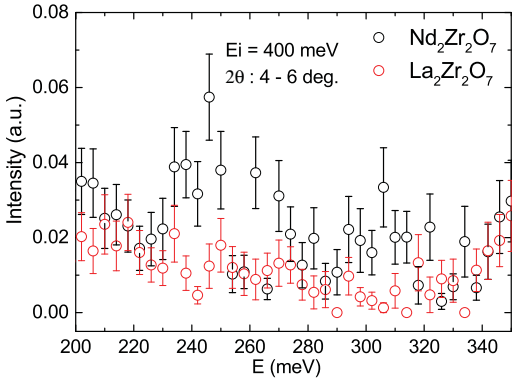

Figure 5.5: Crystal field scattering of the first excited multiplet $^4I_{11/2}$ shown in the data with $E_i = 400$ meV at 5 K. The data is integrated within the 2θ range 4-6 degree.

The refined CEF energy scheme of the GS multiplet $^4I_{9/2}$ is shown in Fig. 5.4 together with the calculated scheme for the first excited multiplet $^4I_{11/2}$ which also matches the experimental INS data well (Fig. 5.5). The wavefunctions of the GS doublet and the first excited doublets within the GS multiplet $^4I_{9/2}$ are found to be

$$\Gamma_{56}^+ = 0.899|^4I_{9/2}, \pm 9/2\rangle \mp 0.252|^4I_{9/2}, \pm 3/2\rangle + 0.330|^4I_{9/2}, \mp 3/2\rangle \mp 0.112|^4I_{11/2}, \pm 9/2\rangle \quad (5.2a)$$

and

$$\Gamma_4^+ = 0.149|^4I_{9/2}, \pm 7/2\rangle + 0.743|^4I_{9/2}, \mp 5/2\rangle \mp 0.643|^4I_{9/2}, \pm 1/2\rangle \pm 0.056|^4I_{11/2}, \pm 7/2\rangle. \quad (5.2b)$$

As shown by Eq. (5.2a), there is a large mixing of $|^4I_{9/2}, \pm 9/2\rangle$ with $|^4I_{9/2}, m_J \neq \pm 9/2\rangle$

terms in the ground state as well as a small mixing with $^4I_{11/2}$ leading to reduction in the moment of Nd^{3+}. The ground state moment calculated from Eq. (5.2a) is $2.65\,\mu_B$ with $g_{zz} \approx 5.30$ and $g_\perp = 0$ in the pseudospin-1/2 model indicating an Ising anisotropy. Moreover the Ising anisotropy can be regarded as very strong when considering the large first excitation energy 23.4 meV. These values agree well with the magnetic data in Chapter 4. However here the g_{zz} is different from the value of 4.793 in Ref. [128] and the value of 4.3 in Ref. [129]. The difference in g_{zz} probably results from the different sets of CEF parameters obtained in Refs. [128, 129]. Since the higher energy excitations have been measured, it is believed that CEF parameters here are more accurate. Furthermore, the ground state is exactly a diploar-octupolar doublet which transforms as Γ_{56}^+ expected when $D_0^2 < 0$ [17].

5.2.3 Crystal field susceptibility and heat capacity

Based on the CEF parameters, eigenvalues and eigenfunctions, the magnetic susceptibility can be calculated with Eq. 2.13. Fig. 5.6 shows the comparison of the susceptibilities measured and calculated by SPECTRE. The good agreement between them supports the validity of the analysis of the INS data and the extracted CEF parameters.

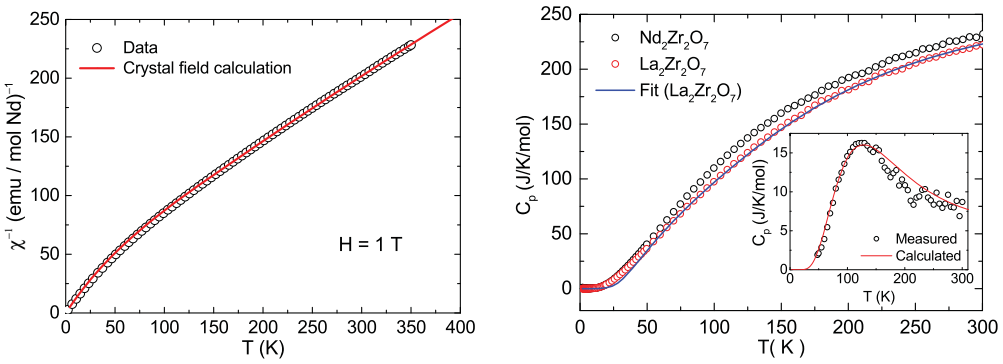

Figure 5.6: Left: inverse magnetic susceptibility χ^{-1} versus temperature T of powder $Nd_2Zr_2O_7$ measured in a field of 1 T. The solid curve is the crystal field susceptibility corresponding to the crystal field parameters obtained from the analysis of INS data. Right: specific heat of $Nd_2Zr_2O_7$ and $La_2Zr_2O_7$ (open circles) and the Debye+Einstein model fit for $La_2Zr_2O_7$ (solid line). Inset: crystal field heat capacity of $Nd_2Zr_2O_7$ (open circles) obtained by subtraction the corrected fitted C_p of the nonmagnetic $La_2Zr_2O_7$, and the calculated CEF specific heat (solid line) according to the CEF level scheme deduced from the inelastic neutron scattering data.

In order to further verify the crystal field model obtained from the INS data, the crystal field specific heat $C_{\mathrm{CEF}}$was calculated with Eq. 2.16 based the obtained CEF level scheme and compared with the measurement as shown Fig. 5.6. The crystal field part in the measured C_{p} data of $Nd_2Zr_2O_7$ is extracted by subtracting the C_{p} of $La_2Zr_2O_7$ which has only the lattice contribution (the data of $La_2Zr_2O_7$ is first fitted to the Debye+Einstein model for smoothing purpose) [162]. Due to the slightly different formula masses and unit cell volumes, a correction is done to the $La_2Zr_2O_7$ data according to [163]

$$\frac{T^{\star}}{T} = \left(\frac{M_B}{M_A}\right)^{1/2} \left(\frac{V_B}{V_A}\right)^{1/3} \approx 1.02, \tag{5.3}$$

where $T^{\star}$ is the corrected temperature and M_α and V_α are the mole masses and unit cell volumes of $La_2Zr_2O_7$ ($\alpha = A$) and $Nd_2Zr_2O_7$ ($\alpha = B$). As shown in Fig. 5.6, the background-subtracted data shows a broad Schottky-type anomaly which is well accounted by the crystal field model.

5.3 Neutron diffraction: "all-in-all-out" magnetic structure

5.3.1 Experiment details

The neutron powder diffraction measurement is performed on the Cold Neutron Powder Diffractometer (DMC) at PSI. The $Nd_2Zr_2O_7$ sample (∼10 g) is sealed in a cylindrical copper can of 10 mm in diameter and then high pressure ^{4}He gas is filled for better thermalization. The sample is mounted onto a dilution refrigerator which could cool down to 0.1 K. First, neutrons of long wavelength ($\lambda = 3.80$ Å) are used with a 5°–90° 2θ range to achieve good resolution in the low-Q region for the determination of the propagation vector $\boldsymbol{k}$ of the magnetic structure. Then, shorter wavelength neutrons (2.46 Å) are used in combination with a 2θ range 10°–90° to access a larger Q range for the magnetic structure refinement. Diffraction patterns at several temperatures between 0.1 K and 4 K are measured with a counting time of ∼ 6 hours for 0.1 and 4 K and ∼ 2 hours for the other 15 temperatures. The patterns are refined using the FullProf Suite [21].

5.3.2 Analyses and results

Neutron diffraction (ND) patterns collected at 0.1 K and 4.0 K using neutrons of wavelength 2.45 Å are shown in Fig. 5.7(a). The inset of Fig. 5.7(a) clearly shows that there are additional intensities for 0.1 K, in particular on top of the nuclear Bragg peaks (220)

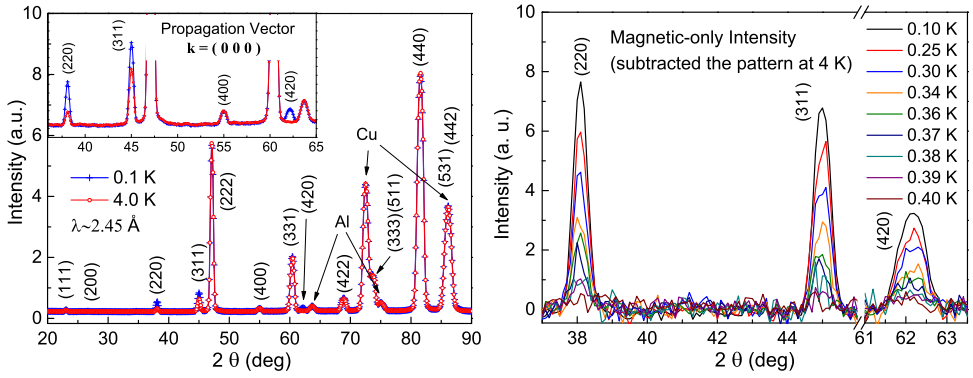

(a) (b)

Figure 5.7: (a) Comparison of the neutron diffraction patterns of $Nd_2Zr_2O_7$ collected at 0.1 K (blue) and 4.0 K (red). The peaks are marked with the $(hk\ell)$ Miller indices. The Cu and Al peaks come from the sample holder and sample environment. (b) Temperature dependence of the intensities of the magnetic Bragg peaks (220), (311) and (420) obtained by subtracting the 4.0 K neutron diffraction pattern from the neutron diffraction patterns at the indicated temperatures.

and (311) which indicates long-range magnetic order. Further, a new peak (420) can be seen where the nuclear Bragg reflection is forbidden, which further confirms the magnetic origin of the additional intensities. The magnetic intensity decreases continuously with increasing temperature (indicating a second order phase transition) and vanishes at 0.4 K [Fig. 5.7(b)], allowing to define the transition temperature as $T_N \approx 0.4$ K consistent with the reported heat capacity data [70, 147] and the ND data in Ref. [129]. No extra peaks were observed at low Q in the ND pattern collected with neutrons of wavelength 3.80 Å (not shown).

The difference pattern obtained by subtracting the 4.0 K ND data from the 0.1 K data is shown in Fig. 5.8 which clearly shows the magnetic Bragg peaks associated with the ordering of Nd^{3+} moments. All the magnetic Bragg peaks can be indexed with the magnetic propagation vector $\boldsymbol{k} = (0\,0\,0)$, which is consistent with Ref. [129]. The wavevector $\boldsymbol{k} = (0\,0\,0)$ also indexes all the magnetic Bragg peaks in AIAO antiferromagnets $Nd_2Sn_2O_7$ [131] and $Nd_2Hf_2O_7$ [130] suggesting a similar magnetic structure for $Nd_2Zr_2O_7$. The representation analysis performed using the program BASIREPS in the FullProf Suite package shows that the magnetic representation of Nd ($16d$ site) can be reduced into four irreducible representations (IRs) of the little group of wavevector

$\boldsymbol{k} = (0\,0\,0)$:

$$\Gamma_{\mathrm{mag\,Nd}} = 1\,\Gamma_3^1 + 1\,\Gamma_6^2 + 1\,\Gamma_8^3 + 2\,\Gamma_{10}^3. \tag{5.4}$$

In the equation above, each IR is multiplied by the number of times it occurs, the superscript of Γ corresponds to the dimensionality of the IR, and the subscript to the order of the IR. All possible magnetic structures can be obtained from the combinations of the basis vectors of the IRs shown in Table 5.2. The base vectors indicates that: Γ_3^1 corresponds to the antiferromagnetic AIAO structure which was first observed in FeF_3; Γ_6^2 describes a structure in which all the spins lie in the local $\langle 111 \rangle$ plane as observed in the XY pyrochlore $Er_2Ti_2O_7$ [25, 33]; Γ_8^3 corresponds to the Palmer-Chalker phase expected for the Heisenberg pyrochlore antiferromagnet with dipolar interactions [92]; the two fold Γ_{10}^3 corresponds to the "two-in-two-out" spin ice manifold.

Table 5.2: Nonzero irreducible representations (IRs) and associated basis vectors ψ_ν for Nd($16d$) site in space group $Fd\bar{3}m$ with propagation vector $\boldsymbol{k}$ = (0, 0, 0). The atoms of the nonprimitive basis are defined according to Nd1: (0.50, 0.50, 0.50); Nd2: (0.25, −0.25, 1.00); Nd3: (−0.25, 1.00, 0.25); Nd4: (1.00, 0.25, −0.25). The real (R) and imaginary (I) part of the complex basis vector are given separately.

IRs	ψ_ν	R/I	Nd1	Nd2	Nd3	Nd4
Γ_3^1	ψ_1	R	(1 1 1)	(−1 −1 1)	(−1 1 −1)	(1 −1 −1)
Γ_6^2	ψ_1	R	(1 −0.5 −0.5)	(−1 0.5 −0.5)	(−1 −0.5 0.5)	(1 0.5 0.5)
		I	(0 −0.87 0.87)	(0 0.87 0.87)	(0 −0.87 −0.87)	(0 0.87 −0.87)
	ψ_2	R	(−0.5 1 −0.5)	(0.5 −1 −0.5)	(0.5 1 0.5)	(−0.5 −1 0.5)
		I	(0.87 0 −0.87)	(−0.87 0 −0.87)	(−0.87 0 0.87)	(0.87 0 0.87)
Γ_8^3	ψ_1	R	(1 −1 0)	(−1 1 0)	(1 1 0)	(−1 −1 0)
	ψ_2	R	(0 1 −1)	(0 1 1)	(0 −1 −1)	(0 −1 1)
	ψ_3	R	(−1 0 1)	(−1 0 −1)	(1 0 -1)	(1 0 1)
Γ_{10}^3	ψ_1	R	(1 1 0)	(−1 −1 0)	(1 −1 0)	(−1 1 0)
	ψ_2	R	(0 0 1)	(0 0 1)	(0 0 1)	(0 0 1)
	ψ_3	R	(0 1 1)	(0 1 −1)	(0 −1 1)	(0 −1 −1)
	ψ_4	R	(1 0 0)	(1 0 0)	(1 0 0)	(1 0 0)
	ψ_5	R	(1 0 1)	(1 0 −1)	(−1 0 −1)	(−1 0 1)
	ψ_6	R	(0 1 0)	(0 1 0)	(0 1 0)	(0 1 0)

The magnetic-only diffraction pattern is refined with all possible magnetic structure models defined by the IRs and a analytical analysis on the structure factor was done for excluding some possibilities in Ref. [164]. The crystallographic parameters are fixed to the ones determined in the synchrotron-XRD refinement and the scale factor is fixed by the refinement of nuclear pattern at 4.0 K. The best fit ($\chi^2 = 1.6$) is obtained for the

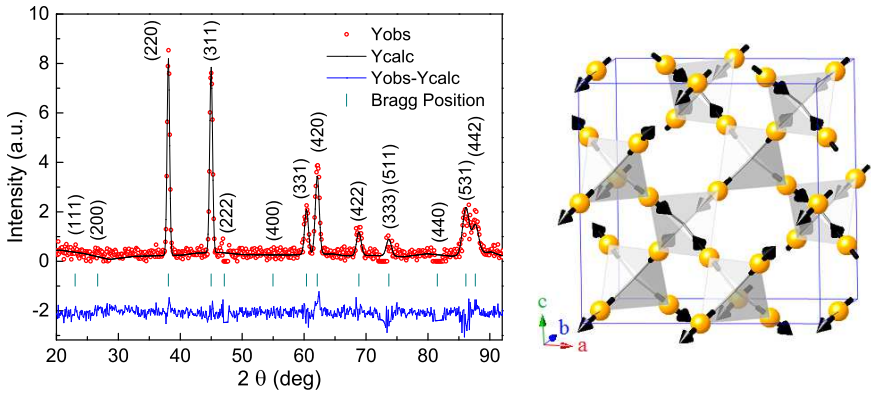

Figure 5.8: Left: magnetic diffraction pattern (red circles) at 0.1 K (obtained from subtracting the 4.0 K pattern from the 0.1 K pattern) together with the calculated magnetic refinement pattern (black line) for an "all-in/all-out" magnetic structure. The difference between the experimental and calculated intensities is shown by the blue curve at the bottom. The green vertical bars show the magnetic Bragg peak positions. The peaks are marked with the $(hk\ell)$ Miller indices. Right: the "all-in/all-out" magnetic structure which is comprised of corner-sharing tetrahedra with magnetic moments pointing alternatively inwards (all-in) or outwards (all-out) the centers of the successive tetrahedra (along the local $\langle 111 \rangle$ direction). The spheres represent Nd atoms and arrows denote the ordered moment directions.

Γ_3^1 corresponding to the "all-in/all-out" (AIAO) magnetic structure shown in Fig. 5.8. All the other models produce very strong intensity for the (111) and/or (200) magnetic Bragg peaks where no intensity is found experimentally, which conclusively excludes them as possible magnetic structures. The refinement of the magnetic-only pattern at 0.1 K for the Γ_3^1 model is shown in Fig. 5.8. The ordered moment obtained from the refinement of ND data is $m = 1.26(2)\,\mu_B$/Nd at 0.1 K. The temperature dependence of the ordered moment is shown in Fig. 5.9 and it is fitted to $m = m_0(1 - T/T_N)^\beta$ giving $T_N = 0.39(2)$ K and $\alpha = 0.37(5)$ which within the error bar is close to the expected critical exponent 0.33 for a three dimensional Ising system. The same magnetic structure was found by Lhotel *et al.* [129] who also found a similar $T_N = 0.41$ K for the powder sample but a much smaller ordered moment of $0.80(5)\,\mu_B$/Nd at 0.15 K. The difference is believed to be related to the synthesis procedure and the quality of the sample. The ordered moments in the AIAO antiferromagnets $Nd_2Sn_2O_7$ ($T_N \approx 0.91$ K) and $Nd_2Hf_2O_7$ ($T_N = 0.55$ K) are found to be $1.708(3)\,\mu_B$/Nd at 0.06 K and $0.62(1)\,\mu_B$/Nd at 0.1 K, respectively [130, 131]. A recent theoretical publication points out that most of the

reduction of the ordered moment of these Nd compounds comes from the pseudospin rotation away from the local [111] axis due to the Dzyaloshinsky-Moriya interaction (the J_{xz} term in the spin Hamiltonian) (see Chapter 6 and Ref. [152]). However, the strong reduction in ordered moments could also reflect the strong quantum fluctuations in the ordered state. Persistent spin dynamics have been observed in the AIAO state of $Nd_2Sn_2O_7$ from the muon spin relaxation (μSR) study [131]. In Chapter 7 the μSR result of $Nd_2Zr_2O_7$ also reveals persistent fluctuations in the ground state.

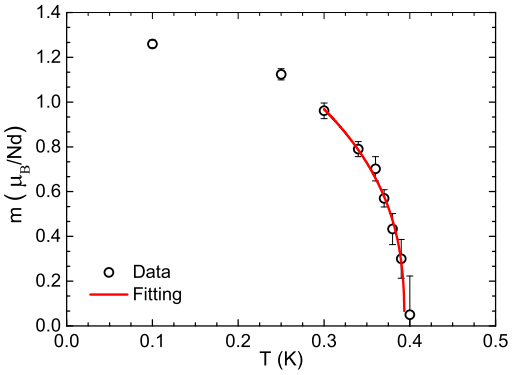

Figure 5.9: Temperature dependence of the ordered Nd^{3+} moment $m(T)$ obtained from the refinement of neutron powder diffraction patterns at different temperatures. The solid curve shows the fitting in $0.3\,\mathrm{K} \leq T \leq T_\mathrm{N}$ by $m = m_0(1 - T/T_\mathrm{N})^\beta$.

Having determined the T_N and magnetic structure of $Nd_2Zr_2O_7$, the effective nearest-neighbor dipolar interaction D_nn and exchange interaction J_nn can be estimated to compare with the dipolar spin ice phase diagram [52, 53] though significant transverse terms appear for $Nd_2Zr_2O_7$ in the spin Hamiltonian (see Chapter 6). The D_nn can be simply estimated by using the equation [25]

$$D_\mathrm{nn} = \frac{5}{3}\left(\frac{\mu_0}{4\pi}\right)\frac{m_\mathrm{Nd}^2}{r_\mathrm{nn}^3}. \tag{5.5}$$

From the distance $r_\mathrm{nn} = (a/4)\sqrt{2} = 3.77$ Å between the nearest neighboring Nd^{3+} ions and the ground state moment $m_\mathrm{Nd} = 2.65\,\mu_\mathrm{B}$ (from the CEF analysis of the inelastic neutron scatting data, see Sec. 5.2), the dipole interaction is calculated to be $D_\mathrm{nn} \approx 0.14$ K and thus $T_\mathrm{N}/D_\mathrm{nn} = 2.86$. According to the dipolar spin ice phase diagram shown in Fig. 2.11 [53], this value of $T_\mathrm{N}/D_\mathrm{nn}$ can place $Nd_2Zr_2O_7$ inside the AIAO AFM ordered phase with magnetic ordering wavevector $\boldsymbol{k} = (0\,0\,0)$ as has been found experimentally. Furthermore, the phase diagram suggests that for this value of $T_\mathrm{N}/D_\mathrm{nn}$, the ratio

$J_{\rm nn}/D_{\rm nn}$ is -1.45 giving the effective nearest neighbour exchange constant $J_{\rm nn} \approx -0.20$ K and thus the total interaction $J_{\rm eff} = J_{\rm nn} + D_{\rm nn} \approx -0.06$ K which is antiferromagnetic in contrast to the effective ferromagnetic interaction inferred from the Curie-Weiss temperature $\theta_{\rm p}$. It can also be seen that $J_{\rm nn}$ is significantly stronger than $D_{\rm nn}$ which contrasts with the observation in spin-ice materials where the dipolar interaction is the stronger one. As such $Nd_2Zr_2O_7$ is not expected to show the frustration prevalent in spin-ice materials, but rather should result in a stable long-range ordered ground state. The discussion above is restricted to the Ising model which is not exactly true for $Nd_2Zr_2O_7$ where significant transverse terms in the Hamiltonian are found in the study of the spin dynamics using inelastic neutron scattering as shown in Chapter 6.

5.4 Conclusions

In this chapter, the magnetic single-ion and collective states of $Nd_2Zr_2O_7$ are investigated using inelastic and elastic neutron scattering, respectively. The crystal field parameters and states have been determined by analysing the INS data with the tensor operator crystal field Hamiltonian. The $J-$mixing effect is included which gives a better model for the crystal field interaction. The single ion ground state is found to be a well-isolated Kramers doublet mainly composed of the $|^4I_{9/2}, \pm 9/2\rangle$ and $|^4I_{9/2}, \pm 3/2\rangle$ terms which is a dipolar-octupolar doublet as suggested by theory [17]. The ground state has Ising anisotropy and the moment of the ground state is determined to be $\sim 2.65\,\mu_{\rm B}$/Nd giving $g_{zz} = 5.30(6)$ and $g_{\perp} = 0$ for the effective spin-1/2 model, which are consistent with magnetization data in Chapter 4. The crystal field interaction was previously analysed with the susceptibility and magnetization data in Ref. [128] and with limited inelastic neutron scattering data in Ref. [129]. Those results are generally consistent with the results presented here but with smaller g factors (4.8 in Ref. [128] and 4.5 in Ref. [129]) which are not consistent with the susceptibility and magnetization data. Therefore, the data and analysis here gives a more complete and accurate result.

The neutron diffraction data reveals that the ground state of $Nd_2Zr_2O_7$ is the "all-in/all-out" long-range order with a transition temperature $T_{\rm N} \approx 0.4$ K and an ordered moment $1.26(2)\,\mu_{\rm B}$/Nd at 0.1 K, which agrees with Ref. [129]. This order is presented in the phase diagram of the dipolar-octupolar pyrochlore (Fig. 2.14) [17]. The ordered moment is strongly reduced compared with the moment of the crystal field ground state of the Nd^{3+} ion. The reduction of the ordered moment was first ascribed to the potential fluctuations in the system which also was proposed to be the reason for the high susceptibility of the AFM ordered state in low fields [129]. However, the spin Hamiltonian

determined in Chapter. 6 indicates that the reduction of the ordered moment is caused by the pseudospin rotation which reduces the $\langle \sigma^z \rangle$ and the non-Ising interaction between the spins is responsible for the high susceptibility in low fields of the ordered state.
The sibling compounds $Nd_2Hf_2O_7$ and $Nd_2Sn_2O_7$ are expected to have similar crystal field states [131]. The INS data for $Nd_2Sn_2O_7$ in a PhD thesis [164] shows very similar CEF transitions. Very recently, Anand *et al.* reported the inelastic neutron scattering study on the crystal field of $Nd_2Hf_2O_7$ where very similar single ion state of Nd^{3+} was found and the CEF parameters are also very close to these of $Nd_2Zr_2O_7$ as a result of the similar crystal structures of the two compounds [165]. $Nd_2Hf_2O_7$ and $Nd_2Sn_2O_7$ also have the "all-in/all-out" long-range order as the ground state [130, 131]. For the search of the quantum spin ice, altering the exchange interaction by applying a high pressure is a possible future project.

6 Spin dynamics of $Nd_2Zr_2O_7$ probed by inelastic neutron scattering

6.1 Introduction

The spin Hamiltonian determines most of the magnetic properties of materials, such as their susceptibility, magnetic specific heat, phase diagram and so on. The measurement and analysis of the spin dynamics is a effective way to determine the spin Hamiltonian. In this chapter, the spin dynamics of $Nd_2Zr_2O_7$ both above and below the transition temperature were studied by the single crystal inelastic neutron scattering (INS) method where the spin dynamics in the E-Q space are measured. In the ordered phase, spin waves were observed and analysed using linear spin wave theory and the nearest-neighbor spin Hamiltonian was determined. The Hamiltonian was used for analysing the data measured above T_N, which reveals that the system may behave like the long-sought quantum spin ice phase above T_N. Further measurements using polarized and unpolarized neutron diffraction under an external magnetic field support the validity of the spin Hamiltonian determined. The neutron diffraction data in a magnetic field applied along the [1-10] crystallographic direction reveal that the field destroys the long-range antiferrmagnetic order and induces ferromagnetic short-range disorder in the system. Finally, the spin Hamiltonian was applied to the magnetization calculation based on the mean field approximation which qualitatively agrees with the experimental data.
During the analysis of the data, two experimental papers were published by other groups which contain some similar data and analyses [129, 155] and one theoretical paper appeared which gives another explanation of the data [152]. In Ref. [129], the data of crystal field neutron inelastic scattering, magnetic neutron diffraction and single crystal DC magnetization (at temperatures down to 90 mK) of $Nd_2Zr_2O_7$ are presented. As mentioned before, the crystal field states and the magnetic order obtained in Ref. [129] are consistent with the results in Chapter 5 but are not as accurate due to problems in the data quality and the limitations of the analysis method. The DC magnetization indicates field-induced transitions (from the AIAO order to FM states) from which a

field-temperature phase diagram is extracted and analysed with the mean-field dipolar-octupolar Hamiltonian containing the J_{yy} and J_{zz} terms. However, the theoretical simulations do not reproduce the magnetization curves well, particularly the high susceptibility observed at low fields and large fluctuations in the system are proposed as its reason. In Ref. [155] by S. Petit *et al.*, cold neutron inelastic scattering and polarized neutron diffraction data of a single crystal $Nd_2Zr_2O_7$ sample are presented where the coexistence of a gapped pinch point pattern and the AIAO Bragg peaks is observed and explained based on the moment fragmentation theory [166] assuming a monopole crystal state of $Nd_2Zr_2O_7$. The excitations are reproduced qualitatively by a similar Hamiltonian as used in Ref. [129] for the magnetization analysis with the random phase approximation (RPA) and assuming an octupole order in $Nd_2Zr_2O_7$. Obviously, these explanations are not compatible with each other which makes it difficult to understand the ground state of $Nd_2Zr_2O_7$ (magnetic AIAO order, monopole crystal or octupolar order). In Ref. [152], Owen Benton gives a comprehensive explanation based on linear spin wave theory with the complete dipolar-octupolar Hamiltonian including the J_{xx}, J_{yy}, and J_{zz} and J_{xz} terms and further suggests that $Nd_2Zr_2O_7$ is proximate to a quantum spin ice phase and above T_N it may show features of this quantum spin ice phase (his recent spinon calculation is compared with the data collected above T_N in this chapter). The analyses of the neutron scattering and AC susceptibility data in this Chapter is based on the Hamiltonian proposed by Owen Benton. A good agreement between the simulations and the data confirms the validity of this Hamiltonian for $Nd_2Zr_2O_7$.

In addition, the magnetic properties of powder $Nd_2Hf_2O_7$ and $Nd_2Sn_2O_7$ were also reported recently which are quite similar to those of $Nd_2Zr_2O_7$ and more importantly, both compounds also show the AIAO order below 0.55 K and 0.91 K, respectively [130, 131]. The determination of the spin Hamiltonian for $Nd_2Zr_2O_7$ could give clues to understand the physics in $Nd_2Hf_2O_7$ and $Nd_2Sn_2O_7$. The compounds $Nd_2Ir_2O_7$ and $Nd_2Mo_2O_7$ with magnetic B^{4+} ($B =$ Ir, Mo) ions were studied at an earlier time focusing on the electric properties (the metal-insulator transition and the anomalous Hall effect) [132–134]. The magnetism in these two compounds is dominated by the B^{4+}-B^{4+} and B^{4+}-Nd^{3+} interactions which result in the AIAO and non-collinear ferromagnetic ordering at 15 K and 95 K, respectively [134–136]. The low-temperature magnetization of $Nd_2Ir_2O_7$ is mostly determined by the Nd^{3+} sublattice which is similar to $Nd_2Zr_2O_7$. The magnetization of $Nd_2Ir_2O_7$ is analysed based on the dipolar-octupolar Hamiltonian with the additional Ir^{4+}-Nd^{3+} exchange interaction treated as a staggered Zeeman field (owning to the ordering of the Ir^{4+} moments) in Ref. [132]. The analysis yields a ferromagnetic J_{zz} in contrast to the antiferrmagnetic one for $Nd_2Zr_2O_7$.

6.2 Experiment details

$Nd_2Zr_2O_7$ single crystals were grown by using the optic floating zone furnace and characterized by X-ray powder and Laue diffraction in Chapter 4. The crystals are cylindrical with a diameter ~ 5 mm. There are two crystals grown: crystal A is ~ 25 mm long and ~ 2.5 g weight; crystal B is ~ 30 mm long and ~ 3.0 g weight. The crystals were aligned with the (HHL) reciprocal plane (containing the three main cubic directions: [100], [110], [111]) in the horizontal scattering plane by tilting the cylindrical crystal axis by about 35° away from the vertical. For better thermalization, the sample was first wrapped in annealed thin oxygen-free copper foil and then bound to a copper frame using cooper wires with the other end of the foil attached to the cold finger of the refrigerator when mounting the sample on the instrument. Fig. 6.1 shows the typical sample holder used for neutron scattering experiments in this thesis.

Figure 6.1: Typical sample holder used for neutron scattering experiments.

The single crystal inelastic neutron scattering experiment was performed on the Cold Neutron Chopper Spectrometer (CNCS) at SNS in Oak Ridge National Lab which is a high-flux high-resolution time-of-flight direct geometry spectrometer. The sample (crystal A) was mounted on a ^{3}He insert for cooling. Neutrons of incident wavelength 4.98 Å (3.315 meV) were used in the high-resolution mode of the instrument (energy resolution $\delta E \sim 0.1$ meV). Data were collected at three temperatures: 240 mK (below T_N), 450 mK (above T_N) and 20 K (background reference). The temperature was monitored also by measuring the magnetic Bragg peak (220) to ensure the sample temperature is lower or higher than T_N. During the measurement, the sample was rotated for 360° with a step size of 2° for first the even and then the odd angle values, respectively and at every step neutrons were counted for 4 minutes for 240 mK and 450 mK and 3 minutes

for 20 K. Due to the limited time (4 days) of the experiment, the scan for the odd-value angles were not finished: 9%, 53%, and 22% were missing for the three temperatures, respectively. Finally, the data were normalized to the monitor and the data at 20 K was simply subtracted as a background from the data at the two low temperature for the same angle region scanned. At 20 K (which is much higher than the energy scale of the exchange interactions), $Nd_2Zr_2O_7$ is essentially a paramagnet whose magnetic scattering is featureless as a function of wave vector. Therefore, the 20 K measurement gives a good approximation to the non-magnetic background. The software Dave [167] and the Matlab package Horace [168] were used for data subtraction and visualization. The open source Matlab package SpinW [22] was used for the spin wave and magnetization calculations (new codes were implemented for the mean field approximation). The spin wave calculation gave the same results as that described in Ref. [152] by Dr. Owen Benton who shared his Mathematica code afterwards. The spinon calculation which is applicable above T_N was done and compared to the data by Dr Owen Benton.

The polarized neutron diffuse scattering with Z-polarization analysis was performed on DNS at FRM2, Munich. The sample (crystal B) was mounted on a copper frame attached to a gonimeter and then fixed on a dilution stick. Because the height of the dilution is not adjustable, the sample centre was slightly lower than the focus of the incident neutron beam. Due to the large size of the gonimeter and the low cooling powder, around two day were spent for cooling to base temperature. During cooling or warming, the X-polarization analysis was used to measured the intensity of the magnetic (220) peak to ensure the sample temperature is below or above the ordering temperature. Data at three temperatures were collected [250 mK, 450 mK and 23 K (background reference)]. The incident wavelength used was 3.3 Å. During the measurement, the sample was rotated for 160° with a step size of 1° for two detector positions. Several scans were done for the measurements at the three temperatures and the total counting times per step are 150 s, 360 s and 480 s for 250 mK, 450 mK and 23 K, respectively. The software Dnsplot was used for the data subtraction and visualization [169].

The unpolarized neutron diffuse scattering experiment with applied magnetic field along the [1-10] direction was performed for crystal A on the E2 diffractometer at HZB. The incident neutron wavelength was 2.38 Å (PG002) but very weak $\lambda/2$, $\lambda/3$ signals were also observed. The magnet VM-4 provided a vertical field perpendicular to the scattering plane up to 4 T and the dilution refrigerator was used to cool the sample down to 50 mK. Due to the shielding from the magnet, only the 2θ angle range of $7-72°$ in the horizontal scattering plane is accessible. During the measurement, the sample was rotated for 30, 90 or 180° with the step size 0.25° for two detector positions in fields of 0, 0.25, 0.5,

0.75, 1.0, 1.25, 1.5, 1.75 and 2.0 T. The monitor count was 90000 ($\sim$ 26 s) for every step. The scans with the 30° angle range cover the reciprocal space region where the most pronounced feature appears.
The AC susceptibility data shown in Chapter 4 were measured by L. Opherden, J. Hornung, T. Herrmannsdörfer and J. Wosnitza at the Hemholtz Zentrum Dresden Rossendorf, Germany and the experimental details are described in Ref. [156].

6.3 Spin wave excitations below T_N

6.3.1 Spin wave excitations

Figure 6.2 shows colour-coded intensity maps of constant energy slices through the INS data in the (HHL) reciprocal plane at 240 mK in the ordered phase (after background subtraction). A highly structured pattern is observed with the symmetry of the scattering plane which evolves with increasing energy transfer: from a pinch point pattern at low energy to a pattern with intensity at the "all-in-all-out" (AIAO) Bragg peak positions at high energy. The excitations are below 0.5 meV which can also be seen clearly in the one-dimensional intensity vs energy cut in Fig. 6.3 where the scattering at different temperatures are compared showing that at 0.5 meV they have the same intensity. The intensity is the strongest at around 0.07 meV where a pinch point pattern is observed and below that energy the pinch point pattern remains unchanged but becomes weaker and weaker in intensity. This indicates that the pinch point pattern arises from a gapped mode. Such gapped excitations were also observed the high-resolution data in Ref. [155]. Above the energy of the pinch point mode, there are some other modes with dispersions starting from the arms of the pinch point pattern and ending at the AIAO Bragg peak positions at $\sim$ 0.30 meV. Above T_N at 450 mK, the gap to the pinch point pattern reduces considerably and the spin wave scattering intensity at high energy becomes very weak due to the loss of the long-range order as shown in Fig. 6.3 at $Q = (220)$ and Fig. 6.4.

6.3.2 Spin Hamiltonian and spin wave calculations

The general form of the spin Hamiltonian for the pyrochlores with a dipole-octupole doublet was first proposed by Huang *et al.* based on a symmetry analysis [17]. Because the crystal field ground state of Nd^{3+} in $Nd_2Zr_2O_7$ is a well-isolated Kramers doublet, it can be treated as a pseudospin-1/2 (σ) system at low temperatures. The wave functions of the ground state doublet are composed of $|\pm 9/2\rangle$ and $|\pm 3/2\rangle$ terms, and under the symmetry operations of the local symmetry group D_{3d}, both the σ_x and σ_z components of the

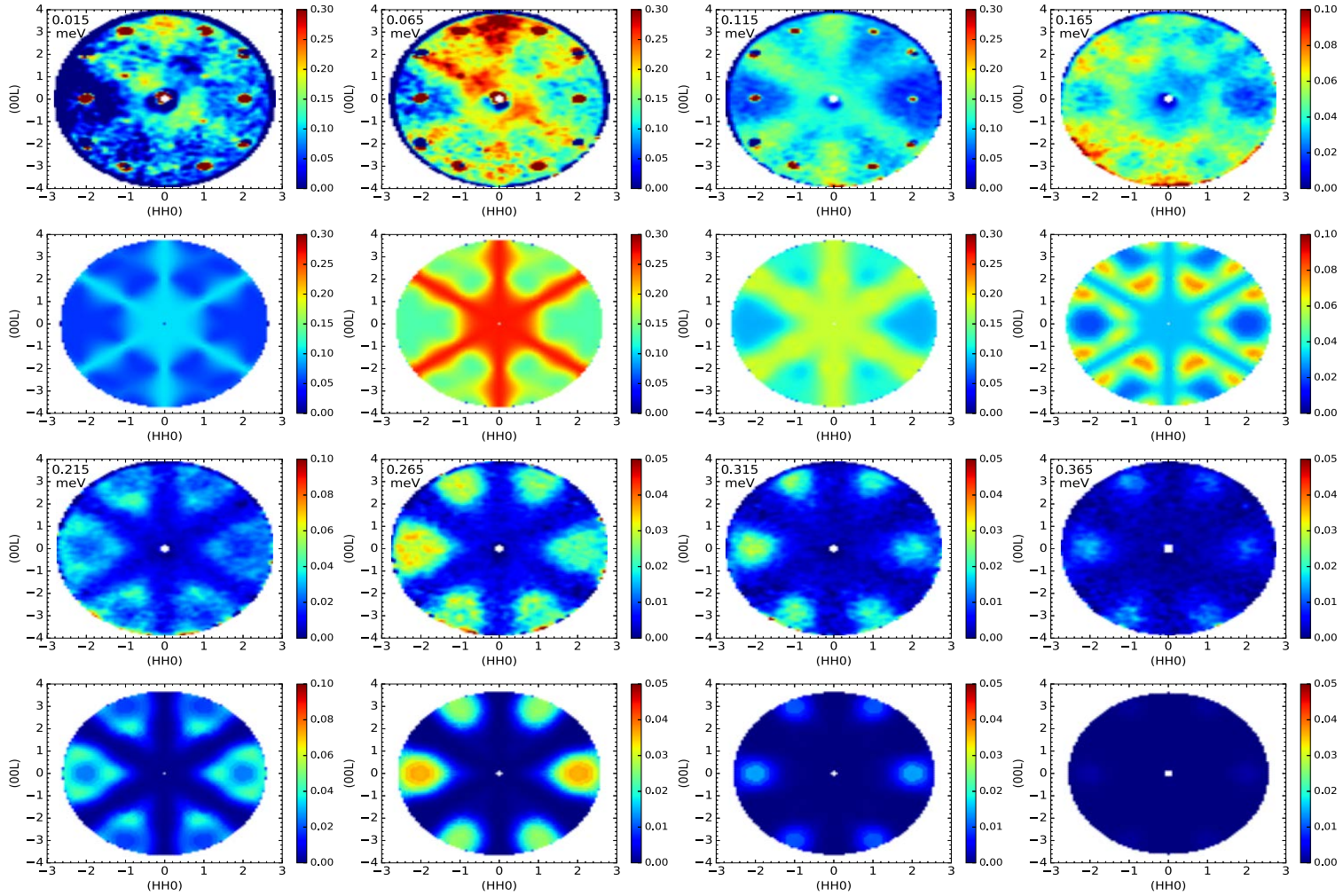

Figure 6.2: (first and third rows) Background subtracted inelastic neutron scattering spectra (in arb. units) measured at 240 mK at the different constant energies indicated. (second and fourth rows) Corresponding spin wave calculation based on the dipolar-octupolar pseudospin-1/2 model. The calculation is convolved with the instrumental resolution of 0.1 meV and normalized to the data by an overall factor for a better comparison.

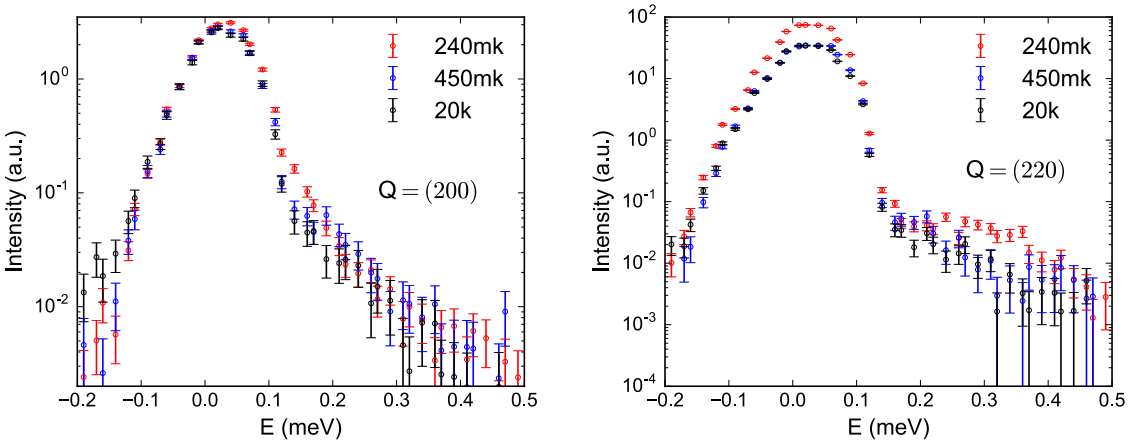

Figure 6.3: Energy dependence of the inelastic neutron scattering intensity at different temperatures at (left) $Q = (200)$ (a pinch point position) and (right) $Q = (220)$ (a Bragg peak position of the AIAO magnetic order). The higher elastic intensity for $Q = (220)$ at 240 mK is due to the magnetic Bragg peak of the AIAO order.

pseudospin transform like the z component of a magnetic dipole moment, while σ_y transforms like a component of the magnetic octupolar tensor ($\sim i(J^+J^+J^+ - J^-J^-J^-)$). As a result, the bilinear coupling of σ_x and σ_z is allowed. In addition, the two states of the doublet do not mix under C_3 rotation, which removes the relative phase factors between the six bonds on the tetrahedron in the general Hamiltonian for the dipolar or dipolar-quadruolar doublet (Eq. 2.28). Finally, the symmetry (time reversal $\otimes$ lattice symmetries) constrained nearest-neighbor spin Hamiltonian for $Nd_2Zr_2O_7$ is [17]

$$\mathcal{H} = \sum_{i,j} J^{xx}\sigma_i^x\sigma_j^x + J^{yy}\sigma_i^y\sigma_j^y + J^{zz}\sigma_i^z\sigma_j^z + J_{i,j}^{xz}(\sigma_i^x\sigma_j^z + \sigma_i^z\sigma_j^x). \tag{6.1}$$

where σ_i^α is the α component of the i^{th} pseudospin which is defined in the local coordinate frame (see Fig. 6.5 and Appendix B) [17, 42] and $J^{\alpha\beta}$ is the nearest-neighbour interaction that couples the α component of a pseudospin with the β component of a neighboring pseudospin. The phase diagram based on this Hamiltonian has been calculated in Ref. [17] (Fig. 2.14) which exhibits the quantum spin ice and the AIAO ordered phases of dipolar and octupolar types.

The novel spin correlations and dynamics of $Nd_2Zr_2O_7$ were first explained based on the moment fragmentation theory and octupole order (assuming a Hamiltonian with only non-zero J^{yy} and J^{zz}) [152, 155, 166]. The moment fragmentation theory explains

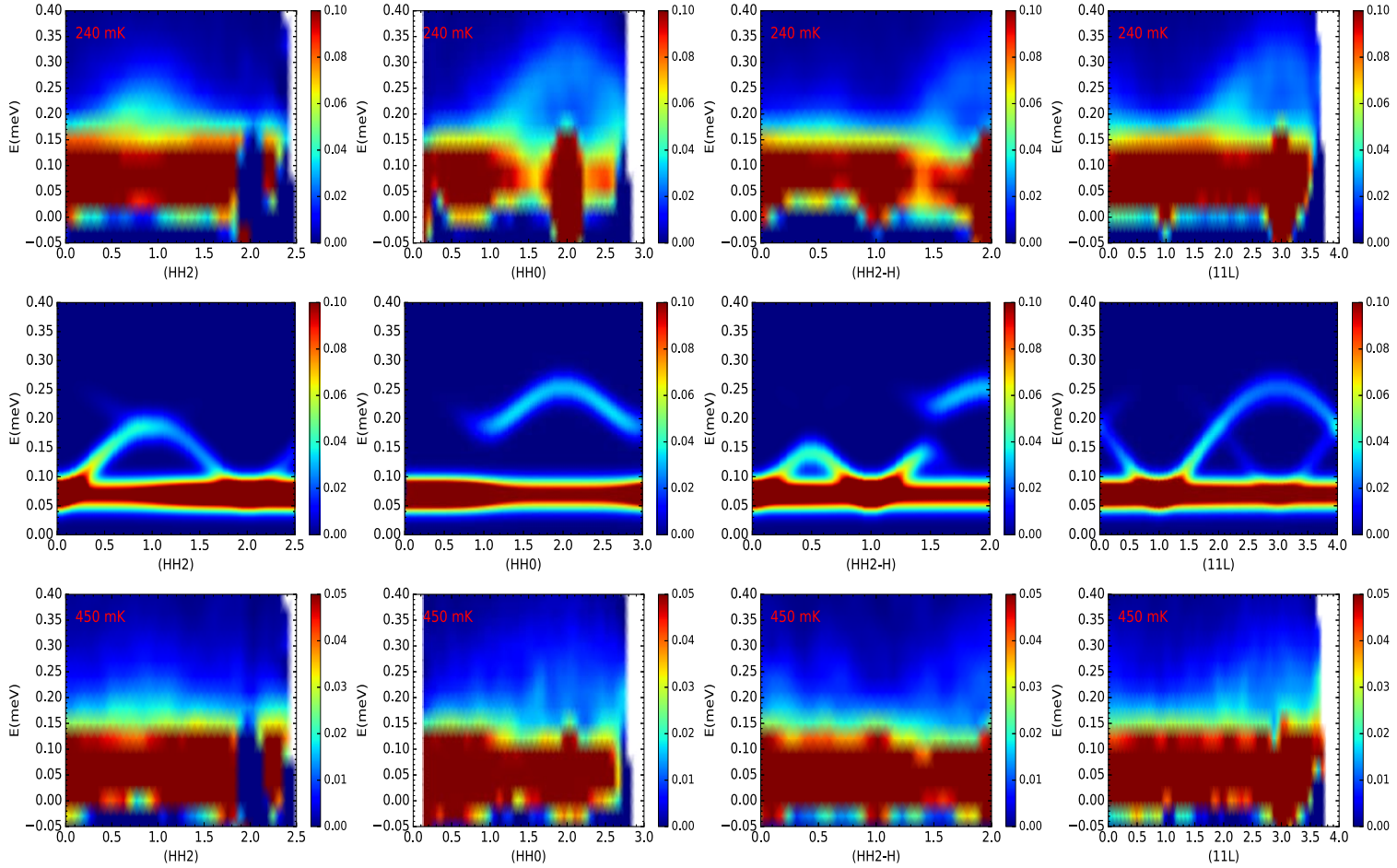

Figure 6.4: (first and third rows) Inelastic neutron scattering spectra (in arb. units) taken at 240 mK and 450 mK along different high symmetry directions presented by color-coded intensity $E - \boldsymbol{Q}$ maps. The background has been subtracted using the high temperature (20 K) dataset. (second row) Corresponding spin wave calculation based on the pseudospin 1/2 model for the ordered phase. The experimental resolution is 0.1 meV while 0.04 meV resolution is used in the calculation in order to show the dispersion clearly. The calculated pattern is normalized to the data by an overall factor for better comparison.

the coexistence of the pinch point pattern from the divergence-free "2-in-2-out" correlations typical for the magnetic Coulomb phase and the Bragg peaks characteristic of the divergent-full AIAO order which are seemingly incompatible with each other. This theory indicates that the ground state of $Nd_2Zr_2O_7$ could be a monopole crystal formed by alternating "3-in-1-out" and "1-in-3-out" spin configurations on the tetrahedra of the pyrochlore lattice which could be decomposed into divergence-full and divergence-free parts through Helmholtz decomposition of the magnetization density [166]. For example, the "3-in-1-out" moment arrangement can be decomposed as

$$\{1, 1, 1, -1\} = \{1/2, 1/2, 1/2, 1/2\} + \{1/2, 1/2, 1/2, -3/2\}.$$

where the fractional numbers means that a certain amount of the moment is pointing into (positive sign) or out of (negative sign) the centre of the tetrahedra. The neutron scattering pattern would be a superposition of the AIAO Bragg peaks (from the first term on right side) and the pinch point pattern (from the second term on right side). However, according to this theory both the pinch point pattern and the AIAO Bragg peaks should appear as elastic signal in the neutron scattering experiment which does not agree with the data. Additionally, it also cannot explain the spin wave dispersion observed in the data due to the disorder and the static nature of the monopole crystal state. The dispersion was explained due to the AIAO octupole order (the order of σ^y) which contradicts the AIAO dipolar σ^z order observed. As a result of the Ising anisotropy, the dynamical correlations of the AIAO dipolar order with the pseudospins along the Ising axes are believed to be invisible for neutrons because they are non-magnetic transverse fluctuations. Therefore, an order where the spins do not point entirely along the local [111] axes is necessary for explaining the data with spin wave theory, such as the octupole order adopted in Ref. [155]. Very recently, Owen Benton found that it is actually a quantum fragmentation of the spin wave excitations [152].
The two features observed in the INS data could be reconciled with a Hamiltonian containing non-zero J^{xx}, J^{zz} and J^{xz}, which was first proposed by Owen Benton in Ref. [152] and also realized in the calculations performed here. For a dominant J^{zz} term, the Hamiltonian reduces to the nearest-neighbor spin ice model and when $J^{zz} < 0$, the ground state is the dipolar AIAO order. The additional non-zero J^{xx} and J^{xz} could induce a ground state with spins tilted away from the local z axes while keeping the magnetization always along the local [111] axes due to the Ising anisotropy of the spins which is expressed by the zero value of $g_\perp$ (Fig. 6.5). The transverse fluctuations of this spin configuration have non-zero projection along the local z axes as shown in Fig. 6.5

which is magnetic, $\delta m_i^z(t) = g_{zz}\,\delta\sigma_i^z(t)\,\mu_\mathrm{B}$, making it observeable in a neutron scattering experiment.

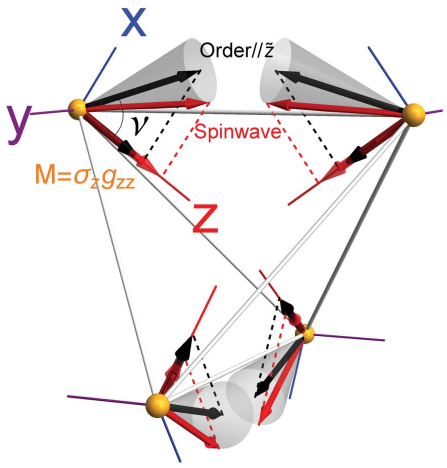

Figure 6.5: Single tetrahedron with Nd^{3+} spins on the vertex showing the local coordinate frames (labelled with x, y, z), canted AIAO spin ordering configuration (black arrows at the centre of the cones, ν is the pseudospin rotation angle) and divergence-free spin wave mode which are the grey cones formed by the precession of the spins (red arrows) around the ordering direction. During the precession, the σ^z projection (red arrows along z axis) of the pseudospin evolves, which modifies a dipolar moment along the local z axes and if there is a π phase between the upper and lower pairs of spins, the "2-large-2-small" [compared to the ordered moment(black arrow along local z axes)] ice rule will be fulfilled which gives the pinch point pattern in neutron scattering.

This picture was supported by the linear spin wave calculation. Firstly, the interaction term J^{xz} can be removed by a rotation of the local frames around the local y axes or in other words, a corresponding pseudospin rotation $\sigma_i^\alpha \to \tilde{\sigma}_i^{\tilde{\alpha}}$ [17, 152],

$$\begin{aligned}
\tilde{\sigma}_i^{\tilde{x}} &= \cos(\vartheta)\sigma_i^x + \sin(\vartheta)\sigma_i^z, \\
\tilde{\sigma}_i^{\tilde{y}} &= \sigma_i^y, \\
\tilde{\sigma}_i^{\tilde{z}} &= \cos(\vartheta)\sigma_i^z - \sin(\vartheta)\sigma_i^x, \\
\vartheta &= \frac{1}{2}\arctan\left(\frac{2J^{xz}}{J^{xx} - J^{zz}}\right),
\end{aligned} \tag{6.2}$$

where ϑ is the angle between the new and old z axes. In the new local coordinate frames,

we have the simple "XYZ" Hamiltonian for the new pseudospin $\tilde{\sigma}$,

$$\mathcal{H}_{XYZ} = \sum_{\langle ij \rangle} \left[\tilde{J}^{\tilde{x}\tilde{x}} \tilde{\sigma}_i^{\tilde{x}} \tilde{\sigma}_j^{\tilde{x}} + \tilde{J}^{\tilde{y}\tilde{y}} \tilde{\sigma}_i^{\tilde{y}} \tilde{\sigma}_j^{\tilde{y}} + \tilde{J}^{\tilde{z}\tilde{z}} \tilde{\sigma}_i^{\tilde{z}} \tilde{\sigma}_j^{\tilde{z}} \right]. \tag{6.3}$$

The exchange constants used in Ref. [152] are,

$$\tilde{J}^{\tilde{x}\tilde{x}} = 0.103,\ \tilde{J}^{\tilde{y}\tilde{y}} = 0,\ \tilde{J}^{\tilde{z}\tilde{z}} = -0.047 \text{ meV}, \tag{6.4}$$

or in the initial local frames

$$\begin{aligned} J^{xx} &= 0.5[(\tilde{J}^{\tilde{x}\tilde{x}} + \tilde{J}^{\tilde{z}\tilde{z}}) + (\tilde{J}^{\tilde{x}\tilde{x}} - \tilde{J}^{\tilde{z}\tilde{z}}) \cos(2\vartheta)], \\ J^{yy} &= 0, \\ J^{zz} &= 0.5[(\tilde{J}^{\tilde{x}\tilde{x}} + \tilde{J}^{\tilde{z}\tilde{z}}) - (\tilde{J}^{\tilde{x}\tilde{x}} - \tilde{J}^{\tilde{z}\tilde{z}}) \cos(2\vartheta)], \\ J^{xz} &= 0.5(\tilde{J}^{\tilde{x}\tilde{x}} - \tilde{J}^{\tilde{z}\tilde{z}}) \sin(2\vartheta). \end{aligned} \tag{6.5}$$

The $\mathcal{H}_{XYZ}$ does not depend on the rotation angle ϑ and thus the spin wave dispersion also does not. But the angle determines the absolute magnitude of the magnetization on each site which can be related to the absolute intensity observed in the inelastic neutron scattering data [152]. The linear spin wave calculation was performed by using the SpinW Matlab package and the details of the setup are described in Appendix B. Fig. 6.2 shows the calculated neutron scattering spectra of the spin waves for the interactions given in Eq. 6.4 (the spectra are convoluted with the instrument resolution function). The very good agreement between the calculation and data supports the validity of the Hamiltonian proposed. Fig. 6.4 presents the data and calculation in color-coded E-Q maps where an energy broadening smaller than the resolution is applied in the calculation for a clear view of the spin wave dispersion.

The positive Curie-Weiss temperature $\sim 0.2\,\mathrm{K}$ could be accounted for with $\vartheta \approx 0.83$ rad [152],

$$\theta_\mathrm{p} = \frac{1}{2k_B} \left(\tilde{J}^{\tilde{z}\tilde{z}} \cos^2(\vartheta) + \tilde{J}^{\tilde{x}\tilde{x}} \sin^2(\vartheta) \right), \tag{6.6}$$

which solves the puzzle that a positive θ_p can support an antiferromagnetic order. We can also calculate the ordered moment for the dipolar AIAO order (with pseudospins

oriented along the new local $\tilde{z}$ axes),

$$\begin{aligned} m_z &= \mu_B g_{zz} \sigma_z, \\ &= \mu_B g_{zz} \left[\tilde{\sigma}^{\tilde{z}} \cos(\vartheta) + \tilde{\sigma}^{\tilde{x}} \sin(\vartheta) \right], \\ &= 5.26 \times 0.5 \times \cos(0.83) \mu_B, \\ &= 1.77\, \mu_B, \end{aligned} \tag{6.7}$$

which is close to the value of $1.26(2)\,\mu_B$/Nd determined from neutron diffraction in Chapter 5. After taking account of the zero-point quantum effect of the spin waves which yields $\langle \tilde{\sigma}^{\tilde{z}} \rangle \approx 0.44$ at zero temperature [152], the ordered moment would be $1.56 \mu_B$/Nd (obtained by replacing 0.5 by 0.44 in Eq. 6.7).

According to Ref. [152], the Hamiltonian for $Nd_2Zr_2O_7$ suggests that $Nd_2Zr_2O_7$ is proximate to the $U(1)$ spin liquid phase or quantum spin ice phase as shown in the phase diagram in Fig. 6.6. $Nd_2Zr_2O_7$ has the ratio $\frac{\tilde{J}^{\tilde{x}\tilde{x}}}{|\tilde{J}^{\tilde{z}\tilde{z}}|} \approx 2.19$ and as this ratio increases, the gap to the flat pinch point band decreases. At $\frac{\tilde{J}^{\tilde{x}\tilde{x}}}{|\tilde{J}^{\tilde{z}\tilde{z}}|} = 3$, the gap closes according to the linear spin wave theory, which signals the formation of an extensive ground state manifold with ice-like character. These ground states can be mixed by quantum fluctuations, which stabilizes a $U(1)$ spin liquid with dynamical emergent gauge fields.

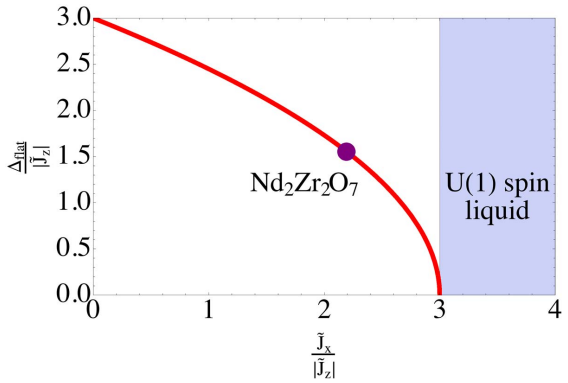

Figure 6.6: Phase diagram for the Hamiltonian with non-zero $\tilde{J}^{\tilde{x}\tilde{x}}$ ($\tilde{J}_{\tilde{x}}$) and $\tilde{J}^{\tilde{z}\tilde{z}}$ ($\tilde{J}_{\tilde{z}}$). With increasing $\tilde{J}^{\tilde{x}\tilde{x}}$, the gap Δ_{flat} for the flat band closes for $\frac{\tilde{J}^{\tilde{x}\tilde{x}}}{|\tilde{J}^{\tilde{z}\tilde{z}}|} = 3$ and the system enters a $U(1)$ quantum spin liquid phase. For $Nd_2Zr_2O_7$, this ratio is $\frac{\tilde{J}^{\tilde{x}\tilde{x}}}{|\tilde{J}^{\tilde{z}\tilde{z}}|} \approx 2.19$. Taken from Ref. [152].

6.4 Spinon excitations and quantum spin ice behaviour above T_N

Above the Neel temperature at 450 mK, the pattern of the INS signal is generally similar to that at 240 mK. However, the pinch point pattern shifts to lower energy and may even be gapless, while the spin wave scattering at higher energy is much weaker and broader (Fig. 6.4 and Fig. 6.7). The weak broad scattering observed at $Q = [220]$ and [113] at low energies could be the new features characterizing this phase (Fig. 6.7).

According to the recent calculation by Dr. Owen Benton (unpublished) based on bosonic many-body theory of quantum spin ice [170], $Nd_2Zr_2O_7$ is probably in a Coulomb phase immediately above T_N where coherently propagating monopoles (or spinons) exist. In this phase, the pinch point pattern should be gapless (Fig. 6.8a) in contrast to the gapped one in ordered phase observed at 240 mK. If there is no gap to the features in the INS data at 450 mK, it is a strong indication that above the transition there is indeed a well-formed Coulomb phase with an emergent gauge field and below the transition this gauge field acquires a gap via the Higgs mechanism.

Besides the pinch point pattern due to the scattering of the Coulomb phase, the neutrons could be scattered by monopoles via two different processes: the incoming neutron flips a spin belonging to a ice-rule tetrahedron creating a pair of monopoles, which gives a continuum at finite energy above a small gap (Fig. 6.8b); secondly at finite temperature where there is a finite density of monopoles already in the system, the incoming neutron can flip a spin belonging to a monopole tetrahedron causing this monopole to hop which gives a continuum of scattering around zero energy (Fig. 6.8b). Fig. 6.8c shows the energy-integrated scattering pattern due to monopole creation and hopping where some intensity builds up at [220] and [113] reciprocal vectors.

In the data at hand, it is clear that the pinch point pattern at 450 mK is at a lower energy than at 240 mK but it is not known whether or not there is a gap. Fig. 6.7 shows the comparison between the data and the calculated scattering pattern where for the calculated pattern the scatterings from the Coulomb phase and monopoles have been added. The calculation seems consistent with the low energy part of the data at 450 mK including the feature at (220). The high energy part (> 0.18 meV) of the data shows scattering similar to that in the 240 mK data but with a much reduced intensity which could be associated with the short-range antiferromagnetic order.

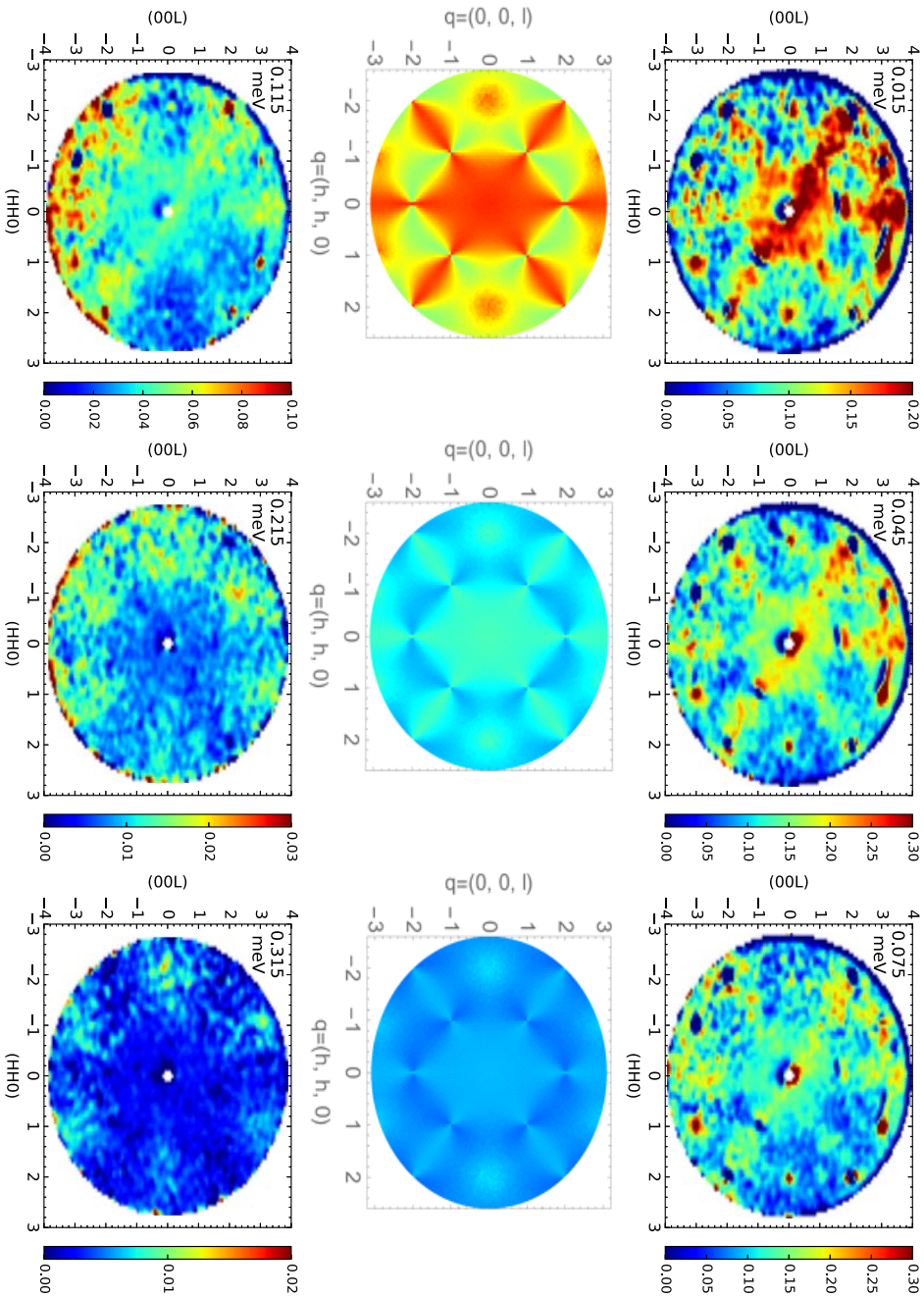

Figure 6.7: (first and third rows) Background-subtracted inelastic neutron scattering spectra (in arb. units) above T_N at 450 mK in the (HHL) reciprocal plane at the different energies indicated. (second row) Corresponding calculated spinion scattering performed by Owen Benton (unpublished) for energies 0.015, 0.045 and 0.075 meV based on the parametrized Hamiltonian determined. The calculation is normalized to the data by the same overall factor and has the same color scale with the corresponding data.

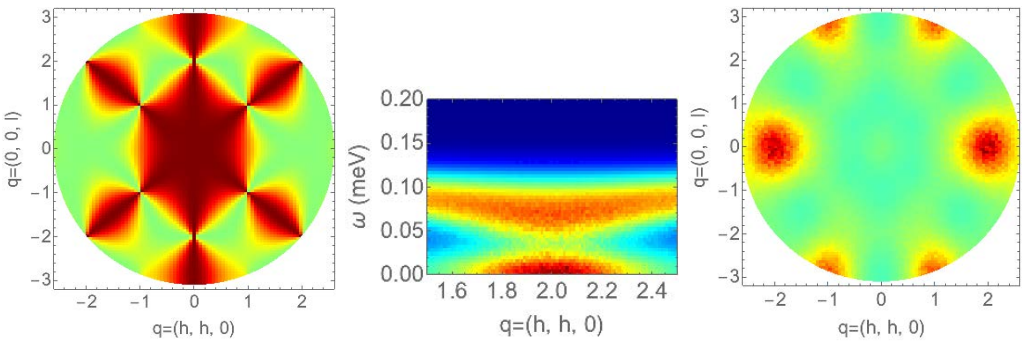

(a) (b) (c)

Figure 6.8: Calculated inelastic neutron scattering pattern of the magnetic Coulomb phase and monopoles using the Hamiltonian of $Nd_2Zr_2O_7$. (a) Gapless pinch point pattern due to the scattering of the Coulomb phase. (b) Monopole scattering around $Q = (220)$ in the spin flip channel of the polarized neutron inelastic scattering: at zero energy is the monopole hopping scattering continuum and above the tiny gap is the scattering due to the creation of monopoles. (c) Energy-integrated scattering pattern of the monopoles at finite temperature. All the calculations were performed by Dr. Owen Benton (unpublished).

6.5 Polarized neutron scattering

The energy-integrated polarized neutron scattering data were collected at 0.24, 0.45 and 23 K (background reference) with the normal Z-polarization geometry. After background subtraction, the data at the two lower temperatures do not show a clearly structured pattern because of the poor data statistics (the signal is too weak). After combining the two datasets and subtracting the background, we can see clearly a pinch point pattern in the (HHL) reciprocal plane in the spin flip channel as presented in Fig. 6.9. The data is consistent with the inelastic neutron scattering data shown in Figs. 6.2 and 6.7 because the pinch point pattern has the strongest intensity among the inelastic signals at both temperatures as mentioned above. The strong intensity at the Bragg peak positions is due to the imperfect flipping ratio corrections and the magnetic Bragg peaks. The non-spin-flip channel shows no clear pattern but only the nuclear Bragg peaks.

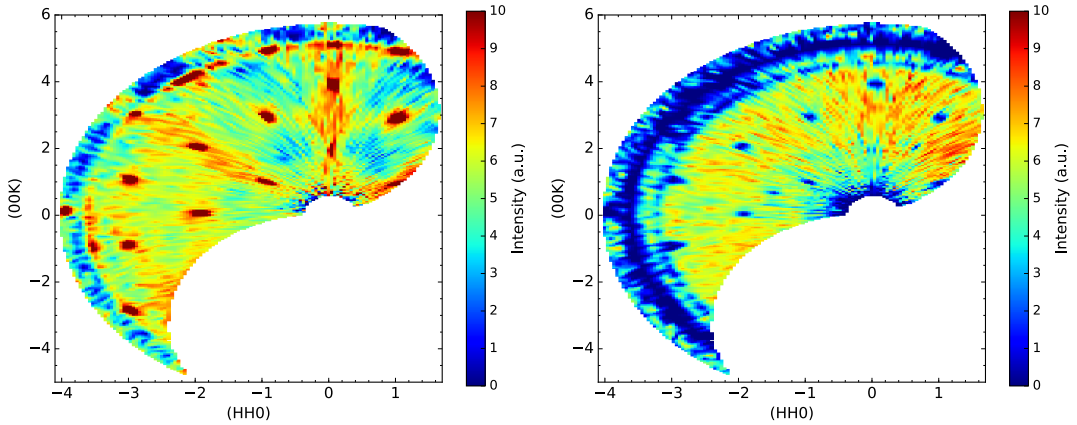

Figure 6.9: Energy-integrated polarized neutron scattering pattern in the Z polarization geometry. (left) Spin flip channel which shows the pinch points appear at (002), (111), (222) and so on; (right) Spin non-flip channel showing no clearly structured pattern.

6.6 Diffuse neutron scattering with applied magnetic field

Figure 6.10 shows the energy-integrated diffuse scattering data at 50 mK under a field of 0.5 T applied along the [1-10] direction which are measured within the (HHL) reciprocal plane with some out-of-plane component along the (1-10) direction. Besides some Bragg peaks and the powder diffraction rings from the sample environment, we can see a two-dimensional scattering sheet perpendicular to the (110) direction passing through the origin. This scattering sheet is present at both 50 mK and 450 mK for all the fields applied 0.25 T-2 T. Fig. 6.11 presents all the data after integrating along the out-of-plane (1-10) axis and the strong scattering streak can be seen perpendicular to the (110) direction which passes through the zero point. Parallel weak streaks also pass through (110) and (220) which can be seen most clearly in the data collected at 0.5 T field. The magnetic Bragg peaks are not discussed here because of the limited resolution which prevents quantitative analysis.

Intuitively, the two-dimensional scattering perpendicular to the (110) direction could be the elastic scattering of isolated chains parallel with the (110) direction. An applied field along [1-10] may separate the pyrochlore lattice into chains that are parallel (α-chains) and perpendicular (β-chains) [along (110) direction] with respect to the field as shown in Fig. 6.12. As a result of the lattice geometry and the local [111] Ising anisotropy, the field along [1-10] only affects the spins on the α chains directly and the spins on the β chains are influenced indirectly through the exchange interactions with the spins on the α

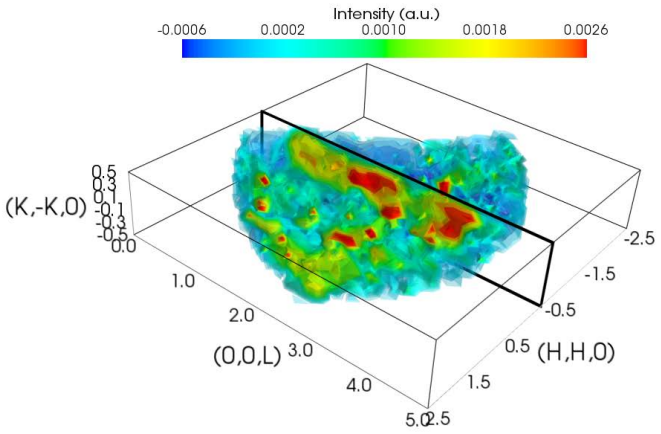

Figure 6.10: Energy-integrated diffuse neutron scattering data (background subtracted) with a 0.5 T field along the (1-10) direction at 50 mK. The black rectangle shows the two-dimensional scattering sheet along the (00L) direction.

chains. Assuming that the β chains show non-collinear FM order (alternating "in/out" order) within the chains and no inter-chain order , the structure factor is calculated which is shown in Fig. 6.13. The calculation is quite consistent with the data. An AFM "all-in/all-out" intra-chain order produces a different (roughly opposite) pattern compared with the data which can thus be excluded as a possible intra-chain order.
Intra-chain FM order and inter-chain disorder of the β chains can happen in the system when the field polarizes the α chains. The $M(H)$ curve in Ref. [129] shows that the field along the [1-10] direction induces a transition from the AFM order to a FM one in the α chains at the critical field ~ 0.08 T at 90 mK. This process is reproduced in Sec. 6.7 with the Hamiltonian determined above. It is found that in the polarized state, the α chain shows an alternating "in/out" spin order and the β chains also show a similar spin configuration (Fig. 6.12). As a result, the spins on the β chains are subjected effectively to a zero molecular field from the α chains because every spin on the β chains interacts with a pair of neighboring "in/out" spins on the α chains from which the molecular fields cancel out. Fig. 6.14 shows the bond energy between the α and β chains as a function of the field during the process of the field-induced transition. The averaged bond energy between the two types of chains becomes zero exactly after the transition. On the other hand, Fig. 6.14 also shows that the bond energy in a β chain gets lower which is because the spin interactions within a β chain lead to a FM "in/out" order with spins pointing alternatively to the positive/negative direction of the local $\tilde{x}$ axes due to the larger positive value of $J^{\tilde{x}}$. The bond energy in a β chain is lower than that of the

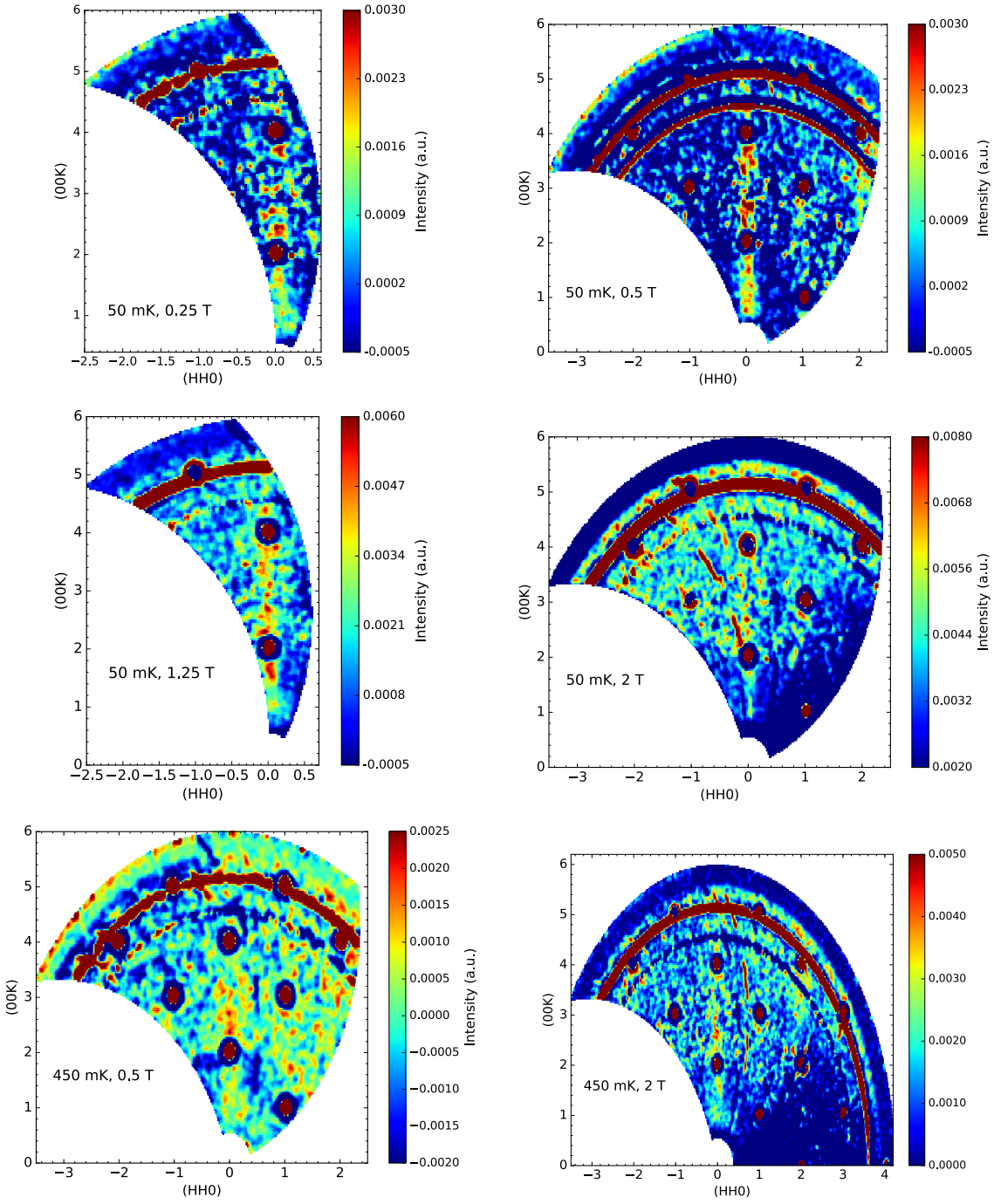

Figure 6.11: Energy-integrated diffuse neutron scattering data with field along the [1-10] direction at 50 mK and 450 mK after background subtraction. The data is a summation over the out-of-plane scattering with the wave vector component along (1-10) in range [-0.2, 0.4].

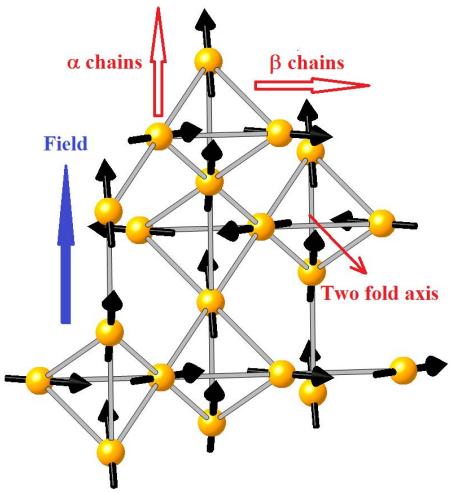

Figure 6.12: Pyrochlore lattice in a field along the [1-10] direction can be separated into parallel (α) chains and perpendicular (β) chains with respect to the field direction. Due to the Ising anisotropy, only the α chains respond to the field directly and a high field reverses the orientations of half of the spins on the chains (comparing to the AIAO order), forming an alternating "in/out" ferromagnetic (FM) order. The β chains only interact with the field indirectly through the exchange interactions with the α chains. When the α chains are polarized ferromagnetically, the β chains are subjected effectively to a zero molecular field from the α chains and the intra-chain interactions lead to a FM order within the β chains. The symmetrical intra-chain FM orders about the two-fold axis are equally possible and the β chains order independently, which results in the disorder between the β chains.

initial AIAO state (Fig. 6.14), which means that the frustration due to the inter-chain or three-dimensional coupling in zero field is relieved after the field decouples the two chains.

The inter-chain disorder induced by the field along the [1-10] direction is a natural result of the symmetry. If only the nearest-neighbor interactions are considered while ignoring the long-range dipole-dipole interaction, the β chains have no direct interaction with each other and due to the symmetry, the spins on the β chain could respond to the perpendicular field in two different ways which are symmetrical about the two-fold axis containing the centre of the tetrahedra and the middle of the bonds in the β chains (see Fig. 6.14). Fig. 6.14 also shows the spin rotation during the process of ramping the field along the [110] direction. Below the critical field, the spins on the α chains and

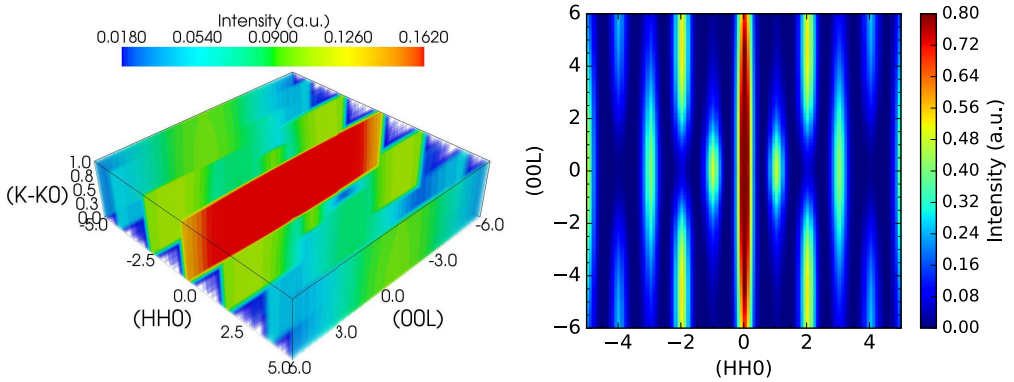

Figure 6.13: Calculated elastic neutron scattering pattern of a β chain with a non-collinear FM order (moments are along the local [111] directions). (left) Three-dimensional pattern showing the scattering sheets perpendicular with the chain. (right) Pattern in the (HHL) plane obtained by integrating the three-dimensional data along (1-10) axis.

the β chains cant away from the zero-field AIAO order gradually as field increases with the spins on the β chain rotating symmetrically about the two-fold axis. At the critical point, half of the spins on the α chain and all the spins on the β chain flip suddenly but the spins on the β chain do not flip symmetrically. The β chain takes a non-collinear FM order while its net moment can be parallel or antiparallel to the β chain direction with equal probability.

The discussion above explains the experimental data. The lowest field applied was 0.25 T at 50 mK which could be well above the transition field ($\sim$ 0.08 T at 90 mK) and that is why the scattering sheets which indicate inter-chain disorder of the β-chains are present for all the fields. Note that the calculated critical field ($\sim$ 0.36 T, see Fig. 6.14) is higher than the experimental one due to the limitation of the mean field approximation. The data at 450 mK (above T_N) show a similar scattering patterns which is due to the short-range intra-chain FM order of the β chains.

6.7 Magnetization calculation

The spin Hamiltonian verified above could also give a qualitative explanation to the low temperature AC susceptibility data shown in Chapter 4 by applying the mean field approximation where the field-induced transition and hysteresis is reproduced. According

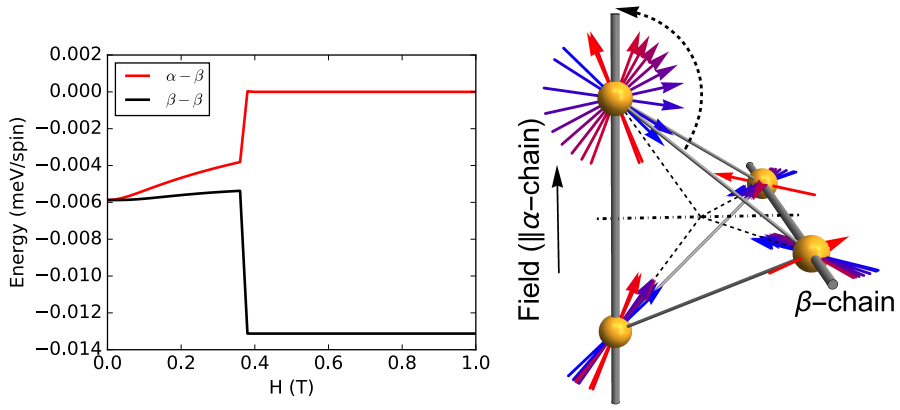

Figure 6.14: Left: averaged bond energy between α and β chains (red line) and bond energy in the β chains (black line) calculated using the Hamiltonian of $Nd_2Zr_2O_7$ with the mean field approximation (Sec. 6.7). The spin configurations in different fields are first calculated and then the bond energy is calculated according to the spin Hamiltonian. The averaged bond energy between the two chains is calculated by averaging bond energies of two bonds between a spin on the β chain and two neighboring spins on the α chain. Right: spin rotation during the process of increasing the field along [1-10] direction from 0 T to 1 T. The blue arrows show the spin configuration in zero field and the red ones show the spin configuration in a field of 1 T where the α chains are polarized. Below the critical field, the spins on the α chain and the β chain rotate gradually with the spins on the β chain rotating symmetrically about the two-fold axis shown by the dot dashed line. At the critical point, half of the spins on the α chain and all the spins on the β chain flip suddenly. The spins on the β chain do not flip symmetrically and form a non-collinear FM order with the net moment parallel or antiparallel to the β chain direction with equal probability).

to Eq. 6.1, the mean field Hamiltonian is given by

$$\mathcal{H}_{\mathrm{MF}} = \sum_i \mathcal{H}_i \tag{6.8}$$

with

$$\mathcal{H}_i = \sigma_i^x \sum_j J^{xx}\langle\sigma_j^x\rangle + \sigma_i^y \sum_j J^{yy}\langle\sigma_j^y\rangle + \sigma_i^z \sum_j J^{zz}\langle\sigma_j^z\rangle + \sum_j J^{xz}(\sigma_i^x\langle\sigma_j^z\rangle + \sigma_i^z\langle\sigma_j^x\rangle) - \mu_B g_{zz}\sigma_i^z H,$$

where $\mathcal{H}_i$ is the Hamiltonian for the i^{th} spin and the summations are over its six nearest neighbours and $\langle\sigma_i^\alpha\rangle(\alpha = x, y, z)$ is the thermal averaged value of the i^{th} spin given by

$$\langle\sigma_i\rangle \quad = \quad \frac{1}{2} \times \frac{1 - \exp(-\mathcal{H}_i/k_BT)}{1 + \exp(-\mathcal{H}_i/k_BT)} \text{(along the mean field direction)}. \tag{6.9}$$

The moment can be calculated by $M_i = g_{zz}\langle\sigma_i^z\rangle\mu_B$.
The calculation starts with a random spin configuration and then iterates over all the spins to calculate their thermal average and update the expectation value of the spin. The procedure is repeated until convergence. For the calculation of the $M(H)$ loops , the calculation for the next field takes the spin configuration in the former field as the starting point.
At base temperature in zero field, the spin configuration gives the AIAO order of dipolar moments (as a result of the anisotropic g factor as mentioned above though the spin orientation is not parallel with the local [111] directions). With increasing the temperature, the ordering parameter $\sigma^{\tilde{z}}$ ($\tilde{z}$ is the new local axis) decreases gradually and becomes zero at $T'_{\text{N}} \approx 0.82\,\text{K}$ indicating the phase transition (Fig. 6.15). This theoretical transition temperature T'_{N} is much larger than the experimental one which may be because the mean field approximation ignores the thermal and quantum fluctuations and the crystal field fluctuations are not included in this Hamiltonian. The crystal field interactions are not included here because the crystal field excitations are very high in energy and the energy scales of the temperature and the field involved here are relatively very low so that it is convenient and reasonable to only consider the crystal field ground state doublet, i.e. the pseudospin-1/2.

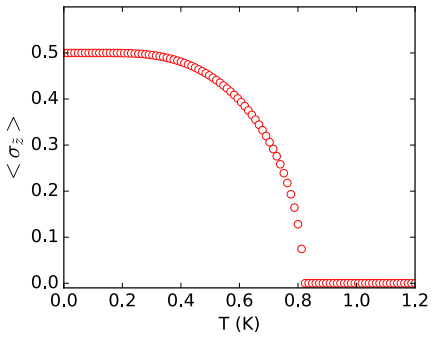

Figure 6.15: Temperature dependence of the ordering parameter $\sigma_{\tilde{z}}$ for the mean-field spin-1/2 model with the exchange interaction obtained from the inelastic neutron scattering data.

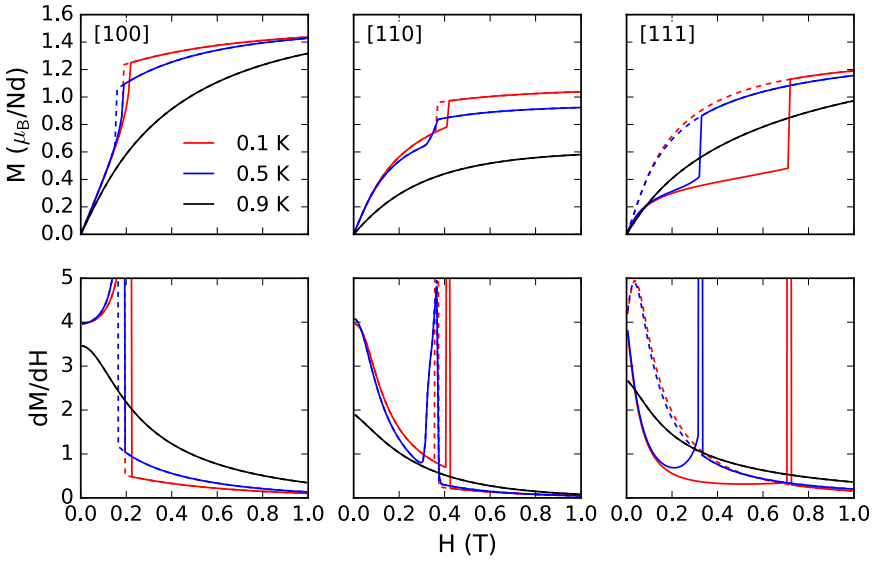

Figure 6.16: Calculated $M(H)$ (upper panels) and corresponding $\mathrm{d}M/\mathrm{d}H$ (lower panels) with field along [100], [110] and [111] directions at temperatures 0.1, 0.5 and 0.9 K for increasing (solid lines) and decreasing (dashed lines) fields based on the mean-field Hamiltonian.

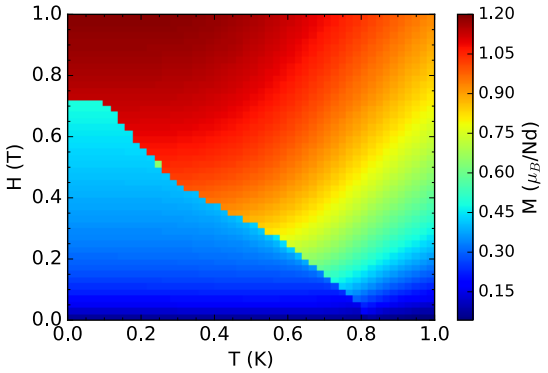

Figure 6.17: Colour contour plot of $M(T, H)$ for field parallel to the [111] direction showing the phase diagram calculated based on the mean field approximation.

Figure 6.16 shows the calculated $M(H)$ and $\mathrm{d}M/\mathrm{d}H$ curves for fields along the [100], [110] and [111] directions at temperatures 0.1, 0.5 (below T_N') and 0.9 K (above T_N'). For all the three directions, $M(H)$ shows the field-induced transition and hysteresis below T_N' and the features are the most pronounced for the [111] direction, which is consistent with the reported magnetization data in Ref. [129] and our AC susceptibility

data in Sec. 4.5.1.2 (the $\mathrm{d}M/\mathrm{d}H$ may serve as a good quantity to compare directly with χ_{AC}). The critical field H_{c} and hysteresis decrease with increasing temperature and above T'_{N} the field-induced transition and the hysteresis disappear. Fig. 6.17 shows the calculated H-T phase diagram with field along the [111] direction where a well-defined phase boundary is shown between the AIAO order and the field-induced order.

After surveying carefully the spin configurations in fields calculated, the sudden jump (field-induced transition) and the hysteresis in $M(H)$ are found to originate from the spin flipping and the irreversibility of the transition which arise from the special geometry of the lattice and the spin anisotropy of $Nd_2Zr_2O_7$. Take the case with field along the [111] direction and the AIAO domain as an example shown in Fig. 6.18. At first, it is convenient to describe the pyrochlore lattice as being composed of two sublattices: kagomé and triangular planar lattices stacked alternately along the [111] direction. When increasing the field, the spins on both sublattices rotate gradually and at the critical field, the spins on the kagomé lattice suddenly change their orientations resulting in the sharp jump in the $M(H)$ curve. Compared with the original spin configuration, the orientations of the spins on the kagomé lattice are almost reversed. However, when decreasing the field it is the spins on the triangle lattice that reverse the direction gradually. Therefore the hysteresis is caused by the irreversibility of the field-induced transition.

In more detail, the spins rotate gradually when the field is below the critical field while the field is increasing, for example in the 0.6 T field in Fig. 6.18. Spins on the triangle lattice tend to point closer to the local [111] directions in order to decrease the Zeeman energy, $E = -\mu_{\mathrm{B}} g_{zz} \langle\sigma\rangle \cos(\theta) H_{[111]}$, where θ is the angle between the spin direction and the field direction or the local [111] direction. In contrast, the spin on the kagomé lattice rotates away from their local [111] directions. With further increasing field, the spins on the kagomé lattice flip suddenly crossing an energy barrier as shown the figure with the field 0.8 T in Fig. 6.18. The spins on the triangle lattice also rotate away from the local [111] direction suddenly because of the sudden change of the molecular field from the six nearest-neighbor spins on the kagomé lattice. For higher fields, spins on both sublattices rotate gradually until saturation where all the spins are along their local [111] directions. When decreasing the field, the spins on the triangle lattice reverse gradually without any sudden flip due to the strong molecular field against the applied magnetic field because they have six broken bonds with their neighbors while the spins on the kagomé lattice only have two. As the field is decreased back to zero, the "all-in/all-out" domain is changed to be the "all-out/all-in" (AOAI) domain, where the former "all-in" or "all-out" tetrahedra change to be "all-out" or "all-in" tetrahedra.

These dramatic features in the $M(H)$ curves with field along the [111] direction only

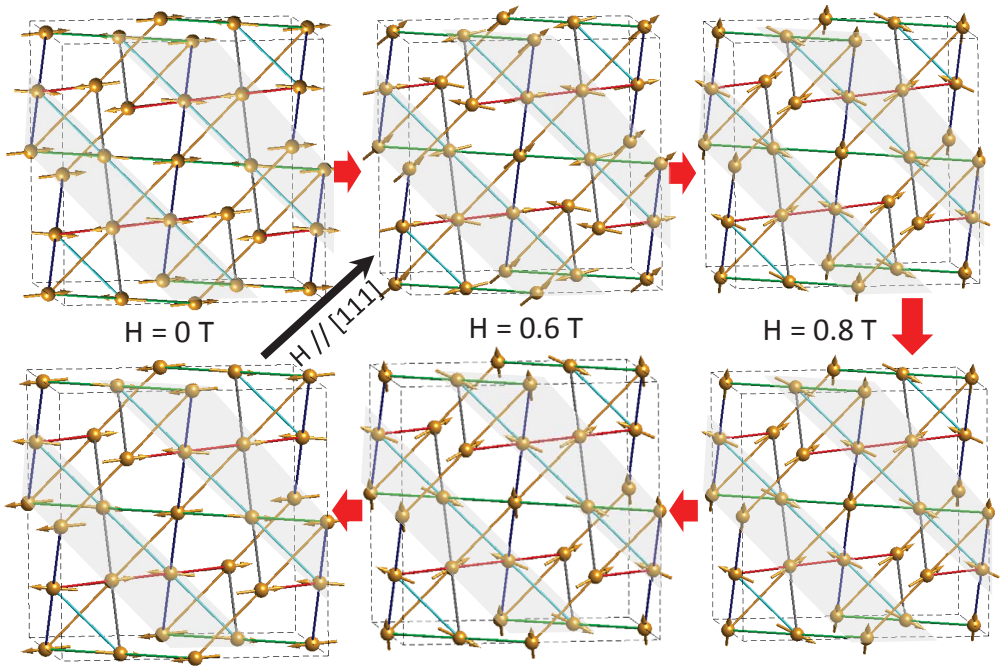

Figure 6.18: Calculated spin configurations in the fields 0, 0.6 and 0.8 T along the [111] direction. The grey planes are the kagomé lattice layers. The AIAO domain is initially chosen and the field is increased from 0 T to 1 T and the decreased back to 0 T following the red arrows. For increasing field, the spins the kagomé lattice reverse their orientations with a sudden jump and in the decreasing field, the spins on the triangle lattice reverse the orientations gradually. Finally the AIAO domain becomes a AOAI domain.

appear for the special case shown in Fig. 6.18. If the field direction is reversed or the magnetic domain is AOAI instead of AIAO, that will not happen as shown in Fig. 6.19 because for both increasing and decreasing fields, it is always the spins on the triangle lattice that reverse their orientations gradually. However, for the cases with fields along the [100] and [110] directions, there is no change with changing domain or reversing field direction, which can be understood based on the symmetry considerations.

6.8 Conclusions

In this chapter, the inelastic neutron scattering data of $Nd_2Zr_2O_7$ at 240 mK and 450 mK are first presented and clear spin wave dispersions are observed in the low-temperature data which are consistent with the recently reported data of a higher resolution (0.06 meV) at a lower temperature (60 mK) where the gapped excitations were better resolved [155].

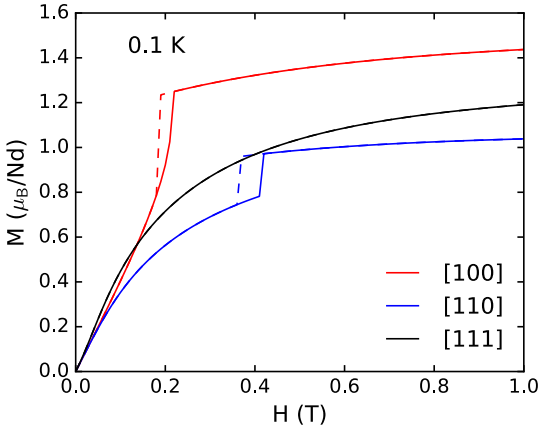

Figure 6.19: Calculated $M(H)$ curves with the reversed field direction or for the other domain (AOAI) comparing to the calculations in Fig. 6.16. The calculations were performed at 0.1 K for increasing (solid lines) and decreasing (dashed lines) fields based on the mean-field Hamiltonian. There is no anomaly for the [111] field in this case. For both increasing and decreasing fields, the orientations of the spins on the triangle lattice reverse orientations gradually and the M-H curves for increasing and decreasing fields are the same as the one for the AIAO domain in decreasing field (Fig. 6.16).

The dispersions can be modelled by linear spin wave theory and the pseudospin Hamiltonian for the dipolar-octupolar crystal field ground state doublet given in Ref. [152] was verified for $Nd_2Zr_2O_7$. The exchange interaction extracted suggests that $Nd_2Zr_2O_7$ is close to the $U(1)$ spin liquid phase or the quantum spin ice phase. Future experiments can be performed under high pressure where the pressure could adjust the spin interactions and may drive the system into the spin liquid phase. The 450 mK data above the Néel temperature shows a pinch point pattern at a lower (or zero) energy and similar dispersions at higher energies but which are broader with much weaker intensity than below T_N. The data were compared to the calculations of the bosonic many body theory with the parametrized Hamiltonian by Dr. Owen Benton, which implies that above T_N $Nd_2Zr_2O_7$ could show features of the magnetic Coulomb phase and the magnetic ordering can be viewed as a Higgs transition (the emergent gauge field of the Coulomb phase is gapped by the condensation of the gauge charges) [152]. Due to the limited resolution of the data at hand, a decisive conclusion cannot be made. Further polarized neutron experiments with high resolution are needed.

The energy-integrated polarized neutron diffuse scattering data at ~ 400 mK shows the pinch point pattern in the (HHL) plane in the Z spin flip channel which is consistent with

the inelastic neutron scattering data (the pinch point pattern has the largest intensity among the inelastic signals).

The energy-integrated unpolarized neutron diffuse scattering data with magnetic fields along the [1-10] direction shows two-dimensional scattering sheets perpendicular to the (110) direction which reveals that the system is separated into two subsystems of isolated chains along and perpendicular to the field direction (α and β chains) with the α chains polarized by the field and the β chains having ferromagnetic intra-chain order and no inter-chain order. This behavior can be modelled by the extracted Hamiltonian. Because of the Ising anisotropy of the spin, only the spins on the α chains can respond to the field directly. According to the mean field calculation, the [1-10] field polarizes the α chains and in this state, as a result the β-chains are subjected effectively to a zero molecular field from the other chains and the intra-chain coupling leads to non-collinear ferromagnetic order within the chain. Due to the symmetry, the net moment of the FM order of a $\beta - chain$ could be parallel or antiparallel to the chain direction with equal probability, which results in the inter-chain disorder. Interestingly, the long-range dipolar interactions do not induce an inter-chain order but short-range inter-chain correlations are observed in a similar experiment for $Dy_2Ti_2O_7$ [171].

The Hamiltonian was also used to calculate the low-temperature magnetization using the mean field approximation which provides a qualitative agreement with the data in Chapter 4 and Refs. [129, 156]. The sudden jump and hysteresis in the $M(H)$ curves is found to originate from the field-induced spin flipping and its irreversibility as a result of the peculiar geometry of the pyrochlore lattice and the Ising anisotropy of Nd^{3+}. The field tends to align the spins destroying the antiferromagnetic order and at the critical point for the transition to the field-induced ferromagnetic order, the spins rotate suddenly because the nearest-neighbor exchange interactions favors ferromagnetic order. The pronounced hysteresis along the [111] direction is discussed in detail and it is caused by the fact that for a certain AIAO domain and a specific field direction along [111], it is the spins on the kagomé lattice that flip when increasing the field but when the field is then decreased it is the spins on the triangle lattice that flip. In the experiment, both AIAO and AOAI domains are generally present in the sample so that the whole $M(H)$ loop with field from $-H$ to H and back always shows hysteresis on both sides of the zero point. For a sample cooled in a high field, only one domain survives after setting the field back to zero and the $M(H)$ loop would only show hysteresis at one side. This experiment could be done in the future.

To date, $Nd_2Zr_2O_7$ is the only member of the Nd pyrochlore compounds ($Nd_2Sn_2O_7$, $Nd_2Hf_2O_7$, $Nd_2Zr_2O_7$, $Nd_2Ir_2O_7$ and $Nd_2Mo_2O_7$) which is well studied with the spin

Hamiltonian determined for the search of quantum spin ice. $Nd_2Sn_2O_7$ and $Nd_2Hf_2O_7$ show the AIAO order like $Nd_2Zr_2O_7$ indicating similar spin Hamiltonians for the three compounds [130, 131]. For the appearance of the quantum spin ice state, a FM Ising exchange term is needed [55] which may be not the case for any of these three compounds. However, it may be true for $Nd_2Ir_2O_7$ as suggested by the magnetization analysis in Ref. [132] though this compound also shows the AIAO order. Pyrochlores with a non-magnetic B^{4+} ion of a radius comparable to that of the Ir^{4+} ion (0.625 Å) could be candidates of quantum spin ice for future study while high-pressure synthesis may be needed to grow such compounds.

$Yb_2Ti_2O_7$ was the first compound reported to be a realisation of the quantum spin ice and has been intensively studied [8]. The Yb^{3+} ion in $Yb_2Ti_2O_7$ also has a well-isolated Kramers doublet ground state but it is dipolar with XY anisotropy [8, 172, 173]. Although the specific heat of $Yb_2Ti_2O_7$ shows a sharp peak at $\sim 0.24\,\mathrm{K}$ accompanied by a strong reduction in the spin dynamics indicated by the μSR and Mössbauer spectroscopies, only very recently has a long-range order been confirmed by neutron diffraction [70, 71, 73, 75–77, 174]. The spin Hamiltonian of $Yb_2Ti_2O_7$ was first obtained by fitting the spin waves exhibited in the high-field neutron scattering data which indicates that $Yb_2Ti_2O_7$ lies close to quantum spin ice phase [8]. However, the exchange parameters are further optimized by analysing the zero-field neutron scattering data and it is found that $Yb_2Ti_2O_7$ sits in the vicinity of the FM/AFM phase boundary rather than close to the quantum spin ice phase [78, 79]. Finally, multiphase competition is proposed to account for the sample dependence and the spin dynamics observed in $Yb_2Ti_2O_7$.

Another well-studied quantum spin ice candidate is $Pr_2Zr_2O_7$. The crystal field ground state of Pr^{3+} in $Pr_2Zr_2O_7$ is an Ising-anisotropic non-Kramers doublet with the first excited state at 9.5 meV [82, 175]. According to the mean field calculation of the anisotropic psudeospin Hamiltonian derived on the crystal field ground state, the ground states of Pr pyrochlores could show cooperative ferroquadrupole and pseudospin chirality [42, 176]. Experimentally, the low-temperature susceptibility and the specific heat of $Pr_2Zr_2O_7$ show spin freezing features with residual entropy similar to the classical spin ice and the neutron scattering indicates spin-ice-like correlations and strong quantum fluctuations [82]. The inelastic neutron scattering in an applied magnetic field shows no dispersions but flat bands shifting with changing the field [84]. The RPA analysis indicates that quenched transverse fields with continuous distribution may play vital roles (the appearance of the transverse field is due to the non-Kramers property of the Pr^{3+} and the resulting electric quadrupole interaction with the local crystal structure) [84]. According to the recent publications, $Pr_2Hf_2O_7$ and $Pr_2Sn_2O_7$ show similar magnetic properties to

$Pr_2Zr_2O_7$ [80, 177] and the RPA analysis of the inelastic neutron scattering data of $Pr_2Hf_2O_7$ suggests antiferroquadrupolar correlations [85]. However, very recent study with high-resolution inelastic neutron scattering and polarised inelastic neutron scattering indicates quantum spin ice state of $Pr_2Hf_2O_7$ [178].

7 Spin dynamics of $Nd_2Zr_2O_7$ probed by muon spin relaxation

7.1 Introduction

In this chapter, the spin dynamics of $Nd_2Zr_2O_7$ is investigated using the muon spin relaxation (μSR) technique which detects the dynamics in a longer time window than neutron diffraction allowing slow fluctuations to be detected. This technique has been applied to many magnetic pyrochlores to study the spin dynamics of emergent novel states and has revealed many interesting phenomena. For example, $Er_2Ti_2O_7$, $Tb_2Sn_2O_7$ and $Yb_2Sn_2O_7$ are found to show persistent spin dynamics or the coexistence of spin dynamics and static long-range magnetic order far below the transition temperature and $Yb_2Ti_2O_7$ and $Yb_2Sn_2O_7$ show anomalously slow paramagnetic spin dynamics [71, 179–183]. For the classical dipolar spin ice phase, the μSR and AC susceptibility measurements reveal that the spins tend to freeze at low temperatures due to the Ising interaction, giving rise to spin-glass-like behaviour [16, 25, 184, 185].

Although $Nd_2Zr_2O_7$ has the long-range order below 0.4 K as shown in Chapter 5, it lies close to a possible spin liquid phase and significant quantum fluctuations still can be expected [152]. A recent μSR study on $Nd_2Sn_2O_7$ which has the same AIAO magnetic order below 0.91 K shows that the muon spin precession is present only below 0.7 T_N which is probably caused by dynamical effects [131]. Here, the μSR data provide direct evidence for even stronger fluctuations in $Nd_2Zr_2O_7$ and confirm that $Nd_2Zr_2O_7$ has weak Ising anisotropy (the Hamiltonian contains additional pronounced transverse terms besides the dominant Ising term) as found in the spin wave analysis of the inelastic neutron scattering data in Chapter 6. In addition, it is also found that a field could increase the fluctuation rate in the ordered state, which is ascribed to a field-induced spin flipping transition as indicated by the macroscopic measurements (Chapter 6 and Ref. [129]). The paramagnetic state shows anomalously slow spin dynamics similar to the quantum spin ice materials $Yb_2Ti_2O_7$ and $Yb_2Sn_2O_7$ [182].

7.2 Experiment details

The longitudinal μSR spectra are collected at PSI on the spectrometers LTF and GPS for the temperature ranges 20 mK-4.2 K and 1.5 K-300 K, respectively. The data are measured in zero field (ZF) and longitudinal fields (LF) up to 0.5 T. For the experiment on LTF, about 2 g of $Nd_2Zr_2O_7$ powder is mixed with ethanol diluted GE varnish and attached to a silver plate for good thermalization (the sample has a thickness $\sim$ 2 mm). A dilution refrigerator is used which achieves a base temperature of 20 mK and a maximum temperature of 4.2 K. The signal from the silver sample holder contributes most of the background and has a small relaxation rate (e.g. $\sim 0.06\,\mu s^{-1}$ at 20 mK) causing a slow damping tail in the spectra which is included in the analysis (see Appendix D). For the measurement on GPS, about 1 g powder sample is packed into a $\sim$ 2 mm thick slab using thin aluminium foil and cooled by a Helium flow cryostat. The background of the GPS data is very low and thus is ignored. The data analysis is performed using the free software Musrfit [186].

7.3 Results of the LTF measurements ($T \leq 4.2$ K)

7.3.1 Zero field μSR measurements

Figure 7.1 shows representative asymmetry spectra in zero field below 4.2 K. It should be pointed out first that the spectra below the transition temperature ($T_N = 0.4$ K) do not show the cosine-function-like oscillations which is a normal signature for static order as found in $Nd_2Sn_2O_7$ [131]. In addition, the asymmetry does not tend to $1/3\,P_z(t=0)$ at long times which is another indicator for a static internal field in a powder sample [113]. The spectra do not show strong temperature dependence and and there is no sudden change at T_N. At lower temperatures ($T < 0.8$ K), the spectra have a weak Gaussian-function relaxation at early times [Fig. 7.1(a)] and an inflection point at 1.5-3 μs with a tiny local minimum [Fig. 7.1(b)]. Both of these features are typical for the dynamical Gaussian Kubo-Toyabe function (dGKT) in the quasi-static limit (the Gaussian-function field distribution width and fluctuation rate are comparable and both are in microsecond range for this case) (see Chapter 3). These two features becomes less pronounced at elevated temperatures such that the spectra become more like an exponential function as a result of the enhanced thermal spin fluctuations (e.g. the spectra at temperatures above 1.2 K).

The conventional dynamical Gaussian Kubo-Toyabe function (dGKT) does not fit the data well however because it gives a deeper dip (Fig. 7.2) similar to the situation

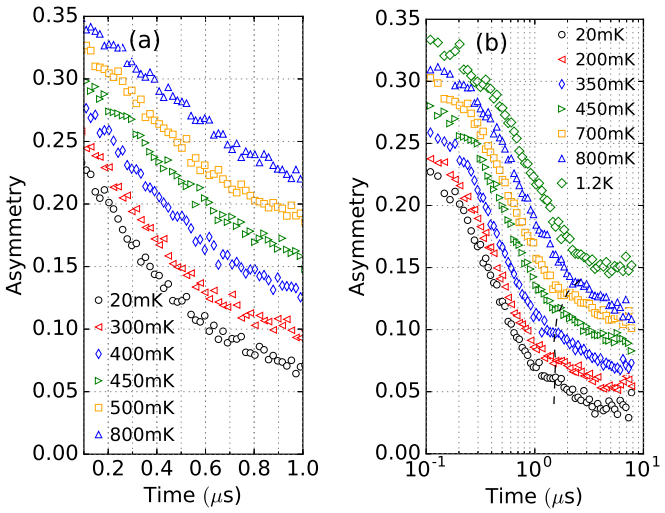

Figure 7.1: (a) Early-time weak Gaussian relaxation of the ZF μSR asymmetry spectra collected at temperatures below 4.2 K on LTF. The data are shifted vertically by 0.02 unit successively for a better visualization. (b) Inflection point at 1.5-3 μs and its evolution (dashed line) in the ZF spectra at different temperatures as a function of $\log(Time)$. The data are shifted vertically by 0.017 unit successively for a better visualization.

of $Yb_2Ti_2O_7$ [71] and $Yb_2Sn_2O_7$ [182]. The dynamical Gaussian-broadened Gaussian Kubo-Toyabe function (dGbGKT) which is described in Chapter 3 fits the data better which is a phenomenological model accounting for the homogeneous disorder by including a collection of Gaussian field distributions with a Gaussian-function-weighted standard deviation [113, 187]. The fitted spectra and parameters are shown in Fig. 7.3. Note that the fitting reproduces most of the features of the spectra but it does not show a clear inflection point and local minimum. The fitting shows that the fluctuation rate ν decreases with decreasing temperature continuously and becomes almost temperature independent below the ordering temperature, indicating persistent spin dynamics. The parameters Δ_0 and R_b characterizing the standard deviation of the field distribution (see Chapter 3) decrease gradually with decreasing temperature and then increase suddenly at the ordering temperature.

There are mainly two reasons for the absence of oscillations in an ordered state: either there is no local field at the muon site, i.e. B_{loc} = zero or the fluctuations are fast, i.e. $\nu \gg \gamma_\mu B_{loc}$ (γ_μ is the muon gyromagnetic ratio). The first case can be due to a cancellation of the dipolar field at the muon stopping sites from different ordered moments [113]. Dipolar field cancellation can happen at high symmetry sites in the

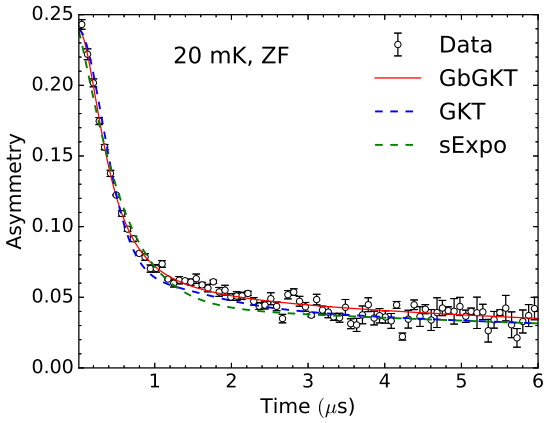

Figure 7.2: Zero field asymmetry spectra measured on LTF (open circles) at base temperature fitted with dynamical Gaussian broadened-Gaussian Kubo-Toyabe function (dGbGKT) (red solid line), the conventional dynamical Gaussian Kubo-Toyabe function (dGKT) (blue dashed line) and the stretched exponential function (sExpo) (Eq. 3.36) (green dashed line). The corresponding χ^2 for the fitting with these three functions are 1.02, 1.17 and 1.30, respectively.

unit cell for the current highly-symmetric magnetic structure. Considering the sites of oxygen anions near to which the positively charged muon generally stops in oxides, the crystallographic 8*b* site has a high symmetry. It is at the centre of the Nd^{3+} tetrahedron where all the four spins at the vertices of the tetrahedron point inwards or outwards. At this site the local field is exactly zero. However, a muon normally stops at a distance 0.9-1.1 Å from the oxygen [113] which is not the centre of the tetrahedron. According to the dipolar field calculation based on the current magnetic structure described in Sec. 7.5, there is almost no place surrounding the oxygen ions at the 8*b* and 48*f* sites that has zero field.

In addition, the related compounds $Nd_2Sn_2O_7$ and $Nd_2Hf_2O_7$ which have the same type of order show oscillations or missing asymmetry (fast oscillations that are not resolved by the instrument), which indicates that there are non-zero static (relative to $\gamma_\mu B_{\rm loc}$) fields at the muon stopping sites in these two compounds [131, 165]. For $Nd_2Zr_2O_7$, it is reasonable to assume that muons stop at similar positions as in $Nd_2B_2O_7$ (B = Sn, Hf) where a non-zero local field should also be present. Moreover, because $Nd_2Zr_2O_7$ and $Nd_2Sn_2O_7$ have a similar magnitude of ordered moment [131, 188], a similar oscillation frequency would be expected. While $Nd_2Sn_2O_7$ shows clear oscillation signal below $0.7\,T_{\rm N}$, $Nd_2Zr_2O_7$ does not show any sign of oscillation even at the temperature $0.05\,T_{\rm N}$,

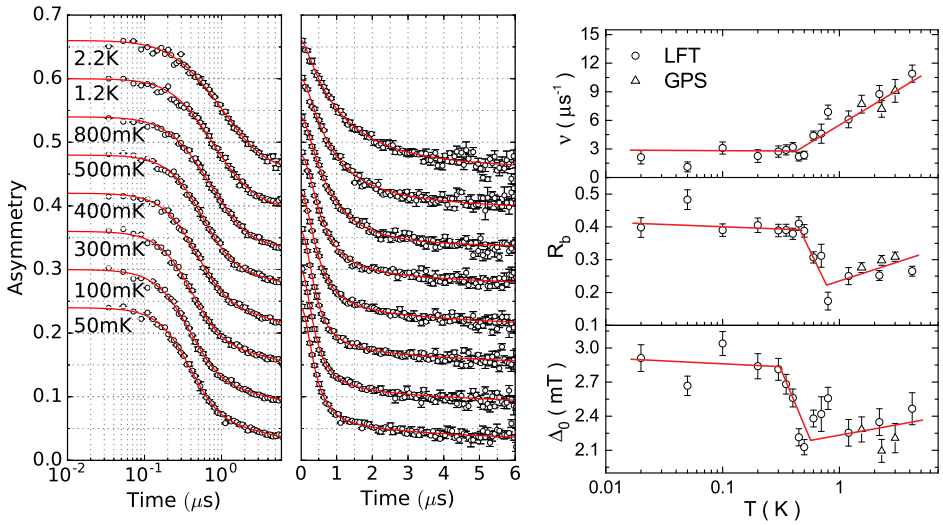

(a) (b)

Figure 7.3: (a) Logarithmic (left) and linear (right) plots of μSR asymmetry spectra (open circles) at different temperatures in zero field from LTF instrument and the corresponding fittings (red solid lines) with dGbGKT function. The data are shifted vertically by 0.06 unit successively for a better visualization and the temperature for every spectrum is given by the text nearby. (b) Temperature dependence of the fitted parameters of the dGbGKT function whose meanings are explained in Chapter 3. The red solid lines are a guide to the eye.

which indicates much stronger dynamics in $Nd_2Zr_2O_7$. It should be mentioned that a very broad distribution of static fields (compared with the average value of the field) can also wash out the oscillation signal. However, the μSR spectra for $Nd_2Sn_2O_7$ indicate that the local field at the muon stopping site can be 127 mT [164] and if we assume that $Nd_2Zr_2O_7$ has a similar static order to $Nd_2Sn_2O_7$, a similar local field can be expected which is at least an order of magnitude larger than the field distribution width ~ 2.9 mT obtained here. The measurement with longitudinal field in Sec. 7.3.2 also excluded this possibility.

Therefore, the absence of the oscillations is attributed to the strong spin fluctuations in the ordered state which is unusual for a system with strong Ising anisotropy. This result is consistent with the existence of a significant transverse coupling between the Ising spins induced by the multipole-multipole interactions as shown in Chapter 6. $Nd_2Zr_2O_7$ seems quite different from its counterpart compounds $Nd_2B_2O_7$ (B = Sn, Hf) as mentioned

above, which are not so surprising in the context that related pyrochlore compounds can show quite different properties, e.g. Yb and Tb titanates and stannates (showing dynamical ground state and static order, respectively). This can be partly understood since the magnitude of the transverse terms in the anisotropic exchange interaction depends on the composition of the crystal field ground state wave functions [16, 42]. The slightly different coordinating environments of Nd^{3+} in these compounds lead to different crystal field levels and ground state wave functions [164] and thus different pseudospin Hamiltonians. In addition, the inter-atom distance and the bond angle are also slightly different which can affect the exchange interactions.

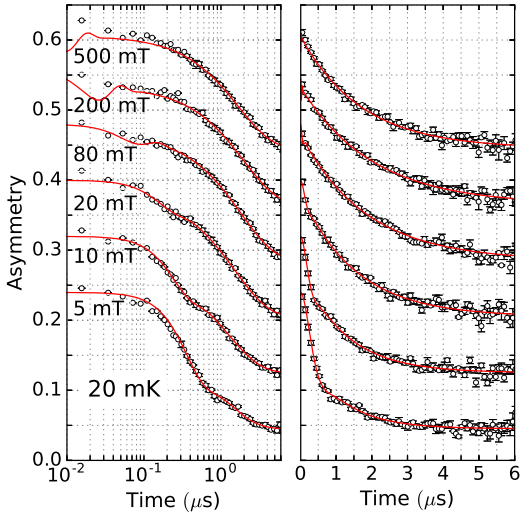

Figure 7.4: Logarithmic (left) and linear (right) plots of the spectra (open circles) recorded at base temperature on LTF in different longitudinal fields (indicated by the labels) and corresponding fits (red solid lines) with the dGKT function with longitudinal field. The data are shifted by 0.08 unit successively for a better visualization.

The μSR results show that the extracted spin fluctuation rate is in the range of megahertz, this is compatible with the observation of a static magnetic structure using neutron diffraction because the energy resolution of the neutron diffractometer has a time scale of larger than $\sim 10^{-12}$ s thus fluctuations that are slower than this may be observed as static [180, 188]. An ordered phase without a spontaneous muon spin precession was also reported for $Tb_2Sn_2O_7$ [180, 181], $Er_2Ti_2O_7$ [179] and $Yb_2Sn_2O_7$ [182]. However $Nd_2Zr_2O_7$ is a special case because it is a strong Ising system with additional multipole interactions that introduce the dynamics while for the others a planar component of the

spin or low-energy crystal field excitations play vital roles [17, 25, 189]. In addition, it is very interesting that the obtained fluctuation rates and field distribution widths in the ordered and paramagnetic states of $Nd_2Zr_2O_7$ are comparable with these of the quantum spin ice materials $Yb_2Ti_2O_7$ (where magnetic order was found recently) and $Yb_2Sn_2O_7$, but are much lower than those of the dynamical spin ice $Tb_2Sn_2O_7$ [71, 76, 180–183].
It is striking that the spectra in the paramagnetic state are also described by the model at the quasi-static limit rather than the simple exponential or the stretched exponential function which is generally the motion-narrowing limit of the model. This points to anomalously slow paramagnetic spin dynamics which can be associated with strong spin correlations or short-range order as was also reported for the similar compound $Nd_2Sn_2O_7$ and the quantum spin ice materials $Yb_2Ti_2O_7$ and $Yb_2Sn_2O_7$ [71, 131, 182, 183]. This is consistent with the magnetic heat capacity which develops at around 10 K [188]. The slow paramagnetic spin dynamics unexpectedly persists in the ordered state resulting in the absence of the oscillations in the ordered state.
Recently, a muon induced effect was reported for $Pr_2B_2O_7$ (B = Zr, Hf, Sn) which makes the system order because the implanted muon stopping around the $48f$ site oxygen modifies the local environment anisotropically of the non-Kramers rare earth ion Pr^{3+} and lifts the degeneracy of the crystal field ground state doublet [190]. This is not expected for the Kramers ion like Nd^{3+} whose Kramers degeneracy is protected by time-reversal symmetry.

7.3.2 Longitudinal field μSR measurements (below 0.5 T)

The strong fluctuations of the ordered state are also confirmed by measurements in a longitudinal field which is usually used to find out whether the damping of the muon polarization is caused by dephasing due to a broad distribution of static fields or relaxation due to field fluctuations [113]. The asymmetry spectra measured in several fields at 20 mK are shown in Fig. 7.4. The spectra show clear field-induced oscillations which evolve gradually with increasing field but no sign of relaxation quenching can be seen, which confirms the dynamical properties of the system.
The dynamical Gaussian Kubo-Toyabe function with longitudinal field gives a good description of the data. The fitted curves for the data at 20 mK in different external fields B_{ext} are shown in Fig. 7.4 and the field dependence of the parameters are shown in Fig. 7.5. As the applied field increases the fluctuation rate ν increases and shows a maximum around 80 mT, which is not a simple field quenching effect. The peak in the fluctuation rate is tentatively ascribed to the field-induced metamagnetic transition from the antiferromagnetic spin configuration to a ferromagnetic one as observed in the single

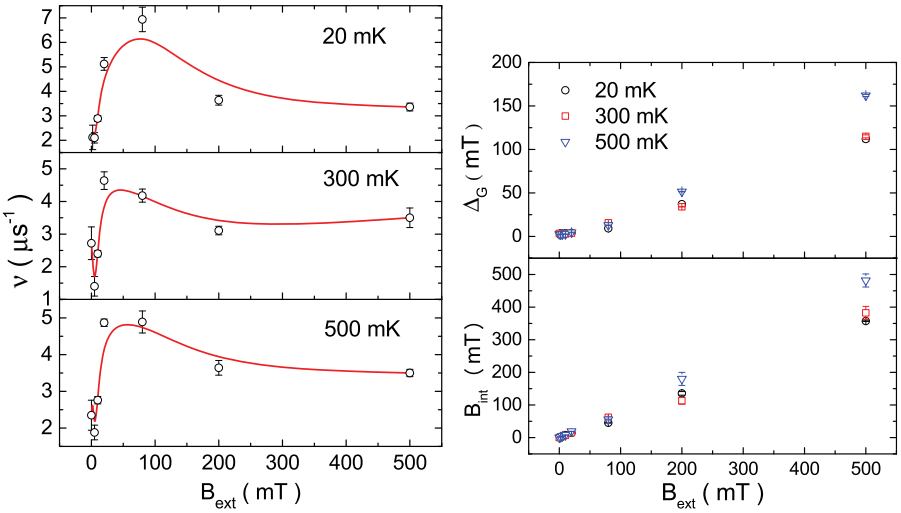

Figure 7.5: Left: fitted fluctuation rate (back circles) in different longitudinal fields B_{ext} for temperatures 20, 300 and 500 mK. The ZF parameters are also shown which are extracted from the fitting with the dGbGKT function. The red lines are a guide to the eye. Right: longitudinal field B_{ext} dependence of the fitted internal field B_{int} (the lower panel) and the fitted internal field distribution standard deviation Δ_{G} (the higher panel) at temperatures 20, 300 and 500 mK.

crystal AC susceptibility and magnetization measurements (the transition fields for the three main cubic directions are around 100 mT at 90 mK) in Chapter 6 and Ref. [129]. The same model also fits the data at 300 mK (below T_{N}) and 500 mK (above T_{N}) as shown in Fig. 7.6 and the corresponding parameters are shown in Fig. 7.5. A similar field induced peak in the fluctuation rate is also observed at 300 mK but at a lower field ~ 30 mT, similar to the magnetization data which shows a decrease in the metamagnetic transition field at higher temperatures [129]. However, at 500 mK in the paramagnetic state, the peak is still present, which might be due to the break down of the short-range antiferromagnetic correlations induced by the field.

In addition, the fitted internal field B_{int} and field distribution standard deviation Δ_{G} increase with increasing the external field almost linearly (Fig. 7.5) similar to $Yb_2Ti_2O_7$ and $Yb_2Sn_2O_7$ [183] but the fitted internal field is slightly smaller than the applied field for the two temperatures below T_{N}. If $|B_{\mathrm{int}} - B_{\mathrm{ext}}|$ can be associated with the demagnetizing field, this agrees with magnetization data which shows a higher magnetization at lower temperatures [129].

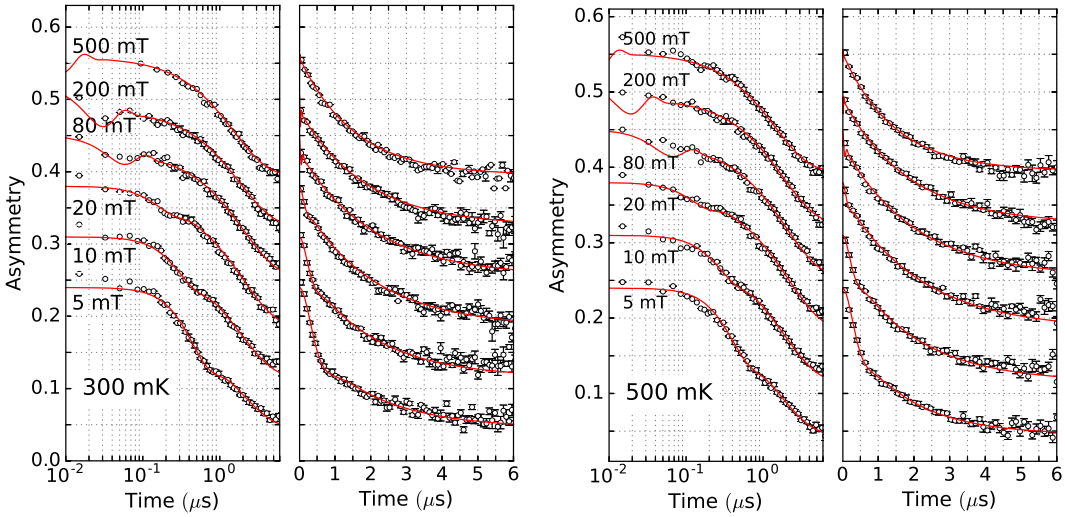

Figure 7.6: Logarithmic and linear plots of the spectra (open circles) recorded at 300 mK (a) and 500 mK (b) in different longitudinal fields (indicated by the labels) measured on LTF and corresponding fits (red solid lines) with the dGKT function with longitudinal field. The data are shifted by 0.07 unit successively for a better visualization.

7.4 Results of the GPS measurements (T $\geq$ 1.55 K)

The data at temperatures between 1.55 K and 300 K in zero field from the GPS instrument are shown in Fig. 7.7. The initial Gaussian-type damping and the tiny local minimum shown in the low-temperature data become very weak or disappear. The spectra are well fitted with the stretched exponential function (Eq. 3.36 in Chapter 3) which is commonly used for a system with a continuous distribution of relaxation processes [113]. Note that the spectra measured on LTF in the temperature range 1.2-4.2 K initially fitted with the dGbGKT function in Sec. 7.3.1 are also described well by the stretched exponential function ($\beta > 1$ for the lower temperatures) and are also shown in Fig. 7.7. The fitted relaxation rate λ and exponent β are shown in Fig. 7.8 as a function of temperature. In zero field, the relaxation rate λ increases with decreasing temperature indicating slowing down of the spin dynamics, which is consistent with the results fitted with the dGbGKT function [Fig. 7.3(b)]. At the same time, the exponent β increases and is larger than one below 2 K showing the evolution of the spectra, which further indicates the slowing down of the system. The increase in the relaxation rate or

the slowing down of the spin fluctuations below 20 K is due to the building up of the spin correlations as observed in the specific heat measurement in Chapter 4. This increase of λ is largely suppressed by the 50 mT longitudinal field, as was also found for $Nd_2Sn_2O_7$ [131], which may be caused by the competition between the exchange interaction and Zeeman interaction (explained below).

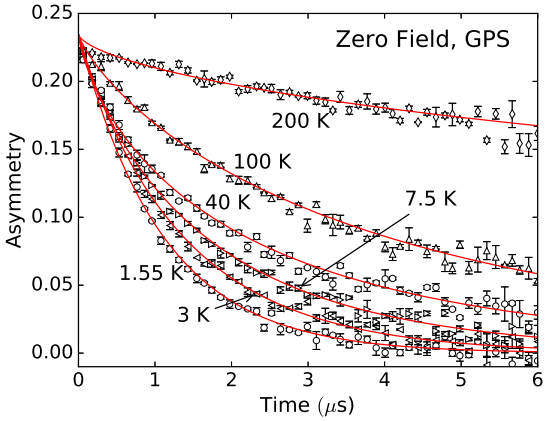

Figure 7.7: Selected spectra (open circles) recorded on the GPS instrument in zero field at different temperatures between 1.55 and 300 K. The temperature for each spectrum is indicated by the text nearby. The red lines show the fitting with stretched exponential function.

The inflection point of λ at $\sim$ 80 K could be induced by an Orbach process: here the magnetic moment of Nd^{3+} relaxes through a real two-phonon process with an excited crystal-field state as an intermediate state. The temperature dependence of the relaxation due to the Orbach process can be described by [191]

$$\lambda^{-1} = \lambda_0^{-1} + \eta \exp[-\Delta_{\mathrm{CEF}}/(k_{\mathrm{B}}T)] \tag{7.1}$$

where λ_0^{-1} is the saturation value at low temperatures, η reflects the strength of the spin-lattice interaction and Δ_{CEF} is the energy gap between the crystal field ground state and the excited state that mediates the spin relaxation process. The fitting of the extracted relaxation rate λ in the field of 50 mT yields $\Delta_{\mathrm{CEF}} = 40(4)$ meV (with $\lambda_0^{-1} = 2.0(1)\,\mu$s, $\eta = 335(30)\,\mu$s) which is close to the energy of the second and third excited crystal field levels (34.4 and 35.7 meV) determined by the inelastic neutron scattering experiments in Chapter 5. Because the two crystal field levels are quite close to each other, fitting with the current data does not allow to distinguish which one participates in the Orbach process. A qualitatively similar result was also found for $Nd_2Sn_2O_7$ [164].

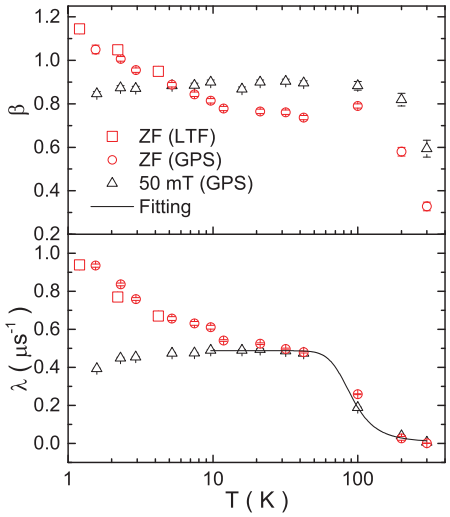

Figure 7.8: Temperature dependence of the fitted exponent β (upper panel) and relaxation rate λ (lower panel). The data from LTF in zero field and the data from GPS in zero and 50 mT fields are shown. The black line is the fitting of the temperature dependence of the relaxation rate due to the Orbach process for the 50 mT data.

As mentioned above, a 50 mT field largely suppresses the increase of λ for 1.5-20 K. At first, it seems that it can be explained using the Redfield formula (Eq. 3.35) which shows that assuming the applied field has no influence on the system and the system is in the fast fluctuation limit, the longitudinal field dependence of the relaxation rate can be described by a Lorentz function with half width at half maximum of ν/γ_μ. Accordingly, for a system with a very small fluctuation rate, λ can be reduced sharply to nearly zero by the field. Fig. 7.3(b) shows that the fluctuation rate in zero field of $Nd_2Zr_2O_7$ is of order of magnitude of 10 MHz corresponding to an internal field of $\sim$ 12 mT which is much smaller than 50 mT. Therefore, it seems that the strong reduction in λ by the 50 mT field is probably due to relatively low paramagnetic fluctuation rate of the system. However, Fig. 7.9 shows that by applying a higher field (below 200 mT), λ does not fall to be zero but stays constant at $\sim 0.43\,\mu s^{-1}$ which is almost the saturation relaxation rate due to the Orbach process at low temperatures. Hence the Redfield formula may be not applicable to this situation. On the other hand, Fig. 7.5 shows that the fluctuation rate of the paramagnetic state (at 500 mK) can be largely increased by a low external field, which clearly shows that the assumption for the Redfield formula is not satisfied in $Nd_2Zr_2O_7$. Therefore, the increase of λ in zero field below 20 K is ascribed to the establishment short-range spin correlations which slow down the system.

And the applied field competes with the exchange interactions or breaks the short-range correlations and thus recovers λ to be the single ion relaxation rate due to the Orbach process by increasing the fluctuation rate. In addition, the increase of λ in high fields ($> 200\,\mathrm{mT}$) shown in Fig. 7.9 is possibly due to the crystal field effect.

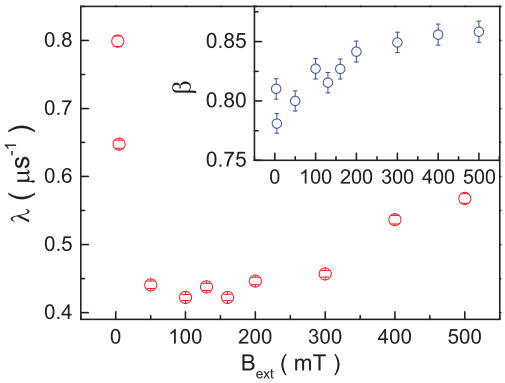

Figure 7.9: Field dependence of the fitted relaxation rate λ and exponent β (inset) at 1.55 K.

7.5 Magnetic dipolar field calculation

In order to find out whether there is a magnetic dipolar field cancellation at the possible muon stopping sites, the dipolar field distribution is calculated for the AIAO magnetic structure. The software *Mmcal* is used for the calculation [192]. First the crystal structure and the AIAO magnetic structure are constructed. The moment of Nd^{3+} used is $1\,\mu_B$ and the result can be extended to different moment sizes conveniently by adding the a scale factor. Second, the minimum radius of the sphere for dipolar field summation is determined to be $5 \times$ (lattice parameter) which gives a fair accuracy (error less that 1%) and a reasonable computation time. Third, the positions in the unit cell for calculating the dipolar field are around the oxygen anions within a distance of 0.9-1.1 Å and more than 0.1 Å and 0.12 Å away from Nd^{3+} and Zr^{4+}, respectively (these values are estimated based on the ionic radii). The volume for the calculation is $\sim 12\,\%$ of the volume of the unit cell and uniformly distributed $\sim 1.2 \times 10^5$ points are selected for the calculation.

Fig. 7.10 shows the calculated probability distribution of the dipolar field in the space. There is almost nowhere that has a zero magnetic field. The dipolar field around O($48f$) contributes most of the probability because most of the oxygen ions are at the $48f$ site.

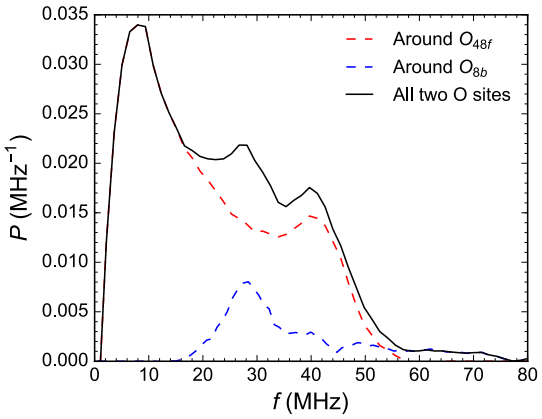

Figure 7.10: Magnetic field distribution around the two oxygen sites in $Nd_2Zr_2O_7$ for the AIAO magnetic structure. The x-axis is the magnetic field converted to be muon oscillation frequency for the case that Nd^{3+} have a ordered moment $1\,\mu_B$. The y axis is the probability per MHz.

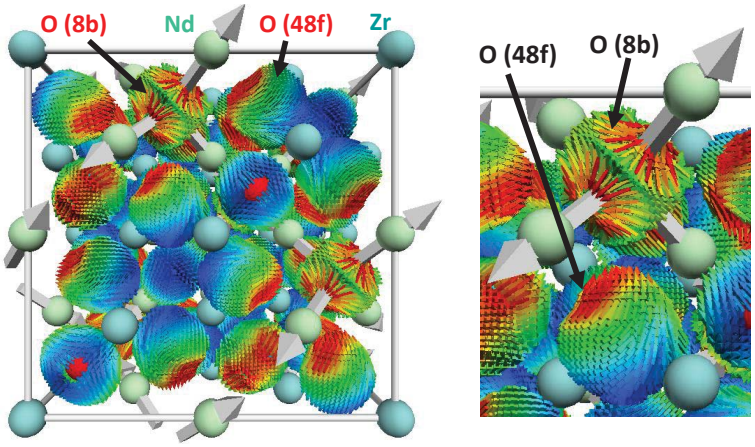

Figure 7.11: Calculated dipolar field in the unit cell (left) and the zoomed view around O($8b$) and O($48f$) (right). The spheres are the ions in the unit cell (oxygen ions are surrounded by small arrows), the large grey arrows are the moments of Nd^{3+} and the small color-coded arrows around the oxygen ions show the field directions and strength at those positions (the strength increases for the colors from blue to red).

The dipolar field around O($8b$) is very strong because the $8b$ site is inside the tetrahedron formed by four Nd^{3+} ions and these cations are very close to the oxygen ion. Fig. 7.11 shows the spacial distribution of the dipolar field in the unit cell. As can be seen, the

local dipolar field is dominated by the field generated by the neighbouring spins. These results suggest that the absence of oscillations in the zero field muon spectrum at low temperatures is not due to cancellation of the dipolar field at the muon site as discussed in Sec. 7.3.

7.6 Conclusions

This chapter presents the μSR study on the spin dynamics of the dipolar-octuplar psuedospin system $Nd_2Zr_2O_7$ which shows the long-range "all-in/all-out" order below $T_N = 0.4\,K$. It is found that the spin dynamics slow down with decreasing temperature and become almost temperature independent below the ordering temperature indicating the presence of persistent spin dynamics in the ground state. No oscillations or missing asymmetry is observed at 20 mK far below T_N, which points to the strong spin fluctuations in the ordered state. This result is consistent with the presence of significant transverse terms in the spin Hamiltonian which enable the spin dynamics in the Ising system. The data in longitudinal fields also reveal the dynamical nature of the ground state and suggest a field-induced metamagnetic transition at $\sim 80\,mT$ consistent with the AC susceptibility data in Chapter 4 and the reported magnetization data in Ref. [129]. Several pyrochlore compounds ($Er_2Ti_2O_7$, $Tb_2Sn_2O_7$ and $Yb_2Sn_2O_7$) have been found to show magnetic Bragg peaks in neutron diffraction but without oscillations in the μSR spectra. This can be understood by considering the different time scales of the two types of techniques where slowly fluctuating spins whose motion is measurable using muon spectroscopy while appear static in neutron diffraction [113, 180]. The strong dynamics in $Nd_2Zr_2O_7$ are remarkable because $Nd_2Zr_2O_7$ has Ising anisotropy and it is the multipolar interactions that introduces the dynamics.

The almost constant fluctuation rate below T_N suggests that the quantum fluctuations may dominate at low temperatures which can be temperature independent. According to the muon spin relaxation rate calculation for the classical dipolar pyrochlore antiferromagnet $Gd_2Sn_2O_7$ which has a gapped spin wave excitations, the relaxation rate should decrease exponentially to zero for $T \to 0$ [193]. As shown in Chapter 6, the spin wave spectrum of $Nd_2Zr_2O_7$ also has a gap ($\sim 0.8\,K$) and the relaxation rate of $Nd_2Zr_2O_7$ at 20 mK should vanish. In contrast, the persistent spin dynamics observed in $Nd_2Zr_2O_7$ could be related the quantum fluctuations in the ground state because $Nd_2Zr_2O_7$ is proximate to the $U(1)$ spin liquid phase [152].

Anomalously slow paramagnetic spin dynamics are also found for $Nd_2Zr_2O_7$ which has been reported for many frustrated magnets, such as $Tb_2Ti_2O_7$, $Yb_2Ti_2O_7$, $Yb_2Sn_2O_7$

and $Nd_2Sn_2O_7$ and related to strong short-range spin correlations in the paramagnetic state [131, 183, 194]. It is possible that $Nd_2Zr_2O_7$ shows some features of the quantum spin ice state above T_N where the long-range order is lost and the spins are highly correlated and fluctuating. As shown in Chapter 6, the ferromagnetic $\tilde{J}^{\tilde{x}\tilde{x}} \sim 1.1$ K is responsible for the ice-rule correlations which is much larger than the antiferromagnetic $\tilde{J}^{\tilde{z}\tilde{z}} \sim -0.6$ K leading to the AIAO order. Thus the ice-like correlations should be dominant in the paramagnetic state and could survive at temperatures much higher than T_N, leading to the anomalously slow paramagnetic spin dynamics.

8 Neutron diffraction and muon spin relaxation studies on $Gd_2Zr_2O_7$

8.1 Introduction

The ground state of the Heisenberg pyrochlore antiferromagnet with large spin moments was predicted to be the classical spin liquid state or a state with infinite degeneracy [86]. Experimentally, several materials were found to show the classical spin liquid state. In the 1994, Harris *et al.* found that $CsNiCrF_6$ with a pyrochlore sublattice of isotropic Cr^{3+} showed a liquid structure factor in the neutron diffraction experiment [29, 91]. In 1996, liquid-like correlations were also observed in the cubic Lavas phase of $(YSc)Mn_2$ [90]. The spinel $ZnCr_2O_4$ which has a Cr^{3+} pyrochlore lattice exhibits a striking state with disordered interacting spin loops as suggested by the neutron scattering experiment above the structural transition temperature [195].

The pyrochlore compounds $Gd_2B_2O_7$ (B can be, for example, Ti, Sn, Pt, Zr, Hf) with nearly isotropic Gd^{3+} (with $\boldsymbol{L} = 0$, $\boldsymbol{S} = 7/2$ and $\boldsymbol{J} = 7/2$) are also candidates for the classical spin liquid. However, the long-range dipolar interaction should be considered in addition to the exchange interaction due to the large moment of Gd^{3+} and a weak single-ion anisotropy may also exist [94, 101–103]. Therefore, the effects of these weak perturbations to the ideal Heisenberg antiferromagnetic system can be studied with these compounds. $Gd_2Ti_2O_7$ and $Gd_2Sn_2O_7$ have been studied with neutron diffraction and two distinct magnetic orders were found [93, 95]. $Gd_2Ti_2O_7$ shows a magnetic structure with ordering wavevector $\boldsymbol{k} = (1/2, 1/2, 1/2)$ and coplanar spin order on the kagomé plane and disorder on the interstitial triangle lattice [95]. However, it is debatable whether it is a single-k or multiple-k structure [96, 97]. $Gd_2Sn_2O_7$ adopts the Palmer-Chalker order due to a specific type of further-neighbour exchange interaction [93]. Recently, the paramagnetic polarized neutron diffraction also shows that fourth-neighbor interactions are important in $Gd_2Sn_2O_7$ [196]. Very recently, a long-range order was also found in $Gd_2Pt_2O_7$ with non-magnetic Pt^{4+} in a μSR experiment [35]. As to the spin dynamics, gapped spin wave excitations are observed in $Gd_2Sn_2O_7$ with

inelastic neutron scattering experiments [100] which results from the dipolar interaction according to the spin wave calculation [94]. Persistent spin dynamics in the ordered state were found in these three compounds by muon spin relaxation and Mössbauer experiments [35, 197–202] but the theoretical calculation for $Gd_2Sn_2O_7$ based on the gapped magnon excitations indicates an exponentially vanishing of the relaxation rate as $T \to 0$ in contrast [193].

In this chapter, the magnetic ground state of $Gd_2Zr_2O_7$ is investigated using powder neutron diffraction and muon spin relaxation (μSR). $Gd_2Zr_2O_7$ does not show magnetic Bragg peaks at temperatures down to 50 mK but only magnetic diffuse scattering though the AC susceptibility and the specific heat indicate a crossover at ~ 0.7 K (see Chapter 4). The diffuse scattering pattern is analysed with the reverse Monte Carlo method which produces the possible spin configurations that fit the data. The analyses reveal dipolar spin correlations in $Gd_2Zr_2O_7$ and a local spin arrangement on a tetrahedron similar to the spin configuration of the Palmer-Chalker phase. The μSR spectra show no static features at temperatures down to 1.55 K. These analyses suggest spin-liquid-like features in $Gd_2Zr_2O_7$ despite the presence of some Gd/Zr disorder at low temperatures.

8.2 Neutron diffraction experiment details

Due to the high neutron absorption cross section of Gadolinium of natural abundance, highly enriched isotope $^{160}Gd_2O_3$ (99.98%) from Oak Ridge National Lab was used to synthesize the sample. Powder $^{160}Gd_2O_3$ and ZrO_2 were first heated to 1000 °C to remove moistures and then solid state reaction was performed as described in Chapter 4. About 1.8 g mixed powder of $^{160}Gd_2O_3$ and ZrO_2 was annealed at 1200, 1400, 1500 and 1550 °C successively with ~ 1 hour intermediate grindings. The last heat treatment was performed at 1400 °C for 4 days to reduce Gd/Zr antisite defects. The sample shows sharp pyrochlore superlattice Bragg peaks in the lab-based X-ray diffraction pattern but also has a tiny trace of impurity peaks of $GdAl_{11}O_{18}$ [203, 204] arising from reactions between the sample and the alumina crucible at 1500 °C.

The AC susceptibility of the sample in Chapter 4 shows a broad peak at ~ 0.7 K, consistent with the reported heat capacity data which shows a sharp peak at 0.769 K indicating an ordering transition [138]. However the neutron diffraction experiment shows no magnetic Bragg peak at temperatures down to 0.05 K which was performed on the DMC diffractometer at PSI. There may be large amount of antisite defects in the sample. Therefore, further annealings were performed successively at 1400, 1300 and 1200 °C for in total more than 20 days with slow cooling (10 °C/hour). The AC susceptibility shows

little change (even the completely disordered sample shows a similar AC susceptibility) and the room-temperature neutron diffraction on D2B diffractometer (ILL) indicates about 20 % Gd/Zr antisite mixing (see Chapter 4). The second neutron diffraction experiment was conducted on the diffractometer D20 at ILL at 0.06 K but there were still no magnetic Bragg peaks observed. The following two paragraphs give the details of neutron diffraction experiments.

The first powder neutron diffraction measurement was performed on the DMC diffractometer at PSI on the initially-prepared sample. About 1.5 g $^{160}Gd_2Zr_2O_7$ powder was sealed in a cylindrical copper can of 5 mm diameter which was filled by high pressure ^{3}He gas for good thermalization. The sample was cooled down to 0.05 K by a dilution refrigerator. Two instrument settings were used: first, neutrons wavelength 2.46 Å, 2θ range 11–92.7 °, temperature range 50 mK–4 K, a counting time of 4 hours for 50 mK and 4 K and 2 hours for the other temperatures; second, wavelength 4.20 Å (LD mode), temperature range 50 mK-20 K, counting time of 4 hours for 50 mK and 20 K and 2 hours for the other temperatures, 2θ ranges of 5.5–136.7 ° for 0.05, 4, 10 and 20 K and 5.5–87.2 ° for the other temperatures.

The second neutron diffraction experiment was conducted on sample after further annealed using the high-flux diffractometer D20 at ILL at temperatures between 60 mK and 20 K. The sample ($\sim$ 10 g) was sealed in a cylindrical copper can of 4 mm diameter and then mounted on a dilution refrigerator. The experiment was performed with different counting times and temperature ranges: for the first measurement, 4, 3 and 3 hours for 0.06, 0.6 and 1.2 K, respectively and 1 hour for the seven other temperatures in the range 0.06–10 K; for the second measurement, a shorter time ($\sim$ 0.5 hour) for eight temperatures in the range 1.7–20 K. The neutron wavelengths used in the two measurements are slightly different: 2.41 Å for the first measurement and 2.4024 Å for the second measurement. The two datasets were normalized according to the scale factor in the Rietveld refinement of the nuclear diffraction pattern. Afterwards, another diffraction pattern was recorded on the high-resolution diffractometer D2B at room temperature to investigate the structural defects. The sample was wrapped in aluminium foils and the neutron wavelength used is 1.051 Å.

For all the measurements, the nuclear diffraction patterns are refined using FullProf Suite [21] and the magnetic diffuse scattering shown in the D20 data was analysed with the reverse Monte Carlo method using the software SPINVERT and its extensions SPINDIFF and SPINCORREL for calculating single crystal neutron scattering pattern and spin correlation function, respectively [205]. Some modifications to SPINVERT and SPINDIFF were made in order to perform the fit with a supercell containing antisite

defects and to calculate single crystal polarized neutron diffuse scattering pattern.

8.3 Reverse Monte Carlo method

Reverse Monte Carlo (RMC) method was used for analysing the magnetic diffuse scattering signal in the neutron diffraction data. This method is commonly used for the determination of short-range correlations in the crystal structure and was recently introduced for studying magnetic correlations [205, 206]. In contrast to the direct Monte Carlo method (starting from a spin Hamiltonian), the RMC method only optimizes the spin configurations or spin correlations to fit the diffuse scattering pattern. This method has been tested by comparing the results with the direct Monte Carlo simulations for several classical magnetic systems [206] and successfully applied to magnetic materials, for example, the hyper-kagomé $Gd_3Ga_5O_{12}$ [207], the classical antiferromagnet MnO [208] and the ordered Heisenburg pyrochlore antiferromagnet $Gd_2Ti_2O_7$ [97], where new insights into the magnetism have been found.
Reverse Monte Carlo refinement is the process of fitting a large spin configuration to the neutron diffuse scattering data. During the process, movements of spin orientations are proposed randomly and then the corresponding diffuse scattering pattern of the new spin configuration is calculated and compared with the measurement. When the movements reduce the difference between the calculation and the data, the movements are accepted and then the same procedure is repeated until convergence. However, to reduce the probability of being trapped in local minima, "bad" movements which enlarge the difference are accepted with a certain probability. The probability P is adjustable which is

$$P = \exp(-w\chi^2), \tag{8.1}$$

where χ^2 is the normal parameter describing the fitting quality and w is a user-defined weight factor which has a similar role as the inverse temperature in the simulated annealing method. During the fitting, χ^2 decreases gradually and the probability of accepting a bad movement increases. At some point, the fitting quality saturates for a given w factor and to improve the fitting quality further a larger w factor can be setted.
SPINVERT is a open source software for the reverse Monte Carlo refinement and is used here for analysing the neutron diffuse scattering data of $^{160}Gd_2Zr_2O_7$ [205]. The software works only for simple lattices with one type of magnetic site. For a particular lattice and spin configuration, the powder averaged neutron scattering intensity is calculated

by (a specific local spherical coordinate system is defined) [205]

$$I(Q) = C\left[\mu f(Q)\right]^2 \left\{ \frac{2}{3} + \frac{1}{N} \sum_{i,j} \left[A_{ij} \frac{\sin Qr_{ij}}{Qr_{ij}} + B_{ij} \left(\frac{\sin Qr_{ij}}{(Qr_{ij})^3} - \frac{\cos Qr_{ij}}{(Qr_{ij})^2} \right) \right] \right\} \quad (8.2)$$

with

$$\begin{aligned} A_{ij} =& S_i^x S_j^x, \\ B_{ij} =& 2S_i^z S_j^z - S_i^x S_j^x, \end{aligned} \quad (8.3)$$

$$\mu^2 = g_J^2 S(S+1), \quad (8.4)$$

$$C = \left(\frac{\gamma_{\mathrm{n}} r_{\mathrm{e}}}{2} \right)^2 = 0.07265\,\mathrm{barn}, \quad (8.5)$$

where N is the number of spins, $f(Q)$ is the form factor of the magetic ion, S_i^α is the α component of the i^{th} spin at the position $\boldsymbol{r}_i$ and r_{ij} is distance between S_i and S_j. The constant 2/3 term accounts for the incoherent scattering or self-correlation of the spins and the second term for pair correlations.

In the software SPINVERT, the spins are taken as classical vectors of unit length, therefore, μ^2 is absorbed in the scale factor. It is convenient to refine the data measured with polarized neutrons where magnetic signal is separated from the nuclear signal. For the data collected with unpolarized neutrons, the magnetic-only pattern is obtained by subtracting the diffraction pattern of the high-temperature paramagnetic state. This treatment removes not only the nuclear scattering but also the paramagnetic scattering which is the constant 2/3 term, resulting in a $I(Q)$ curve oscillating around zero. In this case, the magnitude of the spin correlation is lost unless the data are in the absolute unit (barn/atom) or the scale factor is known.

Our data did not include polarisation analysis and it is not in the absolute unit. One method was suggested in Ref. [207] for processing the data of an antiferromagnet for the refinement. An antiferromagnet generally has zero scattering as $Q \to 0$ at sufficiently low temperatures. Assuming this rule holds for $Gd_2Zr_2O_7$ at 60 mK which is much lower than the Curie-Weiss temperature 6.8 K, the scale factor for the refinement can be

estimated as follows. From the condition $I(Q \to 0) = 0$, we have

$$-sC\left[\mu f(Q)\right]^2 \frac{2}{3} = sC\left[\mu f(Q)\right]^2 \frac{1}{N}\sum_{i,j}\left[A_{ij}\frac{\sin Qr_{ij}}{Qr_{ij}} + B_{ij}\left(\frac{\sin Qr_{ij}}{(Qr_{ij})^3} - \frac{\cos Qr_{ij}}{(Qr_{ij})^2}\right)\right] \sim I_{exp}(Q \to 0), \tag{8.6}$$

where $I_{exp}(Q \to 0)$ is the experimental intensity as $Q \to 0$ ($f(Q) = 1$ at this limit). Then, we get,

$$s\mu^2 = -\frac{3}{2}\frac{I_{exp}(Q \to 0)}{C} \tag{8.7}$$

Once the spin configuration has been refined, the spin correlation function $\langle \boldsymbol{S}(0) \cdot \boldsymbol{S}(r) \rangle$ can be calculated by averaging $\boldsymbol{S}(\boldsymbol{r}_i) \cdot \boldsymbol{S}(\boldsymbol{r}_j)$ within the coordination shell of the radius $r = |\boldsymbol{r}_i - \boldsymbol{r}_j|$.

8.4 Reverse Monte Carlo refinement

8.4.1 Dipolar spin correlations

Figure 8.1 shows the neutron diffraction data of powder $^{160}Gd_2Zr_2O_7$ sample measured at temperatures between 50 mK and 20 K on the DMC diffractometer with neutron wavelength 4.2 Å. With decreasing temperature, the paramagnetic scattering condenses gradually below ~ 20 K at certain Q positions especially at $Q \sim 1.2$ Å^{-1}. However, the pattern at the lowest temperature 50 mK does not show magnetic Bragg peaks but only strongly modulated magnetic diffuse scattering indicating short-range spin correlations. There is no anomaly around 0.7 K at which the AC susceptibility and specific heat shows a broad peak (see Chapter 4) (the reported specific heat shows a sharp peak at 0.769 K [138]). The absence of long range order could be due to the Gd/Zr antisite defects in the sample revealed by diffraction measurements as shown in Chapter 4.

Figure. 8.2 shows the data collected on the sample after further annealing on the D20 instrument (neutron wavelength 2.41 Å) after subtracting the 20 K data. As for the data measured on DMC, only strongly modulated diffuse scattering is observed but no Bragg peaks. The scattering pattern shows a very strong resemblance to the data of the pyrochlore antiferromagnets $(Y_{0.97}Sc_{0.03})Mn_2$ [90] and $CsNiCrF_6$ [91] and to the theoretical scattering patterns calculated with the Monte Carlo method [18] and mean field theory [209] for the classical Heisenberg pyrochlore antiferromagnet.

The scattering in the forward direction (close to $Q = 0$) is depleted at low temperatures compared with that at high temperatures indicating dominant antiferromagnet corre-

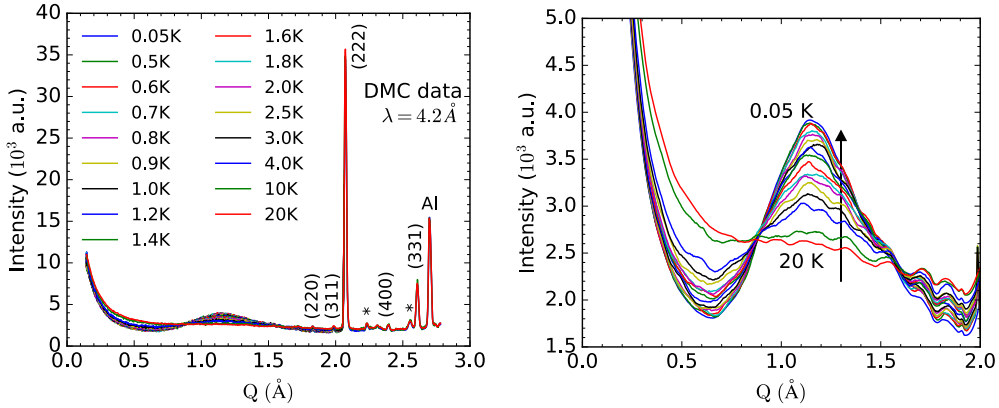

Figure 8.1: Neutron diffuse scattering data of powder $^{160}Gd_2Zr_2O_7$ measured on the DMC instrument with wavelength 4.2 Å at temperatures between 50 mK and 20 K: (left) overview of the all the data; (right) zoomed view for the diffuse scattering. The numbers above the peaks show the index of the Bragg peaks and the stars indicate the impurity peaks. The aluminium peak is also indicated.

lations, in agreement with the negative Curie-Weiss temperature. The strong broad peak at $Q \sim 1.2\,\text{Å}^{-1}$ corresponds to the nearest-neighbor antiferromagnetic correlations similar to the observations for $Gd_2Ti_2O_7$ [96]. For an isotropic antiferromagnet with nearest-neighbor correlations, the powder-averaged neutron scattering intensity is given by [210],

$$I(Q) \sim f^2(Q)\frac{\sin(Qr)}{Qr} \tag{8.8}$$

where $f(Q)$ is the form factor of the magnetic ion and r is the nearest-neighbor distance. For $Gd_2Zr_2O_7$ with $r \approx 3.7\,\text{Å}$, the model gives a similar modulation of $I(Q)$ as depicted in Fig. 8.2. When the temperature is lowered, the intensity of the peaks increases whereas the peak width seems to remain constant. This feature indicates that the spin correlation length never exceeds the nearest-neighbor distance even at temperatures far below the Curie-Weiss temperature -6.8 K, which is similar to the quantum Heisenberg spin-1/2 pyrochlore antiferromagnet [211, 212]. In addition, the patterns at temperatures below 1 K almost do not change indicating that the system is in the ground state. According to the mean field analysis, the nearest-neighbor Heisenberg model shows two degenerate zero-energy dispersionless modes arising from the high frustration and at temperatures lower than the Curie-Weiss temperature, the spin correlations of the two modes dominate which leads to the very weak temperature dependence of the scattering pattern [209, 213].

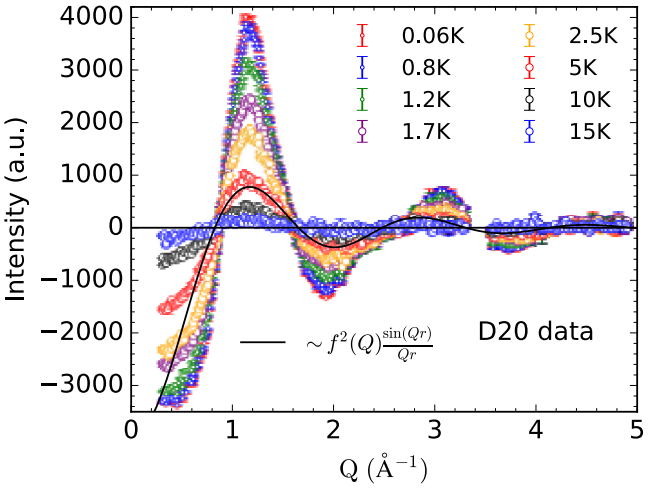

Figure 8.2: Neutron diffuse scattering data of powder $^{160}Gd_2Zr_2O_7$ after additional annealing measured on the D20 diffractometer with wavelength 2.41 Å at temperatures between 60 mK and 15 K. The pattern at 20 K is subtracted as a background which is featureless paramagnetic scattering.

To gain knowledge on the short-range correlations in $Gd_2Zr_2O_7$, the neutron diffuse scattering pattern is analysed with the reverse Monte Carlo refinement. Before fitting the background subtracted data at $T = 0.06$ K, the scattering due to self-correlation is added to the data which is estimated by the method mentioned in Sec. 8.3 and adjusted carefully to remove spurious features of the fit (e.g. extra oscillations in some Q regions, especially the part without data). During the refinement, a $6 \times 6 \times 6$ pyrochlore supercell (3456 spins in total) is generated and randomly oriented magnetic moments are assigned to the Gd^{3+} sites. Throughout the fitting the spin orientations are refined in order to fit the experimental data while the positions of spins are fixed at their crystallographic sites. In total 500 moves per spin are considered in a refinement and 20 individual refinements have been performed to ensure the robustness of the result. The defects in the crystal structure are not included in the current analysis.

The fitted magnetic diffuse scattering pattern is shown in Fig. 8.3, which agrees well with the experimental data ($R_{\mathrm{wp}} = 3.5\%$). The fitted first peak is slightly narrower than the data which could be an effect of the structural defects in the sample (the fitting gets better after including the structural defect as shown below). The fitted spin configurations are used to construct the Q-dependence of the diffuse scattering in the (HHL) reciprocal plane [Fig. 8.4(left)] by using the SPINDIFF program. The pattern shows corner-sharing triangles with strong intensity at $Q = [2, 2, 0] \pm [3/4, 3/4, 0]$ and

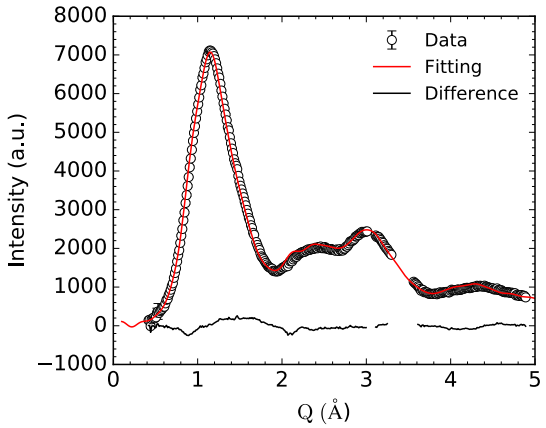

Figure 8.3: Corrected neutron diffuse scattering data of powder $^{160}Gd_2Zr_2O_7$ after annealing measured on D20 (black circles), the reverse Monte Carlo fitting (red line) and the difference between the data and the fit (black line).

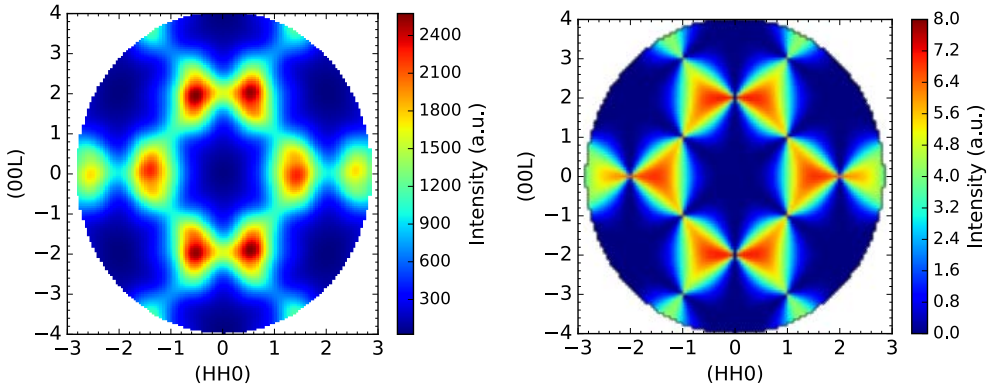

Figure 8.4: Dipolar spin correlations in the pyrochlore antiferromagnet with Heisenberg spin. (left) Calculated neutron diffuse scattering for single crystal $^{160}Gd_2Zr_2O_7$ in the (HHL) reciprocal plane based on the refined spin configurations. (right) Theoretical pinch point pattern reproduced according to Ref. [88, 89].

$[2,0,0] \pm [3/4,3/4,0]$ which is similar with the pinch pattern for Heisenberg pyrochlore antiferromagnets [Fig. 8.4(right)] indicating dipolar correlations [88, 89].

According to Refs. [51, 88, 89], the ground state ensemble of the frustrated pyrochlore antiferromagnet can be mapped to a coarse-grained pseudo "polarization" field satisfying a zero-divergence condition. The local constraint (e.g. ice rule and total spin on a tetrahedron equals zero) and the non-trivial entropic weight [$\sim$(polarization)^2] for a

microscopic ground state lead to dipolar correlations of the pseudo polarization field ($\sim 1/r^3$) [88, 89]. The real spin structure factor can be obtained by decoding the dipolar correlation of the pseudo polarization field. For the Heisenberg spins, the structure factor in the [HHL] reciprocal plane, $\boldsymbol{q} = (q_x, q_x, q_z)$, is given by [88]

$$S_{[\mathrm{HHL}]} = \frac{32[\cos(\frac{q_x}{4}) - \cos(\frac{q_z}{4})]^2 \sin(\frac{q_x}{4})^2}{5 - \cos(q_x) - 4\cos(\frac{q_x}{2})\cos(\frac{q_z}{2})}. \tag{8.9}$$

The calculated pattern shows a "bow-tie" or pinch point pattern [Fig. 8.4(right)] (the form factor of Gd^{3+} is included). The good agreement between the extracted structure factor based on the RMC refinement and the theoretical calculation indicates the presence of a Coulomb-liquid-like phase in $Gd_2Zr_2O_7$ with antisite defects.

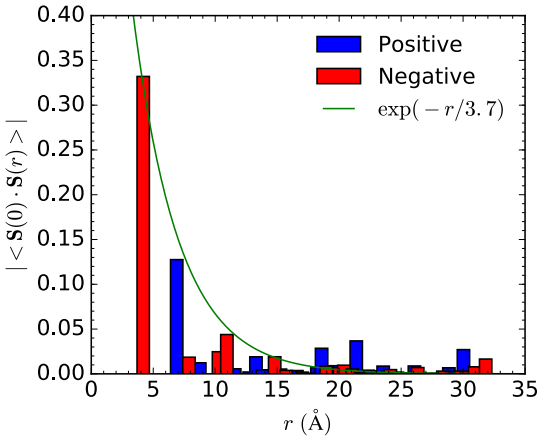

Figure 8.5: Calculated spin correlation function of $^{160}Gd_2Zr_2O_7$ based on the refined spin configurations. Each bar corresponds to a coordination shell for distance r between neighours. The solid line is the exponential correlation functions.

The real space radial spin pair correlation function $\langle \boldsymbol{S}(0) \cdot \boldsymbol{S}(r) \rangle$ is also calculated based on the fitted spin configurations by using the program SPINCORREL. Fig. 8.5 shows the calculated spin correlation function for the coordination shells contained in the supercell. A large absolute value of $\langle \boldsymbol{S}(0) \cdot \boldsymbol{S}(r) \rangle$ indicates a strong preference for a collinear arrangement of the spins separated by a distance r. The sign of $\langle \boldsymbol{S}(0) \cdot \boldsymbol{S}(r) \rangle$ indicates whether the spins are parallel (+) or antiparallel (-) to each other. The spin pair correlation function for the present compound includes both positive and negative values indicating antiferromagnetic spin correlations. The magnitude of the correlations decreases sharply with increasing distance indicating very short-range correlations mostly within the nearest-neighbor distance, which is consistent with the analysis above based

on the peak width. The fit to the exponential correlation function indicates a correlation length of ~ 3.7 Å which is exactly the nearest-neighbor distance. Note that it is the pseudo polarization field that has dopolar correlations not the real spins.
After modifying the software SPINVERT, the fitting with a supercell with Gd/Zr antisite defects can be done. Fig. 8.6 shows the fitting results with 20 % randomly-distributed Gd/Zr antisite defects in the supercell where the fitted curve and the calculated single crystal scattering pattern are shown (the amount of antisite mixing defects is estimated based on the Reitveld refinement of the nuclear diffraction pattern in Chapter 4). The fitting is improved especially around $Q = 1.5$ and 2 Å. and the R_{wp} factor becomes 2.5 % compared to 3.5 % for fitting with a perfect pyrochlore lattice. The calculated single crystal scattering pattern is qualitatively similar to the initial one but a little broader due to the disorder introduced by the defects.

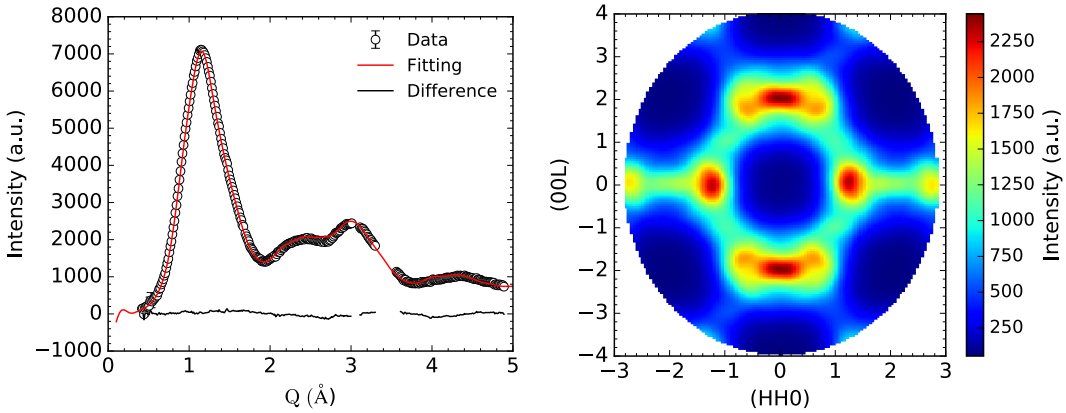

Figure 8.6: Reverse Monte Carlo fitting with a $6 \times 6 \times 6$ supercell containing 20% randomly-distributed Gd/Zr antisite defects. (left) Fitted powder diffraction pattern. (right) Calculated single crystal scattering pattern in the (HHL) reciprocal plane based on the fitted spin configurations.

8.4.2 Palmer-Chalker type local magnetic structure

Inspections to the fitted spin configurations (without structural defects) reveal that the local spin configuration on a tetrahedron is similar to that of the Palmer-Chalker phase shown in Fig. 8.7 which was observed in $Gd_2Sn_2O_7$ [93]. For this type of magnetic order, there are two bonds (bond 1-2 and bond 3-4 in Fig. 8.7) on a tetrahedron with spins oriented antiparallel and perpendicular to the bonds. The two bonds are at the opposite positions on the tetrahedron and the two pairs of antiparallel spins are perpendicular

with each other. The statistical analysis of the refined spin configurations are shown in Fig. 8.8 presented as histogram plots. First, the spins are mostly in the local {111} plane and there is nearly no net magnetization on the tetrahedron as shown in Fig. 8.8(a) and (b). The sum of the spins on a tetrahedron is slightly greater than zero which may be an effect of the antisite defects. Second, two pairs of spins on the tetrahedron are nearly antiparallel and they are generally perpendicular with the bonds connecting them, which is shown in Fig. 8.8(c) and (d). Finally, the two bonds with spins that are nearly antiparallely are mostly on the opposite sides on the tetrahedron with a percentage of 95 %.

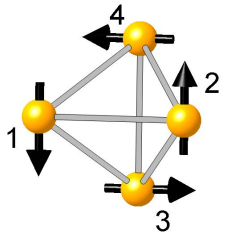

Figure 8.7: Local spin configuration on a tetrahedron of the Palmer-Chalker phase.

8.5 Muon spin relaxation above 1.55 K

8.5.1 Experimental details

The μSR experiment was performed on the GPS instrument at PSI on a normal powder sample (without isotope enrichment) which was prepared using the same annealing procedure as the isotope sample. About 1 g powder was wrapped into a slab about 2 mm thick using aluminium foil which was mounted on a helium-flow refrigerator. Longitudinal spectra were measured at different temperatures between 1.5 and 300 K in zero and 500 mT longitudinal fields. Longitudinal field dependence of the spectrum is measured at 1.55 K. The data was analysed using the software Musrfit [186].

8.5.2 Analyses and results

Figure 8.9 shows the longitudinal μSR spectra in zero field at different temperatures between 1.55 and 300 K. The spectra show a fast damping of the asymmetry and even at 300 K the spectrum is far from the flat line expected at the fast fluctuation limit. The spectra only show an apparent temperature dependence below 5 K and above 5 K the

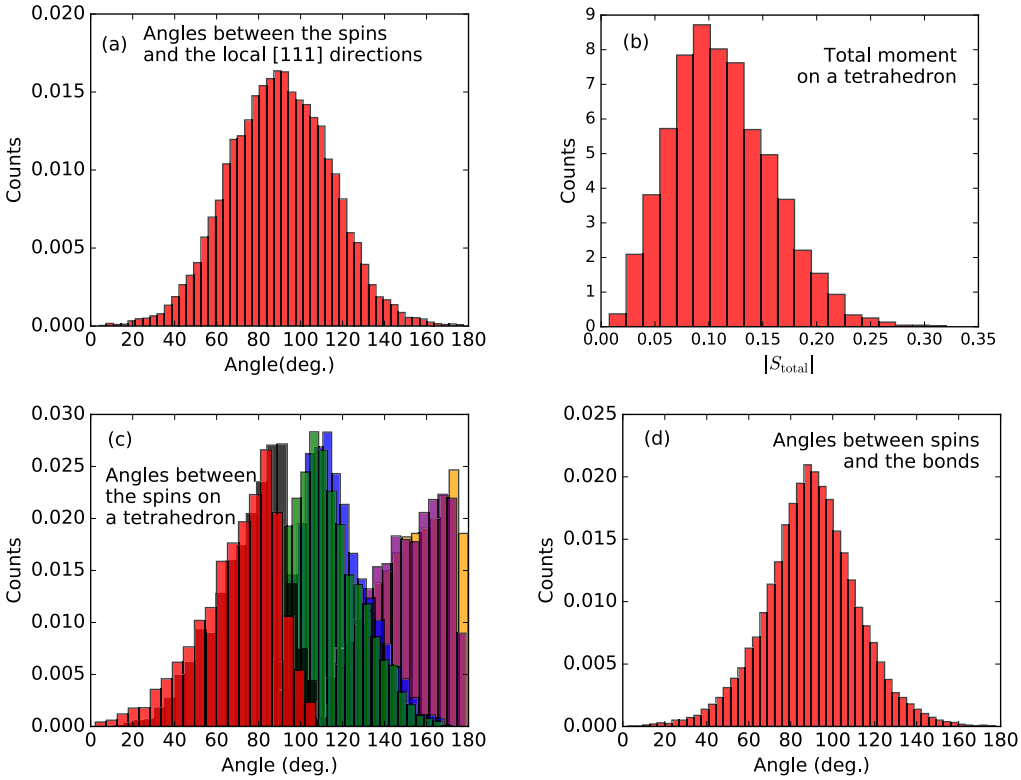

Figure 8.8: Spin orientation statistics of the refined spin configurations of $^{160}Gd_2Zr_2O_7$ excluding defects presented by histogram plots. (a) Angles between the spins and the local [111] directions. (b) Vector sum of the spins on the tetrahedron. (c) Angles between the spins on the six bonds on the tetrahedron (the six angles between the spins on the tetrahedron are first sorted and then the histograms are calculated for the six angles over all the tetrahedra). (d) Angles formed by the nearly antiparallel spins with the bonds connecting them.

spectra are very similar. The data can be fitted with the stretch exponential function Eq. 3.36 which is generally used to describe the μSR spectra of a system with a continuous distribution of relaxation processes [113]. The fitted relaxation rate λ and exponent β are shown in Fig. 8.9. The relaxation rate and the exponent are almost constant above 5 K. At 5 K, λ starts to increase indicating slowing down of the system. This critical temperature is comparable with the Curie-Weiss temperature of -6.8 K which indicates the onset of spin correlations. While the neutron diffraction data reveal that the short-range spin correlations start to build up at 20 K. The difference between the two results

is attributed to the different time scales detected by the two different techniques. Due to the limited energy resolution of the neutron diffractometer, fast fluctuating correlations at high temperatures could be detected.

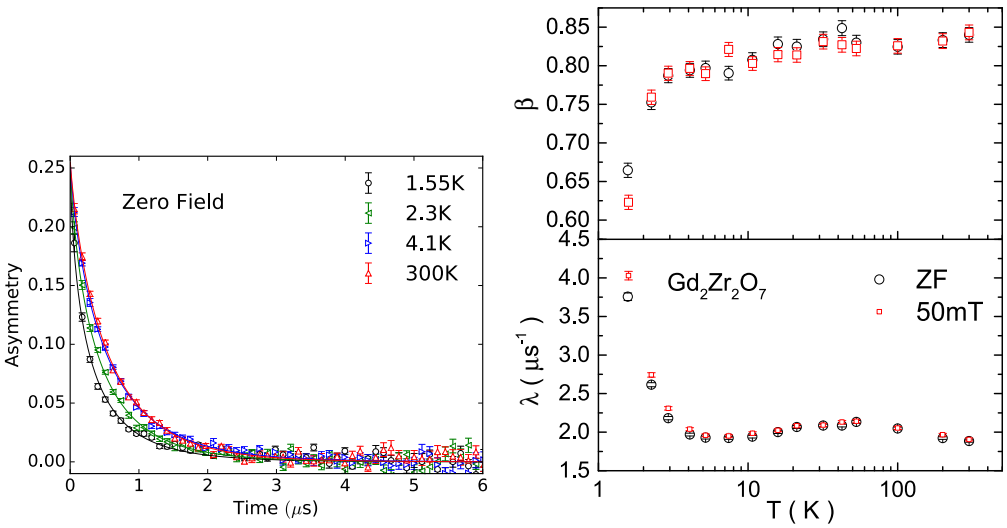

Figure 8.9: (left) μSR spectra in zero field at temperatures between 1.55 K and 300 K. (right) Temperature dependence of the fitted parameters λ and β for the stretched exponential function for zero and 50 mT longitudinal fields.

The spectra in longitudinal fields up to 0.5 T do not show significant differences with the zero field data. Fig. 8.10 shows the data in zero and 0.5 T fields at 1.55 K which nearly overlap. The spectra measured in fields are also fitted with the stretched exponential function. The temperature dependences of λ and β in the 0.05 T field are very similar to those in zero field. For the high temperatures the fitted parameters in the zero and 0.05 T fields are almost the same and at temperatures below $\sim$ 5 K, the relaxation rate in fields is higher than in zero field (Fig. 8.9). The field dependence of the fitted parameters at 1.55 K are shown in Fig. 8.10. With increasing the field, the sample shows a slightly higher relaxation rate.

The weak field dependence of the relaxation rate below 5 K could indicate a large field fluctuation rate of $Gd_2Zr_2O_7$. Assuming the internal field has a Gaussian distribution and at the fast fluctuation limit, the relaxation rate can be related to the distribution width Δ_G, fluctuation rate ν and external field B_{ext} by the Redfield formula [113] (see Chapter 3),

$$\lambda = \frac{2\gamma_\mu^2 \Delta_G^2 \nu}{(\gamma_\mu B_{ext})^2 + \nu^2}. \tag{8.10}$$

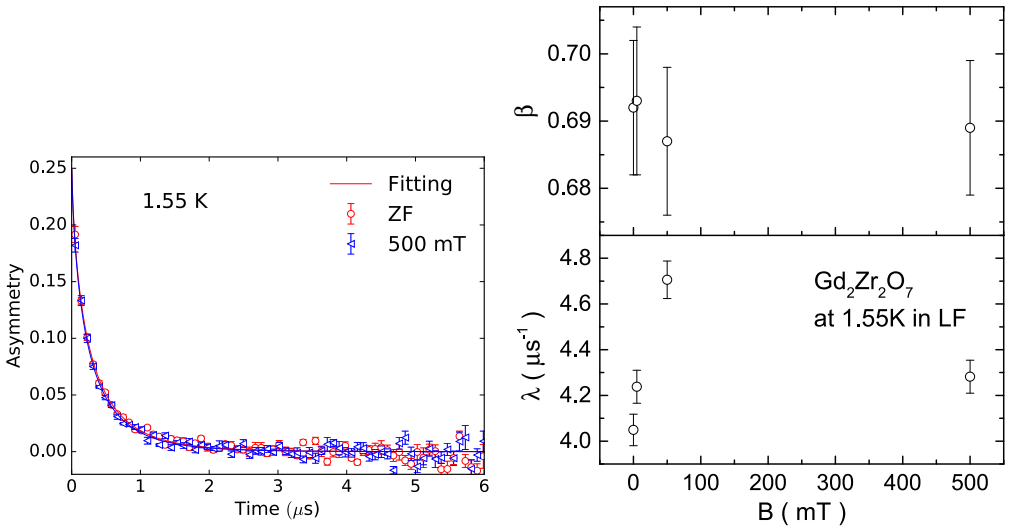

Figure 8.10: (left) μSR spectra in zero and 500 mT fields at 1.55 K; (right) fitted parameters of the stretched exponential function at 1.55 K in different fields.

Accordingly, the longitudinal field dependence of the relaxation rate can be described by a Lorentz function with half width at half maximum to be ν/γ_μ. When the system has a large ν comparing to the external field, the field is not expected to change λ significantly. This could be due to the high frustration and may be an evidence for a fluctuating liquid-like ground state of $Gd_2Zr_2O_7$.

The fast damping at temperatures much higher than the Curie-Weiss temperature is attributed to a large field distribution width as a result of the large magnetic moment of Gd^{3+}. We can estimate the fluctuation rate at high temperatures for $Gd_2Zr_2O_7$ according to the Redfield formula with zero field, $\lambda = 2\gamma_\mu^2\Delta_G^2/\nu$. The field distribution width is taken as being of the same order as the internal fields observed in $Gd_2Ti_2O_7$ and $Gd_2Sn_2O_7$, that is, $\Delta_G \sim 200$ mT corresponding a muon precession frequency $\gamma_\mu\Delta_G \sim 170$ MHz (where $\gamma_\mu = 0.851$ rad/μs/mT) (the muon spin oscillation frequencies of $Gd_2Ti_2O_7$ and $Gd_2Sn_2O_7$ indicate local fields of 194(1) and 149(1) mT, and 206 and 441 mT, respectively [198, 201]). The fluctuation rate is calculated to be 29 GHz, which is reasonable for the paramagnetic state.

8.6 Conclusions

In this chapter, the magnetic ground state of pyrochlore Heisenberg antiferromagnet $Gd_2Zr_2O_7$ is investigated using powder neutron diffraction and μSR. In contrast to the

similar compounds $Gd_2Ti_2O_7$ and $Gd_2Sn_2O_7$ which order magnetically [93, 95], no long-range magnetic order is observed in $Gd_2Zr_2O_7$ at temperatures down to 50 mK far below the anomaly temperature of χ_{AC}. The reverse Monte Carlo analyses reveal dipolar spin correlations indicating a liquid-like state which appears similar to the classical spin liquid state expected for the Heisenberg pyrochlore antiferromagnet [51, 86–89]. The local spin configuration on a tetrahedron is similar to that of the Palmer-Chalker phase. These results suggest that $Gd_2Zr_2O_7$ could be a dipolar pyrochlore antiferromagnet which hosts the short-range Palmer-Chalker order [92]. The absence of long-range order is related to the large amount of Gd/Zr antisite defects in the sample.

The μSR data shows no static features which is different from $Gd_2Ti_2O_7$ and $Gd_2Sn_2O_7$ for which moun spin oscillations were found [198, 201]. The relaxation rate of $Gd_2Zr_2O_7$ only shows a strong temperature dependence below 5 K which is attributed to the onset of spin correlations. The relaxation rate has a weak dependence on the longitudinal field indicating a large fluctuation rate in the system which may be evidence for the fluctuating liquid-like state as revealed by neutron diffraction. The weak frequency dependence in the AC susceptibility (see Chapter 4) excludes the spin glass state with frozen spins. Further μSR experiments at temperatures lower than the critical temperature shown in the χ_{AC} data could give more information on the dynamical properties of this liquid-like state.

Therefore, $Gd_2Zr_2O_7$ is quite different for $Gd_2Ti_2O_7$ and $Gd_2Sn_2O_7$ where long-range orders were observed in both neutron diffraction and μSR experiments. This may be because that the $Gd_2Zr_2O_7$ sample contains a large amount of Gd/Zr antisite defects. However a significant amount of defects are not easy to avoid because this compound is located at the boundary between the pyrochlore and fluorite phase of the rare earth zirconate pyrochlore series. The antisite defects make the magnetic ions diluted on the Gd and Zr sublattices in $Gd_2Zr_2O_7$, which could introduce weakly correlated spins and break the potential long-range order.

9 Crystal field states and spin dynamics of $Sm_2Zr_2O_7$

9.1 Introduction

In this chapter, the crystal field state and spin dynamics of another rare earth zirconate pyrochlore $Sm_2Zr_2O_7$ are studied with inelastic neutron scattering and muon spin relaxation, respectively. As for $Nd_2Zr_2O_7$, $Sm_2Zr_2O_7$ with the Kramers Sm^{3+} ion is expected to show the local [111] Ising anisotropy and the smaller moment and the less localized electrons of Sm^{3+} compared with the heavy rare-earth ions could enhance the transverse fluctuations, which makes it a candidate for quantum spin ice. As shown in Chapter 4, the field dependence of the magnetization of $Sm_2Zr_2O_7$ at 2 K can be described by the pseudospin-1/2 model and the specific heat also supports the pseudospin-1/2 picture and reveals a possible crossover at ~ 0.5 K. These findings make it interesting for further studies.

The crystal field states of both $Sm_2Zr_2O_7$ and $Sm_2Ti_2O_7$ were previously studied using Raman scattering and specific heat measurements [144] and for $Sm_2Ti_2O_7$, the susceptibility was analysed based on the CEF theory allowing the ground state wavefunction to be extracted [145]. A general conclusion that can be made is that the crystal field ground states are well-isolated Kramers doublets for the two compounds however the CEF splitting scheme and ground state wave function are not accurately known. In the Raman spectra of $Sm_2Zr_2O_7$, four modes instead of the two expected from the $^6H_{5/2}$ manifold were proposed to be the CEF transitions which are near 85, 130, 165 and 210 cm^{-1}. But the specific heat data suggests that the expected two CEF levels are at 130 and 210 cm^{-1}. For $Sm_2Ti_2O_7$, the crystal field modes are possibly at 87, 132, 158 and 270 cm^{-1} and while the specific heat data indicate two modes at 50 and 132 cm^{-1}. Therefore, a decisive conclusion cannot be made based on the Raman spectra because of the difficulty in distinguishing the CEF and phonon modes in the spectra especially considering that extra Raman active modes could appear due to structural inhomogeneities [145]. The temperature dependence of the susceptibility of $Sm_2Ti_2O_7$ indicates that

the two CEF excited states are at 172.4 and 212.7 cm^{-1} and the CEF ground sate is a dipolar-octupolar doublet with Ising anisotropy ($g_{zz} = 0.24$) [145].
Here, neutron inelastic scattering (INS) data of $Sm_2Zr_2O_7$ and crystal field analysis provide convincing direct evidence for a dipolar-octupolar CEF ground state with Ising anisotropy and validate the pseudospin-1/2 model. The μSR spectra reveal that strong spin dynamics persist down to 20 mK excluding the possibility of static long-range order of $Sm_2Zr_2O_7$ in the time scale of μSR.

9.2 Inelastic neutron scattering

9.2.1 Experiment details

A low-neutron-absorbing isotope $^{154}Sm_2Zr_2O_7$ powder sample (12 g) was prepared by the solid state reaction method (see Chapter 4 for details). The inelastic neutron scattering experiment was performed on the direct geometry time-of-flight spectrometer Merlin at ISIS, UK. The same measurement on $La_2Zr_2O_7$ (19 g) was also conducted as a background reference. In order to avoid hydrogen scattering from the moisture in the sample, the powder samples were heated at 1000°C overnight and then sealed in glass bottles and kept in a glove box just before the experiment. During the experiment, the samples were sealed in aluminium foil sachets (13 cm long and 4 cm wide) and then put inside a cylindrical can (40 mm in diameter) forming an annular distribution. The cross section of the sample is 40×40 mm^2, the same as the beam size. A closed-cycle refrigerator was used for cooling the sample down to 6.8 K. A vanadium standard sample of the same shape was also measured for converting the data in absolute units.
According to Kramers theorem, the LS-coupling ground state multiplet $^6H_{5/2}$ and the first excited multiplet $^6H_{7/2}$ (at $\sim$130 meV) of Sm^{3+} split into three and four Kramers doublets in $Sm_2Zr_2O_7$ respectively [2]. For the spectrometer, these states are accessible with a good energy resolution (4-7 % of E_i). Therefore, all those transitions were measured in order to have enough data to determined the six crystal field parameters. The inelastic neutron scattering data were collected at different temperatures with different incident neutron energies provided by different choppers. First gadolinium chopper were used for the low energy ranges which can produce multiple incident energies: $E_i = 12 and 30$ meV with the frequency 200 Hz (Setting A); $E_i = 20, 38 and 100$ meV with the frequency 350 Hz (Setting B). Then the sloppy chopper was used for the high energy measurements which produces single incident energies: 39 meV with the frequency 250 Hz (Setting C); 241 meV with the frequency 500 Hz (Setting D). The data of $Sm_2Zr_2O_7$ were collected with different conditions: at 6.3 K with the four settings and at 200 K with Set-

ting B. The data of $La_2Zr_2O_7$ were collected at 6.3 K with Settings C and D. The software SPECTRE was used for the analysis which included the J-mixing effect [157].

9.2.2 Dipolar-octupolar crystal field ground state

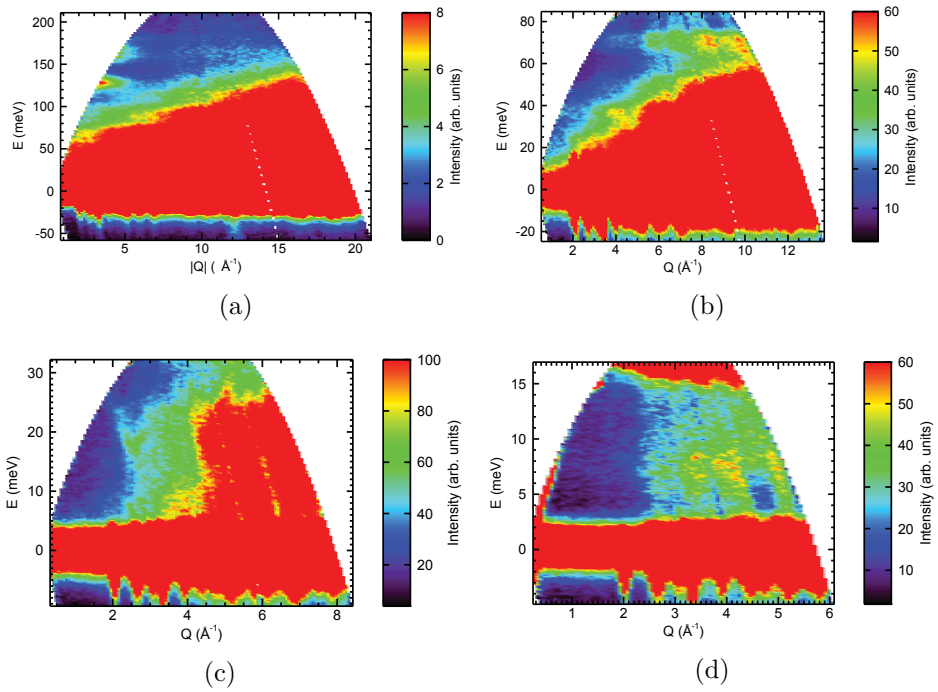

Figure 9.1: Time-of-flight INS data of $^{154}Sm_2Zr_2O_7$ at 6.8 K measured with E_i = 241 meV (a), 100 meV (b) , 38 meV (c), 20 meV (d), respectively.

Fig. 9.1 shows the color-coded $E - Q$ maps of the inelastic neutron scattering data of $Sm_2Zr_2O_7$ with different incident energies at 6.8 K. The two transitions expected within the ground state multiplet $^6H_{5/2}$ at low energies are not observed probably because they are too weak. Fig. 9.2(upper panel) shows the comparison of the data of $La_2Zr_2O_7$ and $Sm_2Zr_2O_7$ measured with $E_i = 39$ meV integrated in different Q ranges which is plotted as a function of energy. According to the form factor for the intra-multiplet transitions shown in Fig. 9.3, a maximum magnetic signal should appear at $Q = 4 \sim 5$ Å^{-1}. Such a magnetic signal cannot be easily spotted because the evolution of the background dominates the Q dependence of the spectra. After subtracting the $La_2Zr_2O_7$ data, the $Sm_2Zr_2O_7$ data shows some possible CEF transitions at around 15 and 27 meV [Fig. 9.2(lower panel)].

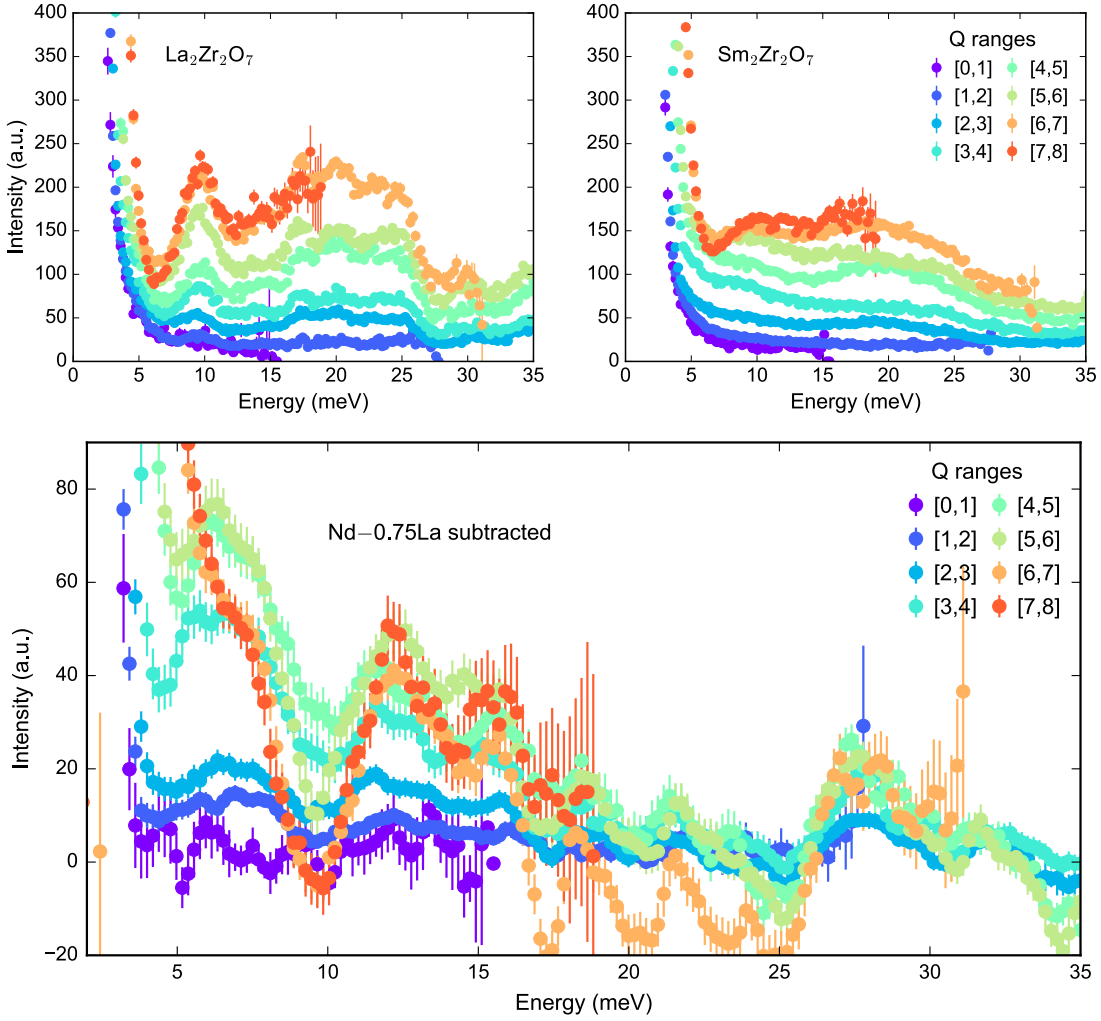

Figure 9.2: (upper panels) Comparison of INS data of $La_2Zr_2O_7$ (at 6.8 K) and $Sm_2Zr_2O_7$ (at 5.0 K) measured with $E_i = 39$ meV. The data have been integrated over different Q-ranges and plotted as a function of energy. (lower panel) Subtracted data with a scale factor 0.75 for the $La_2Zr_2O_7$ data.

At high energies, there are four dispersionless modes observed at around 135, 160, 170 and 180 emV [Fig. 9.1(a)] which have the general magnetic form factor of Sm^{3+} for the inter-multiplet transitions (Fig. 9.3). They are assigned to the inter-multiplet transitions from the ${}^6H_{5/2}$ manifold to the ${}^6H_{7/2}$ manifold. The transitions at around 160 and 170 meV are not resolved well (Fig. 9.4) but considering the instrument resolution, they are identified as two transitions. Fig. 9.4 shows the energy dependence of the spectra of $Sm_2Zr_2O_7$ and $La_2Zr_2O_7$ integrated over a small scattering 2θ range 8-10° where the

four ${}^6H_{5/2} \rightarrow {}^6H_{7/2}$ transitions are clearly shown. It also can be seen that the spectrum of $La_2Zr_2O_7$ gives a good estimate of the background after scaling by a factor due to the differences in the sample mass and nuclear neutron scattering cross section of the two samples. The Q dependence of the scattering intensity of the transition at 130 meV agrees well with the theoretical magnetic form factor for the $J = 5/2 \rightarrow J = 7/2$ transitions (Fig. 9.3 and Fig. 9.5).

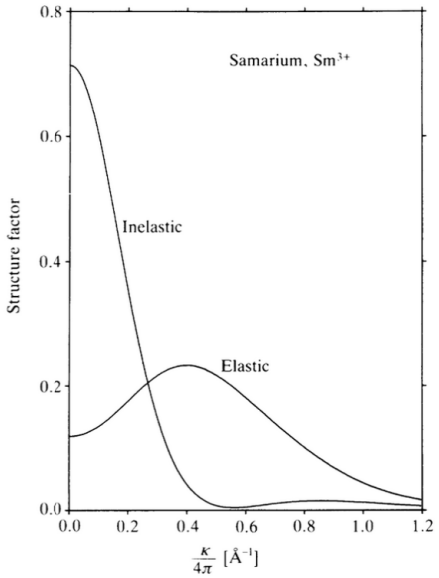

Figure 9.3: Magnetic form factor of Sm^{3+} for neutron scattering from Ref. [214]. The elastic one applies to the intra-multiplet transitions and the inelastic one to the inter-multiplet transitions (${}^6H_{5/2} \rightarrow {}^6H_{7/2}$).

The data are analysed with the crystal field model including the J-mixing effect which is normally large for Sm^{3+} because of the low-lying excited multiplets. The general form of the crystal field Hamiltonian is the same as the one given in Chapter 5 for $Nd_2Zr_2O_7$ in terms of tensor operators because the two compounds have the same site symmetry for the rare earth ions. The CEF parameters of the two compounds are different as a result of the different single-ion properties and slightly different coordination environments. The CEF parameters for $Sm_2Zr_2O_7$ can be estimated based on the parameters of $Nd_2Zr_2O_7$ and some other similar compounds according to the point-charge relation [4],

$$B_q^k(R)/B_q^k(\mathrm{Sm}) = \langle r^k \rangle_R / \langle r^k \rangle_{\mathrm{Sm}}, \tag{9.1}$$

where $\langle r^k \rangle_{\mathrm{R}}$ is the expectation values of the r^k operator over the $4f$ wave function of

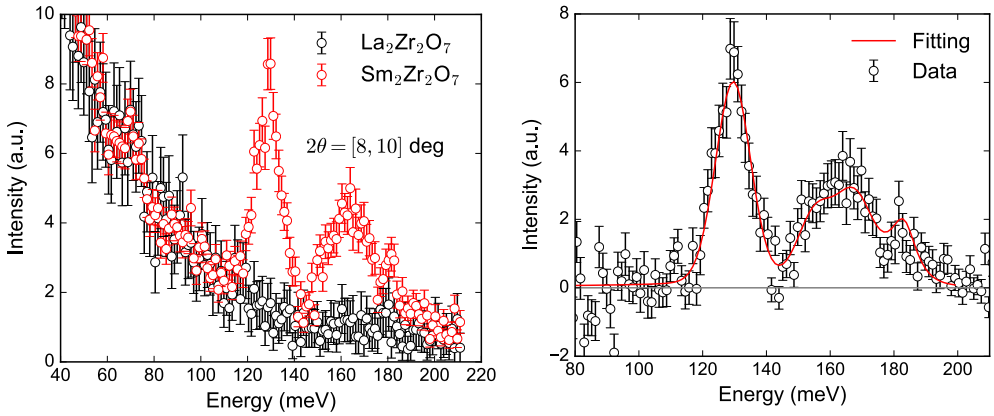

Figure 9.4: Left: constant 2θ cut of the inelastic neutron scattering data of $^{154}Sm_2Zr_2O_7$ and $La_2Zr_2O_7$ at 6 K measured with $E_i = 241$ meV (the $La_2Zr_2O_7$ data is scaled by a factor for serving as a good background); right: the background subtracted data (black circles) and the crystal field fitting (red line).

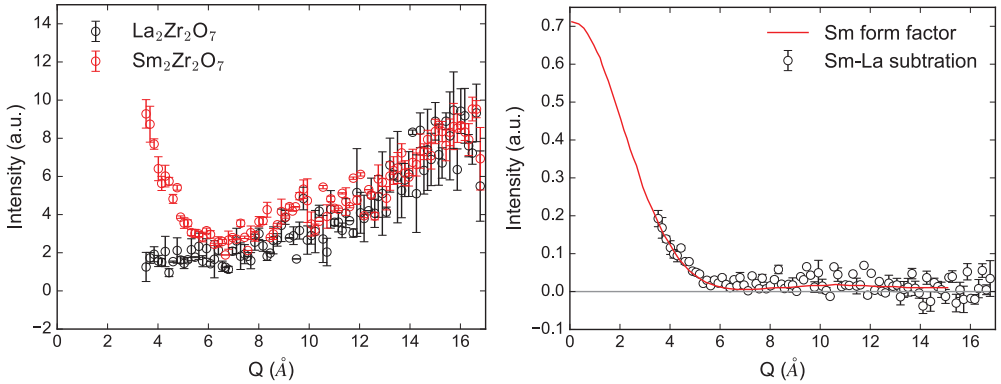

Figure 9.5: Q dependence of the inelastic neutron scattering intensity of the crystal field transition at $\sim$ 130 meV (integrated over the energy range [128,129] meV). Left: comparison between the data of $^{154}Sm_2Zr_2O_7$ and the scaled data of $La_2Zr_2O_7$; right: comparison of the background subtracted $^{154}Sm_2Zr_2O_7$ data with the theoretical form factor of Sm^{3+} for the inter-multiplet $^6H_{5/2} \rightarrow {}^6H_{7/2}$ transitions.

the ion R (i.e. the k^{th} radial moment of the $4f$-electron distribution) which is known for different rare earth ions [215]. After this scaling, the difference of the CEF parameters for the two ions is mostly due to slightly different coordination geometries and the CEF parameters for $Sm_2Zr_2O_7$ will be determined by fitting the data. Due to the high nonlinearity of the model for the least square fitting, good starting parameters are very

Table 9.1: Observed and calculated crystal field transition energies (E) and neutron scattering intensities (I) for the intra-multiplet ($^6H_{5/2}$) and inter-multiplet transitions ($^6H_{5/2} \rightarrow {}^6H_{7/2}$) of $^{154}Sm_2Zr_2O_7$ at 6.8 K (from the CEF ground state). The intensity is the relative intensity with respect to the intensity of the transition at 183 meV. The symbols in the first column indicate the irreducible representation involved [161].

Levels	E_{obs} (meV)	E_{cal} (meV)	I_{obs}	I_{cal}
Γ^+_{56}	0	0	-	0.026
Γ^+_4	-	16.4	-	0.078
Γ^+_4	-	35.7	-	0.022
Γ^+_4	130(3)	130.2	0.37(5)	0.37
Γ^+_{56}	157(5)	156.2	0.26(8)	0.23
Γ^+_4	168(5)	168.7	0.38(8)	0.45
Γ^+_4	183(4)	183.4	1	1

helpful for reaching a global minimum and the scaled CEF parameters from the similar compounds are used as the starting parameters. For the fitting, the CEF Hamiltonian is diagonalized in the Hilbert space formed by the intermediate-coupling bases of the free ion and the obtained eigenvalues and eigenfunctions are the CEF levels and wave functions. The neutron scattering intensity of the transition between the CEF states can be calculated by $f(Q)^2|\langle\phi_i|J_\pm|\phi_j\rangle|^2$ where $f(Q)$ is the magnetic form factor of Sm^{3+} and $|\phi_i\rangle$ is the CEF eigenfunction. The form factors for the intra-multiplet and inter-multiplet transitions are different, as shown in Fig. 9.3.

The fitting is done using the software SPECTRE [157] including the complete 108 intermediate-coupling basis states of the f^5 electron configuration of Sm^{3+}. Because the transitions within the ground state $^6H_{5/2}$ is not observed, only the energies and intensities of the inter-multiplet transitions are used for the fitting which are obtained by fitting the I vs E spectra in the 2θ range 8-10° with the pseudo-Voigt functions scaled by the form factor of Sm^{3+}. The two peaks at around 160 and 170 meV that are not well resolved are fitted with two peaks of the same width. The scaled CEF parameters of $Nd_2Zr_2O_7$ in Chapter 5 were used as the starting values (the scaled parameters of the other related pyrochlores were also tested). Fittings with randomly selecting the starting parameters within certain reasonable ranges are also performed to ensure that the global minimum had been reached. The best fit gives $\chi^2 = 0.2$ and the comparison of the observed and fitted CEF transition energies and intensities are presented in Table 9.1.

The fitted CEF parameters are listed in the Table 9.2 together with the reported pa-

Table 9.2: Fitted crystal field parameters (in meV) for $Sm_2Zr_2O_7$ and the reported ones for some other pyrochlore compounds. The parameters for $Sm_2Ti_2O_7$ are obtained based on the susceptibility analysis and for the other compounds they are obtained by analysing neutron scattering data.

	B_0^2	B_0^4	B_3^4	B_0^6	B_3^6	B_6^6
$Sm_2Zr_2O_7$ (this work)	95.1	411.2	73.4	149.4	-97.8	101.2
$Sm_2Ti_2O_7$ [145]	28.5	370.0	97.0	86.0	-78	123
$Pr_2Sn_2O_7$ [159]	57.9	432.8	161.0	144.5	-107.5	192.3
$Pr_2Hf_2O_7$ [177]	33.8	426.0	192.7	165.3	-111.8	178.6
$Nd_2Zr_2O_7$ [162]	49.2	408.9	121.6	148.1	-98.0	139.1
$Tb_2Ti_2O_7$ [62]	55.3	370	128	114	-114	120
$Dy_2Ti_2O_7$ [69]	67.5	268	153	66.7	77.2	132
$Ho_2Ti_2O_7$ [69]	78.2	285	121	113	-80.8	106

rameters for some other pyrochlore compounds. The determined CEF parameters for $Sm_2Zr_2O_7$ are comparable with those of other rare earth pyrochlores but the parameter B_0^2 seems too large for the light rare earth pyrochlores. The fitting indicates that the unobserved transitions within the ground state multiplet $^6H_{5/2}$ are at 16.4 and 35.7 meV with intensities less than 8% and 3% of the intensity of the strongest transition at 183 meV. The first intra-multiplet transition should be observed considering that amount of intensity but the signal can be broad for several reasons, for example, due to the exchange interactions, which makes it difficult to see [216]. The obtained CEF parameters for $Sm_2Zr_2O_7$ seem quite different from these of the counterpart compound $Sm_2Ti_2O_7$ from Ref. [145] (Table 9.2). These CEF parameters for $Sm_2Ti_2O_7$ are determined by analysing the susceptibility which suggest that the crystal field levels of $Sm_2Ti_2O_7$ lie at 21.4, 26.4, 135.6, 146.8, 162.7 and 186.3 meV which is a slightly smaller splitting of the $^6H_{5/2}$ and $^8H_{7/2}$ manifolds than that of $Sm_2Zr_2O_7$. However, comparing the lattice parameters of $Sm_2Ti_2O_7$ and $Sm_2Zr_2O_7$ (10.227Å vs 10.593Å [144]), a larger CEF splitting is expected for $Sm_2Ti_2O_7$ because its smaller lattice parameter could lead to stronger electric field due to the closer anions.

The calculated susceptibility and specific heat agree qualitatively with the measured values as shown in Fig. 9.6 (the C_p data is taken from Ref. [217]). The discrepancies are possibly because the neutron scattering data has a large uncertainty for the inter-multiplet transitions which are used for the crystal field analysis. Furthermore the susceptibility and specific heat at low temperature are dominated by the contribution of the crystal field states of the ground state multiplet which is not included in the analysis. The C_p data indicate that the two excited crystal field levels of the ground

state multiplet are at about 11 meV and 29 meV which are extracted from fitting the C_{p} data below 300 K considering only the CEF splitting of the ground state multiplet. This result seems to agree with the subtracted neutron data shown in Fig. 9.2 but if the inelastic neutron scattering data is fitted including these two energy levels, the result is not better. The reported Raman spectra of $Sm_2Zr_2O_7$ and the related pyrochlore compounds could be useful for current analysis [217–220]. But these Raman analyses are ambiguous when assigning the peaks in the spectra to the crystal field and the phonon modes [217]. Though the fitted CEF parameters are not able to reproduce the specific heat and susceptibility data quantitatively, they could give an approximate crystal field splitting scheme of $Sm_2Zr_2O_7$.

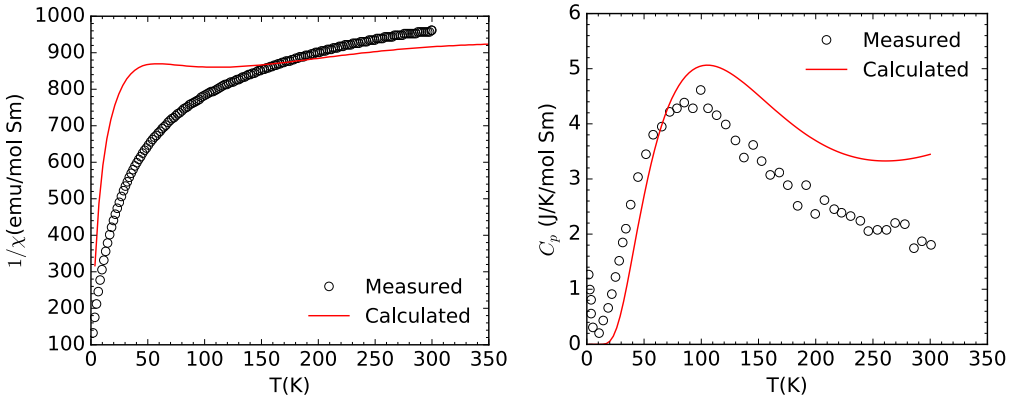

Figure 9.6: Left: comparison of the measured susceptibility and the calculated one; right: comparison of the specific heat data from Ref. [217] and the calculated one.

Based on the obtained CEF parameters, the wave functions of the CEF ground state doublet are calculated to be

$$\begin{aligned}\phi_0(\Gamma_{56}^{+}) = 0.983|^6H_{5/2}, \pm 3/2\rangle \mp 0.065|^6H_{5/2}, \mp 3/2\rangle - 0.085|^6H_{9/2}, \pm 3/2\rangle \\ + 0.058|^6H_{9/2}, \mp 9/2\rangle - 0.085|^6H_{9/2}, \pm 3/2\rangle \mp 0.077|^6H_{7/2}, \pm 3/2\rangle. \quad (9.2)\end{aligned}$$

which is composed of $|\pm 3/2\rangle$ and $|\pm 9/2\rangle$ and dominated by $|^6H_{5/2}, \pm 3/2\rangle$. Therefore, it is another example of dipolar-octupolar Kramers doublet which could support the appearance of the quantum spin ice phase on the pyrochlore lattice [17]. The first excited CEF state is above 10 meV, which means that the pseudospin-1/2 model is valid at low temperatures. The g factor is calculated from the wavefunction to be $g_{zz} \approx 0.50$ and $g_{\perp} = 0$, indicating Ising ansisotropy. The ground state magnetic moment is $g_{zz}\sigma = 0.25\,\mu_{\mathrm{B}}/\mathrm{Sm}$

Table 9.3: Wave functions for the excited crystal field states from the $^6H_{5/2}$ and $^6H_{7/2}$ multiplets of Sm^{3+} ion in $^{154}Sm_2Zr_2O_7$(only the first two leading terms of the wave functions are given).

First and second excited states of the ground state multiplet $^6H_{5/2}$.
$\phi_1(\Gamma_4^+) = 0.950\|^6H_{5/2}, \pm 1/2\rangle \mp 0.248\|^6H_{7/2}, \pm 1/2\rangle$
$\phi_2(\Gamma_4^+) = 0.907\|^6H_{5/2}, \pm 5/2\rangle \pm 0.343\|^6H_{7/2}, \pm 5/2\rangle$
Four doublets of the first excited multiplet $^8H_{7/2}$
$\phi_3(\Gamma_4^+) = 0.901\|^6H_{7/2}, \pm 1/2\rangle \pm 0.334\|^6H_{7/2}, \mp 5/2\rangle$
$\phi_4(\Gamma_4^+) = 0.861\|^6H_{7/2}, \pm 5/2\rangle - 0.281\|^6H_{7/2}, \mp 7/2\rangle$
$\phi_5(\Gamma_{56}^+) = 0.979\|^6H_{7/2}, \pm 3/2\rangle \mp 0.112\|^6H_{7/2}, \pm 3/2\rangle$
$\phi_6(\Gamma_4^+) = 0.813\|^6H_{7/2}, \pm 5/2\rangle + 0.360\|^6H_{7/2}, \mp 1/2\rangle$

($\sigma = 1/2$), consistent with susceptibility analysis ($\mu_{\text{eff}} = g_{zz}\sqrt{\sigma(1+\sigma)} = 0.39\,\mu_B/\text{Sm}$) and the magnetization analysis ($g_{zz} = 0.64$) in Chapter 4. The wavefunctions for the excited CEF states are given in Table 9.3.

9.3 Muon spin relaxation

9.3.1 Experiment details

Longitudinal μSR experiments on $Sm_2Zr_2O_7$ (not the isotope pure sample) were performed on the spectrometers LTF (0.02 - 0.8 K) and GPS (1.55-50 K). For the LTF measurement, the sample was mixed with GE vanish and pasted onto a rectangular silver plate forming a slab ($\sim$ 4 cm long, $\sim$ 2 cm wide and $\sim$ 0.3 cm thick). A Helium dilution refrigerator was used for cooling. The spectra were measured at different temperatures between 20 mK and 0.8 K in zero field. The longitudinal field dependence of the spectrum was measured at 20, 300 and 600 mK with fields up to 1.4 T. For the GPS measurement, the powder sample was wrapped by an aluminium foil forming a slab ($\sim$ 3 cm long, $\sim$ 3 cm wide and $\sim$ 0.2 cm thick). Data were collected at temperatures between 1.55 and 50 K in zero and 500 mT longitudinal fields and at 1.55 K in longitudinal fields up to 0.5 T. The software Musrfit was used for fitting the data [186]. For the LTF measurement, the relaxation of the background signal from silver is included because the relaxation rates of the sample and the silver are of the same magnitude (see Appendix D for more details).

9.3.2 Dynamical ground state

Figure 9.7 shows the μSR spectra at different temperatures in zero field. At high temperature, the muon polarization function is almost flat indicating a very small damping rate which is common at high temperatures at the motion narrowing limit [113]. The damping rate increases slowly with decreasing temperature and even at 20 mK the damping rate is still very low. No oscillations are observed even at the lowest temperature suggesting the absence of long-range magnetic order. Furthermore static magnetism can be ruled out because the asymmetry at long times does not tend to $1/3 \times$ (total asymmetry) but seems to be decreasing below this value. The spectra can be fitted with the stretched exponential function and the fitted relaxation rate λ and exponent β are shown in Fig. 9.7. The relaxation rate increases slowly with decreasing temperature down to $\sim$ 1 K and then increases steeply around 1 K indicating slowing down of the spin dynamics of the system. The relaxation rate becomes nearly constant below 0.5 K pointing to a crossover, which is consistent with the low temperature specific heat data (Chapter 4). The relaxation rate in applied field is slightly lower than in zero field which is shown also in Fig. 9.7. Altogether there are no static features in the μSR spectra at temperatures down to 20 mK, which suggests strong fluctuations in the ground state of $Sm_2Zr_2O_7$.

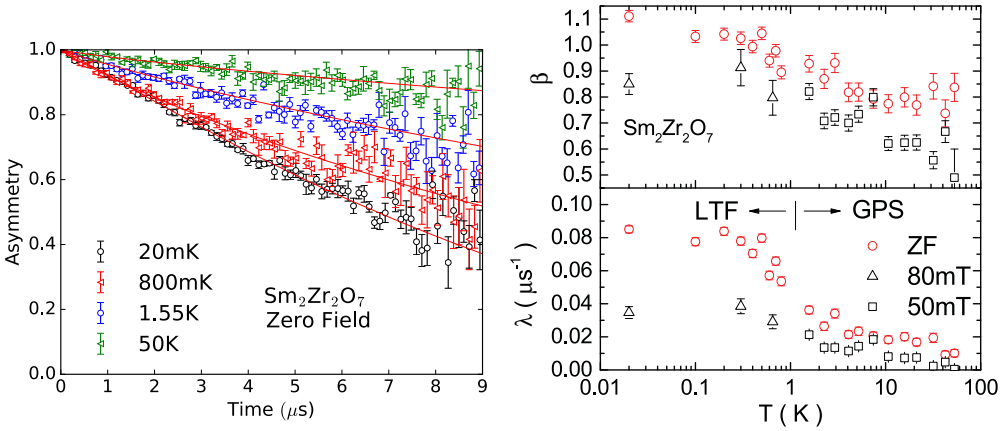

Figure 9.7: (left) Longitudinal μSR spectra of $Sm_2Zr_2O_7$ in zero field (ZF) at different temperatures. The data from the different instruments LTF (below 1 K) and GPS (above 1.55 K) are normalized for a direct comparison (the background is subtracted for the LTF data). (right) Fitted relaxation rate λ and exponent β as a function of temperature in zero, 50 mT field (GPS data above 1.5 K) and 80 mT field (LTF data below 1 K).

Fig. 9.8 shows the data of the decoupling measurement at 20 mK in the 0, 5 and 500 mT

fields and at 1.55 K in the 0 and 500 mT fields. At 20 mK, the field reduces the damping rate significantly but a high field does not make the spectra flat ($\lambda = 0$). A similar field dependence of the spectrum appears also for the other temperatures (300 mK, 650 mK and 1.55 K). The spectra in fields are also fitted with the stretched exponential function and the fitted parameters are shown in Fig. 9.9. As the field increases, the relaxation rate decreases and approaches zero for high fields. The field dependence of λ is related to the Redfield formula (Eq. 3.35 in Chapter 2). According to the Redfield formula, the field dependence of λ is described by a Lorentz function with half width at half maximum of ν/γ_μ (ν_c is the fluctuation rate). Fitting with the Redfield formula indicates that the fluctuation rate of $Sm_2Zr_2O_7$ is of the order of 10 MHz which is larger than those of the quantum spin ice materials, such as $Nd_2Zr_2O_7$ and $Yb_2Ti_2O_7$ and comparable with those of materials with dynamical order, such as $Tb_2Sn_2O_7$ and $Yb_2Sn_2O_7$ [183, 221–223]. Therefore, $Sm_2Zr_2O_7$ has a dynamical ground state which may relate to the dipolar-octupolar quantum spin ice phase and is consistent with the specific heat data which shows no sign of an ordering transition. In addition, the magnitude of the relaxation rate is dependent on the field distribution width Δ_G and the fitting yields that Δ_G is less than 2 mT at low temperatures which is a few times smaller than the values for $Nd_2Zr_2O_7$, $Yb_2Ti_2O_7$ and $Yb_2Sn_2O_7$ as a result of the smaller moment of Sm^{3+} ion [183, 188].

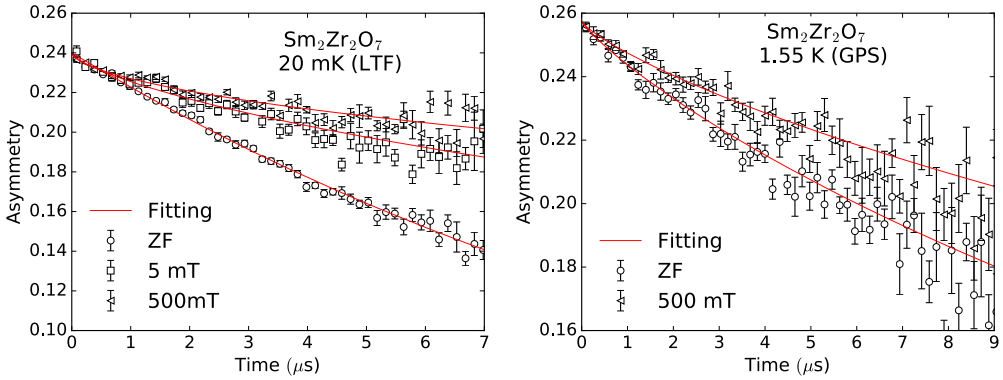

Figure 9.8: μSR spectra in different fields at 20 mK from the LTF instrument (left) and at 1.55 K from the GPS instrument (right).

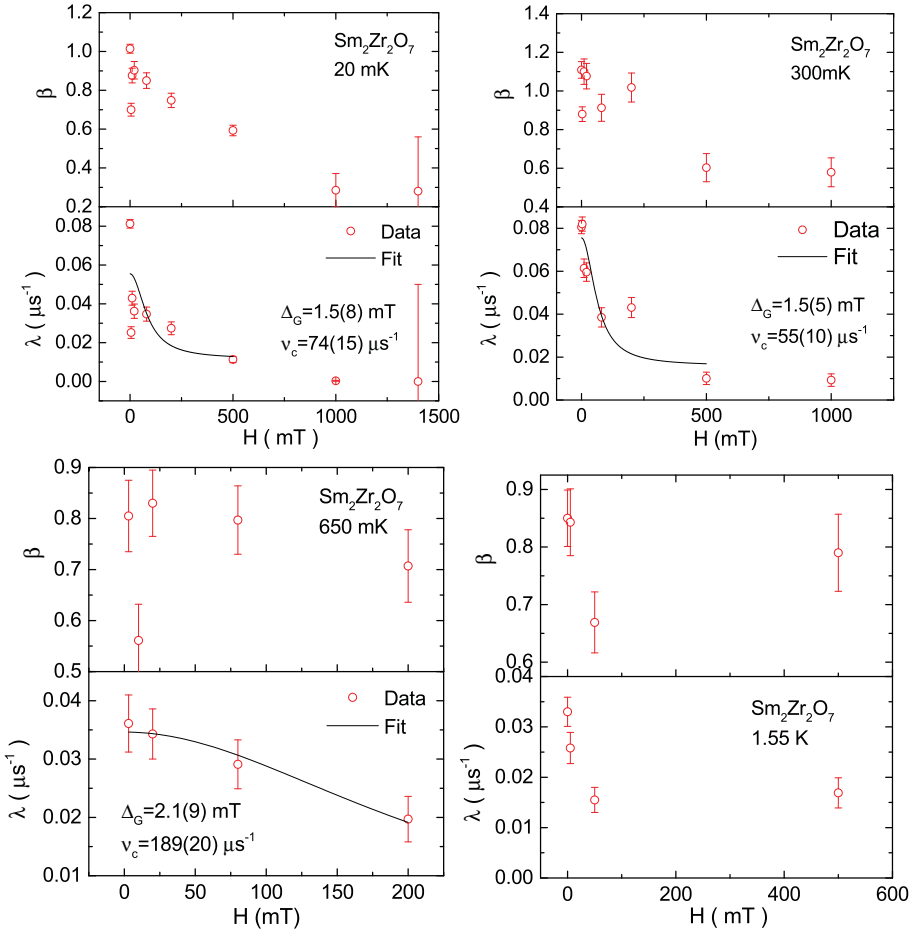

Figure 9.9: Fitted relaxation rate λ and exponent β in different fields at 20, 300 and 650 mK. The black lines show the fitting with the Redfield formula and Δ_G and ν_c is the fitted Gaussian-function field distribution width and fluctuation rate.

9.4 Conclusions

In this chapter, the crystal field and spin dynamics of $Sm_2Zr_2O_7$ are studied with inelastic neutron scattering and muon spin relaxation, respectively. Due to the weak scattering intensity, the intra-multiplet transitions within the ground state ${}^6H_{5/2}$ multiplet are not observed. The four ${}^6H_{5/2} \rightarrow {}^6H_{7/2}$ inter-multiplet transitions are observed at energies between 130 and 185 meV and analysed with crystal field theory. The analysis shows that the CEF ground state of the Sm^{3+} in $Sm_2Zr_2O_7$ is a well-isolated Kramers doublet with the first and second excited crystal field states suggested to be at 16.4 and 35.7 meV.

Therefore, the low-temperature magnetic properties can be described by the pseudospin-1/2 model, which is consistent with the magnetization and specific heat data at low temperature.

The CEF ground state shows Ising anisotropy with $g_{zz} = 0.5$ and $g_{\perp} = 0$ and the magnetic moment is $0.25\,\mu_B$/Sm, agreeing with the macroscopic measurements in Chapter 4. The wave functions of the crystal field ground state doublet are mainly composed of $|^6H_{5/2}, \pm 3/2\rangle$. According to Ref. [17], the ground state doublet is a dipolar-octupolar doublet which has a peculiar symmetry and on the pyrochlore lattice it supports two types of quantum spin ice phases. Such an dipolar-octupolar doublet is also found in $Ce_2Sn_2O_7$ [83] and $Nd_2Zr_2O_7$, and the former compound is reported as a quantum spin ice candidate and the latter compound is found to be close to the $U(1)$ spin liquid phase (see Chapter 5 and Ref. [162]).

The CEF calculation only qualitatively reproduces the susceptibility and crystal field specific heat, which is attributed to the large uncertainty of the data with broad peaks and the overlapping of two peaks. The C_p and $\chi(T)$ data are measured below 300 K where the crystal field splitting of the ground state multiplet plays the main role which unfortunately is not observed directly by neutrons due to the weak transition intensity. To avoid reaching a local minimum in the fitting, more that seven hundred independent fittings were done with different starting CEF parameters within a certain range defined according to the CEF parameters of related pyrochlores and the final result presented is the one with the lowest χ^2. Table 9.4 shows the scaled CEF parameters for $Sm_2Zr_2O_7$ based on the parameters of related pyrochlores. The fitted CEF parameters for $Sm_2Zr_2O_7$ are close to those values except for $B_0^2 = 95.1$ which is relatively large. However, the CEF parameters obtained here should give a correct CEF splitting scheme. The CEF parameters may be improved by doing a high temperature INS measurement. The CEF calculation shows that the scattering intensities of the transitions from the first excited state at ~ 16 meV to the states at ~ 130 meV and ~ 168 meV are 64% and 120% of that of the current strongest transition and measurements at around 150 K with high incident neutron energies (e.g. $E_i = 200$ meV) would be helpful for the determination of the CEF splitting of the ground state multiplet.

The muon spin relaxation data reveals the dynamical nature of the ground state of $Sm_2Zr_2O_7$. The μSR spectra at temperatures down to 20 mK show no static features and are well described by the stretched exponential function. The temperature evolution of the relaxation rate indicates that there is a strong slowing down between 0.5 K and 1 K corresponding to the anomaly of the specific heat. Below 0.5 K the relaxation rate is nearly constant indicating persistent spin dynamics. The μSR and C_p data excludes the

Table 9.4: Fitted crystal field parameters (in meV) for $Sm_2Zr_2O_7$and the scaled ones based on the CEF parameters of related compounds.

	B_0^2	B_0^4	B_3^4	B_0^6	B_3^6	B_6^6
$Sm_2Zr_2O_7$ (fitted)	95.1	411.2	73.4	149.4	-97.8	101.2
$Pr_2Sn_2O_7$ [159]	47	294	109	83	-62	110
$Pr_2Hf_2O_7$ [177]	28	289	95	131	-64	102
$Nd_2Zr_2O_7$ [162]	42	320	103	85	-70	96

possibility of a long-range ordered ground state and considering the dipolar-octupolar crystal field ground state wavefunction, the ground state of $Sm_2Zr_2O_7$ could be the quantum spin ice phase according to the phase diagram for the dipolar-octupolar doublet on the pyrochlore lattice in Ref. [17]. Further neutron diffraction and low energy inelastic neutron scattering experiments can be done to study the ground state of $Sm_2Zr_2O_7$. However, the CEF ground state wavefunction has very little scattering intensity according to Table 9.1 and neutron measurements will be very difficult.

10 Conclusions and perspectives

In this thesis, the experiments and analyses on three pyrochlore compounds $Nd_2Zr_2O_7$, $Sm_2Zr_2O_7$ and $Gd_2Zr_2O_7$ are presented. Both powder and single crystal samples are synthesized and studied with various techniques including macroscopic measurements, X-ray and neutron powder diffraction, single crystal neutron scattering and muon spin relaxation. The main technique used is elastic and inelastic neutron scattering for studying the magnetic ground state. $La_2Zr_2O_7$ is also synthesized and measured in some experiments as a non-magnetic reference.

All the compounds crystallize in the pyrochlore structure (space group $Fd\bar{3}m$, No. 227). Synchrotron X-ray powder diffraction shows no detectable defects in the $La_2Zr_2O_7$, $Nd_2Zr_2O_7$ and $Sm_2Zr_2O_7$. Significant amount of Gd/Zr antisite defects ($\sim 20\%$) in $Gd_2Zr_2O_7$ are suggested by X-ray and neutron powder diffraction. The Debye-Waller factor (overall thermal factor) at 5 K increases successively for the four compounds $La_2Zr_2O_7$, $Nd_2Zr_2O_7$, $Sm_2Zr_2O_7$ and $Gd_2Zr_2O_7$, which is associated with quenched antisite disorder, consistent with the increasing of tendency of R/Zr disorder as a result of the lowering stability of the pyrochlore phase for the four compounds due to the decreasing rare earth ion radius.

In $Nd_2Zr_2O_7$, the Nd^{3+} ion has the LS-coupling ground state $^4I_{9/2}$ and is a Kramers ion. The crystal field splitting scheme of Nd^{3+} is determined by inelastic neutron scattering which is confirmed by the susceptibility and specific heat measurements. The crystal field ground state is found to be a well-isolated dipolar-octupolar doublet of Ising anisotropy with a magnetic moment $2.65\mu_B$, in agreement with the theoretical prediction [17]. Therefore, the system at low temperatures is described by the pseudospin-1/2 model which is consistent with the analyses on the paramagnetic magnetization and low-temperature specific heat (yielding an entropy of $R\ln(2)$/mol Nd). The susceptibility shows a positive Curie-Weiss temperature ~ 0.25 K and the neutron diffraction data reveal that $Nd_2Zr_2O_7$ develops a long-range "all-in/all-out" order below $T_N = 0.4$ K for the powder sample consistent with the report in Ref. [129]. While the transition temperature for the single crystal has dependence on sample which varies from 0.28 to 0.4 K as shown in this thesis and in Ref. [129]. However the magnetic ground states are

the same for the different samples.
The magnetic excitations of $Nd_2Zr_2O_7$ below and above T_N are measured using inelastic neutron scattering. Below T_N spinwave excitations are observed which are analysed with linearly spinwave theory. The data are consistent with the published one which were measured with a higher instrument resolution by S. Petit *et al.* [155]. The analyses confirm the pseudospin-1/2 Hamiltonian suggested by Owen Benton which indicates that $Nd_2Zr_2O_7$ is close to the quantum spin ice phase [152]. The data measured above T_N are comparable with the calculated spinon scattering with the obtained Hamiltonian (performed by Owen Benton), indicating that $Nd_2Zr_2O_7$ is possibly in the quantum spin ice state above T_N. However, a definite conclusion cannot be made due to the limited resolution of the data and more experiments are needed to clarify it, such as polarized neutron inelastic scattering. The energy-integrated polarized neutron diffuse scattering of $Nd_2Zr_2O_7$ shows a pinch point pattern at $\sim 0.4\,K$ in the spin-flip channel corresponding to the intensive gapped flat mode observed in the inelastic neutron scattering experiment. The neutron diffuse scattering data with an applied field along the [1-10] crystallographic direction exhibit two-dimensional scattering sheets perpendicular to the (110) direction suggesting that there are ferromagnetic chains along the (110) direction. This data is explained based on the spin Hamiltonian of $Nd_2Zr_2O_7$. The AC susceptibility with an applied DC field along the [111] direction shows a field-induced spin flip transition with large hysteresis between increasing and decreasing fields which is also modelled with the Hamiltonian.
The muon spin relaxation (μSR) spectra of powder $Nd_2Zr_2O_7$ are recorded at temperatures down to 20 mK and no static feature is observed within the time window of μSR. The data are analysed with the field distribution method. A sudden increase in the field-distribution width at T_N indicates that the quasi-static moment increases at the ordering transition. The fluctuation rate ν_c decreases with decreasing temperature indicating slowing down of the system due to the onset of spin correlations. Below T_N, the fluctuation rate turns to be nearly constant revealing persistent spin dynamics, which is striking for a system with gapped magnon excitations. It is ascribed to the quantum fluctuations resulted from the proximity to the quantum spin ice phase of $Nd_2Zr_2O_7$. Anomalously slow paramagnetic spin dynamics are also found which are related to the possible highly-correlated quantum spin ice state above T_N.
The experiments and analyses on $Nd_2Zr_2O_7$ here confirm the validation of the spin Hamiltonian proposed in Ref. [152] and provides a comprehensive picture of the underlying physics in the pyrochlores containing Nd. The Hamiltonian reveals that $Nd_2Zr_2O_7$ is close to the quantum spin ice state, which makes it interesting to study the similar

pyrochlore compounds $Nd_2Sn_2O_7$, $Nd_2Hf_2O_7$ and $Nd_2Pb_2O_7$ [28, 130, 131, 152].
The Sm^{3+} ion is also a Kramers ion with the LS-coupling ground state ${}^6H_{5/2}$. In the inelastic neutron scattering data, the signals for the crystal field transitions within the ${}^6H_{5/2}$ multiplet are not observed due to their weak intensity but the inter-multiplet transitions from ${}^6H_{5/2}$ to ${}^6H_{7/2}$ are clearly shown. The CEF Hamiltonian and splitting scheme is determined based on the analyses of the inter-multiplet transitions but the resulted CEF susceptibility and specific heat only agrees qualitatively with the measurement probably because of the limited resolution of the data. The CEF ground state doublet is found to be composed of the $|\pm 3/2\rangle$ terms which is an Ising anisotropic dipolar-octupolar doublet with a moment $0.25\,\mu_B$. The calculated first excited doublet is at around 10 meV indicating that the pseudospin-1/2 model is also applicable to $Sm_2Zr_2O_7$ at low temperatures. The paramagnetic magnetization at low temperature also supports the pseudospin-1/2 model and indicates a moment $0.32(1)\,\mu_B$ for the Sm^{3+} ion. The susceptibility of $Sm_2Zr_2O_7$ does not follow the Curie-Weiss law due to the crystal field effect but fitting a small low-temperature region (1.8 - 6 K) indicates $\theta_p \sim -1$ K and $\mu_{eff} \sim 0.39\,\mu_B$/Sm. The low-temperature specific heat shows a broad peak around 0.5 K yielding a entropy close to $R\ln(2)$ /mol Sm, which indicates the building up of magnetic correlations. The μSR spectra of $Sm_2Zr_2O_7$ at temperatures down to 20 mK show a slow down of the spin dynamics at 0.5 K and indicate strong dynamics persistent down to the lowest temperature in the system. Therefore, the Ising anisotropic crystal ground state, the absence of a long range order and the strong fluctuations found here reveal that $Sm_2Zr_2O_7$ is a promising quantum spin ice candidate. However, the low magnetic moment of Sm^{3+} makes it difficult to study it with neutron scattering experiments.
$Gd_2Zr_2O_7$ with nearly isotropic Gd^{3+} ion is an Heisenberg pyrochlore antiferromagnet. The susceptibility and magnetisation of $Gd_2Zr_2O_7$ above 2 K reveals that $\theta_p = -6.8(1)$ K, $\mu_{eff} = 7.84(1)\,\mu_B$/Gd and a saturated magnetization $6.7\,\mu_B$/Gd. The AC susceptibility and specific heat shows an broad peak at ~ 0.7 K though the specific heat for a powder sample in Ref. [138] shows a sharp peak at 0.769 K evidencing an ordering transition. It is interesting that $Gd_2Zr_2O_7$ in the fluorite phase with complete Gd/Zr disorder also shows a similar peak in the AC susceptibility data at nearly the same temperature. The neutron powder diffraction of ${}^{160}Gd_2Zr_2O_7$ shows no magnetic Bragg peaks but strong liquid-like diffuse scattering below 15 K, in contrast to the similar compounds $Gd_2Ti_2O_7$ and $Gd_2Sn_2O_7$ [93, 95]. The absence of the long-range order is attributed to the large amount of Gd/Zr antisite defects in the sample. The long-time low-temperature annealing does not improve this situation obviously. The diffuse

scattering pattern is refined with the reverse Monte Carlo method and the possible short-range spin correlations in $Gd_2Zr_2O_7$ are extracted. Dipolar correlations and local Palmer-Chalker type spin configuration on the tetrahedron are found which suggest a liquid-like ground state of $Gd_2Zr_2O_7$ with antisite defects. The μSR spectra above 1.5 K indicate fast fluctuations in the system and further μSR experiment below the anomaly temperature of χ_{AC} can be done to identify the dynamical properties of the liquid-like correlations.

Appendix A: Powder-averaged magnetization for the pseudospin-1/2 model

If the crystal field ground state is a well-isolated doublet, the low-temperature physics can be described by the pseudospin-1/2 model and the paramagnetic magnetization can be calculated based on the partition function of a spin-1/2 single ion.
For a Ising anisotropic spin, the magnetic moment is $\mu = -g_{zz}\mu_{\rm B}\sigma_z$ (σ_z is the z component of the pseudospin) and is along the Ising axis opposite to the spin direction. In a magnetic field $\boldsymbol{H}$, the Zeeman energy is $u = -\boldsymbol{\mu}\cdot\boldsymbol{H} = g_{zz}\mu_{\rm B}\sigma_z H\cos(\theta)$ where θ is the angle between the field and the Ising axis. If the field is along the Ising axis, the thermal-averaged magnetization is [224]

$$\begin{aligned}\langle M\rangle &= \frac{-g_{zz}\mu_{\rm B}\sigma\exp(-g_{zz}\mu_{\rm B}\sigma H/k_{\rm B}T)+g_{zz}\mu_{\rm B}\sigma\exp(g_{zz}\mu_{\rm B}\sigma H/k_{\rm B}T)}{\exp(-g_{zz}\mu_{\rm B}\sigma H/k_{\rm B}T)+\exp(g_{zz}\mu_{B}\sigma H/k_{\rm B}T)} \\ &= g_{zz}\mu_{\rm B}\sigma\tanh\left(\frac{g_{zz}\mu_{\rm B}\sigma H}{k_{\rm B}T}\right), \qquad (1)\end{aligned}$$

where $\sigma = 1/2$ (the eigenvalue of σ_z).
When there is an angle θ between the field and the Ising axis, the projection of $\langle M\rangle$ onto the field direction is

$$\langle M\rangle = g_{zz}\mu_{\rm B}\sigma\cos(\theta)\tanh\left(\frac{g_{zz}\mu_{\rm B}\sigma H\cos(\theta)}{k_{\rm B}T}\right). \qquad (2)$$

Integrating for all the possible orientations of easy axis, we get the thermal-powder-averaged magnetization

$$\begin{aligned}\langle M\rangle &= \frac{1}{4\pi}\iint_{0,0}^{\pi,2\pi} g_{zz}\mu_{\rm B}\sigma\cos(\theta)\tanh\left(\frac{g_{zz}\mu_{\rm B}\sigma H\cos(\theta)}{k_{\rm B}T}\right)\times\sin(\theta){\rm d}\theta{\rm d}\varphi \\ &= \frac{1}{2}\int_0^{\pi} g_{zz}\mu_{\rm B}\sigma\cos(\theta)\tanh\left(\frac{g_{zz}\mu_{\rm B}\sigma H\cos(\theta)}{k_{\rm B}T}\right)\sin(\theta){\rm d}\theta.\end{aligned}$$

Appendix A: Powder-averaged magnetization for the pseudospin-1/2 model

Taking into account the inversion symmetry,

$$\begin{aligned}\langle M\rangle &= \int_0^{\pi/2} g_{zz}\mu_{\rm B}\sigma\cos(\theta)\tanh\left(\frac{g_{zz}\mu_{\rm B}\sigma H\cos(\theta)}{k_{\rm B}T}\right)\sin\theta{\rm d}\theta \\ &= -\int_1^0 g_{zz}\mu_{\rm B}\sigma\cos(\theta)\tanh\left(\frac{g_{zz}\mu_{\rm B}\sigma H\cos(\theta)}{k_{\rm B}T}\right){\rm d}\cos(\theta).\end{aligned}$$

With some rearrangements, we get

$$\langle M\rangle = -\frac{(k_BT)^2}{g_{zz}\mu_B\sigma H^2}\int_0^{g_{zz}\mu_{\rm B}\sigma H/k_{\rm B}T}\tanh\left(\frac{g_{zz}\mu_B\sigma H\cos(\theta)}{k_BT}\right) \times \frac{g_{zz}\mu_{\rm B}\sigma_z H\cos(\theta)}{k_{\rm B}T}{\rm d}\left(\frac{g_{zz}\mu_{\rm B}\sigma H\cos(\theta)}{k_{\rm B}T}\right).$$

Defining the integration variable $\frac{g_{zz}\mu_{\rm B}\sigma H\cos\theta}{k_{\rm B}T} = x$, we get the desired equation for the thermal-powder-averaged paramagnetic magnetization of an Ising anisotropic magnet

$$\langle M\rangle = \frac{(k_BT)^2}{g_{zz}\mu_{\rm B}\sigma H^2}\int_0^{g_{zz}\mu_{\rm B}\sigma H/k_{\rm B}T} x\tanh(x){\rm d}x. \tag{3}$$

Appendix B: Nearest-neighbor pseudospin-1/2 Hamiltonian

The general form of the pseudospin exchange Hamiltonian on the pyrochlore lattice is given by Eq. 2.28 in Chapter 2 in the local frames. The local frames for the four magnetic ions on a tetrahedron are defined with the local [1,1,1] directions as the local z axes and the local y axes being chosen to keep the two-fold rotation invariance about the three axes that include the centre of the tetrahedron and are parallel to the global crystal a, b and c axes [8, 40, 42]:

$$\begin{array}{ll} \hat{\boldsymbol{z}}_0 = \frac{1}{\sqrt{3}}(1,1,1), & \hat{\boldsymbol{x}}_0 = \frac{1}{\sqrt{6}}(-2,1,1), \\ \hat{\boldsymbol{z}}_1 = \frac{1}{\sqrt{3}}(1,-1,-1), & \hat{\boldsymbol{x}}_1 = \frac{1}{\sqrt{6}}(-2,-1,-1), \\ \hat{\boldsymbol{z}}_2 = \frac{1}{\sqrt{3}}(-1,1,-1), & \hat{\boldsymbol{x}}_2 = \frac{1}{\sqrt{6}}(2,1,-1), \\ \hat{\boldsymbol{z}}_3 = \frac{1}{\sqrt{3}}(-1,-1,1), & \hat{\boldsymbol{x}}_3 = \frac{1}{\sqrt{6}}(2,-1,1), \end{array} \tag{1}$$

with $\hat{\boldsymbol{y}}_i = \hat{\boldsymbol{z}}_i \times \hat{\boldsymbol{x}}_i$.
The phase factors for the six bonds of on a tetrahedron due to the different bond orientations are given by ζ and γ which are 4×4 complex unimodular matrices [8, 42],

$$\zeta = \begin{pmatrix} 0 & -1 & e^{i\frac{\pi}{3}} & e^{-i\frac{\pi}{3}} \\ -1 & 0 & e^{-i\frac{\pi}{3}} & e^{i\frac{\pi}{3}} \\ e^{i\frac{\pi}{3}} & e^{-i\frac{\pi}{3}} & 0 & -1 \\ e^{-i\frac{\pi}{3}} & e^{i\frac{\pi}{3}} & -1 & 0 \end{pmatrix}, \quad \gamma = -\zeta^*. \tag{2}$$

The spin Hamiltonian can be transformed from the local frame to the global crystal coordinate system by

$$\begin{aligned} {}^{\text{global}}\boldsymbol{\sigma}_i &= {}^{\text{local}}\boldsymbol{\sigma}_i \cdot \mathrm{T}'_i, \\ {}^{\text{global}}\boldsymbol{J}_{ij} &= \mathrm{T}'_i \cdot {}^{\text{local}}\boldsymbol{J}_{ij} \cdot \mathrm{T}_j, \end{aligned} \tag{3}$$

where the pseudospin is written as a row vector (σ_x, σ_y, σ_y). T_i is the transformation matrix for the i^{th} spin from the local frame to the global frame which can be obtained

by horizontally stacking the column base vectors $\hat{\boldsymbol{x}}_i'$, $\hat{\boldsymbol{y}}_i'$ and $\hat{\boldsymbol{z}}_i'$ ("$'$" means transpose). $\boldsymbol{J}_{ij}$ is the exchange interaction matrix for the i^{th} and j^{th} spins in the form of

$$\boldsymbol{J}_{ij} = \begin{pmatrix} J_{ij}^{xx} & J_{ij}^{xy} & J_{ij}^{xz} \\ J_{ij}^{yx} & J_{ij}^{yy} & J_{ij}^{yz} \\ J_{ij}^{zx} & J_{ij}^{zy} & J_{ij}^{zz} \end{pmatrix}. \tag{4}$$

In SpinW [22], the spin wave calculation is done in the global coordinate system. After the generation of the lattice and bonds, the interaction matrices for the different types of bonds should be defined in the global frame. It just need the matrix for one of the bonds of the same type and the other bonds of the this type will be generated according to the symmetry (applying three-dimensional rotation transformations). This applies for $Pr_2Zr_2O_7$, $Er_2Ti_2O_7$ and $Yb_2Ti_2O_7$ without an octupolar moment. However, for $Nd_2Zr_2O_7$, the interaction matrices should not be generated with the symmetry transformations because the special symmetry of the dipolar-octupolar doublet of Nd^{3+} (no phase term in the Hamiltonian). The interaction matrices are defined as follows. First, switch off the function doing the symmetry transformation of the software. Second, define the four local coordinate frames (Eq. 1) for the four spins on a tetrahedron. Third, define the interaction matrix ${}^{\text{local}}\boldsymbol{J}_{ij}$ in the local frame as

$${}^{\text{local}}\boldsymbol{J}_{ij} = \begin{pmatrix} J_{ij}^{xx} & 0 & J_{ij}^{xz} \\ 0 & J_{ij}^{yy} & 0 \\ J_{ij}^{zx} & 0 & J_{ij}^{zz} \end{pmatrix}, \tag{5}$$

where only the symmetry-allowed terms are kept. The interaction matrix in the local frame is same for all bonds. Fourth, transform ${}^{\text{local}}\boldsymbol{J}_{ij}$ to be in the global crystal frame with Eq. 6 for all bonds. Finally, transform the $\boldsymbol{g}$ tensor from the local frame to the global frame,

$${}^{\text{global}}\boldsymbol{g}_i = \mathrm{T}_i' \cdot {}^{\text{local}}\boldsymbol{g} \cdot \mathrm{T}_i, \tag{6}$$

where ${}^{\text{local}}\boldsymbol{g}$ is

$$\begin{pmatrix} 0 & 0 & 0 \\ 0 & 0 & 0 \\ 0 & 0 & g_{zz} \end{pmatrix}, \tag{7}$$

which is Ising anisotropic and is the same for all the spins in the local frames.

Appendix C: Nuclear hyperfine specific heat of $Nd_2Zr_2O_7$

The upturn in the specific heat of $Nd_2Zr_2O_7$ below 0.1 K is ascribed to the Nd nuclear contribution due to the hyperfine interactions between the nuclei and electrons. Among the natural Nd isotopes, two of them are generally considered: ^{143}Nd and ^{145}Nd with abundances 12.2 % and 8.3 % whose nuclei are stable and well studied. Their magnetic properties are given in Table 1 including the nuclear spin I, gyromagnetic ratio γ, hyperfine constant $\mathcal{A}$ and magnetic moment m.

Table 1: Nuclear magnetic properties of ^{143}Nd and ^{145}Nd (the magnetic moment is in the unit of nuclear magneton μ_N) [225, 226].

	I	γ (rad s^{-1} T^{-1})	$\mathcal{A}$ (T)	m (μ_N)
^{143}Nd	7/2	-1.457×10^7	0.0209	1.063
^{145}Nd	7/2	-8.895×10^7	0.0131	0.654

The nuclear hyperfine interaction Hamiltonian for $Nd_2Zr_2O_7$ is [164, 223]

$$\mathcal{H}_{\text{hyper}} = -\hbar\gamma B_{\text{hyper}} I_z + \frac{eQV_{zz}}{4I(2I-1)}[3(I_z^2 - I^2) + \frac{\eta}{2}(I_+^2 + I_-^2)], \tag{1}$$

where the first terms is the hyperfine Zeeman interaction and the second term is the electric quadrupole interaction (z is the local [111] direction). B_{hyper} is hyperfine magnetic field at the nucleus position generated by the static electron magnetic moment along the local [111] direction which is $B_{\text{hyper}} = m_{\text{static}}\mathcal{A}/(\hbar\gamma)$ (m_{static} is the static electron moment). e and Q are the proton electric charge and the quadrupole moment of the nucleus. V_{zz} is the electronic field gradient at the location of the nucleus which has contributions from the $4f$ electrons of Nd^{3+} and the surrounding ligands. η is zero due to the axial symmetry of the Nd site in pyrochlores [223]. The hyperfine splitting and the Hamiltonian can be determined by measurements of the nuclear magnetic resonance and Mössbauer spectra. The two interactions are usually of the same order of magnitude. However, the electronic field gradient at the Nd nucleus position in $Nd_2Sn_2O_7$ was

estimated to be very small [131, 164] and thus only the Zeeman term is considered here for $Nd_2Zr_2O_7$ for simplicity.

The hyperfine field is of the order of 10^2 T (e.g. $\sim$ 200 T for the ordered moment $\sim 1.7\,\mu_B$ in $Nd_2Sn_2O_7$) which is much lager than any applied magnetic field [131, 164]. Therefore, the external field $\sim$ 1 T in the specific heat experiment in Chapter 4 is not expected to have a significant effect on the nuclear Zeeman splitting and thus the nuclear C_p. However, the external field could increase the static electron magnetic moment which largely influences the nuclear C_p. This is the case for $Nd_2Zr_2O_7$. At the lowest temperature, the ordered electron moment in $Nd_2Zr_2O_7$ is not the crystal field ground state moment ($\sim 2.6\,\mu_B$) but $\sim 1.2\,\mu_B$ induced by the dipolar-octupolar Hamiltonian. The ordered pseudospin is not along the local [111] axes and the ordered moment is reduced owing to the local [111] Ising anisotropy (see Chapter 6). The magnetic field could rotate the pseudospin towards the local [111] axes as a result of the Ising anisotropy of the spin, which increases the static electron magnetic moment.

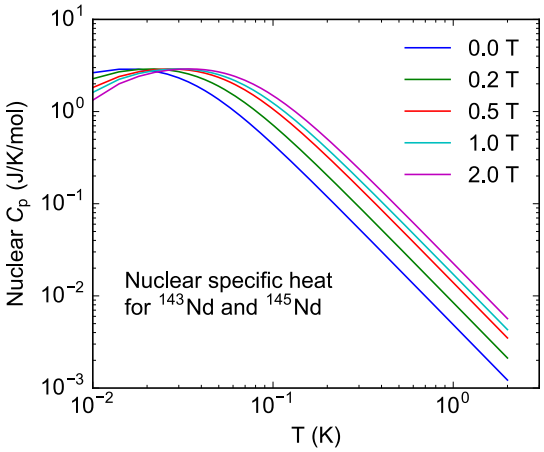

Figure 1: Nuclear specific heat for $Nd_2Zr_2O_7$ in different magnetic fields with only considering the hyperfine Zeeman splitting of the isotopes ^{143}Nd and ^{145}Nd. The magnetic $4f$ electron moments in different fields is estimated based on the magnetization in Ref. [129]. In the high temperature region, the nuclear C_p is $\sim A\,T^{-2}$. Note that here the static electron magnetic moments in different fields are assumed to be independent on temperature, which is only valid for very low temperatures. However, the quadrupole effect has a weak temperature dependence.

According to the neutron diffraction and magnetization data [129], the static $4f$ electron moments of Nd^{3+} in $Nd_2Zr_2O_7$ in fields of 0, 0.2, 0.5, 1.0 and 2.0 T (along the [111]

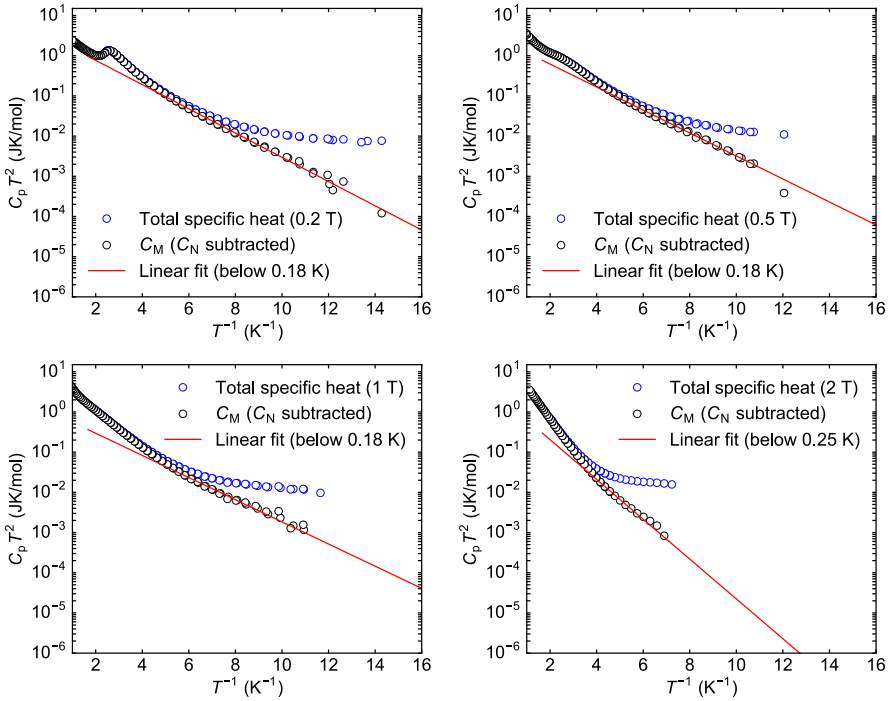

Figure 2: Fitting the low-temperature specific heat of $Nd_2Zr_2O_7$ in fields along the [111] direction to $AT^{-2} + BT^{-2}\exp(-\Delta/T)$. The raw data (blue circles), the nuclear-contribution-subtracted data (black circles) and the fit (red line) are shown. Measured by Akito Sakai *et al.* in Augsburg University.

Table 2: Calculated and fitted parameters for the specific heat of $Nd_2Zr_2O_7$ in different [111] fields. The calculated A is obtained based on the nuclear Hyperfine Zeeman splitting with the estimated static magnetic moments of Nd^{3+} in fields.

	0 T	0.2 T	0.5 T	1.0 T	2.0 T
Calculated A (JK/mol)	0.0050	0.0084	0.014	0.017	0.022
A (JK/mol)	0.0062(1)	0.0075(1)	0.011(1)	0.011(1)	0.016(1)
B (JK/mol)	4.45(20)	3.07(20)	2.31(15)	1.05(24)	1.99(62)
Δ (K)	0.75(1)	0.69(2)	0.66(2)	0.63(4)	1.13(8)

direction) are estimated to be 1.2, 1.6, 2.0, 2.3 and 2.6 μ_B, which are obtained by simply comparing the magnetization in a field with the saturated magnetization. The nuclear C_p in different external fields is calculated based on the thermal populations of the nuclear Zeeman levels (Fig. 1). The calculation shows good agreement with the measured data shown in Chapter 4. For the temperature region in the measurement, the nuclear C_p

can be approximated by AT^{-2} and the calculated A in different fields is shown in Table 1. Due to the uncertainties in the calculation, A is kept as a free parameter in the combined fitting of the nuclear and magnon specific heats in Chapter 4. The inelastic neutron scattering data in Chapter 6 reveals gapped magnon excitations in zero field and the magnon specific heat in fields can be assumed to be $BT^{-2}\exp(-\Delta/T)$ where Δ is the magnon gap. Because that spin wave calculations show that the magnon is always gapped in a field along the [111] direction according to the $Nd_2Zr_2O_7$ spin Hamiltonian, the magnon specific heat in fields are assumed to be $BT^{-2}\exp(-\Delta/T)$. The fittings of the specific heat in fields of 0, 0.2, 0.5, 1.0 and 2.0 T to $AT^{-2} + BT^{-2}\exp(-\Delta/T)$ (A, B and Δ is allowed to vary) are shown in Fig. 2 and the fitted parameters are shown in Table 2.

Appendix D: μSR signal of the silver sample holder

The relaxation rate of the silver sample holder used on the LTF instrument is included in the analyses of the μSR data of $Nd_2Zr_2O_7$ and $Sm_2Zr_2O_7$. The sample holders used in the LTF measurements are "Nr. 328 (I15w015)" and "Nr. 327 (I15w015)" for the two samples, respectively. The temperature dependence of the relaxation rate of the sample holder is shown in Fig. 1.

The sample holder has a very small relaxation rate which causes a slow damping tail in the spectra. It does not have a significant effect for $Nd_2Zr_2O_7$ whose relaxation rate is large. However, the relaxation rate of $Sm_2Zr_2O_7$ is at the same order of that of the sample holder. Therefore, the relaxation rate of the background from the sample holder must be considered. At first, it causes a problem for the determination of the fraction of the sample signal in the calibration measurements. The sample fraction determined for $Nd_2Zr_2O_7$ is used because of the similar sample density and geometry. The background of the GPS instrument can be ignored because the sample holder is thin aluminium foil. Comparing the results from the two instruments also provides a verification for the fraction used. In external fields, the relaxation rate of the silver sample holder is assumed to be zero because a low field could quench the small paramagnetic relaxation.

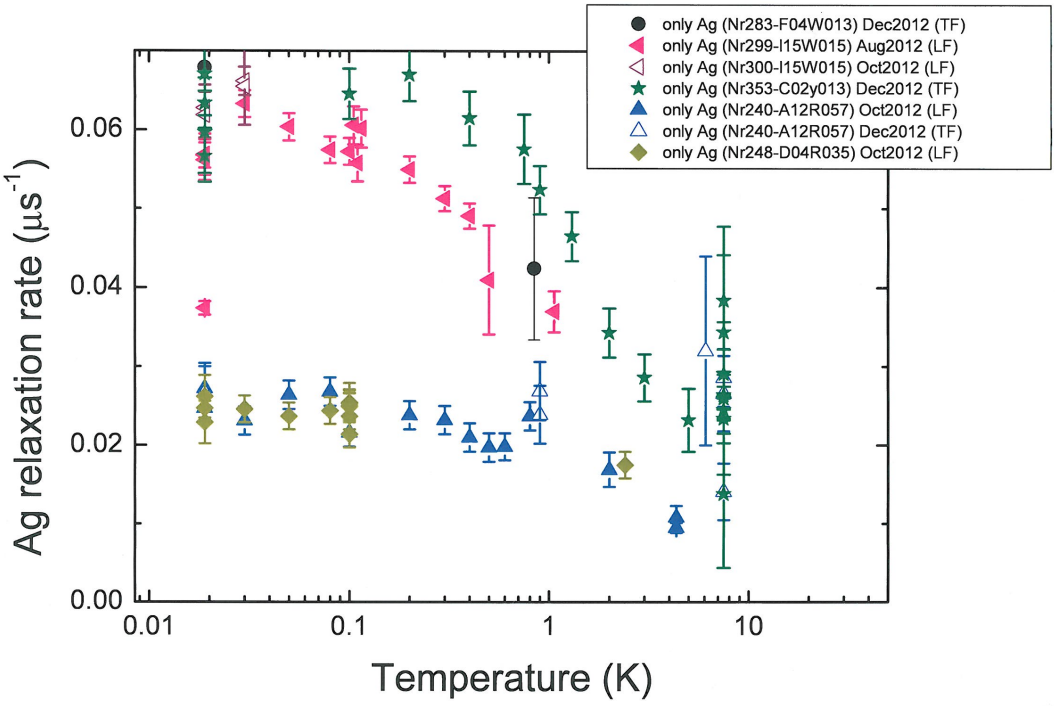

Figure 1: Relaxation rate of the μSR signal from the silver sample holder. The sample holder "I15w015" is used for $Nd_2Zr_2O_7$ and $Sm_2Zr_2O_7$ in the LTF experiments. Supplied by the instrument scientist C. Bains from PSI.

Bibliography

[1] B. G. Wybourne, *Spectroscopic properties of rare earths* (Interscience New York, 1965).

[2] G. Liu and B. Jacquier, *Spectroscopic properties of rare earths in optical materials*, Vol. 83 (Springer Science & Business Media, 2006).

[3] J. M. Coey, *Magnetism and magnetic materials* (Cambridge University Press, 2010).

[4] M. T. Hutchings, Solid State Phys. **16**, 227 (1964).

[5] S. Rosenkranz, A. P. Ramirez, A. Hayashi, R. J. Cava, R. Siddharthan, and B. S. Shastry, J. Appl. Phys. **87**, 5914 (2000).

[6] J. H. Van Vleck, *The theory of electric and magnetic susceptibilities* (Oxford University Press, 1932).

[7] A. Abragam and B. Bleaney, *Electron paramagnetic resonance of transition ions* (OUP Oxford, 2012).

[8] K. A. Ross, L. Savary, B. D. Gaulin, and L. Balents, Phys. Rev. X **1**, 021002 (2011).

[9] S. Bramwell, M. Field, M. Harris, and I. Parkin, J. Phys.: Condens. Matter **12**, 483 (2000).

[10] E. Gopal, *Specific heats at low temperatures* (Springer Science & Business Media, 2012).

[11] J. B. Goodenough, Phys. Rev. **100**, 564 (1955).

[12] J. Kanamori, J. Phys. Chem. Solids **10**, 87 (1959).

[13] I. Dzyaloshinsky, J. Phys. Chem. Solids **4**, 241 (1958).

[14] T. Moriya, Phys. Rev. **120**, 91 (1960).

[15] P. Santini, S. Carretta, G. Amoretti, R. Caciuffo, N. Magnani, and G. H. Lander, Rev. Mod. Phys. **81**, 807 (2009).

[16] J. G. Rau and M. J. P. Gingras, Phys. Rev. B **92**, 144417 (2015).

[17] Y.-P. Huang, G. Chen, and M. Hermele, Phys. Rev. Lett. **112**, 167203 (2014).

[18] J. N. Reimers, Phys. Rev. B **46**, 193 (1992).

[19] V. Naish and R. P. Ozerov, *Neutron diffraction of magnetic materials* (Springer Science and Business Media, 2012).

[20] A. Wills, Le Journal de Physique IV **11**, Pr9 (2001).

[21] J. Rodríguez-Carvajal, Physica B **192**, 55 (1993).

[22] S. Toth and B. Lake, J. Phys.: Condens. Matter **27**, 166002 (2015).

[23] H. Diep, *Frustrated spin systems* (World Scientific, 2013).

[24] C. Lacroix, P. Mendels, and F. Mila, *Introduction to Frustrated Magnetism: Materials, Experiments, Theory* (Springer Berlin, 2013).

[25] J. S. Gardner, M. J. P. Gingras, and J. E. Greedan, Rev. Mod. Phys. **82**, 53 (2010).

[26] Z. L. Dun, M. Lee, E. S. Choi, A. M. Hallas, C. R. Wiebe, J. S. Gardner, E. Arrighi, R. S. Freitas, A. M. Arevalo-Lopez, J. P. Attfield, H. D. Zhou, and J. G. Cheng, Phys. Rev. B **89**, 064401 (2014).

[27] H. D. Zhou, J. G. Cheng, A. M. Hallas, C. R. Wiebe, G. Li, L. Balicas, J. S. Zhou, J. B. Goodenough, J. S. Gardner, and E. S. Choi, Phys. Rev. Lett. **108**, 207206 (2012).

[28] A. M. Hallas, A. M. Arevalo-Lopez, A. Z. Sharma, T. Munsie, J. P. Attfield, C. R. Wiebe, and G. M. Luke, Phys. Rev. B **91**, 104417 (2015).

[29] M. Harris, S. Bramwell, D. McMorrow, T. Zeiske, and K. Godfrey, Phys. Rev. Lett. **79**, 2554 (1997).

[30] C. Castelnovo, R. Moessner, and S. L. Sondhi, Nature **451**, 42 (2008).

[31] D. J. P. Morris, D. Tennant, S. Grigera, B. Klemke, C. Castelnovo, R. Moessner, C. Czternasty, M. Meissner, K. Rule, and J.-U. Hoffmann, Science **326**, 411 (2009).

[32] T. Fennell, P. P. Deen, A. R. Wildes, K. Schmalzl, D. Prabhakaran, A. T. Boothroyd, R. J. Aldus, D. F. McMorrow, and S. T. Bramwell, Science **326**, 415 (2009).

[33] J. D. M. Champion, M. J. Harris, P. C. W. Holdsworth, A. S. Wills, G. Balakrishnan, S. T. Bramwell, E. Čižmár, T. Fennell, J. S. Gardner, J. Lago, D. F. McMorrow, M. Orendáč, A. Orendáčová, D. M. Paul, R. I. Smith, M. T. F. Telling, and A. Wildes, Phys. Rev. B **68**, 020401 (2003).

[34] M. A. Subramanian, G. Aravamudan, and G. V. Subba Rao, Prog. Solid State Chem. **15**, 55 (1983).

[35] A. M. Hallas, A. Z. Sharma, Y. Cai, T. J. Munsie, M. N. Wilson, M. Tachibana, C. R. Wiebe, and G. M. Luke, Phys. Rev. B **94**, 134417 (2016).

[36] C. R. Stanek and R. W. Grimes, J. Am. Ceram. Soc. **85**, 2139 (2002).

[37] M. Rushton, R. W. Grimes, C. Stanek, and S. Owens, J. Mater. Res. **19**, 1603 (2004).

[38] P. Santini, S. Carretta, G. Amoretti, R. Caciuffo, N. Magnani, and G. H. Lander, Rev. Mod. Phys. **81**, 807 (2009).

[39] S. H. Curnoe, Phys. Rev. B **75**, 212404 (2007).

[40] H. Yan, O. Benton, L. Jaubert, and N. Shannon, Phys. Rev. B **95**, 094422 (2017).

[41] A. W. Wong, Z. Hao, and M. J. Gingras, Phys. Rev. B **88**, 144402 (2013).

[42] S. Onoda and Y. Tanaka, Phys. Rev. B **83**, 094411 (2011).

[43] O. Shigeki, J. Phys. Conf. Ser. **320**, 012065 (2011).

[44] W. F. Giauque and M. F. Ashley, Phys. Rev. **43**, 81 (1933).

[45] W. F. Giauque and J. W. Stout, J. Am. Chem. Soc. **58**, 1144 (1936).

[46] L. Pauling, J. Am. Chem. Soc. **57**, 2680 (1935).

[47] A. P. Ramirez, A. Hayashi, R. Cava, R. Siddharthan, and B. Shastry, Nature **399**, 333 (1999).

[48] J. Lago, I. Živković, B. Z. Malkin, J. Rodriguez Fernandez, P. Ghigna, P. Dalmas de Réotier, A. Yaouanc, and T. Rojo, Phys. Rev. Lett. **104**, 247203 (2010).

[49] M. J. Harris, S. T. Bramwell, T. Zeiske, D. F. McMorrow, and P. J. C. King, J. Magn. Magn. Mater. **177-181, Part 2**, 757 (1998).

[50] C. Castelnovo, R. Moessner, and S. L. Sondhi, Annu. Rev. Condens. Matter Phys. **3**, 35 (2012).

[51] C. L. Henley, Annu. Rev. Condens. Matter Phys. **1**, 179 (2010).

[52] H. den, C. Byron, and G. M. J. P., Phys. Rev. Lett. **84**, 3430 (2000).

[53] R. G. Melko and M. J. P. Gingras, J. Phys.: Condens. Matter **16**, R1277 (2004).

[54] M. Hermele, M. P. A. Fisher, and L. Balents, Phys. Rev. B **69**, 064404 (2004).

[55] M. J. P. Gingras and P. A. McClarty, Rep. Prog. Phys. **77**, 056501 (2014).

[56] O. Benton, O. Sikora, and N. Shannon, Phys. Rev. B **86**, 075154 (2012).

[57] L. Savary and L. Balents, Phys. Rev. Lett. **108**, 037202 (2012).

[58] S. Lee, S. Onoda, and L. Balents, Phys. Rev. B **86**, 104412 (2012).

[59] N. Shannon, O. Sikora, F. Pollmann, K. Penc, and P. Fulde, Phys. Rev. Lett. **108**, 067204 (2012).

[60] H. D. Zhou, S. T. Bramwell, J. G. Cheng, C. R. Wiebe, G. Li, L. Balicas, J. A. Bloxsom, H. J. Silverstein, J. S. Zhou, J. B. Goodenough, and J. S. Gardner, Nat. Commun. **2**, 478 (2011).

[61] H. R. Molavian, M. J. P. Gingras, and B. Canals, Phys. Rev. Lett. **98**, 157204 (2007).

[62] A. J. Princep, H. C. Walker, D. T. Adroja, D. Prabhakaran, and A. T. Boothroyd, Phys. Rev. B **91**, 224430 (2015).

[63] M. J. P. Gingras, B. C. den Hertog, M. Faucher, J. S. Gardner, S. R. Dunsiger, L. J. Chang, B. D. Gaulin, N. P. Raju, and J. E. Greedan, Phys. Rev. B **62**, 6496 (2000).

[64] J. S. Gardner, A. Keren, G. Ehlers, C. Stock, E. Segal, J. M. Roper, B. Fak, M. B. Stone, P. R. Hammar, D. H. Reich, and B. D. Gaulin, Phys. Rev. B **68**, 180401 (2003).

[65] J. S. Gardner, B. D. Gaulin, A. J. Berlinsky, P. Waldron, S. R. Dunsiger, N. P. Raju, and J. E. Greedan, Phys. Rev. B **64**, 224416 (2001).

[66] T. Fennell, M. Kenzelmann, B. Roessli, M. Haas, and R. Cava, Phys. Rev. Lett. **109**, 017201 (2012).

[67] S. Petit, P. Bonville, J. Robert, C. Decorse, and I. Mirebeau, Phys. Rev. B **86**, 174403 (2012).

[68] J. P. C. Ruff, B. D. Gaulin, J. P. Castellan, K. C. Rule, J. P. Clancy, J. Rodriguez, and H. A. Dabkowska, Phys. Rev. Lett. **99**, 237202 (2007).

[69] M. Ruminy, E. Pomjakushina, K. Iida, K. Kamazawa, D. T. Adroja, U. Stuhr, and T. Fennell, Phys. Rev. B **94**, 024430 (2016).

[70] H. W. J. Blöte, R. F. Wielinga, and W. J. Huiskamp, Physica **43**, 549 (1969).

[71] J. A. Hodges, P. Bonville, A. Forget, A. Yaouanc, P. Dalmas de Réotier, G. André, M. Rams, K. Królas, C. Ritter, P. C. M. Gubbens, C. T. Kaiser, P. J. C. King, and C. Baines, Phys. Rev. Lett. **88**, 077204 (2002).

[72] Y. Yasui, M. Soda, S. Iikubo, M. Ito, M. Sato, N. Hamaguchi, T. Matsushita, N. Wada, T. Takeuchi, N. Aso, and K. Kakurai, J. Phys. Soc. Jpn. **72**, 3014 (2003).

[73] J. S. Gardner, G. Ehlers, N. Rosov, R. W. Erwin, and C. Petrovic, Phys. Rev. B **70**, 180404 (2004).

[74] K. A. Ross, J. P. C. Ruff, C. P. Adams, J. S. Gardner, H. A. Dabkowska, Y. Qiu, J. R. D. Copley, and B. D. Gaulin, Phys. Rev. Lett. **103**, 227202 (2009).

[75] L.-J. Chang, S. Onoda, Y. Su, Y.-J. Kao, K.-D. Tsuei, Y. Yasui, K. Kakurai, and M. R. Lees, Nat. Commun. **3**, 992 (2012).

[76] J. Gaudet, K. A. Ross, E. Kermarrec, N. P. Butch, G. Ehlers, H. A. Dabkowska, and B. D. Gaulin, Phys. Rev. B **93**, 064406 (2016).

[77] A. Yaouanc, P. D. d. Réotier, L. Keller, B. Roessli, and A. Forget, J. Phys.: Condens. Matter **28**, 426002 (2016).

[78] L. D. C. Jaubert, O. Benton, J. G. Rau, J. Oitmaa, R. R. P. Singh, N. Shannon, and M. J. P. Gingras, Phys. Rev. Lett. **115**, 267208 (2015).

[79] J. Robert, E. Lhotel, G. Remenyi, S. Sahling, I. Mirebeau, C. Decorse, B. Canals, and S. Petit, Phys. Rev. B **92**, 064425 (2015).

[80] H. D. Zhou, C. R. Wiebe, J. A. Janik, L. Balicas, Y. J. Yo, Y. Qiu, J. R. D. Copley, and J. S. Gardner, Phys. Rev. Lett. **101**, 227204 (2008).

[81] R. Sibille, E. Lhotel, M. C. Hatnean, G. Balakrishnan, B. Fåk, N. Gauthier, T. Fennell, and M. Kenzelmann, Phys. Rev. B **94**, 024436 (2016).

[82] K. Kimura, S. Nakatsuji, J. J. Wen, C. Broholm, M. B. Stone, E. Nishibori, and H. Sawa, Nat. Commun. **4** (2013).

[83] R. Sibille, E. Lhotel, V. Pomjakushin, C. Baines, T. Fennell, and M. Kenzelmann, Phys. Rev. Lett. **115**, 097202 (2015).

[84] J. J. Wen, S. M. Koohpayeh, K. A. Ross, B. A. Trump, T. M. McQueen, K. Kimura, S. Nakatsuji, Y. Qiu, D. M. Pajerowski, J. R. D. Copley, and C. L. Broholm, Phys. Rev. Lett. **118**, 107206 (2017).

[85] S. Petit, E. Lhotel, S. Guitteny, O. Florea, J. Robert, P. Bonville, I. Mirebeau, J. Ollivier, H. Mutka, E. Ressouche, C. Decorse, M. Ciomaga Hatnean, and G. Balakrishnan, Phys. Rev. B **94**, 165153 (2016).

[86] J. Villain, Zeitschrift für Physik B Condensed Matter **33**, 31 (1979).

[87] R. Moessner and J. T. Chalker, Phys. Rev. Lett. **80**, 2929 (1998).

[88] S. V. Isakov, K. Gregor, R. Moessner, and S. L. Sondhi, Phys. Rev. Lett. **93**, 167204 (2004).

[89] C. L. Henley, Phys. Rev. B **71**, 014424 (2005).

[90] R. Ballou, E. Lelièvre-Berna, and B. Fåk, Phys. Rev. Lett. **76**, 2125 (1996).

[91] M. J. Harris, M. P. Zinkin, Z. Tun, B. M. Wanklyn, and I. P. Swainson, Phys. Rev. Lett. **73**, 189 (1994).

[92] S. E. Palmer and J. T. Chalker, Phys. Rev. B **62**, 488 (2000).

[93] A. S. Wills, M. E. Zhitomirsky, B. Canals, J. Sanchez, P. Bonville, P. D. d. Réotier, and A. Yaouanc, J. Phys.: Condens. Matter **18**, L37 (2006).

[94] A. Del Maestro and M. J. P. Gingras, Phys. Rev. B **76**, 064418 (2007).

[95] J. D. M. Champion, A. S. Wills, T. Fennell, S. T. Bramwell, J. S. Gardner, and M. A. Green, Phys. Rev. B **64**, 140407 (2001).

[96] J. R. Stewart, G. Ehlers, A. S. Wills, S. T. Bramwell, and J. S. Gardner, J. Phys.: Condens. Matter **16**, L321 (2004).

[97] J. A. M. Paddison, A. B. Cairns, D. D. Khalyavin, P. Manuel, A. Daoud-Aladine, G. Ehlers, O. A. Petrenko, J. S. Gardner, H. Zhou, and A. L. Goodwin, arXiv preprint: arXiv:1506.05045 (2015).

[98] B. Javanparast, Z. Hao, M. Enjalran, and M. J. P. Gingras, Phys. Rev. Lett. **114**, 130601 (2015).

[99] J. A. Quilliam, K. A. Ross, A. G. Del Maestro, M. J. P. Gingras, L. R. Corruccini, and J. B. Kycia, Phys. Rev. Lett. **99**, 097201 (2007).

[100] J. R. Stewart, J. S. Gardner, Y. Qiu, and G. Ehlers, Phys. Rev. B **78**, 132410 (2008).

[101] V. N. Glazkov, M. E. Zhitomirsky, A. I. Smirnov, H.-A. Krug von Nidda, A. Loidl, C. Marin, and J.-P. Sanchez, Phys. Rev. B **72**, 020409 (2005).

[102] V. N. Glazkov, A. I. Smirnov, J. P. Sanchez, A. Forget, D. Colson, and P. Bonville, J. Phys.: Condens. Matter **18**, 2285 (2006).

[103] V. N. Glazkov, M. Zhitomirsky, A. I. Smirnov, C. Marin, J. P. Sanchez, A. Forget, D. Colson, and P. Bonville, J. Phys.: Condens. Matter **19**, 145271 (2007).

[104] P. R. Willmott, D. Meister, S. J. Leake, M. Lange, A. Bergamaschi, M. Böge, M. Calvi, C. Cancellieri, N. Casati, A. Cervellino, Q. Chen, C. David, U. Flechsig, F. Gozzo, B. Henrich, S. Jäggi-Spielmann, B. Jakob, I. Kalichava, P. Karvinen, J. Krempasky, A. Lüdeke, R. Lüscher, S. Maag, C. Quitmann, M. L. Reinle-Schmitt, T. Schmidt, B. Schmitt, A. Streun, I. Vartiainen, M. Vitins, X. Wang, and R. Wullschleger, J. Synchrotron Radiat. **20**, 667 (2013).

[105] D. L. Abernathy, M. B. Stone, M. J. Loguillo, M. S. Lucas, O. Delaire, X. Tang, J. Y. Y. Lin, and B. Fultz, Rev. Sci. Instrum. **83**, 015114 (2012).

[106] C. Kittel, *Introduction to solid state physics*, Vol. 162 (John Wiley & Sons, 1966).

[107] J. Laugier, OrientExpress V3.3 (software), jean.laugier@free.fr.

[108] G. L. Squires, *Introduction to the theory of thermal neutron scattering* (Cambridge university press, 2012).

[109] P. J. Brown, Institute Laue Langevin, Grenoble, FRANCE, https://www.ill.eu/sites/ccsl/ffacts/ffachtml.html.

[110] Powder diffraction, http://pd.chem.ucl.ac.uk/pdnn/diff2/kinemat2.htm.

[111] H. M. Rietveld, J. Appl. Cryst. **2**, 65 (1969).

[112] DMC instrument description, https://www.psi.ch/sinq/dmc/description.

[113] A. Yaouanc and P. D. De Réotier, *Muon spin rotation, relaxation, and resonance: applications to condensed matter* (Oxford University Press, 2011).

[114] E. S. Jeff, *Muon Spin Rotation/Relaxation/Resonance*, Simon Fraser University.

[115] R. S. Hayano, Y. J. Uemura, J. Imazato, N. Nishida, T. Yamazaki, and R. Kubo, Phys. Rev. B **20**, 850 (1979).

[116] S. Andreas and W. Bastian, *Musrfit User Manual*.

[117] G. Sala, M. J. Gutmann, D. Prabhakaran, D. Pomaranski, C. Mitchelitis, J. B. Kycia, D. G. Porter, C. Castelnovo, and J. P. Goff, Nat. Mater. **13**, 488 (2014).

[118] R. D. Shannon and A. W. Sleight, Inorg. Chem. **7**, 1649 (1968).

[119] D. Prabhakaran, S. Wang, and A. Boothroyd, J. Cryst. Growth , (2016).

[120] T. Moriga, A. Yoshiasa, F. Kanamaru, K. Koto, M. Yoshimura, and S. Somiya, Solid State Ionics **31**, 319 (1989).

[121] R. C. Ewing, W. J. Weber, and J. Lian, J. Appl. Phys. **95**, 5949 (2004).

[122] B. Tolla, A. Demourgues, O. Isnard, M. Menetrier, M. Pouchard, L. Rabardel, and T. Seguelong, J. Mater. Chem. **9**, 3131 (1999).

[123] A. Yaouanc, P. Dalmas de Réotier, C. Marin, and V. Glazkov, Phys. Rev. B **84**, 172408 (2011).

[124] T. Uehara, K. Koto, F. Kanamaru, and H. Horiuchi, Solid State Ionics **23**, 137 (1987).

[125] R. D. Shannon and C. T. Prewitt, Acta Cryst. **26**, 1046 (1970).

[126] R. S. Roth, J. Res. Nat. Bur. Stand **56**, 17 (1956).

[127] S. Lutique, P. P. Javorský, R. J. M. Konings, A. C. G. van Genderen, J. C. van Miltenburg, and F. Wastin, J. Chem. Thermodyn. **35**, 955 (2003).

[128] M. C. Hatnean, M. R. Lees, O. A. Petrenko, D. S. Keeble, G. Balakrishnan, M. J. Gutmann, V. V. Klekovkina, and B. Z. Malkin, Phys. Rev. B **91**, 174416 (2015).

[129] E. Lhotel, S. Petit, S. Guitteny, O. Florea, M. Ciomaga Hatnean, C. Colin, E. Ressouche, M. R. Lees, and G. Balakrishnan, Phys. Rev. Lett. **115**, 197202 (2015).

[130] V. K. Anand, A. K. Bera, J. Xu, T. Herrmannsdörfer, C. Ritter, and B. Lake, Phys. Rev. B **92**, 184418 (2015).

[131] A. Bertin, P. Dalmas de Réotier, B. Fåk, C. Marin, A. Yaouanc, A. Forget, D. Sheptyakov, B. Frick, C. Ritter, A. Amato, C. Baines, and P. J. C. King, Phys. Rev. B **92**, 144423 (2015).

[132] Z. Tian, Y. Kohama, T. Tomita, H. Ishizuka, T. H. Hsieh, J. J. Ishikawa, K. Kindo, L. Balents, and S. Nakatsuji, Nat. Phys. **12**, 134 (2016).

[133] Y. Yasui, Y. Kondo, M. Kanada, M. Ito, H. Harashina, M. Sato, and K. Kakurai, J. Phys. Soc. Jpn. **70**, 284 (2001).

[134] Y. Yasui, S. Iikubo, H. Harashina, T. Kageyama, M. Ito, M. Sato, and K. Kakurai, J. Phys. Soc. Jpn. **72**, 865 (2003).

[135] K. Ueda, J. Fujioka, Y. Takahashi, T. Suzuki, S. Ishiwata, Y. Taguchi, and Y. Tokura, Phys. Rev. Lett. **109**, 136402 (2012).

[136] K. Tomiyasu, K. Matsuhira, K. Iwasa, M. Watahiki, S. Takagi, M. Wakeshima, Y. Hinatsu, M. Yokoyama, K. Ohoyama, and K. Yamada, J. Phys. Soc. Jpn. **81**, 034709 (2012).

[137] M. Watahiki, K. Tomiyasu, K. Matsuhira, K. Iwasa, M. Yokoyama, S. Takagi, M. Wakeshima, and Y. Hinatsu, J. Phys.: Conf. Ser. **320**, 012080 (2011).

[138] M. D. Alice, K. Peter, and L. R. Corruccini, J. Phys.: Condens. Matter **20**, 235208 (2008).

[139] N. P. Raju, M. Dion, M. J. P. Gingras, T. E. Mason, and J. E. Greedan, Phys. Rev. B **59**, 14489 (1999).

[140] V. Bondah-Jagalu and S. T. Bramwell, Can. J. Phys. **79**, 1381 (2001).

[141] O. A. Petrenko, M. R. Lees, G. Balakrishnan, and D. M. Paul, Phys. Rev. B **70**, 012402 (2004).

[142] O. A. Petrenko, M. R. Lees, G. Balakrishnan, V. N. Glazkov, and S. S. Sosin, Phys. Rev. B **85**, 180412 (2012).

[143] R. S. Freitas and J. S. Gardner, J. Phys.: Condens. Matter **23**, 164215 (2011).

[144] S. Singh, S. Saha, S. K. Dhar, R. Suryanarayanan, A. K. Sood, and A. Revcolevschi, Phys. Rev. B **77**, 054408 (2008).

[145] B. Z. Malkin, T. T. A. Lummen, P. H. M. v. Loosdrecht, G. Dhalenne, and A. R. Zakirov, J. Phys.: Condens. Matter **22**, 276003 (2010).

[146] F. Gozzo, A. Cervellino, M. Leoni, P. Scardi, A. Bergamaschi, and B. Schmitt, Zeitschrift für Kristallographie Crystalline Materials **225**, 616 (2010).

[147] S. Lutique, P. Javorský, R. J. M. Konings, J. C. Krupa, A. C. G. van Genderen, J. C. van Miltenburg, and F. Wastin, J. Chem. Thermodyn. **36**, 609 (2004).

[148] P. E. R. Blanchard, R. Clements, B. J. Kennedy, C. D. Ling, E. Reynolds, M. Avdeev, A. P. J. Stampfl, Z. Zhang, and L.-Y. Jang, Inorg. Chem. **51**, 13237 (2012).

[149] T. Moriga, A. Yoshiasa, F. Kanamaru, K. Koto, M. Yoshimura, and S. Somiya, Solid State Ionics **31**, 319 (1989).

[150] L. Minervini, R. W. Grimes, and K. E. Sickafus, J. Am. Ceram. Soc. **83**, 1873 (2000).

[151] P. J. Brown, Calculator for magnetostatic energy and demagnetizing factor, http://www.magpar.net/static/magpar/doc/html/demagcalc.html.

[152] O. Benton, Phys. Rev. B **94**, 104430 (2016).

[153] H. Fukazawa, R. G. Melko, R. Higashinaka, Y. Maeno, and M. J. P. Gingras, Phys. Rev. B **65**, 054410 (2002).

[154] Y. Onose, Y. Taguchi, T. Ito, and Y. Tokura, Phys. Rev. B **70**, 060401 (2004).

[155] S. Petit, E. Lhotel, B. Canals, M. Ciomaga Hatnean, J. Ollivier, H. Mutka, E. Ressouche, A. R. Wildes, M. R. Lees, and G. Balakrishnan, Nat. Phys. **12**, 746 (2016).

[156] L. Opherden, J. Hornung, T. Herrmannsdörfer, J. Xu, A. T. M. N. Islam, B. Lake, and J. Wosnitza, Phys. Rev. B **95**, 184418 (2017).

[157] A. T. Boothroyd, SPECTRE – a program for calculating spectroscopic properties of rare earth ions in crystals (1990–2014).

[158] A. T. Boothroyd, S. M. Doyle, D. M. Paul, and R. Osborn, Phys. Rev. B **45**, 10075 (1992).

[159] A. J. Princep, D. Prabhakaran, A. T. Boothroyd, and D. T. Adroja, Phys. Rev. B **88**, 104421 (2013).

[160] J. Zhang, K. Fritsch, Z. Hao, B. V. Bagheri, M. J. P. Gingras, G. E. Granroth, P. Jiramongkolchai, R. J. Cava, and B. D. Gaulin, Phys. Rev. B **89**, 134410 (2014).

[161] G. F. Koster, *Properties of the thirty-two point groups*, Vol. 24 (The MIT Press, 1963).

[162] J. Xu, V. K. Anand, A. K. Bera, M. Frontzek, D. L. Abernathy, N. Casati, K. Siemensmeyer, and B. Lake, Phys. Rev. B **92**, 224430 (2015).

[163] M. Bouvier, P. Lethuillier, and D. Schmitt, Phys. Rev. B **43**, 13137 (1991).

[164] B. Alexandre, *Geometrical frustration and quantum origin of spin dynamics*, université Grenoble Alpes, P.h.D thesis.

[165] V. K. Anand, D. L. Abernathy, D. T. Adroja, A. D. Hillier, P. K. Biswas, and B. Lake, Phys. Rev. B **95**, 224420 (2017).

[166] M. E. Brooks-Bartlett, S. T. Banks, L. D. C. Jaubert, A. Harman-Clarke, and P. C. W. Holdsworth, Phys. Rev. X **4**, 011007 (2014).

[167] R. T. Azuah, L. R. Kneller, Y. Qiu, P. L. Tregenna-Piggott, C. M. Brown, J. R. Copley, and R. M. Dimeo, Journal of Research of the National Institute of Standards and Technology **114**, 341 (2009).

[168] R. A. Ewings, A. Buts, M. D. Le, J. van Duijn, I. Bustinduy, and T. G. Perring, Nucl. Instrum. Methods Phys. Res., Sect. A **834**, 132 (2016).

[169] Plot.py project, http://plotpy.sourceforge.net/.

[170] Z. Hao, A. G. R. Day, and M. J. P. Gingras, Phys. Rev. B **90**, 214430 (2014).

[171] T. Fennell, O. A. Petrenko, B. Fåk, J. S. Gardner, S. T. Bramwell, and B. Ouladdiaf, Phys. Rev. B **72**, 224411 (2005).

[172] J. A. Hodges, P. Bonville, A. Forget, M. Rams, K. Królas, and G. Dhalenne, J. Phys: Condens. Matter **13**, 9301 (2001).

[173] H. B. Cao, A. Gukasov, I. Mirebeau, and P. Bonville, J. Phys: Condens. Matter **21**, 492202 (2009).

[174] Y. Yasui, M. Soda, S. Iikubo, M. Ito, M. Sato, N. Hamaguchi, T. Matsushita, N. Wada, T. Takeuchi, and N. Aso, J. Phys. Soc. Jpn. **72**, 3014 (2003).

[175] P. Bonville, S. Guitteny, A. Gukasov, I. Mirebeau, S. Petit, C. Decorse, M. C. Hatnean, and G. Balakrishnan, Phys. Rev. B **94**, 134428 (2016).

[176] S. Onoda and Y. Tanaka, Phys. Rev. Lett. **105**, 047201 (2010).

[177] R. Sibille, E. Lhotel, M. C. Hatnean, G. Balakrishnan, B. Fåk, N. Gauthier, T. Fennell, and M. Kenzelmann, Phys. Rev. B **94**, 024436 (2016).

[178] R. Sibille, N. Gauthier, H. Yan, M. C. Hatnean, J. Ollivier, B. Winn, G. Balakrishnan, M. Kenzelmann, N. Shannon, and T. Fennell, arXiv preprint arXiv:1706.03604 (2017).

[179] J. Lago, T. Lancaster, S. J. Blundell, S. T. Bramwell, F. L. Pratt, M. Shirai, and C. Baines, J. Phys.: Condens. Matter **17**, 979 (2005).

[180] P. Dalmas de Réotier, A. Yaouanc, L. Keller, A. Cervellino, B. Roessli, C. Baines, A. Forget, C. Vaju, P. C. M. Gubbens, A. Amato, and P. J. C. King, Phys. Rev. Lett. **96**, 127202 (2006).

[181] F. Bert, P. Mendels, A. Olariu, N. Blanchard, G. Collin, A. Amato, C. Baines, and A. D. Hillier, Phys. Rev. Lett. **97**, 117203 (2006).

[182] A. Yaouanc, P. Dalmas de Réotier, P. Bonville, J. A. Hodges, V. Glazkov, L. Keller, V. Sikolenko, M. Bartkowiak, A. Amato, C. Baines, P. J. C. King, P. C. M. Gubbens, and A. Forget, Phys. Rev. Lett. **110**, 127207 (2013).

[183] A. Maisuradze, P. Dalmas de Réotier, A. Yaouanc, A. Forget, C. Baines, and P. J. C. King, Phys. Rev. B **92**, 094424 (2015).

[184] J. Lago, S. J. Blundell, and C. Baines, J. Phys.: Condens. Matter **19**, 326210 (2007).

[185] J. Snyder, J. S. Slusky, R. J. Cava, and P. Schiffer, Nature **413**, 48 (2001).

[186] MUSRFIT, a programme developed by Andreas Suter and Bastian Wojek in the Paul Scherrer Institute.

[187] S. Andreas and W. Bastian, *Musrfit User Manual*, note that in Ref.[113] $\Delta_{\text{eff}}^2 = (1 + R_b^2)\Delta_0^2$ is used in the equation instead of Δ_0.

[188] J. Xu, C. Balz, C. Baines, H. Luetkens, and B. Lake, Phys. Rev. B **94**, 064425 (2016).

[189] H. R. Molavian, M. J. P. Gingras, and B. Canals, Phys. Rev. Lett. **98**, 157204 (2007).

[190] F. R. Foronda, F. Lang, J. S. Möller, T. Lancaster, A. T. Boothroyd, F. L. Pratt, S. R. Giblin, D. Prabhakaran, and S. J. Blundell, Phys. Rev. Lett. **114**, 017602 (2015).

[191] P. Dalmas de Réotier, A. Yaouanc, P. C. M. Gubbens, C. T. Kaiser, C. Baines, and P. J. C. King, Phys. Rev. Lett. **91**, 167201 (2003).

[192] MμCalc, a software for calculating fields inside crystals developed by A. J. Steele; *Quantum magnetism probed with muon-spin relaxation*, Oxford University, PhD thesis.

[193] P. A. McClarty, J. N. Cosman, A. G. D. Maestro, and M. J. P. Gingras, J. Phys: Condens. Matter **23**, 164216 (2011).

[194] B. G. Ueland, G. C. Lau, R. J. Cava, J. R. O Brien, and P. Schiffer, Phys. Rev. Lett. **96**, 027216 (2006).

[195] S. H. Lee, C. Broholm, W. Ratcliff, G. Gasparovic, Q. Huang, T. H. Kim, and S. W. Cheong, Nature **418**, 856 (2002).

[196] A. M. P. Joseph, E. Georg, A. P. Oleg, R. W. Andrew, S. G. Jason, and J. R. Stewart, J. Phys.: Condens. Matter **29**, 144001 (2017).

[197] E. Bertin, P. Bonville, J. P. Bouchaud, J. A. Hodges, J. P. Sanchez, and P. Vulliet, Eur. Phys. J. B **27**, 347 (2002).

[198] Y. Chapuis, D. de Réotier, C. Marin, A. Yaouanc, A. Forget, A. Amato, and C. Baines, Physica B: Conden. Matter **404**, 686 (2009).

[199] P. Bonville, J. A. Hodges, M. Ocio, J. P. Sanchez, P. Vulliet, S. Sosin, and D. Braithwaite, J. Phys.: Condens. Matter **15**, 7777 (2003).

[200] P. Bonville, J. A. Hodges, E. Bertin, J.-P. Bouchaud, P. D. de Réotier, L.-P. Regnault, H. M. Rønnow, J.-P. Sanchez, S. Sosin, and A. Yaouanc, Hyperfine Interact. **156**, 103 (2004).

[201] A. Yaouanc, P. D. de Réotier, V. Glazkov, C. Marin, P. Bonville, J. A. Hodges, P. C. M. Gubbens, S. Sakarya, and C. Baines, Phys. Rev. Lett. **95**, 047203 (2005).

[202] S. R. Dunsiger, R. F. Kiefl, J. A. Chakhalian, J. E. Greedan, W. A. MacFarlane, R. I. Miller, G. D. Morris, A. N. Price, N. P. Raju, and J. E. Sonier, Phys. Rev. B **73**, 172418 (2006).

[203] N. Matyushenko, E. Shevyakova, E. Lifshits, and N. Lapina, Russ. J. Inorg. Chem. **30**, 942 (1985).

[204] U. Kolitsch, H. Seifert, and F. Aldinger, J. Alloys Compd **257**, 104 (1997).

[205] A. M. P. Joseph, J. R. Stewart, and L. G. Andrew, J. Phys.: Condens. Matter **25**, 454220 (2013).

[206] J. A. M. Paddison and A. L. Goodwin, Phys. Rev. Lett. **108**, 017204 (2012).

[207] J. A. M. Paddison, H. Jacobsen, O. A. Petrenko, M. T. Fernández-Díaz, P. P. Deen, and A. L. Goodwin, Science **350**, 179 (2015).

[208] J. A. M. Paddison, M. J. Gutmann, J. R. Stewart, M. G. Tucker, M. T. Dove, D. A. Keen, and A. L. Goodwin, arXiv preprint arXiv:1602.08420 (2016).

[209] B. Canals and D. A. Garanin, Can. J. Phys. **79**, 1323 (2001).

[210] E. Bertaut and P. Burlet, Solid State Commun. **5**, 279 (1967).

[211] B. Canals and C. Lacroix, Phys. Rev. Lett. **80**, 2933 (1998).

[212] B. Canals and C. Lacroix, Phys. Rev. B **61**, 1149 (2000).

[213] D. A. Garanin and B. Canals, Phys. Rev. B **59**, 443 (1999).

[214] E. Balcar and S. Lovesey, J. Phys. C: Solid State Phys. **19**, 4605 (1986).

[215] A. J. Freeman and R. Watson, Phys. Rev. **127**, 2058 (1962).

[216] J. G. Rau, L. S. Wu, A. F. May, L. Poudel, B. Winn, V. O. Garlea, A. Huq, P. Whitfield, A. E. Taylor, M. D. Lumsden, M. J. P. Gingras, and A. D. Christianson, Phys. Rev. Lett. **116**, 257204 (2016).

[217] S. Singh, S. Saha, S. K. Dhar, R. Suryanarayanan, A. K. Sood, and A. Revcolevschi, Phys. Rev. B **77**, 054408 (2008).

[218] Z. Qu, C. Wan, and W. Pan, Chem. Mater. **19**, 4913 (2007).

[219] M. Maczka, J. Hanuza, K. Hermanowicz, A. F. Fuentes, K. Matsuhira, and Z. Hiroi, J Raman Spectrosc. **39**, 537 (2008).

[220] B. P. Mandal, A. Banerji, V. Sathe, S. K. Deb, and A. K. Tyagi, J. Solid State Chem. **180**, 2643 (2007).

[221] P. Dalmas de Réotier, A. Yaouanc, L. Keller, A. Cervellino, B. Roessli, C. Baines, A. Forget, C. Vaju, P. C. M. Gubbens, A. Amato, and P. J. C. King, Phys. Rev. Lett. **96**, 127202 (2006).

[222] F. Bert, P. Mendels, A. Olariu, N. Blanchard, G. Collin, A. Amato, C. Baines, and A. D. Hillier, Phys. Rev. Lett. **97**, 117203 (2006).

[223] A. Yaouanc, P. Dalmas de Réotier, P. Bonville, J. A. Hodges, V. Glazkov, L. Keller, V. Sikolenko, M. Bartkowiak, A. Amato, C. Baines, P. J. C. King, P. C. M. Gubbens, and A. Forget, Phys. Rev. Lett. **110**, 127207 (2013).

[224] S. Blundell, *Magnetism in Condensed Matter* (Oxford University Press, 2003).

[225] G. E. Barberis, D. Davidov, J. P. Donoso, C. Rettori, J. F. Suassuna, and H. D. Dokter, Phys. Rev. B **19**, 5495 (1979).

[226] G. Fuller and V. W. Cohen, *NUCLEAR SPINS AND MOMENTS.* (1969).

List of Publications

- *Observation of long-range magnetic ordering in pyrohafnate $Nd_2Hf_2O_7$: A neutron diffraction study*, V. K. Anand, A. K. Bera, **J. Xu**, T. Herrmannsdörfer, C. Ritter, and B. Lake, Phys. Rev. B **92**, 184418 (2015)

- *Magnetic structure and crystal-field states of the pyrochlore antiferromagnet $Nd_2Zr_2O_7$*, **J. Xu**, V. K. Anand, A. K. Bera, M. Frontzek, D. L. Abernathy, N. Casati, K. Siemensmeyer, and B. Lake, Phys. Rev. B **92**, 224430 (2015)

- *Spin dynamics of the ordered dipolar-octupolar pseudospin-1/2 pyrochlore $Nd_2Zr_2O_7$ probed by muon spin relaxation*, **J. Xu**, C. Balz, C. Baines, H. Luetkens, and B. Lake, Phys. Rev. B **94**, 064425 (2016)

- *Physical properties of the candidate quantum spin-ice system $Pr_2Hf_2O_7$*, V. K. Anand, L. Opherden, **J. Xu**, D. T. Adroja, A. T. M. N. Islam, T. Herrmannsdörfer, J. Hornung, R. Schönemann, M. Uhlarz, H. C. Walker, N. Casati, and B. Lake, Phys. Rev. B **94**, 144415 (2016)

- Evolution of antiferromagnetic domains in the all-in-all-out ordered pyrochlore $Nd_2Zr_2O_7$, L. Opherden, J. Hornung, T. Herrmannsdörfer, **J. Xu**, A. T. M. N. Islam, B. Lake, and J. Wosnitza, Phys. Rev. B **95**, 184418 (2017)

Eidesstattliche Versicherung

Hiermit versichere ich an Eides Statt, dass ich meine Dissertation mit dem Titel:

“Magnetic Properties of Rare Earth Zirconate Pyrochlores”

selbstständig verfasst habe. Alle benutzten Hilfsmittel und Quellen sind in der Arbeit aufgeführt.

Berlin, den 12. 07. 2017 Jianhui Xu